S   A   I   W

G   T -T   I

by

Alexander S. Korobov

A thesis
presented to the University of Waterloo
in fulfilment of the
thesis requirement for the degree of
Doctor of Philosophy
in
Applied Mathematics

Waterloo, Ontario, Canada, 2007

I hereby declare that I am the sole author of this thesis. This is a true copy of the thesis, including any required final revisions, as accepted by my examiners.

I understand that my thesis may be made electronically available to the public.

Abstract

Internal waves in the deep ocean play a deciding role in processes such as climate change and nutrient cycles. Winds and tidal currents over topography feed energy into internal waves at large scales; through nonlinear interaction the energy then cascades to turbulence scales and contributes to deep-ocean mixing. The connection of internal waves to deep-ocean mixing is what makes them important. In this thesis we address the problem of energy transfer in internal waves by modelling a two-dimensional flow over idealized topography and analysing the spectra of the generated wave fields. The main tool used is the nonparametric spectral analysis, some aspects of which are reviewed in one of the chapters. The numerical experiments were performed for a number of latitudes, topographies and background flows. The wave field generated by tide-topography interaction includes both progressive and trapped internal waves. The wave spectrum was found to exhibit a self-similar structure with prominent peaks at tidal harmonics and interharmonics, whose magnitudes decay exponentially as a function of the frequency. Subharmonics are generated by an instability of tidal beams, which is particularly strong for near-critical latitudes, where the Coriolis frequency is half the tidal frequency; other interharmonics are produced through resonant and non-resonant triad wave-wave interaction. As the triad interaction can be either resonant or non-resonant, some harmonics and interharmonics correspond to progressive waves, if the frequency is within the free internal wave range, while the others are trapped waves if the frequency is outside the range. Spatial scales of harmonics and interharmonics were investigated. In particular, it was shown that interharmonics typically have smaller vertical scales. Through the use of spatial analysis it was shown that there is a discrete number of wave-wave interactions responsible for the total energy transfer. The results of the thesis provide insight into the complex nature of internal wave interactions and may be helpful for interpreting recent observational results.

Acknowledgments

I would like to acknowledge and extend my gratitude to the following persons who have made the completion of this thesis possible: my supervisor, Prof. Kevin Lamb, for his guidance and support; Prof. Marek Stastna for useful discussions; Prof. Stanley Lipshitz for his advice on spectral analysis; all Applied Mathematics faculty members and staff.

Contents

3 Temporal Spectral Analysis: Part I

List of Figures

x

xiii

List of Tables

Chapter 1

Introduction

1.1 History

An internal wave is a periodic oscillation in a density stratified fluid that arises due to restoring buoyancy forces. The first recorded observation of internal waves, according to Lamb (1932), was by Benjamin Franklin. In a letter dated December 1, 1762, he describes oscillations of the interface between oil and water in a sea lantern:

> . . . the surface of the oil was perfectly tranquil, and duly preserved its position with regard to the brim of the glass, the water under the oil was in great commotion, rising and falling in irregular waves. . .

The earliest theoretical study of internal waves took place almost a century later. Stokes (1847) developed the first theory of waves occurring at an interface of a light fluid overlaying a heavy fluid. Stokes' theory was extended to waves in a continuously stratified fluid by Rayleigh (1883).

Present everywhere in the ocean and atmosphere, internal waves are not readily visible. However, there are some manifestations of the phenomenon in our everyday life: for example, the rippled cloud pattern occurring when the vapour gathers along the wavefronts of internal waves; or the pattern of parallel slicks on the ocean surface, caused by tidally generated internal waves.

The most striking manifestation of internal waves, which was not originally associated with internal waves, is the phenomenon called "dead water". A ship travelling in "dead water" appears to be held back and becomes difficult to manoeuvre. The strange circumstance was well known to seafarers since antiquity, and the measures against it, according to the old mariners'

lore, included the most unpredictable antics, such as firing guns into the water, pouring oil on the water ahead of the vessel, slashing and beating the water beside the ship with oars, banishing monks from the ship, etc.

Explanations of the phenomenon were of comparable imagination. Lucan (AD 39–65), according to his epic poem "Pharsalia" (book 6, verses 797–799), Pliny the Elder (AD 23–79), according to his "Natural History" (volumes IX and XXXII), and many others later, believed that the cause of "dead water" was a small fish, called *echeneis remora*, capable of checking a ship's motion by attaching itself to the rudder of the vessel. Plutarch, AD 46, suggested an alternative mechanical explanation, algae accumulated at the bottom of the ship. Other explanations included magnetic rocks attracting iron parts of the ship, minuscule invisible strings and hooks attached to the ship and occult powers of various sorts (see Copenhaver, 1991). An explanation, closest to the truth, was, perhaps, by a French natural philosopher Gassendi (1654), who guessed that a ship may be checked in motion due to adverse undercurrents.

The tale of the magic fish survived the Middle Ages and the Renaissance. In the literature of those periods we can find a great number of allusions to *echeneis remora*, as in "Pantagruel" by François Rabelais (1532):

> The sucking-fish, with secret chains
> Clung to the keel, the swiftest ship detains...

The legendary fish-shipholder was also reflected in various paintings of the early time (see Gudger, 1930). Figure 1.1 shows an illustration from a 14th-century copy of "Der Naturen Bloeme" by Jacob van Maerlant (1225–1300), a Flemish poet of the Middle Ages, and another more recent depiction of *remora* from the book "Emblemata" by an Italian Renaissance writer Andrea Alciato (1492–1550).

If the magic fish can indeed be identified with the "dead water" phenomenon, then it is possible that the undesirable effect might have changed the course of history more than once. For example, internal waves might have been the cause of Mark Antony's defeat in September 2, 31 BC. The battle of Actium took place in the Adriatic Sea near the shore where there is a constant runoff of fresh river water. If we refer to the "Natural History" of Pliny the Elder, book XXXII (E. H. Warmington's translation), we find the following interpretation of the historical event:

> It is said that at the battle of Actium the fish stopped the flagship of Antonius, who was hastening to go round and encourage his men, until he changed his ship for another one, and so the fleet of Cæsar at once made a more violent attack.

In a similar fashion, internal waves appear in the histories of Caligula and Periander.

| Der Naturen Bloeme (1350) | Emblemata (1621) |

F   1.1: Two depictions of the magic fish *echeneis remora*.

The puzzle of "dead water" was solved only at the beginning of the 20th century after one of the North Polar expeditions by a famous Norwegian explorer Fridtjof Nansen (see Walker, 1991; Parker, 1999). On August 1893 he recorded that the expedition ship *Fram* travelling off the Taymyr Peninsula encountered what Norwegian mariners called *dödvand*: the ship did not answer the helm properly and was greatly slowed. Five years later, in November 1898, Nansen wrote a letter to his former fellow student, the eminent physicist and meteorologist of that time Vilhelm Bjerknes, inquiring on what could be the cause of the phenomenon. Bjerknes replied that the ship must generate internal waves at the boundary between the fresh and salty water typical for the geographical location and that "the great resistance experienced by the ship was due to the work done in generating these invisible waves". Then, he assigned a talented student, a famous oceanographer in the years to come, Walfrid Ekman, to study Nansen's observations and perform laboratory experiments in order to resolve the problem. Figure 1.2 shows the portraits of the three famous Scandinavian scientists. Ekman (1904) used a model boat in a tank of stratified fluid and showed that the explanation of Bjerknes was correct: unless the boat exceeds the maximum speed of internal waves, i.e. about $6.4 \ \mathrm{km \, h^{-1}}$, it will lose most of its energy to the generation of internal waves.

According to Ekman (1931) and Munk (1980), Nansen, on his North Polar Expedition during 1893–1896, was also the first to observe internal oscillations in the deep ocean (Nansen, 1902). The discovery was followed by a number of similar observations during 1900–1904 made by him and by Helland-Hansen (for the overview, see Helland-Hansen and Nansen, 1909). After that time internal waves became a special object of investigation studied by various mathematicians and oceanographers including such historical figures as Geoffrey Taylor, Walfrid Ekman, Horace Lamb, etc. Due to the complexity of the phenomenon, the understanding of internal waves in the deep ocean developed very slowly. It was not clear what the main sources of internal waves

Fridtjof Nansen   Vilhelm Bjerknes   Walfrid Ekman

F   1.2: Famous Scandinavian scientists who started the study of internal waves in the ocean.

were, how internal wave properties depended on geographical location and season, where and how the waves dissipate or break. Bigelow (1931) summarizes the problems in oceanography of that time:

> Our present knowledge of submarine boundary (or internal) waves in the open oceans has hardly advanced beyond the realization that such things exist and that they may be set up by a variety of forces. We need to learn what conditions give rise to progressive boundary waves, what conditions to standing waves; their periods; their relation to the free tidal wave; and their rôle in general in the sea, including such points as their frequency in different regions at different seasons, their vertical amplitudes, their lengths from crest to crest, and so forth.

Among the questions concerning internal waves in the ocean, one of the most pressing questions, since the discovery of internal waves in the ocean, was about main sources. The question has had a history of controversy from the beginning of internal wave research. In particular, much difficulty was met when trying to understand tides as sources of internal waves.

Not much later after Nansen's discovery, Pettersson (1908) observed vertical internal movements in Danish sounds and found that they seemed to exhibit tidal periodicity. Internal waves of tidal frequency are now called internal tides (for a modern overview of internal tides, see, for example, Garrett and Kunze, 2007). Although Pettersson followed his discovery with admirable energy and repeatedly carried out observations showing a connection between tides and internal waves, Pettersson's mathematical explanation of the observations was quite far-fetched and unconvincing (see Ekman, 1931).

We can now identify two misconceptions that lingered in the minds of the pioneers of internal wave research. The first one was the misleading belief that tide-generating forces give rise to internal waves directly, i.e. astronomical bodies such as the moon and sun directly attract layers of fluid causing internal waves. The second misconception was that internal waves' kinematics

4

are similar in nature to those of surface waves (that is why internal waves were often referred to as "boundary waves"). The theory developed in the framework of a two-phase fluid did not give adequate results.

Discrepancies arising from these incorrect assumptions puzzled early observers and prevented scientists from finding the correct causal connection between internal waves and tides (see Hendershott, 1980). Thus, there were doubts whether tides are sources of internal waves. For example, in the paper "On Internal Waves", Ekman (1931) concludes that "the tide-generating force has little or no tendency to raise or maintain internal waves". In his paper, he also mentions two possible, but "unlikely" explanations of how tides might generate internal waves: first, small waves generated by tides directly can attain large values through a resonance, and, second, internal waves of tidal periods may be, in fact, the so-called "secondary boundary waves", generated "by ordinary tidal currents running over an uneven sea-bottom". Ekman's second guess was in fact correct: it is now known that tidal currents flowing over rough topography represent one of the most important mechanisms for internal wave generation. In his second guess, Ekman was alluding to the work of Zeilon (1912, 1913) who, through his mathematical and experimental study, had come up with the following result:

> If the bulk of water (deep-water and top layer) is performing an alternating motion like e.g. a tidal or seiche-current, and if it has to pass a bottom ridge or a hump or the like, the disturbing effect of the latter will reach the top layer and will give rise in the common boundary to an internal wave-motion, emerging from the place of disturbance and having the same period as the original alternating current.

However, Ekman believed that this effect was too weak to explain the observed internal waves of 10 or 20 metres in height. According to LaFond (1962), the issue was resolved after Zeilon (1934) showed experimentally that strong internal waves do occur when a tidal current flows over a coastal bank. Around the same time, as if to help to overcome difficulties with the mathematical explanation of such internal waves, Fjeldstad (1933) developed a theory for internal waves in a heterogeneous fluid.

Half a century later, the possible sources of the internal waves in the ocean were well known, but their relative importance was not clear at all. In a review by Müller et al. (1986), we find: "The major energy source or sources of the deep ocean internal wave field have ... not yet been identified." The present answer to the question under debate is that there are two major sources of internal waves, both of approximately equal strengths: winds and tides (see, for example, Munk and Wunsch, 1998).

1.2 Importance

Internal waves in the ocean are important for a number of reasons, some of which are listed below: they affect long-term global processes such as the Earth's climate and abyssal circulation; play a role in biological and chemical cycles in the ocean; represent a hazard for oil drilling operations and submarines; distort sound transmission; have an impact on life of cetaceans, i.e. whales, dolphins and porpoises.

The reason why internal waves affect such seemingly remote processes as the Earth's climate and abyssal circulation, is due to the connection of internal waves to deep-ocean mixing (Garrett, 2003). Mixing in the deep ocean conveys heat from the upper layer of the ocean to the abyssal cold waters, and, thus, helps sustain the meridional overturning circulation, in which the water masses from the abyss slowly upwell to the surface. Internal waves play a crucial role in transferring energy from the primary sources of oceanic mechanical energy, i.e. from tides and winds, to mixing (Dewar et al. (2006) suggests that the marine biosphere is another important source of energy for mixing). This role makes internal waves much more than a background noise in the medium: internal waves are an important dynamical part of global processes in the ocean, including climate change and nutrient cycles.

Internal waves affect biological and chemical cycles. Vertically mixed regions of the ocean are usually characterized by high concentrations of zooplankton and plants (see Sverdrup, 1955; Kamykowski, 1974; McGowan and Hayward, 1978). By inducing mixing, internal waves enhance marine productivity, as is the case, for example, in the Bay of Biscay (New, 1988) and Monterey Bay, California (Shea and Broenkow, 1982). Apart from enhancing marine productivity through mixing, internal waves can transport significant amounts of nutrients and chemicals directly. The oceanic slicks, for example, can have a high concentration of plankton; the concentration is actually higher throughout the water column near the internal wave troughs, not just at the surface (Parker, 1999).

Internal waves, especially large solitary waves, are a hazard for deepwater offshore constructions and submarine vessels. The first observation of this was in late 1975 and early 1976, when Osborne and Burch noticed strong internal solitary waves, with velocities reaching up to 1.8 m s^{-1}, battering an oil drilling vessel off the coast of Sumatra in the Andaman Sea (Osborne and Burch, 1980). Internal waves are capable of imposing large stresses on vertical elements of constructions such as risers and tethers. For the self-propelled drillships that use dynamic positioning, the hazard is even more obvious (Parker, 1999).

The hazardous effects of internal waves are also linked to a few submarine losses, the most famous one is the loss of the US submarine Thresher on April 10, 1963, in the Gulf of Maine. According to the Navy, at some point the submarine plunged below its crush depth and, then, sank. Two days before the tragedy, a large storm traversed the Gulf of Maine, which may have

generated a large internal wave. It was speculated that it could have been the large internal wave that carried the submarine below its crush depth (Parker, 1999).

Internal waves affect the acoustic transmission in the ocean. Internal waves change the sound speed by disturbing the density field and, thus, distort response functions used in tomography. For example, DeFerrari and Nguyen (1986), during acoustic tomography experiments in the Straits of Florida, observed anomalous transmission losses, or "acoustic scintillations". Almost ten years later, the unexplained result was shown to be due to internal waves (Tang and Tappert, 1997). The appreciation of internal waves as the dominant cause of the "acoustic scintillations" starts with the work by Flatté et al. (1979). The effects of internal waves on sound transmission have some important implications, e.g. submarine detection.

Internal waves play a role in the life of cetaceans. For example, in the South China Sea, short-finned pilot whales have been observed to follow the internal solitary waves and, presumably, feed on fish and squid entrained in the cores of solitary waves (Moore and Lien, 2007). Tidally generated internal waves are also known to attract the animals. The large ocean mammals can also utilize internal waves by riding on the wave fronts, as a surfer rides surface waves. Porpoises tilt their body so that they are aligned with the front of internal waves, and that allows them to create the effect of constant sliding down the hill (Silber and Smultea, 1990).

It is likely that some of the effects of internal waves are yet to be discovered or readdressed. In such a complex process as climate, where "everything is connected and nothing separate" and where the relative importance of each interconnection is uncertain, the role of internal waves may be reconsidered in future. Apart from connections that are currently regarded influential, there are other connections that may complicate the overall picture: for example, the connection between internal waves and life of cetaceans, where both are contributors to deep-ocean mixing.

1.3 Primary question: energy cascade

The primary question of modern internal wave research is how and where energy cascades through the internal wave spectrum (LeBlond, 2002). This is important to understanding how much energy from the main sources of internal waves, such as tides and winds, is transferred at a given time to scales where mixing occurs. The energy cascade process can be compared to a black box: it is known how the energy enters the system (from tide-topography interaction and winds) and it is known how the energy is released (through mixing and dissipation). The modern research is focused on understanding what is inside this black box.

In this thesis we restrict ourselves to an investigation of the laws governing nonlinear energy transfers in internal waves generated by tidal flow over topography. We use a numerical model

to simulate internal wave dynamics over an idealized topography, and, further, we use spectral analysis techniques to study nonlinear energy transfers.

The thesis is organized as follows. This chapter will be continued by section 1.4 where we describe the framework that we used: physical assumptions and governing equations. Important concepts from the internal wave theory that are used throughout the thesis are presented in section 1.5. The consideration of the spectral analysis concepts is given in Chapter 2. Chapter 3 starts with an overview of the current understanding of the spectrum of internal waves. The overview is followed by the detailed description of the set-up of numerical experiments, including the description of the geometry of the domain, boundary conditions, the numerical model solving the governing equations and the data that we analyzed. The main part of Chapter 3 is dedicated to the main results obtained using temporal spectral analysis along with the explanation of the underlying internal wave dynamics. Chapter 4 answers some additional questions that arise based on the material given in Chapter 3. Chapter 4 is concluded with a discussion of two alternative techniques that are sometimes used for the internal wave analysis: bispectral and wavelet analysis. The results of spatial spectral analysis are presented in Chapter 5.

1.4 Framework

1.4.1 Assumptions

In order to model internal wave dynamics, we have made several assumptions, which fall into three categories: (1) assumptions concerning the domain under study; (2) assumptions on fluid properties; (3) approximations concerning the Earth's rotation.

The most restrictive assumption is the two-dimensionality of the flow. It does, however, have the advantage that use of a two-dimensional model allows much higher resolution than could be achieved with a three-dimensional one. Another restriction on the domain is the rigid lid approximation where we assume that the movement of the surface is negligibly small. As the depth of the domain is 5 km and oscillations of the surface associated with internal waves are typically on the order of a few centimetres, the dynamics of the flow is not significantly modified by use of the rigid lid approximation.

For simplicity of interpretation of the results, we assume that the fluid is incompressible, inviscid and linearly stratified. These assumptions also enable us to compare our study to some previous analytic studies.

In this study the traditional f-plane approximation is used, i.e. the Coriolis frequency is assumed constant throughout the domain.

The last approximation that we use is the Boussinesq approximation, i.e. the density variations are assumed negligible in every term of the governing equations except for the gravity term. The Boussinesq approximation is very good for the ocean (see, for example, Kundu and Cohen, 2002), and it also facilitates solving the governing equations.

1.4.2 Governing equations

Under the assumptions described in the previous section, the equations governing internal wave dynamics are the two-dimensional incompressible Euler equations under the Boussinesq approximation (Lamb, 1994):

$$\mathbf{u}_t + \mathbf{u} \cdot \nabla \mathbf{u} + f \mathbf{k} \times \mathbf{u} = -\nabla p - \rho g \mathbf{k}, \tag{1.1a}$$

$$\rho_t + \mathbf{u} \cdot \nabla \rho = 0, \tag{1.1b}$$

$$\nabla \cdot \mathbf{u} = 0. \tag{1.1c}$$

Here, $\nabla = (\partial/\partial x, 0, \partial/\partial z)$ and the unit vector in the z direction is $\mathbf{k} = (0, 0, 1)$. The coordinate z is measured upward with the origin at the water surface.

In (1.1) there are three unknowns depending on time t and spatial coordinates x and z: the velocity vector $\mathbf{u} = (u, v, w)$; the normalized density perturbation ρ, such that physical density ρ_{ph} is given by $\rho_{ph} = \rho_0(1 + \rho)$, where ρ_0 is the reference density; and the normalized pressure p related to the physical pressure p_{ph} by the formula $p_{ph} = p_{atm} + \rho_0(p - gz)$, where p_{atm} is the atmospheric pressure. Equations (1.1) have two parameters: the Coriolis frequency f related to the latitude θ by $f = 2\Omega \sin(\theta)$, where $\Omega \approx 0.73 \times 10^{-4}$ s^{-1} is the angular velocity of the Earth, and the gravitational acceleration $g = 9.81$ m s^{-1}.

The Euler equations, whose modified version we use in this thesis, were derived more than 250 years ago, in 1755, in Euler's famous work "General Principles of the Motion of Fluids". Essentially, they provide a mathematical formulation of the three fundamental conservation laws applied to the physics of an incompressible fluid: conservation of momentum (equation 1.1a), conservation of energy (equation 1.1b), and conservation of mass (equation 1.1c) (for an explanation, see Kundu and Cohen, 2002). The conservation of matter, momentum and energy was stated as the universal law of nature by Mikhail Lomonosov in his "Reflections on the Solidity and Fluidity of Bodies" in 1760. Interestingly, using the same expressions, Lomonosov clearly expressed his ideas on universal conservation laws earlier in a letter to Leonhard Euler, dated July 5, 1748, before Euler derived his equations.

1.5 Important concepts from internal wave theory

1.5.1 Linearized equations of motion

Let us define the perturbation density ρ' and perturbation pressure p' such that $\rho_{\mathrm{ph}} = \bar{\rho}(z) + \rho'$ and $p_{\mathrm{ph}} = \bar{p}(z) + p'$, where $\bar{\rho}(z)$ and $\bar{p}(z)$ are the background density and pressure, respectively. The background density is related to the buoyancy frequency $N_{\mathrm{b}}(z)$:

$$N_{\mathrm{b}}^2(z) = -g\frac{\mathrm{d}\bar{\rho}}{\mathrm{d}z}. \tag{1.2}$$

When the buoyancy frequency $N_{\mathrm{b}} = \text{const}$, the fluid is linearly stratified. Using the perturbation density ρ', we can rewrite the density equation (1.1b) as follows:

$$\rho'_t + \mathbf{u} \cdot \nabla\rho' - \frac{N_{\mathrm{b}}^2(z)}{g}w = 0 \tag{1.3}$$

Removing the nonlinear terms from the momentum equation (1.1a) and density equation (1.3) leads to the following linearized equations of motion:

$$\mathbf{u}_t + f\mathbf{k} \times \mathbf{u} = -\nabla p' - \rho'g\mathbf{k}, \tag{1.4a}$$

$$\rho'_t - \frac{N_{\mathrm{b}}^2(z)}{g}w = 0, \tag{1.4b}$$

$$\nabla \cdot \mathbf{u} = 0. \tag{1.4c}$$

The set of equations (1.4) can be reduced to a single equation for w (Kundu and Cohen, 2002):

$$\nabla^2 w_{tt} + N_{\mathrm{b}}^2(z)\nabla_{\mathrm{H}}^2 w + f^2 w_{zz} = 0, \tag{1.5}$$

where

$$\nabla_{\mathrm{H}}^2 = \frac{\partial^2}{\partial x^2} + \frac{\partial^2}{\partial y^2}. \tag{1.6}$$

1.5.2 Dispersion relation

Let us consider a wave propagating in a linearly stratified fluid, when the buoyancy frequency $N_{\mathrm{b}} = \text{const}$. The coefficients in (1.5) are then all constant, so we can look for plane wave solutions of the form

$$w = w_0 e^{\mathrm{i}(kx+ly+mz-\omega t)}, \tag{1.7}$$

where w_0 is the amplitude of the wave, ω is the frequency, and (k, l, m) are the wavenumbers in the three Cartesian directions.

In order to obtain the dispersion relation, we substitute (1.7) into (1.5) and obtain the following:

$$-[(k^2 + l^2 + m^2)\omega^2]w_0 + [N_b^2(k^2 + l^2)]w_0 + f^2 m^2 w_0 = 0. \tag{1.8}$$

The expression (1.8) leads to the dispersion relation of internal waves:

$$\omega^2 = \frac{N_b^2(k^2 + l^2) + f^2 m^2}{k^2 + l^2 + m^2}. \tag{1.9}$$

In the case of two-dimensional flow, independent of the coordinate y, the wavenumber l in the dispersion relation (1.9) is set to zero.

1.5.3   Group and phase velocity

Definition 1 (Group velocity). The group velocity of an internal wave is defined as

$$\mathbf{c}_g = \frac{d\omega}{d\mathbf{K}} = \mathbf{i}\frac{\partial\omega}{\partial k} + \mathbf{j}\frac{\partial\omega}{\partial l} + \mathbf{k}\frac{\partial\omega}{\partial m} , \tag{1.10}$$

where $\mathbf{K} = (k, l, m)$ is the wave vector and $\{\mathbf{i}, \mathbf{j}, \mathbf{k}\}$ are the unit vectors in the three Cartesian directions.

When the wave is propagating on the xz-plane, so that $l = 0$, the group velocity, according to (1.9), is given by

$$\mathbf{c}_g = \frac{k}{m} \frac{N_b^2 - f^2}{\left(1 + \left[\frac{k}{m}\right]^2\right)^{3/2} \left(N_b^2 + f^2\left[\frac{m}{k}\right]^2\right)^{1/2}} \left(\mathbf{i}\frac{1}{k} - \mathbf{k}\frac{1}{m}\right). \tag{1.11}$$

Definition 2 (Phase velocity). The phase velocity of an internal wave of frequency ω is defined as

$$\mathbf{c} = \frac{\omega}{|\mathbf{K}|}\frac{\mathbf{K}}{|\mathbf{K}|} , \tag{1.12}$$

where $|\mathbf{K}| = \sqrt{k^2 + l^2 + m^2}$. The vector $\mathbf{K}/|\mathbf{K}|$ is the unit vector in the direction of $\mathbf{K}$.

Definition 3 (Phase speed in the x-direction). The phase speed of an internal wave in the x-direction is defined as

$$c_H = \frac{\omega}{K_H} , \tag{1.13}$$

where $K_H = \sqrt{k^2 + l^2}$.
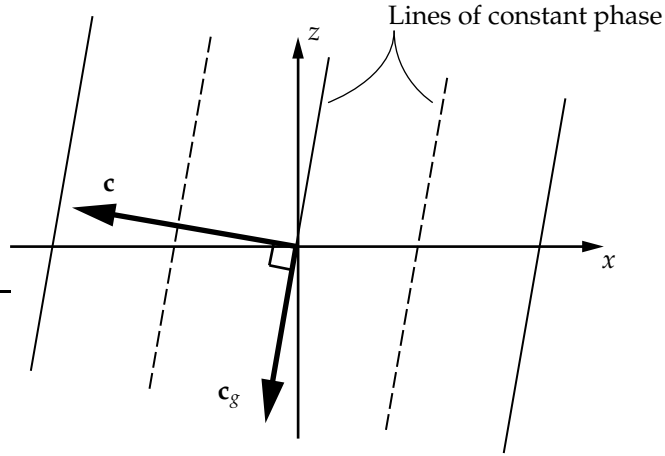
F   1.3: Group and phase velocities of an internal wave.

On the xz-plane, the phase velocity is given by

$$\mathbf{c} = \frac{\left(N^2k^2 + f^2m^2\right)^{1/2}}{\left(k^2 + m^2\right)^{3/2}} \left(\mathbf{i}k + \mathbf{k}m\right).$$ (1.14)

It follows from (1.11) and (1.14) that the group and phase velocities are perpendicular:

$$\mathbf{c}_g \cdot \mathbf{c} = 0.$$ (1.15)

An illustration of the group and phase velocities of an internal wave is given in figure 1.3.

1.5.4   Vertical modes

Let us consider another solution of (1.5). If the fluid is bounded by solid horizontal boundaries at $z = 0$ (surface) and $-H$ (bottom), we can look for solutions of the form

$$w = \psi(z)e^{i(kx+ly-\omega t)},$$ (1.16)

satisfying the boundary conditions $w = 0$ at $z = 0$ and $-H$. Once the function $\psi(z)$ is found, all the unknowns $\{u, v, w, \rho, p\}$ can be constructed by substituting (1.16) into (1.4).

To find the function $\psi(z)$, we substitute (1.16) into (1.5), and obtain the following equation:

$$\psi_{zz} + \left(\frac{N_b^2(z) - \omega^2}{\omega^2 - f^2}\right) K_H^2 \psi = 0, \tag{1.17}$$

where $K_H = \sqrt{k^2 + l^2}$. For the xz-plane, when $l = 0$, we notice that, according to the dispersion relation (1.9), the coefficient in front of ψ in (1.17) is the square of the vertical wavenumber $m^2(z)$:

$$\left(\frac{N_b^2(z) - \omega^2}{\omega^2 - f^2}\right) K_H^2 = m^2(z) \tag{1.18}$$

Thus, the equation (1.17) along with the boundary conditions leads to an eigenvalue problem for the vertical wavenumber $m(z)$:

$$\begin{cases} \psi_{zz} + m^2(z)\psi = 0, \\ \psi(z) = 0 \text{ at } z = 0, -H. \end{cases} \tag{1.19}$$

The solution of the eigenvalue problem (1.19) is given by the eigenfunctions $\psi_n(z)$, called vertical modes. In the case $N_b(z)$ is constant, $\psi_n(z)$ are given by

$$\psi_n(z) = \sin(m_n z), \tag{1.20}$$

corresponding to the eigenvalues

$$m_n = \frac{\pi n}{H}, \tag{1.21}$$

where $n \in \{1, 2, \ldots, \}$ is the mode number.

Vertical modes are characterized by their horizontal group velocity $\mathbf{c}_g$ and phase speed in the x-direction c_H. According to (1.11), (1.13) and the dispersion relation (1.9), both $\mathbf{c}_g$ and c_H are inversely proportional to the mode number n:

$$\begin{aligned} c_g &= \frac{AH}{n\pi} \propto \frac{1}{n}, \\ c_H &= \frac{BH}{n\pi} \propto \frac{1}{n}, \end{aligned} \tag{1.22}$$

where

$$A = \frac{N_b^2 - f^2}{\left(1 + \left[\frac{k}{m}\right]^2\right)^{3/2} \left(N_b^2 + f^2 \left[\frac{m}{k}\right]^2\right)^{1/2}},$$

$$B = \left(\frac{N_b^2 + f^2 \left[\frac{m}{k}\right]^2}{1 + \left[\frac{k}{m}\right]^2}\right)^{1/2},$$

(1.23)

which depend solely on the three frequencies f, ω and N_b.

1.5.5 Parametric Subharmonic Instability (PSI)

In the linear approximation, internal waves do not interact amongst themselves. However, in the more realistic nonlinear case, internal waves do interact and, as a consequence, exchange energy. The interaction is especially strong when the participant waves form a resonant triad. Three waves that have wave vectors $\mathbf{K}_1$, $\mathbf{K}_2$, $\mathbf{K}_3$ and frequencies ω_1, ω_2 and ω_3 form a resonant triad if two conditions are satisfied:

I. $\mathbf{K}_3 = \mathbf{K}_1 \pm \mathbf{K}_2$, $\omega_3 = \omega_1 \pm \omega_2$,

II. each wave vector $\mathbf{K}_1$, $\mathbf{K}_2$ and $\mathbf{K}_3$ is related to the frequency ω_1, ω_2 and ω_3, respectively, through the dispersion relation (1.9).

The resonant triad interaction can be interpreted as follows. For any two progressive waves with wavenumbers $\mathbf{K}_1$ and $\mathbf{K}_2$ and frequencies ω_1 and ω_2, the nonlinear term $\mathbf{u} \cdot \nabla \mathbf{u}$ in the momentum equation (1.1a) works as a forcing term at the combination frequencies $\omega_1 + \omega_2$ or $\omega_1 - \omega_2$ and at combination wavenumbers $\mathbf{K}_1 + \mathbf{K}_2$ or $\mathbf{K}_1 - \mathbf{K}_2$. If the combination frequency and wavenumber satisfy the dispersion relation, then the forcing given by the nonlinear term and the linear part of the solution are in resonance.

Parametric Subharmonic Instability (PSI) is an important class of resonant triad interactions characterized by a low vertical wavenumber m_2 decaying into two high vertical wavenumber modes m_1 and $-m_3$ of about half the frequency.

Chapter 2

Spectral Analysis Concepts

An internal wave field in a stratified fluid depends on three spatial variables and time. In order to obtain the spectrum of the field, one needs a spectral representation of the process defined by three wavenumbers and frequency. The four-dimensional spectral representation can be evaluated by developing spectral representations for each dimension successively. This can be done by applying, one after another, appropriate spectral transforms, such as Fourier transforms, to each dimension. The problem, thus, can be reduced to estimation of the spectrum in one dimension.

The spectrum of a one-dimensional process defines energetics across the entire range of frequencies involved in the process. Depending on the type of process and the domain where the process is defined, the spectrum can be of various types: discrete or continuous, periodic or non-periodic, symmetric with respect to the origin or non-symmetric.

As there may be different spectral representations for the same process, and, consequently, more than one way to assign energy to frequencies, some ambiguity arises. For example, there is a large number of Fourier-related transforms that can be used for spectral representation: cosine transform, sine transform, Hartley transform, etc. For a brief comparative review, refer to the paper by Ersoy (1994). Each of the Fourier-related transforms uses specific basis functions to decompose a signal. Different transforms may correspond to different domains in the spectral space. For example, the discrete cosine transform uses cosines on a different set of frequencies than used by the discrete Fourier transform. As a result, the spectrum defined through the discrete cosine transform and discrete Fourier transform may be different.

In this chapter, we present the methodology that is later used for the spectral analysis of internal wave fields arising in the numerical simulations. The main goal of this chapter is to define the term spectrum and compare the available nonparametric techniques for its estimation.

15

The presented methods, as we show with an example of actual observational data, can be efficiently employed in other works where an estimation of internal wave spectra is needed.

2.1   Historical development of spectral analysis

The ideas preceding the modern theory of spectral analysis, were, for the most part, developed during the nineteenth century and the beginning of the twentieth century. The early history of spectral analysis can be associated with the following four topics: (a) interpolation using trigonometric series; (b) tabular Fourier analysis; (c) periodogram; and (d) statistical approaches. Figure 2.1 provides a schematic view of the early development of spectral analysis and highlights some important works discussed below.

In the 18$^{\text{th}}$ century it was realized that trigonometric series provide an important tool for interpolation. Several distinguished mathematicians contributed to this early stage of the development of spectral analysis. Leonhard Euler studied infinite cosine series as early as in 1748 (Euler, 1748). One of his contemporaries, Alexis-Claude Clairaut (1754) was concerned with formulas analogous to what is currently known as the discrete cosine transform. At about the same time Daniel Bernoulli (1753) calculated the form of a vibrating string in terms of infinite sine and cosine series. A little later, another historical figure in mathematics, Joseph Louis Lagrange (1762), provided the earliest formula for an analogue of the modern discrete sine transform.

The earliest general formulas for the discrete Fourier transform were found by Carl Friedrich Gauss (1866) in his treatise on interpolation theory, written, according to Heideman et al. (1985), in October–November 1805 and published posthumously in 1866. Gauss is also the author of the fast Fourier transform (see Goldsteine, 1977), the famous computationally efficient method for the calculation of the discrete Fourier transform rediscovered almost a hundred years later by Cooley and Tukey (1965). The discovery of Cooley and Tukey was a turning point in digital signal processing, and their paper became the most frequently cited mathematics paper by the end of the twentieth century (see Kammler, 2000). The reason why Gauss' work was neglected and forgotten was the fact that he wrote in neo-Latin and used non-traditional notation, which made it difficult for a regular mathematician to refer to Gauss' work directly.

There were many independent researchers apart from Cooley and Tukey who were studying efficient techniques for harmonic analysis and unaware of Gauss' work. For example, one of the other early FFT-type methods was suggested by Francesco Carlini in 1828.

Historically, spectral analysis and Fourier transforms are associated with the name of Jean Baptiste Joseph Fourier and his work "Representation of functions with infinite harmonic series" (Fourier, 1822). In 1807, when Fourier was presenting the work to the Academy of Science in Paris, it was not well received. As a result, it was not published until 1822. If the dates for the

Euler, 1748

Bernoulli, 1753

Clairaut, 1754

Lagrange, 1762

Interpolation

Gauss, 1805

Fourier, 1807

Carlini, 1828

Ballot, 1847

Thomson, 1876

Tabular Fourier analysis

Stewart, 1879

Statistical approaches

Schuster, 1906

Einstein, 1914

Cramer, 1942

Periodogram
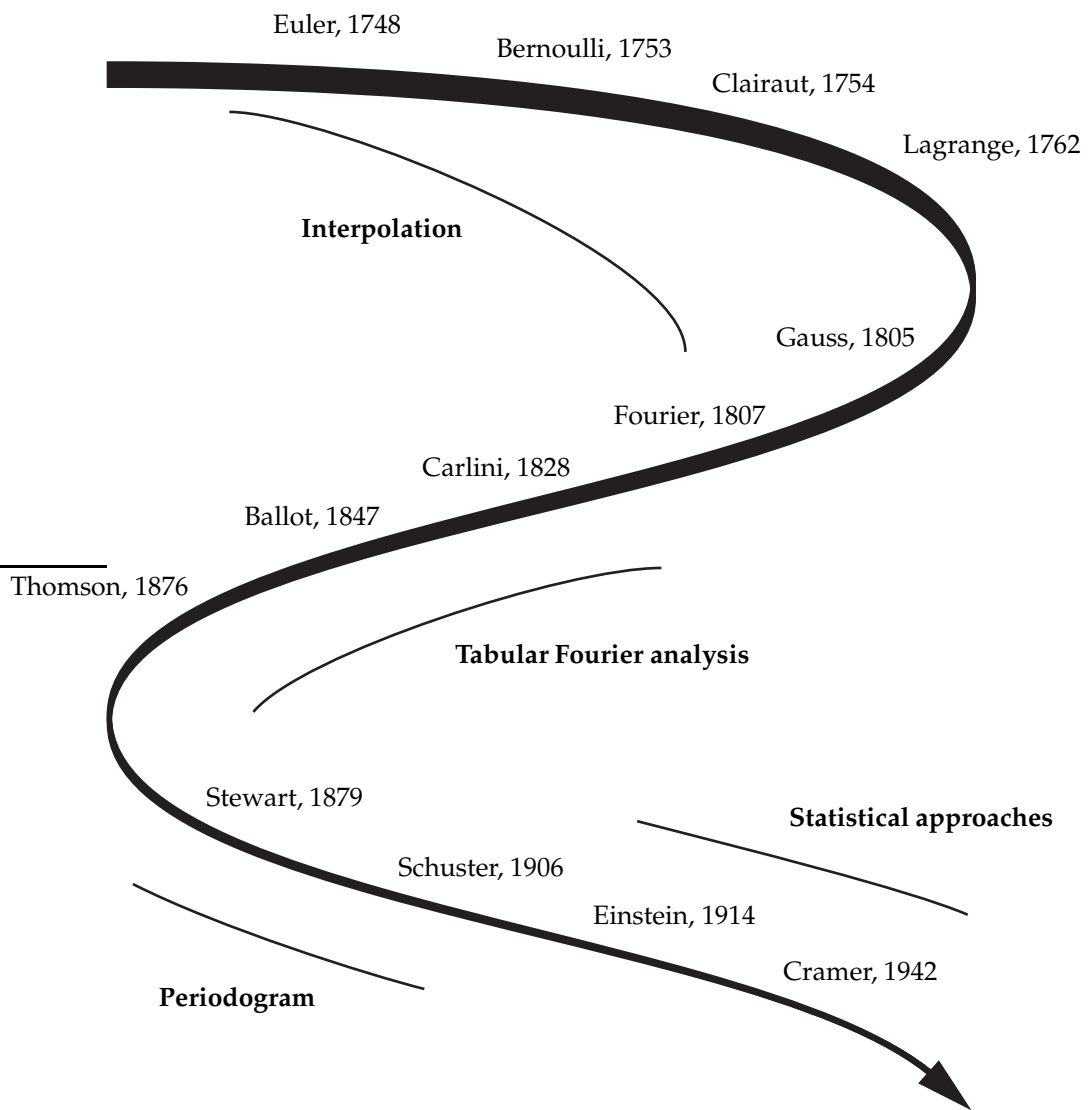
F   2.1: Historical development of spectral analysis.

completion of Gauss' work are correct, it seems probable that Fourier shared the luck of Cooley and Tukey as his work on harmonic analysis was also predated by that of Gauss (for details, see Heideman et al., 1985).

The second half of the nineteenth century is marked with numerous works on tabular methods for harmonic analysis. Methods were generally aimed at detecting and extracting components from data with known period, e.g. from tidal, meteorological and astronomical time series. The early methods include a widely used method by Buys-Ballot described in Whittaker and Robinson (1944), and its more sophisticated version by Stewart and Dodgson (1879). The mechanical harmonic analyser described and built by Thomson (1878) was claimed to increase the speed of a typical calculation by a factor of 10. According to Stokes (1879), it was also able to determine some unknown periods in a time series .

Arthur Schuster was the first who introduced the concept of *periodogram* and applied the periodogram analysis to a problem of sunspot series (Schuster, 1906). Another major application of the peridogram analysis for a real-world problem of that time was by Beveridge (1921) who used the same techniques as Schuster to analyse wheat prices in connection with weather periodicities.

The concept of the spectrum as it is used in the modern statistical theory of time series, was, for the first time, addressed by Einstein (1914). There, he also suggested the smoothing technique for reducing a periodogram's variance. This technique was reconsidered by Daniell (1946). The spectral theory of stochastic processes was developed in the 20s and 30s of the twentieth century. A remarkable work from this period is by Cramér (1942) where he proved the spectral representation theorem for a stationary process.

2.2 Spectra of regular functions

In applications, we usually deal with signals that are given by a truncated and/or discretized realization of a continuous process. Formally, the spectrum of each physical representation is given by the absolute square of the spectral representation. However, the spectral representations are different for different physical representations, e.g. continuous *vs.* discrete. In most cases, we can evaluate the exact spectral representation of a signal at hand. For example, an exact spectral representation of a time series is given by the discrete Fourier transform. However, it is not the spectral representation of the discrete time series that we are interested in, but the spectral representation of the continuous process that the time series represents. In this section, we discuss the relations and properties of different physical and spectral representations. In the next section, we provide methods for the estimation of spectra based on spectral representations of discrete time series.

2.2.1 Fourier transforms of regular functions

For a certain class of functions, called *regular* functions, the spectrum can be evaluated exactly as the squared Fourier representation. Let us introduce formally four classes of *regular* functions:

I. $f(t)$ — an absolutely integrable piecewise smooth function defined on $\mathbb{R} = (-\infty, +\infty)$;

II. $g(t)$ — a piecewise smooth p-periodic function defined by its values on $\mathbb{T}_p = [0, p)$;

III. $\phi[n]$ — an absolutely summable function defined on $\mathbb{Z} = \{\ldots, -2, -1, 0, 1, 2, \ldots\}$;

IV. $\gamma[n]$ — an N-periodic function defined by its values on $\mathbb{P}_N = \{0, 1, \ldots, N-1\}$.

Figure 2.2 shows a visual interpretation of a function f on the continuum line $\mathbb{R}$, g on the circle $\mathbb{T}_p$ with circumference p, ϕ on the integer numbers $\mathbb{Z}$ and γ on the polygon $\mathbb{P}_N$ with N nodes.
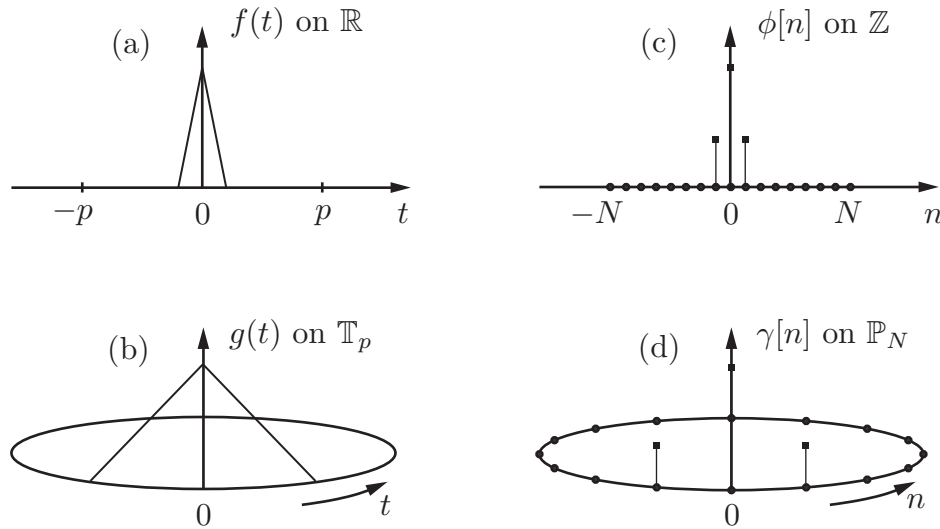
F   2.2:   Visual interpretation of the classes I–IV of regular functions.

The motivation for introducing the classes I-IV is as follows. Suppose, a continuous process is described by the regular function $f(t)$. The function $f(t)$ can be either truncated to a function $g(t)$ with $t \in [0, p)$ or discretized to a function $\phi[n]$ with $n \in \mathbb{Z}$. Then, the function $g(t)$, in its turn, can be discretized or the function $\phi[n]$ can be truncated producing a function $\gamma[n]$ with $n \in \{0, 1, \ldots, N-1\}$. Associating the function f, g, ϕ and γ with the domain $\mathbb{R}$, $\mathbb{T}_p$, $\mathbb{Z}$ and $\mathbb{P}_N$, respectively, results in the classification I–IV. This argument relating different physical representations of a process is visually presented in figure 2.3. In an application, the ultimate
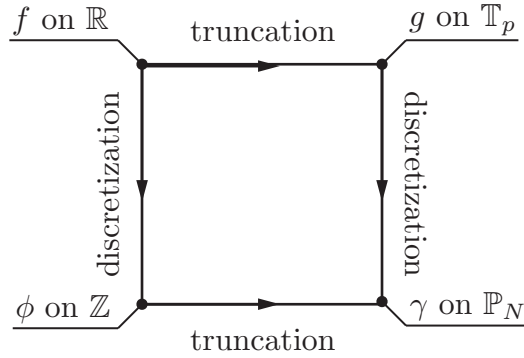
F   2.3: Relation among different physical representations of the function *f* through truncation and discretization.

goal would be to evaluate the spectral representation of the function f based on the spectral representation of the function γ.

Each physical representation of the function f, i.e. functions f, g, ϕ and γ, has a unique spectral representation given by the following Fourier transforms (synthesis and analysis equations):

Functions on $\mathbb{R}$ ($F : \mathbb{R} \longrightarrow \mathbb{R}$):

$$f(t) = \int_{s=-\infty}^{\infty} F(s)e^{2\pi i s t}\,ds; \qquad (2.1)$$

$$F(s) = \int_{t=-\infty}^{\infty} f(t)e^{-2\pi i s t}\,dt. \qquad (2.2)$$

Functions on $\mathbb{T}_p$ ($G : \mathbb{T}_p \longrightarrow \mathbb{Z}$):

$$g(t) = \sum_{k=-\infty}^{\infty} G[k]e^{2\pi i k t/p}; \qquad (2.3)$$

$$G[k] = \frac{1}{p} \int_{t=0}^{p} g(t)e^{-2\pi i k t/p}\,dt. \qquad (2.4)$$

Functions on $\mathbb{Z}$ ($\Phi : \mathbb{Z} \longrightarrow \mathbb{T}_p$):

$$\phi[n] = \int_{s=0}^{p} \Phi(s)e^{2\pi i s n/p}\,ds; \qquad (2.5)$$

$$\Phi(s) = \frac{1}{p} \sum_{n=-\infty}^{\infty} \phi[n]e^{-2\pi i s n/p}. \qquad (2.6)$$

Functions on $\mathbb{P}_N$ ($\Gamma : \mathbb{P}_N \longrightarrow \mathbb{P}_N$):

$$\gamma[n] = \sum_{k=0}^{N-1} \Gamma[k]e^{2\pi i k n/N}; \qquad (2.7)$$

$$\Gamma[k] = \frac{1}{N} \sum_{n=0}^{N-1} \gamma[n]e^{-2\pi i k n/N}. \qquad (2.8)$$

Basic properties of Fourier transforms for real functions include *linearity* and *symmetry*. The linearity property states that the Fourier transform of a linear combination of signals is the linear combination of the Fourier transforms of the constituents. The symmetry property states that the

transform has symmetric parts; only one part of the transform, which is symmetric to the other one, is sufficient to describe the signal completely. The mathematical description of linearity and symmetry is given in table 2.1 for regular functions on different domains.

Property	Function	Transform
Linearity	$\alpha_1 f_1(t) + \alpha_2 f_2(t), t \in \mathbb{R}$	$\alpha_1 F_1(s) + \alpha_2 F_2(s), s \in \mathbb{R}$
$(\alpha_1, \alpha_2 \in \mathbb{R})$	$\alpha_1 g_1(t) + \alpha_2 g_2(t), t \in \mathbb{T}_p$	$\alpha_1 G_1[k] + \alpha_2 G_2[k], k \in \mathbb{Z}$
	$\alpha_1 \phi_1[n] + \alpha_2 \phi_2[n], t \in \mathbb{Z}$	$\alpha_1 \Phi_1(s) + \alpha_2 \Phi_2(s), s \in \mathbb{T}_p$
	$\alpha_1 \gamma_1[n] + \alpha_2 \gamma_2[n], t \in \mathbb{P}_N$	$\alpha_1 \Gamma_1[n] + \alpha_2 \Gamma_2[n], n \in \mathbb{P}_N$
Symmetry	$f(t), t \in \mathbb{R}$	$F(s) = \overline{F(-s)}, s \in \mathbb{R}$
	$g(t), t \in \mathbb{T}_p$	$G[k] = \overline{G[-k]}, k \in \mathbb{Z}$
	$\phi[n], n \in \mathbb{Z}$	$\Phi(s) = \overline{\Phi(-s)}, s \in \mathbb{T}_p$
	$\gamma[n], n \in \mathbb{P}_N$	$\Gamma[k] = \overline{\Gamma[-k]}, k \in \mathbb{P}_N$

T   2.1: Fourier transform properties: linearity and symmetry.

Suppose a given signal is translated or dilated. Table 2.2 gives the rules defining the Fourier transform after *translation* and *dilation* of a signal. Two other typical manipulations of a signal are *convolution* and *multiplication*, i.e. when the signal is convolved or multiplied with some other function. The product of two functions transforms into a convolution of their respective Fourier transforms. Due to the similarity of the synthesis and analysis equations for the Fourier transforms (or similarity between the forward and inverse Fourier transforms), the product of two functions transforms into a convolution of the corresponding Fourier transforms. The rules of convolution and multiplication for different domains are described in table 2.3.

2.2.2   Connecting representations

When the functions g, ϕ and γ are constructed in the physical domain from the function f by truncation and discretization as shown in figure 2.3, there is no definite relation among the Fourier transforms F, G, Φ and Γ. However, if we construct the functions in the physical space in a slightly different manner by using p-summation and h-sampling described below, it is possible to get an exact relation among the Fourier transforms. When a function produced through the successive

Rule	Function	Transform
Translation	$f(t - t_0), t \in \mathbb{R}$	$e^{-2\pi i s t_0} F(s), s \in \mathbb{R}$
$(t_0 \in \mathbb{R})$	$g(t - t_0), t \in \mathbb{T}_p$	$e^{-2\pi i k t_0/p} G[k], k \in \mathbb{Z}$
$(n_0 \in \mathbb{Z})$	$\phi[n - n_0], n \in \mathbb{Z}$	$e^{-2\pi i s n_0/p} F(s), s \in \mathbb{T}_p$
	$\gamma[n - n_0], n \in \mathbb{P}_N$	$e^{-2\pi i k n_0/N} F[k], k \in \mathbb{P}_N$
Dilation	$f(at), t \in \mathbb{R}$ ($a \neq 0$ is real)	$|a|^{-1} F(s/a), s \in \mathbb{R}$
	$f(mt), t \in \mathbb{T}_p$	$\begin{cases} F(k/m), & \text{if } m \mid k; \\ 0, & \text{otherwise.} \end{cases}$
	$f[mn], m \in \mathbb{N}, n \in \mathbb{Z}$	$\dfrac{1}{m} \displaystyle\sum_{l=0}^{m-1} F(s/m - lp/m), \ s \in \mathbb{T}_p$
	$f[mn], n \in \mathbb{P}_N, m \mid N$	$\begin{cases} \displaystyle\sum_{l=0}^{m-1} F[k/m - lN/m], & \text{if } m \mid k; \\ 0, & \text{otherwise.} \end{cases}$
	$f[mn], n \in \mathbb{P}_N$; m and n are relatively prime	$F[m'k], m \in \mathbb{P}_N; mm' = 1$

T   2.2: Fourier transform rules for a manipulated signal: translation and dilation.

Rule	Function	Transform
Convolution	$(f_1 * f_2)(t) = \int_{t'=-\infty}^{\infty} f_1(t')f_2(t-t')\mathrm{d}t'$ $(f_1, f_2$ on $\mathbb{R})$	$F_1(s) \cdot F_2(s)$ $(F_1, F_2$ on $\mathbb{R})$
	$(g_1 * g_2)(t) = \int_{t'=0}^{p} g_1(t')g_2(t-t')\mathrm{d}t'$ $(g_1, g_2$ on $\mathbb{T}_p)$	$pG_1[k] \cdot G_2[k]$ $(G_1, G_2$ on $\mathbb{Z})$
	$(\phi_1 * \phi_2)[n] = \sum_{m=-\infty}^{\infty} \phi_1(m)\phi_2(n-m)$ $(\phi_1, \phi_2$ on $\mathbb{Z})$	$p\Phi_1(s) \cdot \Phi_2(s)$ $(\Phi_1, \Phi_2$ on $\mathbb{T}_p)$
	$(\gamma_1 * \gamma_2)[n] = \sum_{m=0}^{N} \gamma_1(m)\gamma_2(n-m)$ $(\gamma_1, \gamma_2$ on $\mathbb{P}_N)$	$N\Gamma_1[k] \cdot \Gamma_2[k]$ $(\Gamma_1, \Gamma_2$ on $\mathbb{P}_N)$
Multiplication	$f_1(t) \cdot f_2(t)$ $(f_1, f_2$ on $\mathbb{R})$	$(F_1 * F_2)(s)$ $(F_1, F_2$ on $\mathbb{R})$
	$g_1(t) \cdot g_2(t)$ $(g_1, g_2$ on $\mathbb{T}_p)$	$(G_1 * G_2)[k]$ $(G_1, G_2$ on $\mathbb{Z})$
	$\phi_1[n] \cdot \phi_2[n]$ $(\phi_1, \phi_2$ on $\mathbb{Z})$	$(\Phi_1 * \Phi_2)(s)$ $(\Phi_1, \Phi_2$ on $\mathbb{T}_p)$
	$\gamma_1[n] \cdot \gamma_2[n]$ $(\gamma_1, \gamma_2$ on $\mathbb{P}_N)$	$(\Gamma_1 * \Gamma_2)[k]$ $(\Gamma_1, \Gamma_2$ on $\mathbb{P}_N)$

T   2.3: Fourier transform rules for a manipulated signal: convolution and multiplication.

application of truncation and discretization is close to the function produced through h-sampling and p-summation, the spectral representations of the two functions can be approximated through each other. In this section, we will see that the operation of h-sampling applied in the physical space is mirrored by the operation of p-summation in the spectral space and vice versa. This important concept has far-reaching implications in the spectral analysis known as leakage and aliasing, which will be described in the end of the section.

Definition 4 (h-sampling). Let f be a regular function defined on the continuum $\mathbb{R}$. We can construct a discrete function ϕ on $\mathbb{Z}$ such that

$$\phi[n] = f(nh), \ n \in \mathbb{Z}, \tag{2.9}$$

where h is a discretization parameter. This operation is called h-sampling. For a function g defined on the domain $\mathbb{T}_p$ the definition of h-sampling is analogous. The discretization parameter is set to $h = p/N$, and the corresponding discrete function γ is:

$$\gamma[n] = g\left(\frac{np}{N}\right), \ n \in \mathbb{P}_N. \tag{2.10}$$

Definition 5 (p-summation). Let f be a regular function defined on the continuum $\mathbb{R}$. We can construct a p-periodic function g on $\mathbb{T}_p$ such that

$$g(t) = \sum_{m=-\infty}^{+\infty} f(t - mp), \ t \in \mathbb{R}. \tag{2.11}$$

This operation is called p-summation. We can also use p-summation for a regular discrete function ϕ defined on the domain $\mathbb{Z}$. The corresponding constructed function γ on $\mathbb{Z}$ is N-periodic and defined by

$$\gamma[n] = \sum_{m=-\infty}^{+\infty} \phi[n - mN], \ n \in \mathbb{Z}. \tag{2.12}$$

Changing truncation to p-summation and formalizing the operation of discretization with h-sampling, we can construct the functions g, ϕ and γ from the function f as shown in figure 2.4. Under the assumption that the tails of the function f are small, for example, when f is a localized impulse, the operation of truncation can be replaced by p-summation without significant loss of information. In the special case when the function f is identically zero outside the interval $[0, p)$, the p-summation will be equivalent to truncation.

Using the Fourier transforms (2.1)–(2.8) for the functions constructed with p-summation and
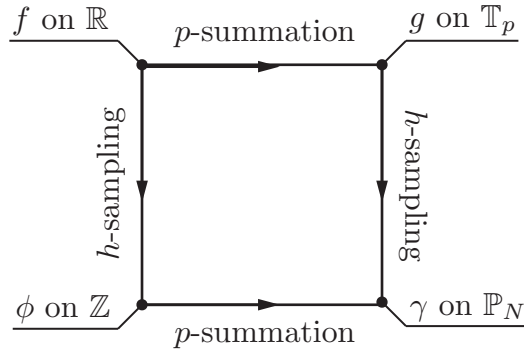
F   2.4: Relation among different physical representations of the function f through h-sampling and p-summation.

h-sampling we have the following relations:

$$g(t) = \sum_{m=-\infty}^{+\infty} f(t - mp), \ G[k] = \frac{1}{p}F\left(\frac{k}{p}\right), \tag{2.13}$$

$$\gamma[n] = \sum_{m=-\infty}^{+\infty} \phi[n - mN], \ \Gamma[k] = \frac{p}{N}\Phi\left(\frac{kp}{N}\right), \tag{2.14}$$

$$\phi[n] = f\left(\frac{np}{N}\right), \ \Phi(s) = \sum_{m=-\infty}^{+\infty} F\left(s - \frac{mN}{p}\right), \tag{2.15}$$

$$\gamma[n] = g\left(\frac{np}{N}\right), \ \Gamma[k] = \sum_{m=-\infty}^{+\infty} G[k - mN]. \tag{2.16}$$

The relations (2.13)–(2.16) suggest that all the representations of a function, both in spectral and physical space, are connected by the operations of summation and sampling. The diagram called the Fourier-Poisson cube illustrating these relations is shown in figure 2.5. The diagram is adapted from Kammler (2000).

As can be seen in figure 2.5, sampling in physical space is compensated by summation in the spectral space and summation is compensated by sampling. This idea underlies two important concepts of aliasing and leakage, which arise from the discretization and truncation of a signal, respectively. Suppose a regular function f on $\mathbb{R}$ has the spectral representation F on $\mathbb{R}$. Let us illustrate the concept of aliasing and leakage by considering the transformation that the spectral representation F undergoes as we truncate or discretize the function f. Note that the spectral representations of g and ϕ undergo similar transformations when g and ϕ are discretize and truncated, respectively. When a function is both discretized and truncated, both effects, i.e. leakage and aliasing, take place.

25

f on $\mathbb{R}$ synthesis analysis F on $\mathbb{R}$

p-sum $1/p$-sample & $1/p$-scale

g on $\mathbb{T}_p$ synthesis analysis G on $\mathbb{Z}$

p/N-sample N/p-sum

p/N-sample N-sum

ϕ on $\mathbb{Z}$ synthesis analysis Φ on $\mathbb{T}_{N/p}$

N-sum $1/p$-sample & $1/p$-scale

γ on $\mathbb{P}_N$ synthesis analysis Γ on $\mathbb{P}_N$
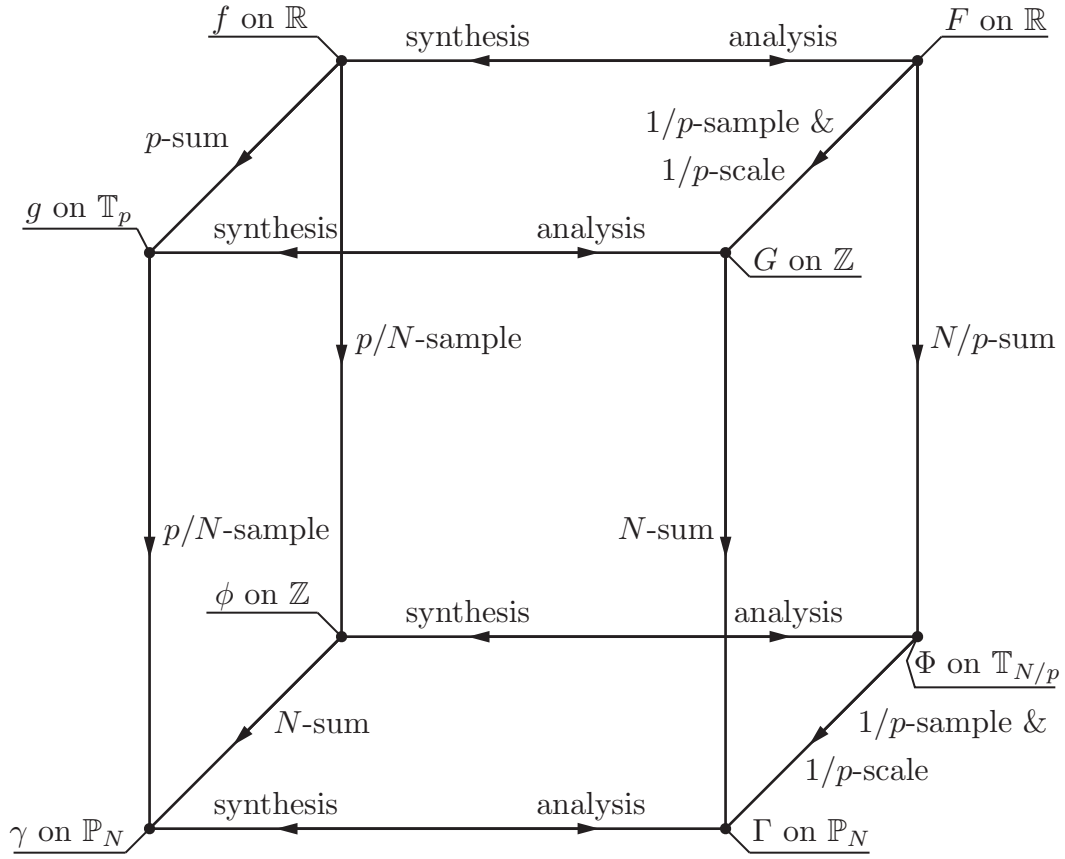
F   2.5: Fourier-Poisson cube (Kammler, 2000).

If the function f is discretized using h-sampling, then its spectral representation will be truncated to frequencies less than the Nyquist frequency: $|s| < s_{\text{Nyq}} = 1/(2h)$, and, in addition, all the energy contained in the frequencies larger than s_{Nyq} will be *aliased* to the range $[0, 1/(2h))$ through p-summation. This effect is known as aliasing. By decreasing the sampling interval h, we increase the Nyquist frequency and, consequently, reduce aliasing. In practical situations, the function f is not bandlimited, i.e. its spectral representation F does not have a finite support (Press et al., 1992), so discretization always introduces some degree of aliasing. However, if the Fourier representation F rapidly decays as $s \to \infty$, then the effect of aliasing can be reduced to an acceptable level by choosing a sufficiently small sampling interval h.

If the function f is truncated to g on an interval $[0, p)$, the spectral representation undergoes the following transformation. If the truncation was preceded by p-summation, then the spectral representation of g would simply become a $1/p$-sampling of F. However, the operation of truncation is different from the operation of p-summation. Thus, there is additional bias to

26

the discrete version of F: the spectral rerrepresentation of g is, in fact, the discretized spectral representation of the discontinuous function $\tilde{f}$ equal to f on the interval $[0, p)$ and equal to zero outside the interval. The discontinuities of the function $\tilde{f}$ lead to the following: in the spectral representation, energy from the energetic frequencies "leaks" to the surrounding frequencies. This effect is called leakage.

To summarize, when a function is truncated, its spectral representation is discretized; the larger the domain of truncation, the finer the sampling interval. In addition, the discontinuities arising in the physical representation at the boundaries of the domain lead to leakage in the spectral representation. The successive discretization of the truncated function leads to truncation of the spectral representation; the finer the sampling in physical space, the larger the domain of truncation in spectral space. Energy in the spectral representation is aliased into the truncated range of frequencies from outside through p-summation.

2.2.3 Spectrum through Fourier representations

Let us consider the functions f, g, ϕ and γ constructed as in figure 2.4. The aggregate squared sizes of the functions are related to the sizes of the Fourier transforms F, G, Φ and Γ through the *Plancherel* identities (see table 2.4).

Aggregate size type	*Function*	*Plancherel identity*
Energy	f on $\mathbb{R}$	$\displaystyle\int_{-\infty}^{+\infty} \left|f(t)\right|^2 \, \mathrm{d}t = \int_{s=-\infty}^{+\infty} |F(s)|^2 \, \mathrm{d}s$
Power	g on $\mathbb{T}_p$	$\displaystyle\frac{1}{p}\int_0^p \left|g(t)\right|^2 \, \mathrm{d}t = \sum_{k=-\infty}^{+\infty} |G[k]|^2$
Discrete energy	ϕ on $\mathbb{Z}$	$\displaystyle\sum_{n=-\infty}^{+\infty} \left|\phi[n]\right|^2 \frac{p}{N} = \int_0^{N/p} |\Phi(s)|^2 \, \mathrm{d}s$
Discrete power	γ on $\mathbb{P}_N$	$\displaystyle\frac{1}{N}\sum_{n=0}^{N-1} \left|\gamma[n]\right|^2 = \sum_{k=0}^{N-1} |\Gamma[k]|^2$

T   2.4: Plancherel identities.

Using these identities, we can define the deterministic spectra through the absolute squared values of the Fourier transforms:

27

$\lvert F(s)\rvert^2$	—	energy spectral density function for a continuous function f on $\mathbb{R}$; the integral $\int_a^b \lvert F(s)\rvert^2 \mathrm{d}s$ is the contribution to the energy of the signal from the sinusoids with frequencies from the interval $[a, b]$;
$\lvert G[n]\rvert^2$	—	discrete power spectrum of a p-periodic function g on $\mathbb{T}_p$; $\lvert G[n]\rvert^2$ is the contribution to the power from the sinusoid with frequency n/p;
$\lvert\Phi(s)\rvert^2$	—	N/p-periodic energy spectral density function of a discrete function ϕ on $\mathbb{Z}$;
$\lvert\Gamma[n]\rvert^2$	—	N-periodic discrete power spectrum of a discrete function γ on $\mathbb{P}_N$.

From the symmetry property of the Fourier transform $F(s)$ for real functions follows the symmetry of the spectrum $\lvert F(s)\rvert^2$ with respect to $s = 0$: $\lvert F(s)\rvert^2 = \lvert F(-s)\rvert^2$. Thus, one side of the spectrum provides all the information about the spectrum, and the other side contains redundant information. According with the symmetry property, we can define the one-sided spectrum $\lvert F_{\mathrm{one}}(s)\rvert^2$ (as opposed to the *two-sided spectrum* $\lvert F(s)\rvert^2$) as follows:

$$\lvert F_{\mathrm{one}}(s)\rvert^2 = \begin{cases} 2\lvert F(s)\rvert^2, & s > 0; \\ \lvert F(s)\rvert^2, & s = 0; \\ 0, & s < 0. \end{cases} \tag{2.17}$$

Then, the total energy of the function $f(t)$ is given by

$$\int_{-\infty}^{\infty} f^2(t)\mathrm{d}t = \int_0^{\infty} \lvert F_{\mathrm{one}}(s)\rvert^2 \mathrm{d}s. \tag{2.18}$$

The spectrum $\lvert G[n]\rvert^2$ with corresponding discrete frequencies $s[n] = n/p$ for $n = -\infty, \ldots, -1, 0, 1, \ldots, +\infty$ is also symmetric with respect to the frequency $s = 0$. Similarly, the spectra $\lvert\Phi(s)\rvert^2$ and $\lvert\Gamma[n]\rvert^2$ have symmetric parts. Recall that the spectrum $\lvert\Phi(s)\rvert^2$ has frequencies in the interval $[0, N/p)$ and $\lvert\Gamma[n]\rvert^2$ has frequencies $s[n] = n/p$ for $n = 0, 1, \ldots, N - 1$. The spectra $\lvert\Phi(s)\rvert^2$ and $\lvert\Gamma[n]\rvert^2$ are symmetric with respect to the Nyquist frequency $s_{\mathrm{Nyq}} = N/(2p)$.

An important point to be emphasized is that for the regular functions the spectrum is defined exactly as the absolute square spectral representation. It is not an approximation. In particular, that means that the spectrum of a discrete time series γ is given by $\lvert\Gamma[n]\rvert^2$ that can be evaluated exactly. However, once again, we are usually interested in approximation of the spectra that can not be evaluated exactly. In this regard let us consider two typical situations that will be faced in this thesis. One is when the domain of the function is finite; for example, when we analyse vertical profiles of the horizontal velocity. Another is when we analyse time series on an unbounded domain.

In the case when the function g is defined on a bounded domain $[0, p)$, its spectrum $\lvert G[n]\rvert^2$ for $n \in \mathbb{Z}$ can be approximated through $\lvert\Gamma[n]\rvert^2$ evaluated for the function γ constructed by h-sampling

the function g. The approximation $|\Gamma[n]|^2$ is a truncated version of the real spectrum $|G[n]|^2$ and is subject to aliasing. The aliasing can be reduced to a sufficiently low level by choosing an appropriately small sampling interval h. Although in this case the effect of aliasing can be efficiently removed from the approximation, there is one problem that makes the definition of the spectrum ambiguous. The problem is that the spectral representation $|G[n]|^2$ given through the Fourier transform of the function g is not the only possible spectral representation: there are other spectral representations, such as the cosine transform, Hilbert transform and so on. Sometimes, other representations are more advantageous than the Fourier transform. For example, in our simulations, the vertical profiles of the horizontal velocity away from the topography may be better represented by a discrete cosine transform by analogy with the vertical mode decomposition.

Let us consider the case when the domain of a regular function f is unbounded. The discrete spectrum $|p\Gamma[n]|^2$ evaluated for a truncated and discretized signal is a crude estimate of the continuous spectrum $|F(s)|^2$ at the Fourier frequencies $s_n = n/p$. We know that the rough approximation $|p\Gamma[n]|^2$ is a truncated and discretized version of $|F(s)|^2$ and is subject to aliasing and leakage. This approximation can be found in some works on digital signal processing (see, for example, Cameron, 1995) and in the analysis of meteorological two-dimensional fields (e.g. , Errico, 1985). Although this approximation is seldom used, it serves as a good illustration of the problems that we must confront when performing a spectral estimation.

2.2.4   Example: crude approximation

Let us construct the functions f, g, ϕ and γ shown in figure 2.6(a) as follows. We make up the function $f(t)$ so that it would have a continuous spectrum with two dominant frequencies $s = 1/\pi \approx 0.32$ and $3/(2\pi) \approx 0.48$:

$$f(t) = [\cos(2t) + \sin(3t)]\exp\left[-\frac{(t-4)^2}{7^2}\right].\tag{2.19}$$

The corresponding p-periodic function g is constructed by p-summation for $p = 10$ on the interval $[0, 10]$. The discrete function ϕ is constructed by h-sampling with $h = 0.5$ at the discrete points $t_n = hn$ with $n = 0, \pm1, \pm2, \ldots, \pm\infty$. The function γ discretizes the function g on the discrete points t_n for $n = 0, 1, \ldots, N$, where $N = 20$.

The spectra of the functions $f(t)$, $g(t)$, $\phi[n]$ and $\gamma[n]$ are given by $|F(s)|^2$, $|G[n]|^2$, $|\Phi(s)|^2$ and $|\Gamma[n]|^2$, respectively. The Fourier transform $F(s)$ of the function $f(t)$ has an exact analytical form:

$$F(s) = -\frac{7}{2}\sqrt{\pi}\left[\mathrm{i}\exp(294\pi s - 441/4 + 24\mathrm{i}) - \exp(294\pi s - 441/4 + 24\mathrm{i})\right].\tag{2.20}$$

Thus, the spectrum $|F(s)|^2$ is defined by an explicit formula. Using (2.13)–(2.16), we can also obtain

explicit analytical forms for the spectra $|G[n]|^2$, $|\Phi(s)|^2$ and $|\Gamma[n]|^2$. In particular, at frequencies $s_n = n/p$, we have $|F(s_n)|^2 = |pG[n]|^2$ for $n \in \mathbb{Z}$.

Now, let us construct the function $\hat{\gamma}[n]$ on $\mathbb{P}_N$ by truncation and discretization of the function f, so that $\hat{\gamma}[n] = \phi[n]$ for $n = 0, 1, \ldots, N-1$. The function $\hat{\gamma}$ is an example of a function that we would be given in a real application. The spectrum $|F(s)|^2$ at frequencies s_n can be roughly approximated with $|p\hat{\Gamma}[n]|^2$. Figures 2.6(*b,c*) illustrate the difference between $|F(s_n)|^2$ and $|p\hat{\Gamma}[n]|^2$ in our example on linear and logarithmic scale, respectively. The estimation $|p\hat{\Gamma}[n]|^2$ has several important problems. One problem is that the relatively low spectral resolution prevents the approximation $|p\hat{\Gamma}[n]|^2$ from reflecting adequately the continuous shape of the spectrum. Another problem is that $|p\hat{\Gamma}[n]|^2$ underestimates values of $|F(s_n)|^2$ near the peaks: the values of the spectrum approximation at $s = \pm 0.5$ are smaller than the values of the actual spectrum. Lastly, there is bias in the slope of the spectrum on the logarithmic scale due to both aliasing and leakage.

2.2.5   Discontinuity

As was shown in the example, there are several factors that separate the spectrum $|F(s)|^2$ from its approximation defined through the discrete Fourier transform. One of the factors, coming from the truncation of a signal, is that the spectral approximation is discrete whereas the actual spectrum is continuous. There are two methods to decrease the sampling interval in the spectral space. One obvious way to do this is to increase the domain where the discretized and truncated version of f is defined, as the sampling interval is proportional to $1/p$. However, if the time series γ is already given, it is impossible to increase its domain.

Another convenient way to approximate the spectrum on a finer set of frequencies, is to interpolate the spectral representation $\Gamma[n]$. This can be efficiently done by zero-padding of the function γ (for details, see Kammler, 2000).

2.2.6   Slope of the spectrum

Another factor that separates the spectrum $|F(s)|^2$ from its discrete approximation $|p\Gamma[n]|^2$ is the bias in the slope of the spectrum. It is due to both leakage and aliasing. In this section we first discuss what the actual slope in the spectrum should be, then we discuss how the slope is altered when the spectrum is approximated and, finally, we show how the bias can be controlled.

In most typical situations the spectrum of a function decays as $s \to \infty$. More specifically, if $f(t), f'(t), \ldots, f^{(n)}(t)$ are regular functions on $\mathbb{R}$, then the absolute value of the Fourier transform $|F(s)|$ decays at least as fast as $1/s^n$ in the limit $s \to \infty$. If, in addition, $f^{(n)}(t)$ is piecewise constant, the rate of decay is at least $1/s^{n+1}$ (Kammler, 2000).
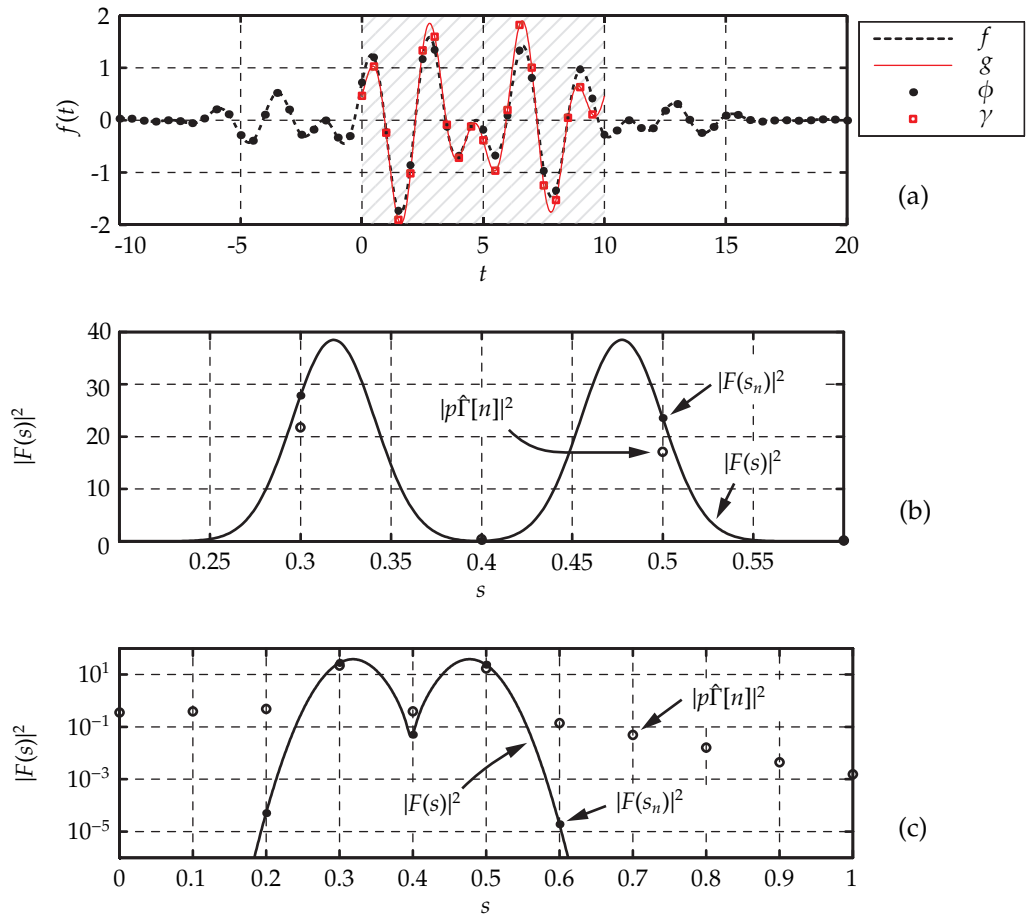
F   2.6: Example on how actual spectrum compares with the discrete approximation: (a) different representations of the function f, g, ϕ and γ; (b) comparison of $|F(s_n)|^2$ and $|p\hat{\Gamma}[n]|^2$ on linear scale; (c) the same comparison on logarithmic scale.

As an example, let us consider the Fourier transform of a rectangular window, for which the exact analytic expression can be calculated. The rectangular window is a piecewise constant function given by

$$\Pi(t) = \begin{cases} 1, & -1/2 < t < 1/2; \\ 0, & \text{elsewhere.} \end{cases}$$

The Fourier transform of the function $\Pi(t)$ is known as the *sinc*-function:

$$\text{sinc}(s) = \begin{cases} \dfrac{\sin(\pi s)}{\pi s}, & s \neq 0; \\ 1, & s = 0. \end{cases} \tag{2.21}$$

The function $|\text{sinc}(s)| < 1/s$ as $s \to \pm\infty$, so it decays as fast as $1/s$, as expected.

When the spectrum $|F(s)|^2$ is approximated with $|p\Gamma[n]|^2$, the slope of the spectrum is altered: the leakage and aliasing introduce bias to the estimation. In order to explain bias, let us trace once again what happens to the spectral representation of the function f when f is truncated on an interval $(-1/2, 1/2)$ and discretized.

The operation of truncation on $(-1/2, 1/2)$ is equivalent to multiplying the function f by the rectangular window Π. According to the convolution rule (see table 2.3), the Fourier transform of the function $f(t) \cdot \Pi(t)$ is $F(s) * \text{sinc}(s)$. Thus, the spectral representation of the function f after truncation is the discretized function $F(s) * \text{sinc}(s)$. Thus, the bias due to leakage is introduced through the convolution of the function f with the rectangular window. If the Fourier transform $F(s)$ has a decay rate higher than $1/s$ at $s \to \infty$, the biased slope will decay as $1/s$. The operation of discretization will, in addition to bias due to leakage, introduce bias due to aliasing.

If the function $f(t)$ is multiplied by a function other than the rectangular window or its dilate, one can control the bias due to leakage. For example, let us construct a window giving a bias less than that of the rectangular window. Convolving the rectangular window with itself, for example, produces a triangular window $\Lambda(t)$:

$$\Lambda(t) = \begin{cases} 1 - |t|, & -1 < t < 1; \\ 0, & \text{elsewhere.} \end{cases}$$

The Fourier transform of the triangular window is $\text{sinc}^2(s)$. Provided the slope of the Fourier transform $F(s)$ is less than $1/s^2$, the slope of the convolution $F(s) * \text{sinc}^2(s)$ is $1/s^2$. Changing the slope of the spectral representation with the use of different windows underlies the main technique in spectral estimation for reducing bias.
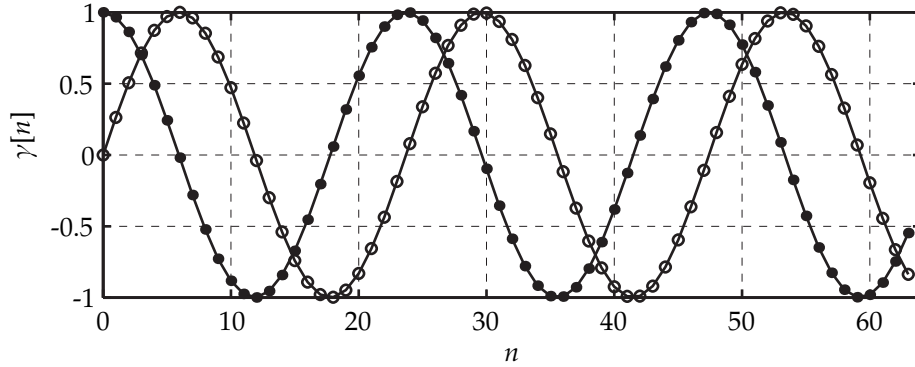
F   2.7: The function γ on $\mathbb{T}_N$ for $\alpha = 2.7$ and $N = 64$: real part (dots), imaginary part (circles).

2.3   Example: single sinusoid

Let us consider an example of how bias due to leakage is reduced when a single frequency signal is multiplied by different windows. Let the function γ on $\mathbb{P}_N$ be a continuous sinusoidal function with a single frequency $\alpha \in \mathbb{R}$:

$$\gamma[n, \alpha] = e^{2\pi i \alpha n/N}, n = 0, 1, \ldots, N - 1. \tag{2.22}$$

The function γ for $\alpha = 2.7$ and $N = 64$ is shown in figure 2.7.

The Fourier transform of the function $\gamma[n, \alpha]$ is

$$F[k, \alpha] = e^{-\pi i (N-1)(k-\alpha)/N} \frac{\text{sinc}(k - \alpha)}{\text{sinc}[(k - \alpha)/N]}. \tag{2.23}$$

When $\alpha \neq 0, \pm 1, \pm 2, \ldots$, the spectrum $|F[k, \alpha]|^2$ has a peak at $k = \lfloor \alpha \rfloor$ or $k = \lceil \alpha \rceil$ and away from the peak it will decay as $|k - \alpha|^{-2}$. The spectrum $|F[k, \alpha]|^2$ for $\alpha = 2.7$ and $N = 64$ is shown in figure 2.8.

In practical situations the $|k - \alpha|^{-2}$ decay can make other features of the spectrum invisible. For example, if the signal $\gamma[n, 2.7]$ shown in figure 2.7 contained another weaker sinusoid $10^{-4} \exp 2\pi i \alpha n/N$ for $\alpha = 10$, then the Fourier transform F of the combined signal would not reflect that. Nor would it be possible to see the small amplitude oscillation in the signal itself. In this situation a window may be helpful.

Let $\hat{f}[n, \alpha] = w[n] \cdot f[n, \alpha]$ so that $\hat{F}[k, \alpha] = (W * F)[k, \alpha]$. The Hann window is given by $w[n] = \frac{1}{2}\{1 - \cos[\pi(2n + 1)/N]\}$. The Fourier transform of the Hann window can be evaluated explicitly:

$$W[k] = -\frac{1}{4}e^{i\pi/N}\delta[k - 1] + \frac{1}{2}\delta[k] - \frac{1}{4}e^{-i\pi/N}\delta[k + 1]. \tag{2.24}$$
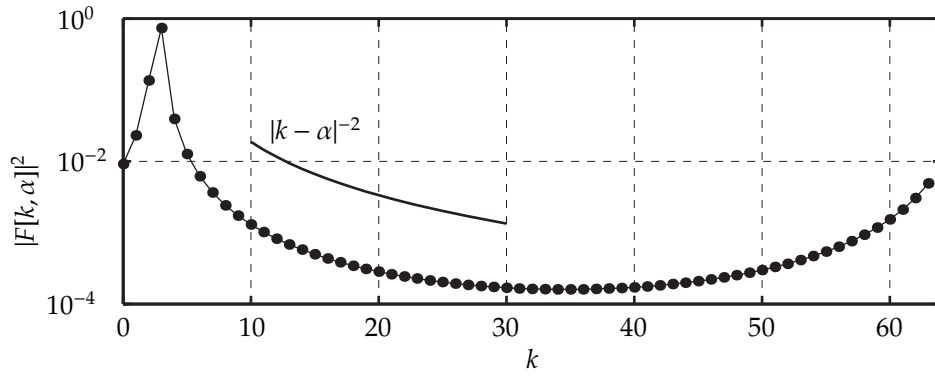
F   2.8: The function $|F[k, \alpha]|^2$ on $\mathbb{T}_N$ for $\alpha = 2.7$ and $N = 64$.
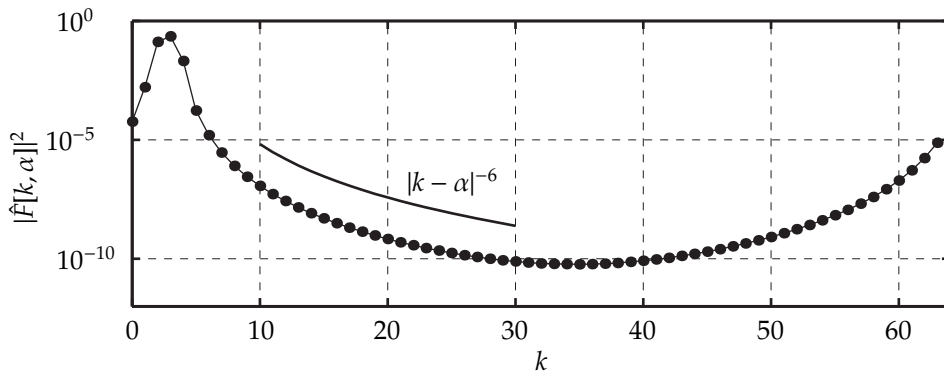
F   2.9: The function $|\hat{F}[k, \alpha]|^2$ for the Hann window on $\mathbb{T}_N$, $\alpha = 2.7$ and $N = 64$.

Then, the Fourier transform of the function $f[n, \alpha]$ multiplied by the Hann window is

$$\hat{F}[k, \alpha] = -\frac{1}{4}e^{i\pi/N}F[k - 1, \alpha] + \frac{1}{2}F[k, \alpha] - \frac{1}{4}e^{-i\pi/N}F[k + 1, \alpha]. \tag{2.25}$$

The spectrum $|\hat{F}[k, \alpha]|^2$ for $\alpha = 2.7$ and $N = 64$ is shown in figure 2.9. For the Hann window, the spectrum $|\hat{F}[k, \alpha]|^2$ decays as $|k - \alpha|^{-6}$ and, thus, it can expose more spectral features than the spectrum $|F[k, \alpha]|^2$ with the default rectangular window.

2.4 Spectra of stochastic processes

In practical applications, we usually deal with processes that are not of finite energy and, at the same time, not strictly periodic. Such processes are not described by regular functions. Moreover, signals from observations or numerical experiments are often contaminated by noise. The spectral representation of such processes is different from the Fourier representation. Such processes are better dealt with in the framework of stochastic processes. Oceanic waves and, in particular, internal waves are typical stochastic processes.

Although the spectral representations of stochastic and deterministic processes are different , the spectral estimation techniques are quite similar. The problems of leakage and aliasing have similar nature. And the measures against leakage and aliasing are also similar. In this section we define the spectral representation and spectrum of a stochastic process and classify available non-parametric spectral estimation techniques that were used in the research.

2.4.1 Stochastic processes

Definition 6 (Stochastic process). A stochastic process $\{f(t) : t \in T\}$ is a set of random functions indexed by t, where T is some given index set, e.g. the set of all real numbers $\mathbb{R}$, the set of all integers $\mathbb{Z}$, an interval $[0, p]$, *etc.*

To distinguish between processes defined on a discrete and continuous sets, we will follow notation similar to the one introduced in the previous section:

- $\{f[n]\}$ — discrete stochastic process defined on $\mathbb{Z}$;

- $\{f(t)\}$ — continuous stochastic process defined on $\mathbb{R}$.

We will indicate when the process is defined on a domain different from $\mathbb{Z}$ or $\mathbb{R}$.

By stationarity of a stochastic process we mean the covariance stationarity described in the following definition.

Definition 7 (Covariance stationary stochastic process). A stochastic process $\{f(t)\}$ is covariance stationary if its average value $\mathsf{E}\{f(t)\} = \mu$ is independent of time and the autocovariance $v(\tau) = \mathrm{cov}\{f(t), f(t + \tau)\} \equiv \mathsf{E}\{f(t) \cdot f(t + \tau)\} - \mu^2$ is a function of τ only.

Stochastic processes represent a broader class of processes in comparison with the regular functions. Examples of the processes include:

- Not strictly periodic wave processes;

- Noise;

- Waves contaminated by noise.

2.4.2 Spectral representation

For regular functions, the spectral representation is given by a Fourier transform. For a stochastic process, there exists an analogous spectral representation. However its definition is somewhat more complicated.

Theorem 1 (Spectral representation theorem for a discrete stationary process). *Let $\{f[n]\}$ be a real-valued discrete stationary process with the mean μ. There exists an orthogonal stochastic process $\{Z(s)\}$ defined for $|s| \leq s_{Nyq} \equiv 1/(2\Delta t)$, such that*

$$f[n] = \mu + \int_{-s_{Nyq}}^{s_{Nyq}} e^{2\pi i s n \Delta t} dZ(s), \tag{2.26}$$

Theorem 2 (Spectral representation theorem for a continuous stationary process). *Let $\{f(t)\}$ be a real-valued continuous stationary process with the mean μ. There exists an orthogonal stochastic process $\{Z(s)\}$ defined for $s \in \mathbb{R}$, such that*

$$f(t) = \mu + \int_{-\infty}^{\infty} e^{2\pi i s t} dZ(s). \tag{2.27}$$

For a more detailed description of stochastic processes in the context of spectral analysis, refer to the work by Percival and Walden (1993). Here we only note that:

1. The process $\{Z(s)\}$ is orthogonal if $\mathrm{cov}\{dZ(\omega + d\omega), dZ(\omega)\} = 0$.

2. The stochastic Stieltjes integral in (2.26) and (2.27) is defined as the limit in mean square of appropriate stochastic sums.

The spectral representation of a stochastic process for the discrete and continuous cases differ essentially only in the limits of the integrals in Eq. (2.26) and (2.27), or, alternatively in the domains

of the process $\{Z(s)\}$. For a discrete process, the spectrum is continuous and only frequencies up to some maximum frequency, namely s_{Nyq}, can be resolved.

Definition 8 (Spectral density function (SDF)). The spectral density function $\Upsilon(s)$ of a discrete or continuous stationary stochastic process is defined through the spectral representation $\{Z(s)\}$ as follows:

$$\Upsilon(s)\mathrm{d}s = \mathsf{E}\{|\mathrm{d}Z(s)|^2\} \tag{2.28}$$

It can be formally shown (Percival and Walden, 1993) that the spectral density function makes a Fourier pair with the autocovariance function $v(\tau)$. For a discrete stochastic process, the autocovariance function and SDF are related by the following:

$$v[n] = \int_{-s_{\text{Nyq}}}^{s_{\text{Nyq}}} \Upsilon(s)e^{2\pi i s n \Delta t}\mathrm{d}s; \tag{2.29}$$

$$\Upsilon(s) = \Delta t \sum_{n=-\infty}^{\infty} v[n]e^{-2\pi i s n \Delta t}. \tag{2.30}$$

For a continuous stochastic process, the relations are

$$v(\tau) = \int_{-\infty}^{\infty} \Upsilon(s)e^{2\pi i s \tau}\mathrm{d}s; \tag{2.31}$$

$$\Upsilon(s) = \int_{-\infty}^{\infty} v(\tau)e^{-2\pi i s \tau}\mathrm{d}\tau. \tag{2.32}$$

As the spectral density function can be related to the autocovariance function by the Fourier transforms, an alternative way to introduce the SDF is through the relations Eq. (2.30) or (2.32).

The typical problem of spectral estimation can be formulated as follows: given a realization $f[n]$ for $n = 0, 1, \ldots, N-1$ of a discrete stationary stochastic process $\{f[n]\}$, estimate the continuous spectral density function $\Upsilon(s)$.

2.4.3 Periodogram

The spectral density function $\Upsilon(s)$ is defined through the autocovariance function $v[n]$, see (2.30). The latter must be estimated in order to evaluate the spectral density function. The autocovariance for a discrete stationary process with the mean μ (either known or unknown) is, by definition,

$$v[k] = \mathsf{E}\{(f[n] - \mu)(f[n+k] - \mu)\}. \tag{2.33}$$

For a time series $f[n]$ of length N there are two most commonly used methods to estimate the autocovariance function defined by Eq. (2.33):

- 'Unbiased' autocovariance estimator $\tilde{v}[k]$ for $k = 0, \pm 1, \ldots, \pm(N-2)$:

$$\tilde{v}[k] = \frac{1}{N - |k|} \sum_{n=0}^{N-|k|-1} (f[n] - \mu)(f[n + |k|] - \mu). \tag{2.34}$$

- 'Biased' autocovariance estimator $\hat{v}^{(\mathrm{p})}[k]$ for $k = 0, \pm 1, \ldots, \pm(N-2)$:

$$\hat{v}^{(\mathrm{p})}[k] = \frac{1}{N} \sum_{n=0}^{N-|k|-1} (f[n] - \mu)(f[n + |k|] - \mu) = \left(1 - \frac{|k|}{N}\right)\tilde{v}[k]. \tag{2.35}$$

The labels 'biased' and 'unbiased' have historical origin. Strictly speaking, estimators of the autocovariance $\tilde{v}[k]$ and $\hat{v}^{(\mathrm{p})}[k]$ are unbiased and biased, respectively, only if the mean value μ is known. If the mean μ is unknown (as is often the case), then, both estimators are biased. In some cases the 'unbiased' estimator happens to be even more biased than the 'biased' one (Percival, 1993).

Let us simplify the analysis by considering processes with zero mean. Any other process can be reduced to that with zero mean by the subtraction of the mean value μ (either known or estimated) from each realization.

Substituting the 'biased' estimator $\hat{v}^{(\mathrm{p})}[k]$ into Eq. (2.30), truncating appropriately the sum over the lag k, and manipulating the resulting double sum, we obtain the periodogram estimation of the SDF $\Upsilon(s)$:

$$\begin{aligned}
\hat{\Upsilon}^{(\mathrm{p})}(s) &= \Delta t \sum_{n=-\infty}^{\infty} \hat{v}^{(\mathrm{p})}[n]e^{-2\pi i s n \Delta t} \\
&= \frac{\Delta t}{N} \sum_{k=-(N-2)}^{N-2} \sum_{n=0}^{N-|k|-1} f[n]f[n + |k|]e^{-2\pi i s k \Delta t} \\
&= \frac{\Delta t}{N} \left| \sum_{n=0}^{N-1} f[n]e^{-2\pi i s n \Delta t} \right|^2.
\end{aligned} \tag{2.36}$$

The periodogram evaluated at the Fourier frequencies, i.e. $s = n/(N\Delta t)$ for $n = 0, 1, \ldots, N-1$ coincides with $p|\Gamma[n]|^2$, where Γ is the discrete Fourier transform of f and $p = N\Delta t$. As the domain grows and $N \to \infty$, the periodogram approaches the spectrum $\Upsilon(s)$ (Percival and Walden, 1993), just like $p|\Gamma[n]|^2$ approaches the continuous Fourier transform divided by the length of the domain.

The periodogram estimator suffers from two artifacts: (1) bias, given by $|\Upsilon(s) - \mathsf{E}\{\Upsilon^{\mathrm{p}}(s)\}|$, due to leakage and aliasing, and (2) variance, given by $\mathrm{var}(\Upsilon^{\mathrm{p}}(s))$. To understand both parts of the error, let us consider the mathematical expectation of the periodogram $\mathsf{E}\{\hat{\Upsilon}^{(\mathrm{p})}(s)\}$ and the variance $\mathrm{var}\{\hat{\Upsilon}^{(\mathrm{p})}(s)\}$.

It can be shown that the mathematical expectation of the periodogram $\mathsf{E}\{\hat{\Upsilon}^{(p)}(s)\}$ is the convolution of the true SDF $\Upsilon(s)$ and the Fourier transform of the rectangular window given by *Fejér's kernel* $\mathcal{F}(s)$:

$$\mathsf{E}\{\hat{\Upsilon}^{(p)}(s)\} = \int_{-s_{\text{Nyq}}}^{s_{\text{Nyq}}} \mathcal{F}(s - s')\Upsilon(s')\mathrm{d}s', \tag{2.37}$$

where

$$\mathcal{F}(s) = \frac{\Delta t \sin^2(N\pi s\Delta t)}{N \sin^2(\pi s\Delta t)}. \tag{2.38}$$

The variance of the periodogram can be estimated with the following asymptotic relation:

$$\text{var}\{\hat{\Upsilon}^{(p)}(s)\} = \Upsilon^2(s), \; 0 < |s| < s_{\text{Nyq}}, \; \text{as } N \to \infty. \tag{2.39}$$

The bias and variance of the periodogram can be efficiently reduced. Bias can be reduced by the use of windows, and variance can be reduced by the use of either smoothing or some sort of averaging. We consider these techniques below.

2.4.4 Windowing

In order to reduce bias in the periodogram, i.e. in order to minimize $|\Upsilon(s) - \mathsf{E}\{\Upsilon^p(s)\}|$, let us introduce the Direct Spectral Estimator (DSE), which is a modification of the periodogram:

$$\hat{\Upsilon}^{(d)}(s) = \Delta t \left| \sum_{n=0}^{N-1} h[n]f[n]e^{-2\pi i s n\Delta t} \right|^2, \tag{2.40}$$

where $h[n]$ is a window applied to the original time series $f[n]$ with the aim of reducing bias in the estimation. The mathematical expectation of the DSE is

$$\mathsf{E}\{\hat{\Upsilon}^{(d)}(s)\} = \int_{-s_{\text{Nyq}}}^{s_{\text{Nyq}}} \mathcal{H}(s - s')\Upsilon(s')\mathrm{d}s', \tag{2.41}$$

where $\mathcal{H}(s)$ is the spectral window playing similar role as the Fejér's kernel in the periodogram. The spectral window $\mathcal{H}(s)$ is related to the Fourier transform $H(s)$ of the window $h[n]$:

$$\mathcal{H}(s) = \frac{1}{\Delta t}|H(s)|^2 = \Delta t \left| \sum_{n=0}^{N-1} h[n]e^{-2\pi i s n\Delta t} \right|^2. \tag{2.42}$$

In the special case when $h[n] = 1/\sqrt{N}$ for $n = 0, 1, \ldots, N - 1$ the DSE coincides with the periodogram and the spectral window is equal to the Fejér's kernel: $\mathcal{H}(s) = \mathcal{F}(s)$.

Convolving $\Upsilon(s)$ with $\mathcal{H}(s)$ introduces bias to the actual spectrum $\Upsilon(s)$. The main idea of windowing is to choose the window $h[n]$ such that the sidelobes of the spectral window $\mathcal{H}(s)$ would be smaller than the sidelobes of the kernel $\mathcal{F}(s)$ and, at the same time, the mainlobe width of the spectral window $\mathcal{H}(s)$ would allow capture of all separate peaks in the spectrum.

The variance of the DSE can be actually larger or smaller than that of the periodogram. For processes with absolutely summable autocovariance function, it can be shown that in the asymptotic case the variance is the same as for the periodogram:

$$\text{var}\{\hat{\Upsilon}^{(\text{d})}(s)\} = \Upsilon^2(s),\ 0 < |s| < s_{\text{Nyq}},\ \text{as } N \to \infty. \tag{2.43}$$

2.4.5 Optimal windows

There is a great deal of literature comparing and analyzing different windows (for example, Harris, 1978; Gade and Herlufsen, 1987). The choice of a window for each particular case is non-obvious and hard to justify. Quite often, when the circumstances are favourable, there is effectively no difference between typical window functions, such as Bartlett, Hann, Welch or other similar windows (Press et al., 1992). Moreover, according to Broersen (2000), "it is fiction that objective choices between windowed periodograms can be made". Yet, different windows can be characterized with definite properties that can help to decide whether a window is appropriate or inappropriate for a given situation. One such property is the spectral concentration measure. Using this property, one can select a window whose corresponding kernel has the highest concentration of energy in a given bandwidth, called the spectral resolution bandwidth. Consequently, outside the spectral resolution bandwidth, such a window has the lowest possible amount of energy, and, thus, the lowest possible bias due to leakage. One of the first optimal discrete windows for the spectral estimation, based on such principle, was constructed by Eberhard (1973).

Suppose the window $h[n]$ has the Fourier transform $H(s)$ defined on $s \in [-s_{\text{Nyq}}, s_{\text{Nyq}}]$. Let us define the spectral concentration measure $\beta^2(W)$ in the interval $[-W, W]$ through the following:

$$\beta^2(W) = \int_{-W}^{W} |H(s)|^2 \mathrm{d}s \Big/ \int_{-s_{\text{Nyq}}}^{s_{\text{Nyq}}} |H(s)|^2 \mathrm{d}s\ , \tag{2.44}$$

where $|W| < s_{\text{Nyq}}$. The length of the interval $[-W, W]$ equal to $2W$ defines the spectral resolution bandwidth. Large values of $\beta^2(W)$ signify high concentration of energy in the interval $[-W, W]$. Following Slepian (1978), the concentration $\beta^2(W)$ can be rewritten as:

$$\beta^2(W) = \sum_{n=0}^{N-1} \sum_{m=0}^{N-1} h[n]h[m] \frac{\sin[2\pi W(n-m)]}{\pi(n-m)} \Big/ \sum_{n=0}^{N-1} h^2[n]\ . \tag{2.45}$$

Let **h** be a vector of N values of the window $h[n]$:

$$\mathbf{h} = \begin{vmatrix} h[0] \\ h[1] \\ \vdots \\ h[N-1] \end{vmatrix}. \tag{2.46}$$

Let **S** be the $N \times N$ matrix with the elements

$$S_{nm} = \frac{\sin[2\pi W(n-m)]}{\pi(n-m)}, \tag{2.47}$$

where $n = 0, 1, \ldots, N-1$ and $m = 0, 1, \ldots, N-1$.

The concentration C can be expressed in terms of **h** and **S**:

$$C = \frac{\mathbf{h}^{\mathrm{T}} \mathbf{S} \mathbf{h}}{\mathbf{h}^{\mathrm{T}} \mathbf{h}}, \tag{2.48}$$

where $(\cdot)^T$ denotes the transpose of a matrix. From the Eq. (2.48), we have the following eigenvalue problem:

$$\mathbf{S}\mathbf{h} = C\mathbf{h}. \tag{2.49}$$

This problem has N distinct eigenvalues $\lambda_k(N, W), k = 0, 1, \ldots, N-1$. We can order the eigenvalues so that $\lambda_0(N, W) > \lambda_1(N, W) > \ldots > \lambda_{N-1}(N, W)$. Then, the maximum eigenvalue $\lambda_0(N, W)$ is the maximum possible concentration for given parameters N and W. The corresponding eigenfunctions $v_{k,n}(N, W)$ form a set of orthogonal windows. To obtain the final set of orthonormal windows $h_k^{\mathrm{Slep}}[n]$ maximizing the spectral energy concentration C, called Slepian windows or discrete prolate spheroidal sequences (DPSS), we need to standardize $v_{k,n}(N, W)$ so that

$$\sum_{n=0}^{N-1} v_{j,n}(N, W) \cdot v_{k,n}(N, W) = \delta_{j,k}, \tag{2.50}$$

where $j = 0, 1, \ldots, (N-1), k = 0, 1, \ldots, (N-1)$ and $\delta_{j,k}$ is the Kronecker delta function. An efficient algorithm for constructing Slepian windows is given by Bell et al. (1993).

The parameter W defines the order of a discrete prolate spheroidal sequence. When W is equal to the first Fourier sampling frequency $1/(N\Delta t)$, the sequence is said to be of the first order; when $W = 2/(N\Delta t)$, the sequence is of the second order, and so on. However, the parameter W characterizing the spectral resolution bandwidth does not have to be a Fourier frequency, it can be any real number less than s_{Nyq}, for example, $1.3/(N\Delta t)$.

2.4.6 Smoothing

Using windowing reduces bias associated with the sidelobe leakage. However, the DSE still lacks in terms of variance, which is not reduced by windowing.

In order to reduce variance, we can smooth the DSE by convolving it with a $2s_{\mathrm{Nyq}}$-periodic smoothing window $W(s)$:

$$\hat{\Upsilon}^{(\mathrm{lw})}(s) = \int_{-s_{\mathrm{Nyq}}}^{s_{\mathrm{Nyq}}} W(s - s')\hat{\Upsilon}^{(\mathrm{d})}(s)\mathrm{d}s'. \tag{2.51}$$

$\hat{\Upsilon}^{(\mathrm{lw})}(s)$ is the lag window spectral estimator.

The mathematical expectation of the lag window spectral estimator is

$$\mathsf{E}\{\hat{\Upsilon}^{(\mathrm{lw})}(s)\} = \int_{-s_{\mathrm{Nyq}}}^{s_{\mathrm{Nyq}}} \mathcal{U}(s - s')\Upsilon(s')\mathrm{d}s', \tag{2.52}$$

where

$$\mathcal{U}(s) = \int_{-s_{\mathrm{Nyq}}}^{s_{\mathrm{Nyq}}} W(s - s')\mathcal{H}(s')\mathrm{d}s'. \tag{2.53}$$

In practice the smoothing of the DSE is done by the discrete convolution rather than by the continuous one. The resulting estimator is defined for the discrete set of frequencies $s[k] = k/(N'\Delta t)$ where $N' \geq N$. The discretely smoothed direct spectral estimator $\hat{\Upsilon}^{(\mathrm{ds})}(s)$ is given by

$$\hat{\Upsilon}^{(\mathrm{ds})}(s[k]) = \sum_{j=-M}^{M} \eta[j]\hat{\Upsilon}^{(\mathrm{d})}(s'[k - j]), \tag{2.54}$$

where $\eta[j]$ are the smoothing coefficients defined for integers $j \in [-M, M]$. The lag window spectral estimator can be expressed through the discretely smoothed direct spectral estimator at the discrete frequencies $s[k]$ by choosing an appropriate set of smoothing coefficients $\eta[j]$.

To get an idea of how much the variance of the DSE decreases after smoothing, let us consider a special case of the smoothed direct spectral estimator:

$$\bar{\Upsilon}(s[k]) = \frac{1}{2M + 1} \sum_{j=-M}^{M} \hat{\Upsilon}^{(\mathrm{d})}(s[k - j]). \tag{2.55}$$

The estimator $\bar{\Upsilon}(s[k])$ averages neighboring values of the DSE. Let us assume that the DSE $\hat{\Upsilon}^{(\mathrm{d})}(s)$ is an unbiased estimator of the SDF $\Upsilon(s)$, that the values of the DSE at the discrete frequencies $s[k]$ are uncorrelated and that the SDF $\Upsilon(s)$ is a slowly varying function such that

$$\Upsilon(s[k - M]) \approx \ldots \approx \Upsilon(s[k]) \approx \ldots \approx \Upsilon(s[k + M]). \tag{2.56}$$

Then the variance of the estimator $\bar{\Upsilon}(s[k])$ is reduced by a factor $(2M + 1)$ in comparison with the DSE as follows:

$$\text{var}\{\bar{\Upsilon}(s[k])\} \approx \frac{\text{var}\{\hat{\Upsilon}^{(\text{d})}\}}{2M + 1}. \tag{2.57}$$

2.4.7 Multitapering

A multitaper estimator is a linear combination of several direct spectral estimators utilizing a set orthonormal windows (also called tapers, hence, the term 'multitapering'). The simplest version of the multitaper estimator is the average of K spectral estimators:

$$\hat{\Upsilon}^{(\text{mt})}(s) = \frac{1}{K} \sum_{k=0}^{K-1} \hat{\Upsilon}_k^{(\text{d})}(s), \tag{2.58}$$

where $\hat{\Upsilon}_k^{(\text{d})}(s)$ is a DSE using the Slepian window $h_k^{\text{Slep}}[n]$. For each DSE there is a corresponding spectral window

$$\mathcal{H}_k(s) = \Delta t \left| \sum_{n=1}^{N-1} h_k[n] e^{-2\pi i s n \Delta t} \right|^2 . \tag{2.59}$$

The mathematical expectation of the estimator $\hat{\Upsilon}^{(\text{mt})}(s)$ is

$$\mathsf{E}\{\hat{\Upsilon}^{(\text{mt})}(s)\} = \int_{-s_{\text{Nyq}}}^{s_{\text{Nyq}}} \overline{\mathcal{H}}(s - s')\Upsilon(s')\mathrm{d}s', \tag{2.60}$$

where

$$\overline{\mathcal{H}}(s) = \frac{1}{K} \sum_{k=0}^{K-1} \mathcal{H}_k(s). \tag{2.61}$$

The protection of the multitaper estimator against sidelobe leakage is equal to the average protection of the DSE estimators $\hat{\Upsilon}_k^{(\text{mt})}(s)$. The averaging of spectral windows, at the same time, assures that the variance of the estimator $\hat{\Upsilon}^{(\text{mt})}(s)$ is reduced by a factor of $1/K$, provided that the direct spectral estimators $\hat{\Upsilon}_k^{(\text{mt})}(s)$ are uncorrelated. Approximate uncorrelatedness of the direct spectral estimators follows from the orthogonality of the corresponding windows.

The algorithm for the multitaper estimation is the following:

I. Set the resolution bandwidth $2W$;

II. Compute K 'unbiased' spectral estimators $\hat{\Upsilon}_k^{(\text{mt})}(s)$ for $k = 0, \ldots K - 1$ with $K \leq 2NW\Delta t$;

III. Average the spectra $\hat{\Upsilon}_k^{(\text{mt})}(s)$.

Instead of simple averaging, more complicated methods of combining the spectra $\hat{\Upsilon}_k^{(\text{mt})}(s)$ exist, e.g. methods using weighted averages.

2.4.8 Segment averaging (Welch's method)

The basic idea of Welch's method is to reduce variance by estimating spectra for several blocks of a given time series and then averaging them. The idea was suggested before Welch in the article by Bartlett (1950). The main steps of the estimation were the following:

I. Split the original time series $f[n]$ into N/M consecutive blocks assuming that M is the number of blocks and N/M is an integer.

II. Calculate the periodogram for each block;

III. Average all the periodograms.

Welch (1967) improved the method by making the blocks overlapping and changing the periodogram on each block into a direct spectral estimator. The algorithm for calculating Welch's estimator is described below.

Let N_{block} be the length of each block and let $h[n]$ for $n = 0, 1, \dots, N_{\text{block}} - 1$ define a window applied to each block. The direct spectral estimators computed for each block starting at the index l are given by

$$\hat{\Upsilon}_l^{(\text{d})}(s) = \Delta t \left| \sum_{n=0}^{N_{\text{block}}-1} h[n] \cdot f[n+l] e^{-2\pi i s n \Delta t} \right|^2, \ 0 \leq l \leq N - N_{\text{block}}. \tag{2.62}$$

We define Welch's spectral estimator as

$$\hat{\Upsilon}^{(\text{w})}(s) = \frac{1}{M} \sum_{j=0}^{M-1} \hat{\Upsilon}_{j \cdot n_{\text{s}}}^{(\text{d})}(s), \tag{2.63}$$

where $M = N - N_{\text{block}} + 1$ is the total number of blocks and n_{s} is the shift value such that $0 < n \leq N_{\text{block}}$ and $n_{\text{s}}(M-1) = N - N_{\text{block}}$.

The mathematical expectation of Welch's estimator coincides with the mathematical expectation of each direct spectral estimator $\hat{\Upsilon}_l^{(\text{d})}(s)$:

$$\mathsf{E}\{\hat{\Upsilon}^{(\text{w})}(s)\} = \int_{-s_{\text{Nyq}}}^{s_{\text{Nyq}}} \mathcal{H}(s - s')\Upsilon(s')\mathrm{d}s'. \tag{2.64}$$

44

The improvement in variance can be readily seen for the special case when the blocks are non-overlapping ($n_{\mathrm{s}} = N_{\mathrm{block}}$):

$$\mathrm{var}\{\hat{\Upsilon}^{(\mathrm{w})}(s)\} \approx \frac{1}{M} \sum_{j=0}^{M-1} \Upsilon^2(s). \tag{2.65}$$

2.4.9 Averaging realizations

If several realizations of the same process are available, then, to reduce variance, one can average estimators calculated for each realization. Suppose there are N_{r} realizations $f_l[n]$ for $l = 0, 1, \ldots, (N_{\mathrm{r}} - 1)$. Let $\hat{\Upsilon}_l(s)$ define a spectral estimation for each realization, obtained using any of the estimators described above. Then, the average estimator is

$$\hat{\Upsilon}^{(\mathrm{ave})}(s) = \frac{1}{N_{\mathrm{r}}} \sum_{l=0}^{N_{\mathrm{r}}-1} \hat{\Upsilon}_l(s). \tag{2.66}$$

The mathematical expectation of the estimator $\hat{\Upsilon}^{(\mathrm{ave})}(s)$ is the same as for each estimator $\hat{\Upsilon}_l(s)$. The variance, on the other hand, is reduced by a factor $1/N_{\mathrm{r}}$.

2.5 Example: observations of van Haren et al. (2002)

Let us consider how the described techniques work for a time series from observations described in the paper by van Haren et al. (2002). We analyse the flow speed $u(t)$ measured at a mooring near the Bay of Biscay at the depth of 4.81 km. The analysed time series is given by

$$u_n = u(t_n), \ t_n = n\Delta t, \ n = 0, 1, \ldots, N,$$

where $\Delta t = 20$ min, $N = 22100$. The total length of the time domain is $T = 306.94$ days. The time series u_n is pre-processed by subtracting the arithmetic average. A fragment of the time series u_n is shown in figure 2.10.

All the spectral estimations for this example, are evaluated at the Fourier sampling frequencies, i.e. at the frequencies $\omega_n = 2\pi n/T$, where $n = 0, 1, \ldots, N/2$. As the domain length is large, the Fourier frequencies provide a sufficiently dense distribution of frequencies. The estimations will be shown for the frequencies $\omega \in [0, 6 \times 10^{-4}] \text{ s}^{-1}$. The Nyquist frequency is $\omega_{\mathrm{Nyq}} = 2.6 \times 10^{-3} \text{ s}^{-1}$.

Figure 2.11 shows the periodogram. The naive estimation is characterized by high variance, so it is hard to make out the peaks corresponding to tidal harmonics and the inertial frequency.

Figure 2.12 shows the direct spectral estimation $\Upsilon^{\mathrm{d}}(\omega)$ evaluated using a Hann window and the corresponding smoothed estimation $\bar{\Upsilon}(s)$. The fragment of the direct spectral estimation is
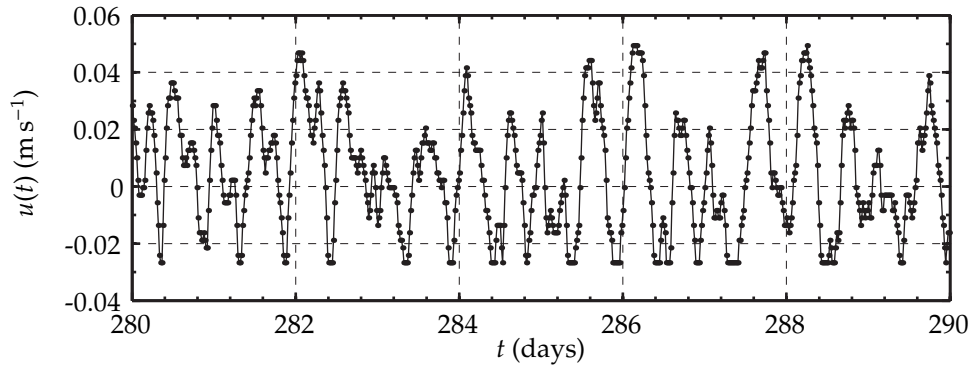
F   2.10: Observation example: a fragment of the time series u_n corresponding to the speed $u(t)$, $t \in [280, 290]$ days.
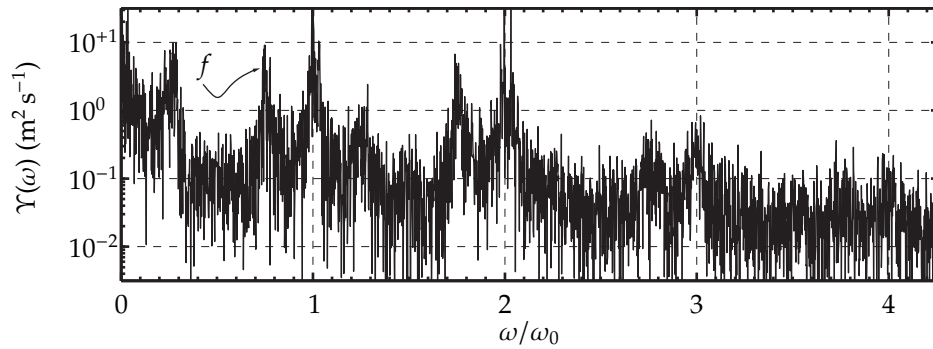
F   2.11: Observation example: the periodogram.
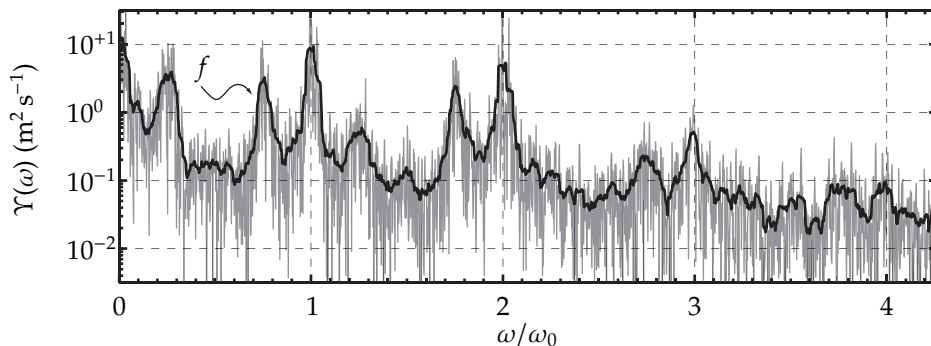
F   2.12: Observation example: the direct spectral estimation $\Upsilon^{\mathrm{d}}(\omega)$ evaluated using the Hann window (gray line) and the corresponding smoothed version $\tilde{\Upsilon}(s)$ evaluated with $M = 12$ (thick black line).

similar to the periodogram in figure 2.11. As the structure of the spectrum does not change after applying the Hann window, leakage is not an issue for the frequency interval shown. Smoothing the direct spectral estimation effectively reduces the variance, approximately by a factor of $2M + 1 = 25$. The prominent peaks at frequencies ω_0, $2\omega_0$, $3\omega_0$, etc. are clearly seen. There is a peak at the Coriolis frequency f and its multiples. In addition, there are weaker peaks at the combinations of the frequencies ω_0 and f, e.g. $\omega_0 - f$, $\omega_0 + f$, $2\omega_0 - f$, etc. Our estimations of the flow speed spectrum show the same energetic frequencies as the kinetic energy spectra estimated by van Haren et al. (2002). The weak peaks in our estimation are more distinguishable than they are in the estimation of van Haren et al.

Figures 2.13 and 2.14 demonstrate two other techniques: the multitaper and Welch estimators. Both techniques adequately capture the energetic frequencies. The Welch method is very smooth in comparison with other methods.

2.6   Conclusion

In this chapter we defined the concept of spectrum for regular functions and stochastic processes. We also presented some efficient methods for dealing with bias and variance in the estimations of the spectrum: windowing, smoothing, multitapering, segment averaging and averaging over realizations. All of the concepts presented in this chapter were used during the research. In particular, when seeking an optimal spectral estimation, different estimation techniques were compared. Presented spectra, however, will be shown only for the simplest techniques providing satisfying results. For example, whenever the multitaper spectral estimator provided similar
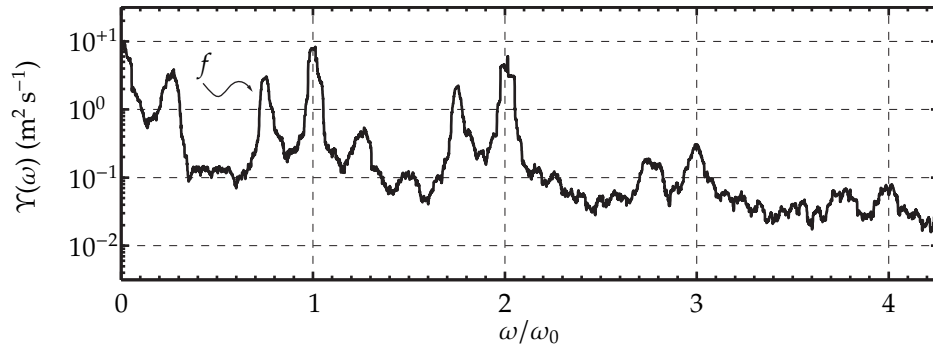
F   2.13: Observation example: the multitaper estimation of the twelfth order $\Upsilon^{\mathrm{mtm}}(\omega)$.
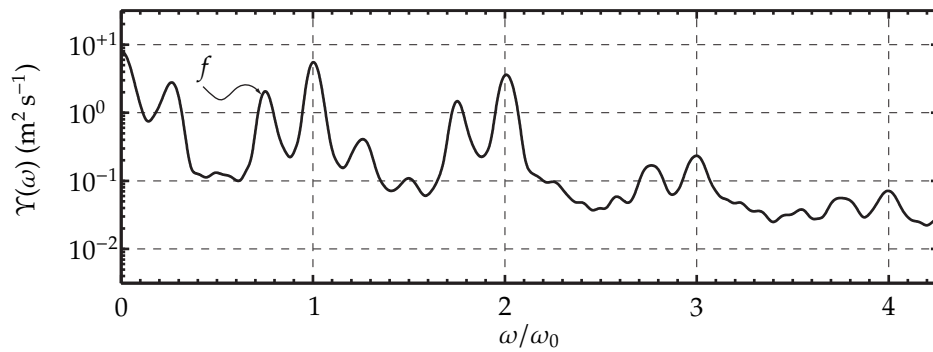
F   2.14: Observation example: the Welch estimation $\Upsilon^{\mathrm{w}}(\omega)$ evaluated using the Hann window on 49 segments with 50% overlapping.

results as the smoothed or averaged direct spectral estimator, the preference was given to the direct spectral estimation, as its internal structure is simpler and easier to interpret.

Chapter 3

Temporal Spectral Analysis: Part I

3.1 Spectral content of internal waves

A periodic disturbance in a stably, continuously stratified fluid generates a spectrum of internal waves. Depending on their frequency, they may propagate away from the disturbance or they may be trapped near the generation site. In the case of finite-amplitude disturbances, the generation process and the resulting fluid motion are usually too complex to be described directly in terms of particle displacements or velocities. However, there is evidence that the spectrum of the wavefield has a much simpler structure which allows insight into the nature of the flow. The deep ocean, for example, abounds with internal waves, generated primarily by two sources, tides and winds (Munk and Wunsch, 1998); the variety and multitude of factors that affect the internal wave field make a direct description of the waves impossible. Yet, the energy spectrum of the waves has a simple algebraic representation, known as the Garrett-Munk spectrum (Garrett and Munk, 1975), which is universal throughout the deep ocean, away from the strong generation sites. With this in mind, in order to understand the essential physics of a flow generated by a periodic disturbance, be it an oscillating body in a stratified fluid or a tidal flow over topography, one may seek to study the fluid dynamics in association with the energy transfers within the spectrum (see, for example, Winters and D'Asaro, 1997; Hibiya, Niwa, and Fujiwara, 1998; Furue, 2003; Furuchi, Hibiya, and Niwa, 2005; Gerkema, Staquet, and Bouruet-Aubertot, 2006; Legg and Huijts, 2006; MacKinnon and Winters, 2007).

Many facts about the energy cascade in internal waves are known. The first one is rather obvious: if the oscillating source has the fundamental frequency ω_0, most of the internal waves generated directly by the source are of the same frequency, and, consequently, a considerable amount of energy may be put into progressive waves of frequency ω_0. Historically, the presence

of a dominant frequency was the first property of internal waves to be noticed. For example, in 1907, not long after the discovery of the internal waves in the ocean by Nansen (1902), Otto Pettersson discovered the tidal periodicity of vertical internal movements in Danish sounds, which was a discovery of great importance, considering that tides were not known as a source of internal waves at that time. Internal waves of the fundamental frequency were also the target of the earliest experimental studies. For example, Görtler (1943); Mowbray and Rarity (1967); Thorpe (1968) and many others later, observed internal wave beams of the fundamental frequency generated by a body oscillating in a linearly stratified fluid. In the special case of linear stratification, when the buoyancy frequency N_b and Coriolis frequency f are constant, the beam of frequency $\omega \in (f, N_b)$ has constant slope r given by

$$r^2 = \frac{\omega^2 - f^2}{N_b^2 - \omega^2},$$

(3.1)

and internal waves are manifested in the famous St Andrew's Cross pattern. The consideration of the oceanic analogues, topographically-generated beams of tidal frequency, can be found in numerical studies (for example, Holloway and Merrifield, 1999), and in several field observations (for example, Pingree and New, 1991). However, the best confirmation of the fact that waves of the fundamental frequency represent the first candidate to drain energy from the source comes from the spectra of internal waves. In the deep ocean, for example, the spectra of internal waves near rough topography and near the surface are often characterized by prominent peaks at the tidal and Coriolis frequencies (Olbers, 1983), both being the fundamental frequencies of the two sources.

Waves of the fundamental frequency ω_0 generated by an oscillating source are usually accompanied by weaker waves of higher harmonics $n\omega_0$, where $n \in \{2, 3, \ldots\}$. Although the harmonics have been observed in most experiments on internal waves (e.g., Mowbray and Rarity, 1967), their nature and energetics were obscure until the work by Bell (1975). He considered a linearly stratified tidal flow over isolated topography in a non-rotating fluid of infinite depth, and used the first-order approximation of the nonlinear operator in the governing equations. The solution that Bell obtained is a linear superposition of tidal harmonics emanating from the ridge. It was realized later that harmonics may also be produced by higher-order nonlinear interactions at locations where waves of harmonic frequencies cross. The generation of the higher harmonics through the collision or reflection of internal wave beams can be found in the numerical experiments by Lamb (2004) and Gerkema et al. (2006). Recent laboratory experiments confirmed the existence of higher-harmonic beams generated through reflection of a single beam (Peacock and Tabaei, 2005). There are also field observations where internal waves are generated by nonlinear superposition of tidal harmonics (Stashchuk and Vlasenko, 2005). The fact that the interaction of internal wave beams can generate harmonics inspired a theoretical investigation of the nonlinear

interactions by seeking a weakly nonlinear solution (Tabaei, Akylas, and Lamb, 2005). On the whole, there is plenty of evidence that the harmonics represent a family of frequencies that can efficiently receive energy from the source and later transfer it to other waves.

As internal waves are both strongly nonlinear (Holloway, 1980) and intrinsically unstable (Koudella and Staquet, 2006), the set of possible frequencies is not limited to harmonics only. When a single internal wave of frequency ω_0 is subject to a small perturbation, an instability of the parametric subharmonic type (PSI) will inevitably set in (Hasselmann, 1967), i.e. there may be generated two other waves of frequencies ω_1 and ω_2, such that $|\omega_1| + |\omega_2| = |\omega_0|$. The maximum growth rate occurs for the frequencies $|\omega_1| = |\omega_2| = |\omega_0/2|$ (Staquet and Sommeria, 2002). The earliest laboratory studies confirming the destabilization of a single standing wave by PSI include the works by Thorpe (1968) and McEwan (1971). There was also a number of numerical works on PSI within an oceanic context during 1970–1980 reviewed by Orlanski (1981). However, it was shown that PSI (along with other resonant triad interactions), occurring in a random internal wave field, is too slow to be the dominant mechanism for energy transfers in the deep ocean (Olbers and Pomphrey, 1981).

Instabilities occurring in the vicinity of highly nonlinear regions where a subharmonic wave is generated can be much stronger, sometimes leading to wave breaking on time-scales much shorter than those of PSI for a single wave (de Silva, Imberger, and Ivey, 1997). The regions where the forced nonlinear instabilities may occur include regions of reflection of an internal wave beam from the boundary (Javam, Imberger, and Armfield, 1999) and regions where two strong beams intersect (McEwan, 1973; Teoh, Ivey, and Imberger, 1997; Javam, Imberger, and Armfield, 2000). The strong subharmonics observed in numerical simulations of internal tides by MacKinnon and Winters (2003); Lamb (2004); Gerkema et al. (2006) are also generated by forced nonlinear instabilities. It is likely that the strong subharmonics seen in field observations (e.g., Carter and Gregg, 2006) are also the result of strong nonlinear instabilities. In a paper by MacKinnon and Winters (2007), the authors refer to the instability occurring to the internal wave beam of tidal frequency as "rapid parametric subharmonic instability". However, it should be noticed, that although the forced instabilities and PSI are kindred phenomena, the former do not have to be resonant triad interactions (Teoh et al., 1997; Javam et al., 1999, 2000). The frequencies of strong subharmonics generated through the forced instability may be different from $\omega_0/2$ predicted for PSI (Lamb, 2004). Moreover, the overturning that may follow the instability is more likely to occur in cases when energy is accumulated in trapped waves, not in progressive ones. In other words, the impact of non-resonant triad interaction on the flow may change the dynamics completely, before any resonant triad interaction comes into play. In this sense, the forced instabilities, or non-resonant triad interactions, may be more important than PSI and resonant triad interactions.

If there are several sources of internal waves with fundamental frequencies ω_1, ω_2 and so on, then, strong waves can be generated at the combination frequencies, such as $|\omega_1 - \omega_2|$, $|2\omega_1 - \omega_2|$,

$|2\omega_2 - \omega_1|$, etc. This was studied experimentally by Teoh et al. (1997); Chashechkin and Nekludov (1990), theoretically by Kistovich and Chashechkin (1991), and numerically by Javam et al. (2000). Strong waves at combination frequencies have been observed in the ocean. For example, van Haren, Maas, and van Aken (2002) show that the spectra of internal waves have strong peaks at combination frequencies of the two fundamental frequencies, the tidal and Coriolis frequency.

In this chapter, we consider the spectral content of the internal wave fields in our simulations and show that apart from the harmonics and subharmonics, waves of interharmonic frequencies greater than the fundamental frequency are generated. Interharmonics are defined as frequencies lying between the multiples of the fundamental frequency; subharmonics are a subclass of interharmonics corresponding to frequencies less than the fundamental frequency. In our numerical experiments, subharmonics are generated by the instability of the tidal beam near strongly nonlinear regions. Through wave-wave interactions energy transfers from subharmonics to higher interharmonics, so that the interharmonic frequencies observed in the flow spectra happen to be the combination frequencies of the strongest subharmonics and harmonics. The magnitude of waves produced by resonant and non-resonant triad interaction is comparable, i.e. the flow has no preference for one or the other type of interaction.

3.2 Numerical experiments set-up

3.2.1 Domain

Equations (1.1) are solved in a symmetric two-dimensional domain representing a vertical cross-section of the ocean with a flat-topped ridge at the bottom:

$$R = \{(x,z) \,\|\, -L/2 \le x \le L/2, -H + h(x) \le z \le 0\},$$

where L is the horizontal length of the domain, H is the water depth away from the ridge, and $h(x)$ defines the topography of the ocean bottom. The shape of the topography was adapted from the work by Shore (1996):

$$h(x) = A \exp\left[-\left(\frac{x}{d}\right)^4\right], \tag{3.2}$$

with $A = 1800$ m being the amplitude and $d = 12500$ m defining the width of the ridge. The hill $h(x)$ is supercritical, i.e. its maximum slope is steeper than the slope r_0 of the radiated internal tide. The criticality parameter corresponding to the topography is defined as $\alpha = \max\left[h'(x)\right]/r_0$ and is within the range $[1.54, 2.07]$ for the considered cases. With respect to the second harmonic, the topography is subcritical in all cases, i.e. $\max\left[h'(x)\right]/r_2 \in [0.75, 0.79]$, where r_2 is the slope corresponding to the second harmonic at one of the five latitudes. Typical parameters associated

with the domain description are summarized in table 3.1 along with other parameters. The development of the fluid flow is considered on the time domain $[0, T_{tot}]$, where $T_{tot} = 30$ days.

The governing equations (1.1) are subject to boundary conditions at each side of the domain and an initial condition. At the left boundary the flow is forced with a periodic tidal current $U(t) = U_0 \cos(\omega_0 t)$. The following typical values for the amplitude U_0 and the semidiurnal tidal frequency ω_0 were used: $U_0 = 0.025$ m s^{-1} and $\omega_0 = 1.4075 \times 10^{-4}$ s^{-1}. At the bottom of the domain an impermeability condition is imposed: $\mathbf{u} \cdot \mathbf{n} = 0$, where $\mathbf{n}$ is a vector normal to the boundary. At the top of the domain we also use an impermeability condition $w = 0$. At the right boundary an outflow boundary condition is applied allowing long waves to propagate away freely without reflection. The model is initialized with the peak rightward barotropic flow: $u(x, z, t = 0) = Q/[H - h(x)]$, and $v(x, z, t = 0) = 0$, where Q is the maximum barotropic volume flux given by $Q = U_0 H$. Incompressibility then dictates the vertical velocity component: $w(x, z, t = 0) = -Qh'(x)z/(H - h(x))^2$. The fluid density at time $t = 0$ is linearly stratified, so that the buoyancy frequency

$$N_b \equiv \left(-\frac{g}{\rho_0} \frac{d\rho_{ph}}{dz} \right)^{\frac{1}{2}} = 10^{-3} \text{ s}^{-1} \tag{3.3}$$

is constant.

3.2.2 Model

The numerical scheme used to solve equations (1.1) is a Finite Volume Method based on the second-order projection technique developed by Bell, Collela, and Glaz (1989) and extended to stratified flows by Bell and Marcus (1992) and to quadrilateral grids by Bell, Solomon, and Szymczak (1989). The description of the model can be found in the paper by Lamb (1994).

The model uses a terrain-following grid. The total domain R is discretized with two staggered grids for the evaluation of scalar and vector unknowns: vector grid points are located at the centers of finite volumes and scalar grid points are located at the nodes of the finite volumes. Each grid can be split into three parts with respect to the horizontal resolution: the central region of length $L_{cent} = 819.2$ km with a relatively high horizontal resolution of $\Delta x = 100$ m and two side regions of length $L_{side} \approx 2887$ km with lower horizontal resolution of $\Delta x = 1500$ m. The grid spacing varies smoothly from one region to another. The purpose of the side regions is to allow the fast large-scale waves generated at the centre to propagate away from the source without reflection. The length of the domain is chosen so that the waves have just enough time to reach the boundaries, but not enough time to affect the middle part after reflection.

The vector grid discretizing the central part of the domain is given by the physical coordinates

Category:	Parameter			Value
Physical:	Coriolis frequency	$f(\theta = 0°)$	$=$	0 s^{-1}
		$f(\theta = 10°)$	$=$	$0.2535 \times 10^{-4} \text{ s}^{-1}$
		$f(\theta = 20°)$	$=$	$0.4993 \times 10^{-4} \text{ s}^{-1}$
		$f(\theta = 30°)$	$=$	$0.7300 \times 10^{-4} \text{ s}^{-1}$
		$f(\theta = 40°)$	$=$	$0.9385 \times 10^{-4} \text{ s}^{-1}$
	maximum tidal speed (deep water)	U_0	$=$	0.025 m s^{-1}
	tidal frequency	ω_0	$=$	$1.4075 \times 10^{-4} \text{ s}^{-1}$
	tidal excursion distance (deep water)	L_{tid}	$=$	355.2398 m
	gravitational acceleration	g	$=$	9.81 m s^{-2}
Domain:	total length	L	$=$	6000 km
	water depth	H	$=$	5 km
	ridge amplitude	A	$=$	1.8 km
	ridge width parameter	d	$=$	12.5 km
	total time	T_{tot}	$=$	30 days
Discretization:	central region length	L_{cent}	$=$	819.2 km
	# of horizontal points in the centre	I_{cent}	$=$	8192
	# of horizontal points on sides	I_{side}	$=$	2000
	# of vertical points	J	$=$	192
	cell width (central domain)	Δx	$=$	100 m
	cell height (deep water)	Δz	$=$	26.042 m
	cell height (shallow water)	Δz	$=$	16.667 m
	maximum time-step	$\mathrm{d}t$	$=$	30 s
Nondimensional:	criticality parameter	$\alpha(\theta = 0°)$	$=$	1.5424
		$\alpha(\theta = 10°)$	$=$	1.5681
		$\alpha(\theta = 20°)$	$=$	1.6497
		$\alpha(\theta = 30°)$	$=$	1.8040
		$\alpha(\theta = 40°)$	$=$	2.0696
	tide intensity	L_{tid}/d	$=$	0.0284
	ridge aspect ratio	d/A	$=$	6.9444
	ratio of elevation and depth	A/H	$=$	0.36

T   3.1: Problem parameters.

$\{x_{ij}, z_{ij}\}$:

$$
\begin{cases}
x_{ij} = -L_{\text{cent}}/2 + \left(i + \dfrac{1}{2}\right)\Delta x, & \Delta x = \dfrac{L_{\text{cent}}}{I}, \\
z_{ij} = -H + h(x) + (j + \dfrac{1}{2})\Delta z_{ij}, & \Delta z_{ij} = \dfrac{H - h(x_{ij})}{J},
\end{cases}
\tag{3.4}
$$

where $I = 8192$ and $J = 192$ are the number of points in the vertical and horizontal direction, respectively.

The time-stepping procedure allows a variable time-step based on the Courant–Friedrichs–Lewy (CFL) condition for the upwind method. However, the maximum time-step was set to a relatively small value $dt = 30$ s, so the time-step did not actually change throughout the computation, except for some small intervals of time.

3.2.3   Reference frame

In order to choose an appropriate sampling time step Δt and an appropriate reference frame, we compared spectra of the baroclinic horizontal velocity in the Lagrangian, Eulerian and barotropic-Lagrangian reference frame. Both the sampling time interval and reference frame affect the spectrum of the velocity. The sampling rate defines the amount of aliasing in the spectral estimation. The reference frame may lead to the appearance of Doppler shifted frequencies in the spectral estimation. Ideally, working in the Lagrangian reference frame eliminates all Doppler shifted frequencies. However, it is expensive to calculate all data sets in the Lagrangian reference frame. We found that the barotropic-Lagrangian reference frame with the sampling time interval of 30 min is an acceptable compromise for our purposes. In order to illustrate why the barotropic-Lagragian reference frame suits us best, let us consider a concrete example of the spectral estimation performed for different reference frames.

The first set of time series, representing the baroclinic velocity in the Eulerian reference frame, is given by $u^{\text{Eul}}(x, z, t) = u(x, z, t) - U(t)H/[H - h(x)]$ sampled in time with the sampling interval $\Delta t = 5$ min at the locations shown in figure 3.1.

The second set of time series, representing the baroclinic velocity in the Lagrangian reference frame, is given by $u^{\text{Lag}}(\tilde{\xi}, \tilde{\eta}, t) = u(\tilde{\xi}, \tilde{\eta}, t) - U(t)H/[H - h(\tilde{\xi})]$ corresponding to the fluid particles whose trajectories are given by $(\tilde{\xi}(t), \tilde{\eta}(t))$ and whose initial locations are shown in figure 3.1; the time series are sampled in time with the sampling interval $\Delta t = 5$ min.

The third set of time series, representing the baroclinic velocity in the barotropic-Lagrangian reference frame, is given by $u^{\text{bar}}(\xi, \eta, t) = \tilde{u}(\xi, \eta, t) - U(t)H/[H - h(\xi)]$ such that at the initial moment (ξ, η) coincide with the coordinates (x, z) at the locations shown in figure 3.1; the time series are sampled in time with the sampling interval $\Delta t = 30$ min.
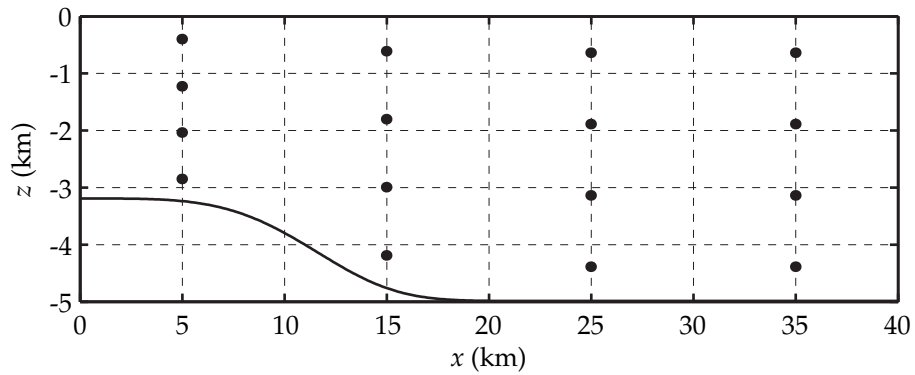
F   3.1: The locations where velocities at different reference frames were calculated (dots).
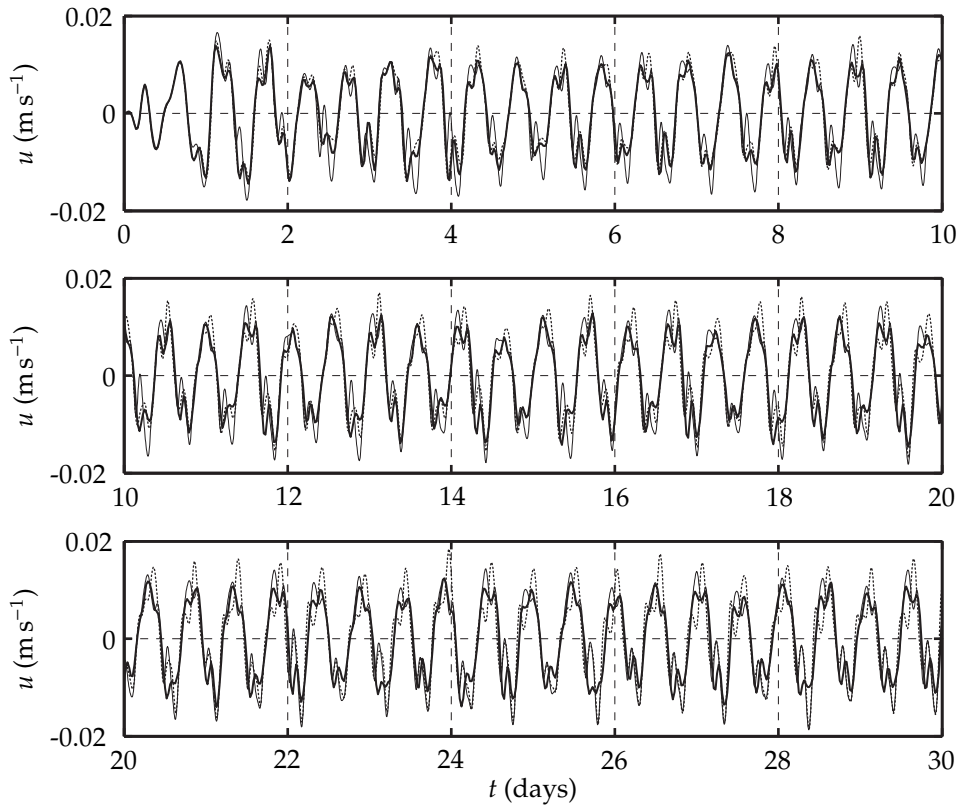
F   3.2: Velocity in different reference frames for the location $(x, z) = (4.970, -2.037)$ km: Lagrangian reference frame (dots), Eulerian reference frame (thin solid line), barotropic-Lagrangian reference frame (thick solid line). Panels correspond to time intervals $[0, 10]$, $[10, 20]$ and $[20, 30]$ days.
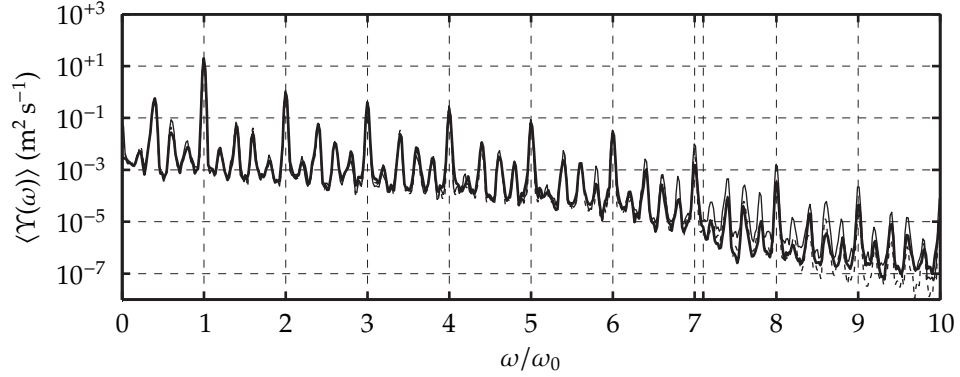
F   3.3: One-dimensional spectra of the horizontal velocity at latitude $0°$ for the locations shown in figure 3.1: Lagrangian reference frame (thick solid line), Eulerian reference frame (thin solid line), barotropic-Lagrangian reference frame (dashed line).

Figure 3.2 compares the time series corresponding to the three reference frames for one of the locations. The time series start deviating after the time period of about one day; however, the difference does not grow significantly in time. The spectra $\Upsilon^{\mathrm{Eul}}(\omega)$, $\Upsilon^{\mathrm{Lag}}(\omega)$ and $\Upsilon^{\mathrm{bar}}(\omega)$, corresponding to the time series $u^{\mathrm{Eul}}(x,z,t)$, $u^{\mathrm{Lag}}(\tilde{\xi},\tilde{\eta},t)$, and $u^{\mathrm{bar}}(\xi,\eta,t)$ at different locations, were evaluated using the direct spectral estimator. For the estimator we used a window given by the prolate spheroidal sequence of the third order. The Nyquist frequency for the sampling time interval $\Delta t = 30$ min is $\omega_{\mathrm{Nyq}} \approx 12.4\omega_0$, six times smaller than the Nyquist frequency for the sampling interval $\Delta t = 5$ min. Figure 3.3 compares the spectra $\left\langle \Upsilon^{\mathrm{Eul}}(\omega) \right\rangle$, $\left\langle \Upsilon^{\mathrm{Lag}}(\omega) \right\rangle$ and $\left\langle \Upsilon^{\mathrm{bar}}(\omega) \right\rangle$ for the three reference frames, where $\langle \cdot \rangle$ denotes averaging over different locations.

All the spectra are fairly close and capture the peaks at the same frequencies, consisting of harmonics and interharmonics. Thus, to define the spectral content of the flow, we could use any of the three reference frames. The decay rate of the three spectral estimations is approximately the same, indicating that the level of aliasing, which should be more pronounced for the spectrum $\Upsilon^{\mathrm{bar}}(\omega)$, is insignificant.

Although all of the spectra show similar energetic frequencies, the spectrum $\left\langle \Upsilon^{\mathrm{bar}}(\omega) \right\rangle$ is closer to the spectrum $\left\langle \Upsilon^{\mathrm{Lag}}(\omega) \right\rangle$ than is the spectrum $\left\langle \Upsilon^{\mathrm{Eul}}(\omega) \right\rangle$. For the frequency range $\omega \in [5\omega_0, 10\omega_0]$, the spectrum $\left\langle \Upsilon^{\mathrm{Eul}}(\omega) \right\rangle$ is larger than the other two. Thus, for the frequencies $\omega \in [0, 10\omega_0]$, the spectrum $\left\langle \Upsilon^{\mathrm{bar}}(\omega) \right\rangle$ represents a better approximation of the spectrum $\left\langle \Upsilon^{\mathrm{Lag}}(\omega) \right\rangle$.

Figure 3.4 demonstrates an analogous comparison of the spectra $\left\langle \Upsilon^{\mathrm{Eul}}(\omega) \right\rangle$, $\left\langle \Upsilon^{\mathrm{Lag}}(\omega) \right\rangle$ and $\left\langle \Upsilon^{\mathrm{bar}}(\omega) \right\rangle$ for the case $\theta = 20°$ N. The spectra are similar and capture the same frequencies. The main differences are observed outside the free internal wave range. For the frequencies $\omega > N_{\mathrm{b}}$, the spectrum $\left\langle \Upsilon^{\mathrm{Eul}}(\omega) \right\rangle$ is again larger than the other two. Also, the spectrum $\left\langle \Upsilon^{\mathrm{Lag}}(\omega) \right\rangle$
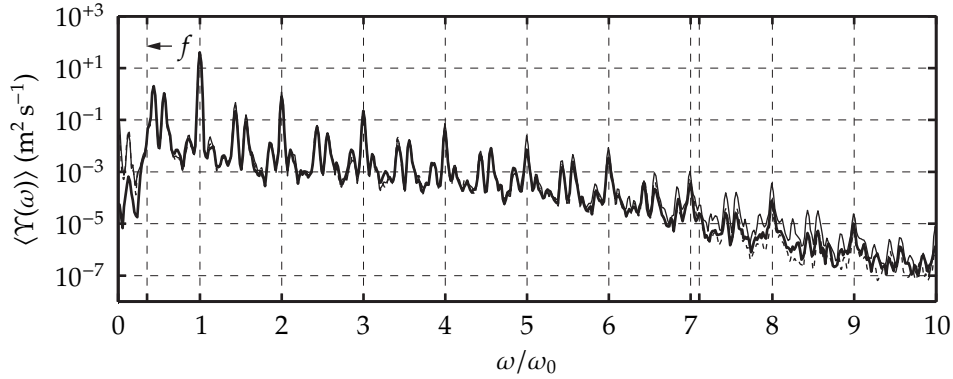
F   3.4: One-dimensional spectra of the horizontal velocity at latitude $20°$ for the locations shown in figure 3.1: Lagrangian reference frame (thick solid line), Eulerian reference frame (thin solid line), barotropic-Lagrangian reference frame (dashed line).

corresponding to the Lagrangian reference frame has a weaker peak at the subinertial range.

In the rest of the work we will analyse the spectrum of the horizontal velocity in the barotropic-Lagrangian reference frame.

3.2.4   Data

Five main numerical experiments that we discuss in this work are defined by the Coriolis frequencies listed in Table 3.1, corresponding to latitudes $\theta = 0°, 10°, 20°, 30°$ and $40°$ North. For each experiment the model was set up to store a data set composed of time-series at 30 minute intervals of the horizontal velocity u at each grid point in the central domain. Values of u are denoted by $\{u_{ij}^n\}$, where $i = 0, 1, \ldots, I-1, j = 0, 1, \ldots, J-1$ are the indices of the corresponding grid coordinates $\{x_{ij}, z_{ij}\}$; the superscript $n = 0, 1, \ldots, N-1$ corresponds to the temporal equipartition $t_n = (n+1)\Delta t$ covering the time period of 30 days, where the sampling interval is $\Delta t = 30$ min and the number of samples $N = 1440$. Even if the time-step dt is not always 30 s, the model guarantees that the data are stored at the equidistributed sampling times by changing appropriately the time-step just before storing the data.

Additional numerical experiments with similar setups are discussed separately. In particular we consider latitudes $25°$, $26°$, …, $35°$ N. Also, latitude $20°$ N is considered with different strengths of background flow: $0.8U_0$ and $1.2U_0$. Further, we consider the case $20°$ N for different amplitudes of topography: $0.8A_0$ and $1.2A_0$. Lastly, we consider the case $0°$ with corrugated topography constructed using the spectrum based primarily on topographic data from the eastern central North Pacific.

Apart from the horizontal velocity in the Eulerian reference frame given by $\{u^n_{ij}\}$, we also calculated the baroclinic velocity in the barotropic-Lagrangian reference frame, i.e. in a reference frame moving with the barotropic tide of horizontal velocity $U_b(x,t) = U_0 \cos(\omega_0 t)H/[H - h(x)]$. This yielded the matrix $\{\tilde{u}^n_{ij}\} = \{u(\xi^n_{ij}, \eta^n_{ij}, t_n) - U_b(\xi^n_{ij}, t_n)\}$ corresponding to the discretized coordinates $\{\xi^n_{ij}, \eta^n_{ij}\}$ in the barotropic-Lagrangian reference frame. We set $\{\xi^0_{ij}, \eta^0_{ij}\} = \{x_{ij}, z_{ij}\}$.

3.2.5 Spectral analysis

To analyze energy transfers within the modeled flow, we estimate two functions: the average spectrum $\Upsilon(\omega)$ characterizing the distribution of energy in the flow with respect to different frequencies; and the spectrogram $S(\omega, t)$ representing the evolution of the spectrum with respect to time.

Spectrum

Let r be a generic function representing the horizontal baroclinic velocity $\tilde{u}$ in our simulations. We let **r** be the set of N values of the function r at the time moments $t_n = n\Delta t$:

$$\mathbf{r} = \begin{vmatrix} r_0 \\ r_1 \\ \vdots \\ r_{N-1} \end{vmatrix} \quad \text{with } r_n = r(t_n), \ n = 0, 1, \ldots, N - 1.$$

Let $S(\omega)$ with $\omega \in [0, \infty)$ be the continuous one-sided power spectrum of the process $r(t)$, such that $S(\omega)\mathrm{d}\omega$ is the average contribution to the power from components with frequencies from the interval $[\omega, \omega + \mathrm{d}\omega]$. The power of the process $r(t)$ on the time interval $[0, T_{\mathrm{tot}}]$ is, then,

$$P \equiv \frac{1}{T_{\mathrm{tot}}} \int_0^{T_{\mathrm{tot}}} r^2(t)\mathrm{d}t = \int_0^{+\infty} S(\omega)\mathrm{d}\omega \approx \frac{1}{T_{\mathrm{tot}}} \sum_{n=0}^{N-1} r_n^2 \Delta t. \tag{3.5}$$

We estimate the spectrum $S(\omega)$ using the direct spectral estimator:

$$\hat{S}(\omega) = \frac{\Delta t}{\pi} \left| \sum_{n=0}^{N-1} g_n r_n \exp(-i\omega t_n) \right|^2, \quad \omega \in [0, \omega_{\mathrm{Nyq}}) \tag{3.6}$$

where $\omega_{\mathrm{Nyq}} = \pi/\Delta t \approx 1.75 \times 10^{-3} \ \mathrm{s}^{-1}$ is the Nyquist frequency and g_n is a data window satisfying
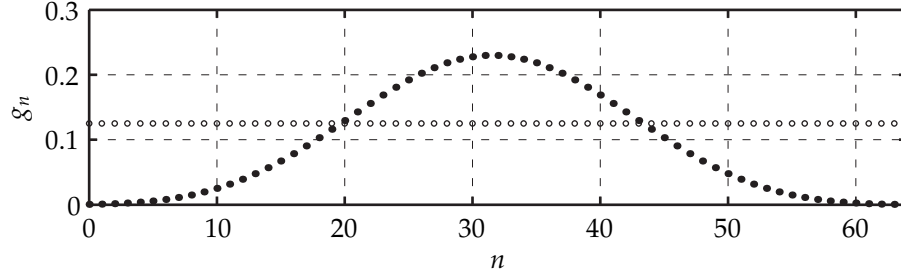
F   3.5: The shape of the window given by a discrete prolate spheroidal sequence used for the spectral analysis (dots) compared to the default rectangular window (circles) for $N = 64$.

the condition

$$\sum_{n=0}^{N-1} g_n^2 = 1. \tag{3.7}$$

The spectral estimator $\hat{S}(\omega)$ in (3.6) is defined on a continuous interval $[0, \omega_{\mathrm{Nyq}})$. We use (3.6) directly when we need to calculate the spectrum at a single given frequency. The evaluation of the spectral estimation $\hat{S}(\omega)$ at a large number of frequencies can be efficiently done with the use of zero-padding and the Fast Fourier Transform (FFT) described by Cooley and Tukey (1965). In this chapter, we use 2^{13} frequencies to discretize the interval $[0, \omega_{\mathrm{Nyq}})$.

The spectral estimator $\hat{S}(\omega)$ suffers from bias and variance. As the spectral estimation is essentially the convolution of the real spectrum and the squared Fourier transform of the window, the bias can be efficiently reduced by the use of an appropriate data window. The optimal window for approximation of the spectrum with a certain spectral resolution is given by a discrete prolate spheroidal sequence (Slepian, 1978). Spectral resolution is associated with the smallest frequency scale of the estimation. As there is a trade-off between high spectral resolution and leakage, an optimal window is the one with the highest resolution for which the leakage is negligible.

We chose the spectral resolution to be $12\pi/T_{\mathrm{tot}} \approx 1.4544 \times 10^{-5}\,\mathrm{s}^{-1}$, so that each energetic frequency in the spectrum is represented by a peak with the bandwidth $12\pi/T_{\mathrm{tot}}$. We compared several spectral estimations with different resolution and found that with a resolution of $12\pi/T_{\mathrm{tot}}$ the spectral estimation has no appreciable leakage in the high-frequency range of the spectrum, and, also, most of the observed energetic frequencies in the spectral estimation are well-resolved. Figure 3.5 illustrates the shape of the window given by a discrete prolate spheroidal sequence that we used in this work for $N = 64$.

The variance of the spectral estimator $\hat{S}(\omega)$ can be reduced by averaging spectra for different realizations of the process **r**. For example, let us consider the procedure of calculating the average spectrum of the flow within 40 km of the hill. For each coordinate $(\xi_{ij}^n, \eta_{ij}^n)$ in the

61

barotropic-Lagrangian reference frame, such that $|\xi_{ij}^0| < 40\,\text{km}$, we calculate the spectrum $\hat{S}_{ij}(\omega)$ of the corresponding time-series $\tilde{u}_{ij}^n$. Next, we average the spectra $\hat{S}_{ij}(\omega)$ over i and j and obtain the average spectrum $\Upsilon(\omega)$:

$$\Upsilon(\omega) = \left\langle \hat{S}_{ij}(\omega) \right\rangle,$$

where the triangular brackets stand for averaging over indices i and j.

Spectrogram

When the time-series $\mathbf{r}$ is part of a non-stationary signal, it is useful to estimate the spectrum on consecutive intervals of time in order to see how the spectrum evolves in time. In order to calculate the spectrogram, we split the sequence $\mathbf{r}$ into $N - M + 1$ subsequences of length M:

$$
\begin{aligned}
\mathbf{r}^0 \quad &= \quad \{ \quad r_0, \qquad r_1, \qquad \ldots \quad , r_{M-1} \quad \}, \\
\mathbf{r}^1 \quad &= \quad \{ \quad r_1, \qquad r_2, \qquad \ldots \quad , r_{M} \quad \}, \\
&\qquad\qquad \ldots\ldots\ldots\ldots\ldots\ldots\ldots\ldots\ldots\ldots\ldots\ldots\ldots \\
\mathbf{r}^{N-M} \quad &= \quad \{ \quad r_{N-M}, \quad r_{N-M+1}, \quad \ldots \quad , r_{N-1} \quad \},
\end{aligned}
\tag{3.8}
$$

where each subsequence $\mathbf{r}^k$ corresponds to a time-interval $[t_k, t_{k+M-1}]$. For each subsequence $\mathbf{r}^k$ we calculate the spectral estimation $\hat{S}^k(\omega)$ using the estimator (3.6) with the same window. We define the spectrogram $\hat{S}(\omega, t)$ at the discrete times corresponding to the centers of the time-intervals $[t_k, t_{k+M-1}]$ as follows:

$$\hat{S}\left(\omega, \frac{t_k + t_{k+M-1}}{2}\right) = \hat{S}^k(\omega). \tag{3.9}$$

The choice of the subsequence length is arbitrary; however, it should be short enough to capture the evolution appropriately while long enough to ensure that the significant features of the spectrum are resolved. Taking into account this trade-off, we found that the length of subsequence $M = N/3 = 480$ is a reasonable value, it gives the evolution of spectrum over the time period of 20 days with a spectral resolution of $12\pi/T$, where $T = 10$ days.

3.3   Results

For the purpose of systematic analysis, our results may be considered under the following headings: (1) underlying dynamics; (2) the average spectra; (3) spatial distribution of harmonics and interharmonics; and (4) evolution of the spectra in time based on spectrograms.

3.3.1 Underlying dynamics

The solution to (1.1) consists of progressive and trapped internal waves, whose dominant frequencies, according to the spectrum of the flow, form a discrete set of tidal harmonics and interharmonics. Both progressive and trapped waves can be seen in figures 3.6 and 3.7 that show snapshots of the horizontal velocity field within 40 km of the ridge at time $t = 30$ days for the latitudes 0°, 10°, 20°, 30°, 40° N (figure 3.6) and 25°, 27°, 28°, 28.82°, 29° N (figure 3.7). The progressive and trapped waves are generated where the flow is highly nonlinear: the region near the ridge and regions where strong progressive internal waves collide or reflect from the boundary. Only the strongest waves are seen in the velocity snapshots.

Progressive waves have frequencies within the range (f, N_b). Since N_b is constant, waves of a single frequency ω can form a straight beam. The slope r of a beam, given by (3.1), is determined by the three frequencies ω, N_b and f. As the topography is supercritical, strong waves of tidal frequency generated at the edges of the ridge, where the slope is critical, propagate both upward and downward, so that pronounced tidal beams are seen above the top and along the side of the ridge. The second harmonic $2\omega_0$ and other higher harmonics have slopes steeper than any part of the ridge, so their corresponding beams emanating from the generation sites at the edges of the ridge, are directed upward only. For most cases, progressive waves dominate the flow, which is manifested in the pronounced beam structure (figures 3.6*a,b,c,e* and 3.7*a,b,c*). As the latitude approaches the critical latitude, the beam structure disappears and gradually transforms into patches of trapped waves (see figure 3.7).

Trapped waves have frequencies outside (f, N_b) and some of them are seen as horizontally elongated patches near the generation sites. For example, when $\theta = 30°$ N the strong waves of a subtidal frequency close to $\omega = 0.5\omega_0$ do not propagate away but are trapped near the ridge and near the regions where the tidal beams hit the surface (see figure 3.6*d*).

The spectra of the internal waves (figures 3.10 and 3.11) that will be explained in the next section, have a discrete set of dominant frequencies, either tidal harmonics or interharmonics; here, we consider how tidal harmonics and interharmonics appear in the velocity field. The major part of the energy in the flow is concentrated in tidal harmonics, i.e. waves corresponding to the multiples of the tidal frequency: $\omega = n\omega_0$ where $n \in \mathbb{N}$, except at 20° and 30° N where the strong subharmonic spectral peak is greater in magnitude than the peak at frequency $2\omega_0$. Some of the beams corresponding to the strongest harmonics are seen in figure 3.6, e.g. the first and second harmonics are seen to be the dominant features of the velocity field for the cases $\theta = 0$ and 10° N. Tidal harmonics with $n < N_b/\omega_0$ are progressive waves that contribute to the far field away from the generation site, while tidal harmonics with $n \geq N_b/\omega_0$ are trapped near the generation site. During the early stages of the flow development, tidal harmonics are generated through tide-topography interaction near the edges of the ridge. At this stage the solution is similar to the
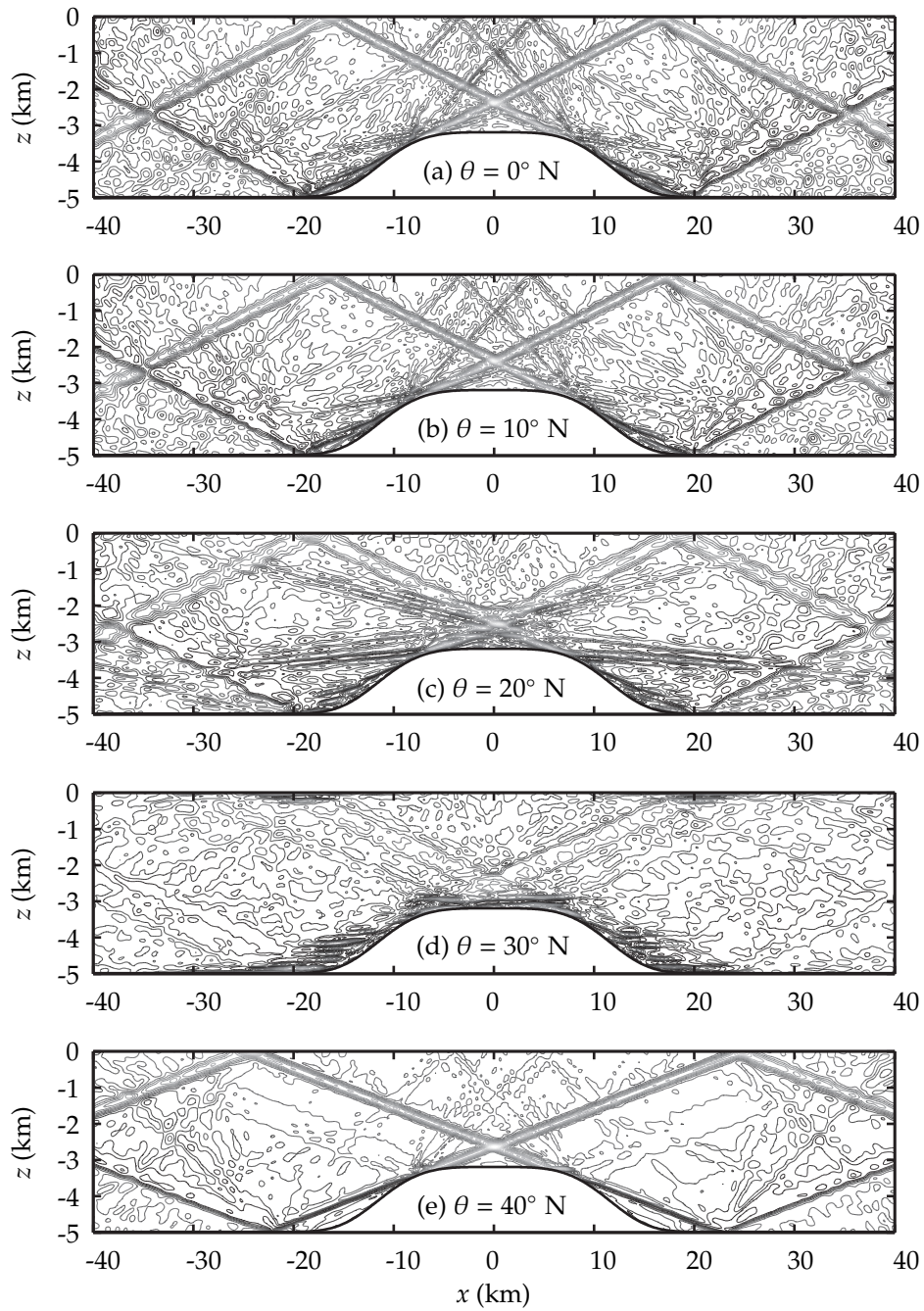
F   3.6: Contours of the horizontal velocity field at latitudes $\theta = 0°$, $10°$, $20°$, $30°$ and $40°$ N at $t = 30$ days.
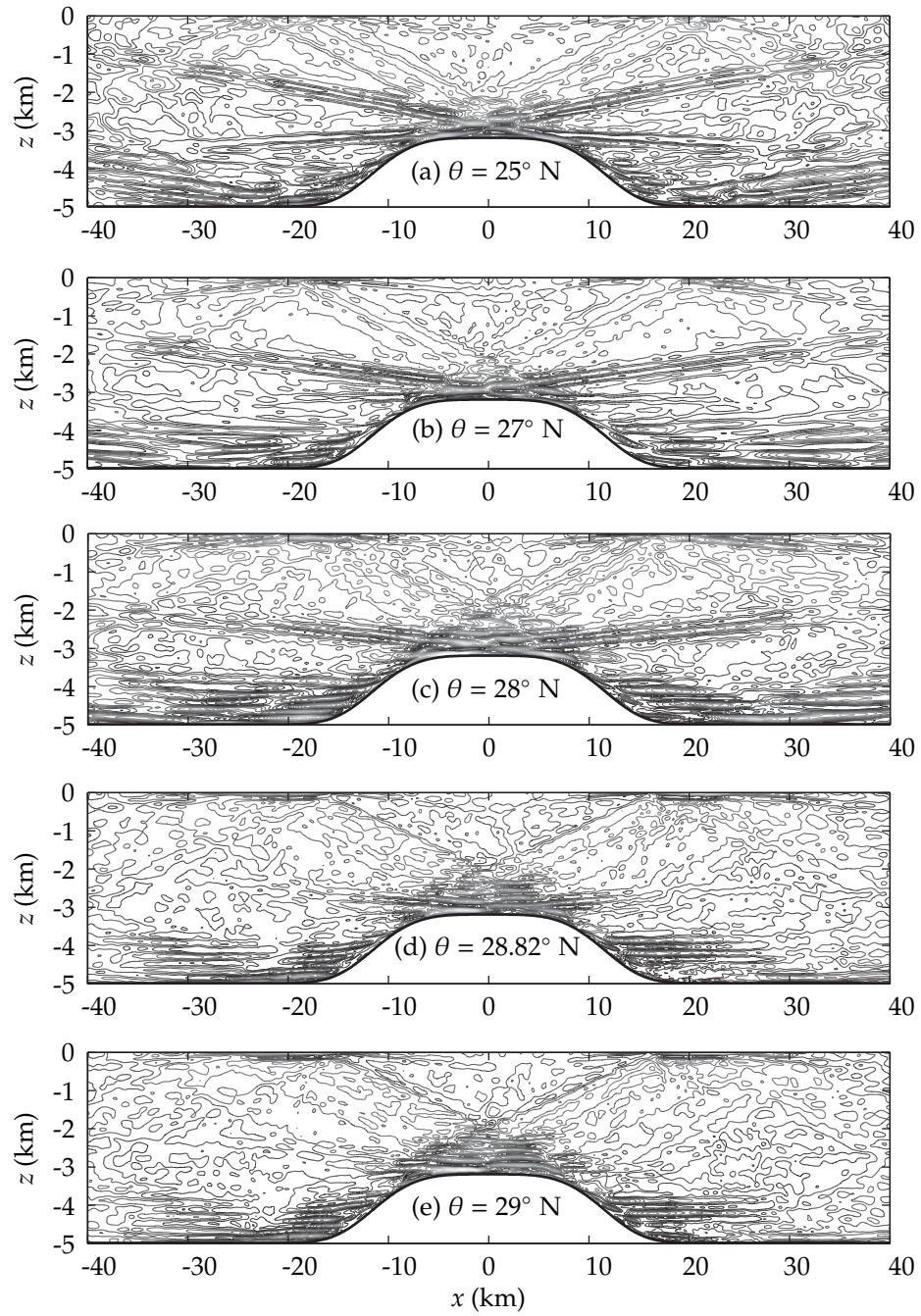
F   3.7: Contours of the horizontal velocity field at the near-critical latitudes $\theta = 25°, 27°, 28°,$
28.82° and 29° N at $t = 30$ days..

analytical one obtained by Bell (1975). Bell considered a similar problem in a non-rotating fluid of infinite depth, and approximated the operator $\mathbf{u} \cdot \nabla$ in the governing equations with $U(t)\partial/\partial x$, i.e., only advection by the horizontal component of the barotropic tide plays a role. Bell's solution was later extended to the case of finite depth by Khatiwala (2003). The solutions obtained by Bell and Khatiwala are given by linear superpositions of tidal harmonics emanating from near the ridge; as in our simulations, the energy in harmonics $n\omega_0$ decays rapidly with n.

The progressive tidal beam harmonics produced by tide-topography interaction propagate away from the ridge and eventually either intersect with other waves or reflect from a boundary. For either of these events, the incident wave interacts nonlinearly with the encountered or the reflected wave, and, as a result, may produce waves at the combination frequencies, which are also from the set of tidal harmonics $n\omega_0$ with $n \in \mathbb{N}$. For example, if a wave of frequency $2\omega_0$ interacts with itself after reflection, it produces a wave of frequency $4\omega_0$, then the generated wave interacts with the initial wave producing a wave of frequency $6\omega_0$, and so on. The interaction and the energetics of colliding and reflecting internal wave beams in a non-rotating fluid was described analytically by Tabaei et al. (2005). They assumed that the flow away from the generation sites was weakly nonlinear and sought the solution as a composition of tidal harmonics. If the flow was indeed weakly nonlinear, the internal wave field within a finite distance of the ridge would eventually resolve into a quasi-steady beam structure.

The flow consisting of tidal harmonics is far from reaching an equilibrium: the strong beams of tidal frequency are perturbed periodically by the topography and other beams, and soon become unstable. Figures 3.8 and 3.9 show how the patterns of destabilization change with latitude for the tidal beam on top of the ridge. For latitudes 0–25° N the pattern of destabilization has a characteristic slope decreasing as the latitude increases (figure 3.8). As the latitude approaches the critical latitude, the pattern of destabilization becomes predominantly horizontal (figure 3.9). As the tidal beams become unstable, waves of interharmonic frequencies are generated.

Among all interharmonics generated in the flow and seen in the spectra (figures 3.10 and 3.11), the most evident are subharmonics, i.e. interharmonics of subtidal frequency $\omega < \omega_0$ (e.g., figure 3.6a–c). Beams of subharmonic frequencies are less steep than any of the beams with frequency $n\omega_0$, so subharmonics are easily detected in a velocity field. For example, in case of $\theta = 20°$ and 25° N, four strong beams of subtidal frequencies (determined by the slope) emanate from the two destabilized beams of tidal frequency above the top of the ridge (figure 3.6c). Similar beams of subharmonic frequencies, although less pronounced, can be seen for the cases $\theta = 0°$ and 10° N (figure 3.6a and b). For the latitudes approaching θ_{cr}, in particular, case 28° N, the frequency of the beams directed downward falls below the Coriolis frequency and the beams become patches of trapped waves; at the same time, the other beam of subharmonic frequency remains a progressive wave. The subharmonics are generated not only above the ridge, but everywhere where the tidal beam becomes unstable, i.e. on the sides of the ridge and where the
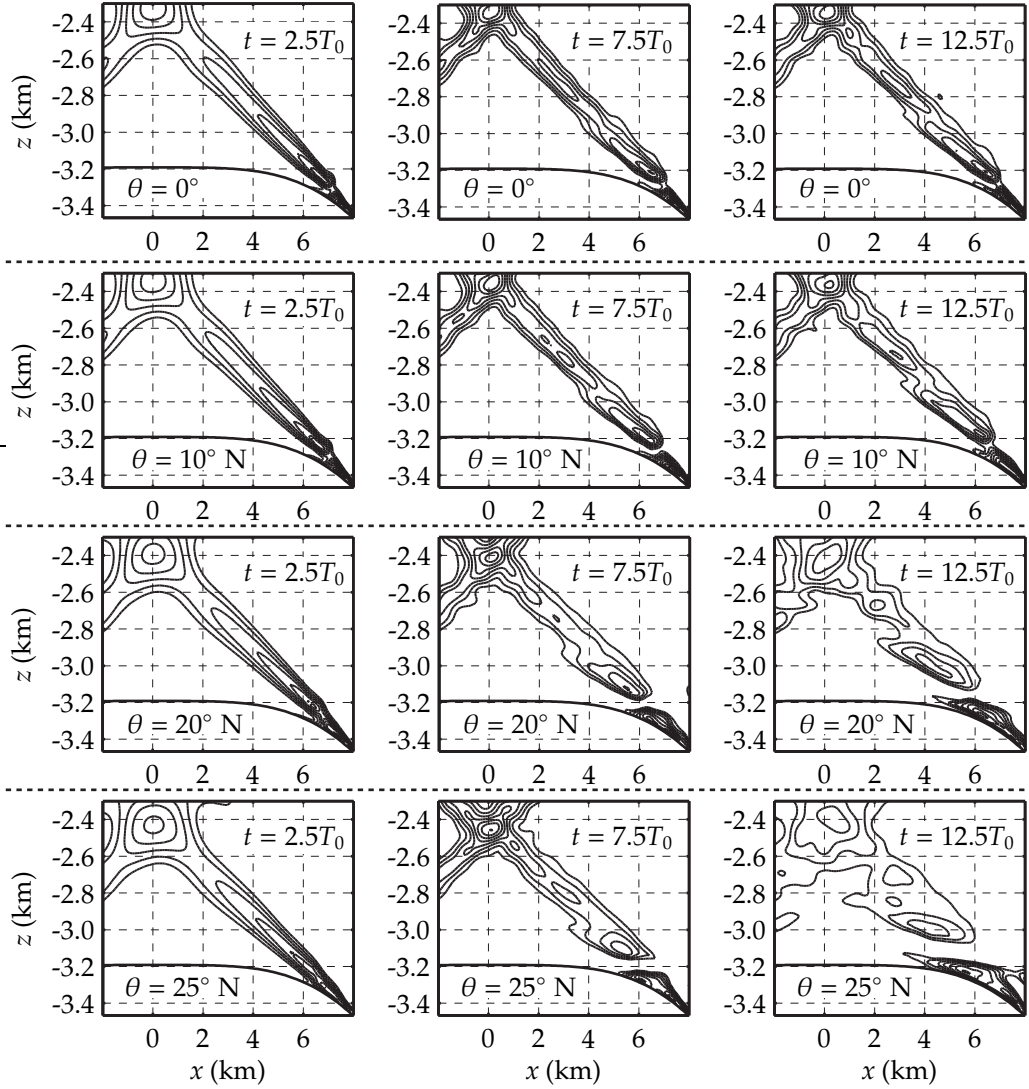
F   3.8: The tidal beam undergoing instability for the cases $\theta = 0°$–$25°$ N, given by the contours $|u| = \{0.05, 0.06, \dots, 0.13\}$ m s^{-1} at different time moments. $T_0 = 12.4$ hrs is the tidal period.
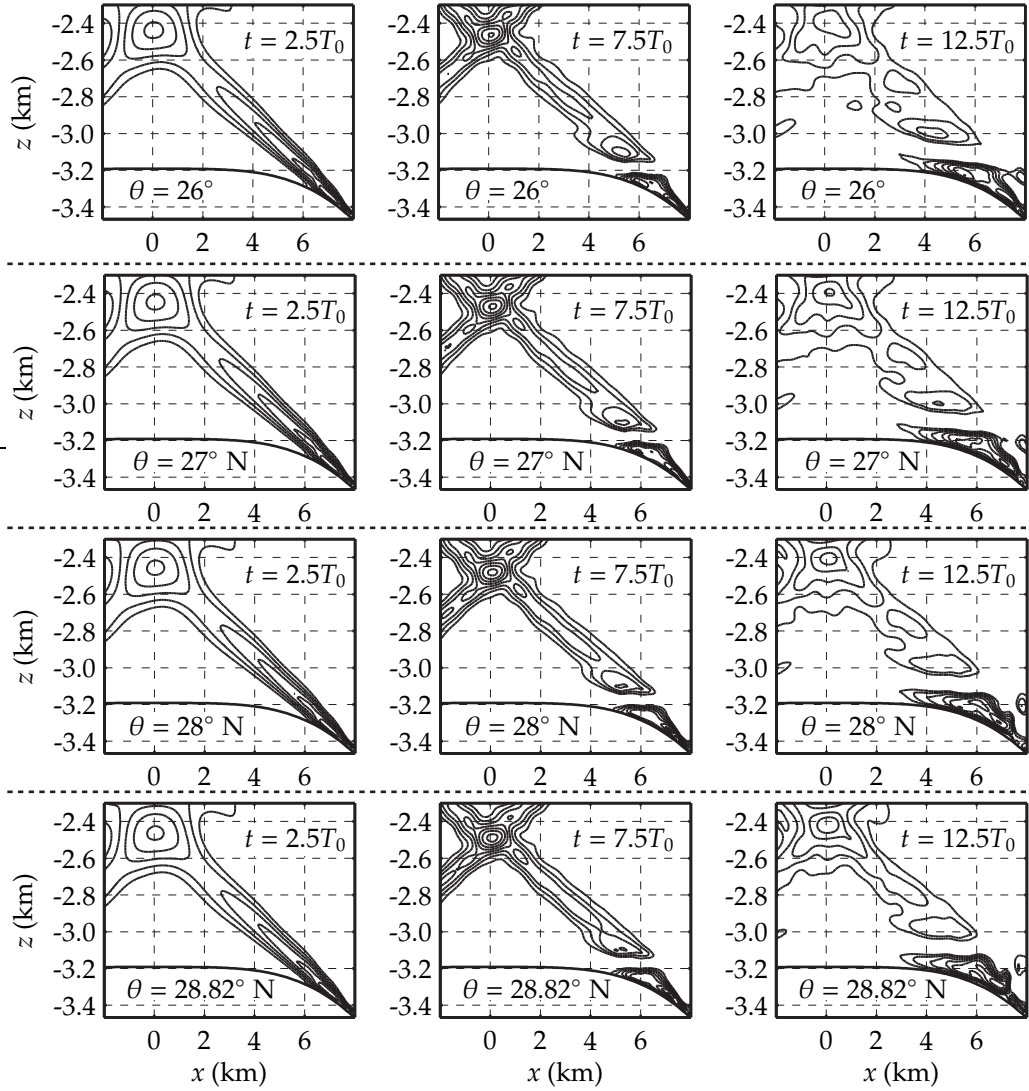
F   3.9: The tidal beam undergoing instability for the cases $\theta = 26°$–$28.82°$ N, given by the contours $|u| = \{0.05, 0.06, \ldots, 0.13\}$ m s^{-1} at different time moments. $T_0 = 12.4$ hrs is the tidal period.

tidal beams are reflected from the top and the bottom of the domain. The locations where the subharmonics are generated are especially well seen when the subharmonics are trapped.

Apart from subharmonics, the flow has other interharmonics whose frequencies are larger than the tidal frequency. Their presence can be explained from the following simple reasoning: any subharmonic ω_α interacting with harmonics $n\omega_0$, can produce waves of frequency $n\omega_0 + \omega_\alpha$, $n \in \mathbb{N}$. If the energy of a subharmonic is comparable to that of the dominant harmonic ω_0, then the energetics of higher interharmonics should be comparable to those of higher harmonics $n\omega_0$ with $n \geq 2$. In general, the generation of a wave at frequency $\omega_\alpha \in [0, \omega_0)$ should be accompanied by the generation of waves at frequencies $\omega_\alpha + n\omega_0$ with $n \in \mathbb{N}$. The higher interharmonics are harder to detect directly in a velocity field, not only because they are weaker, but, also, because their slopes can be easily mistaken for those of tidal harmonics. Their presence becomes obvious after considering the average spectra of the flow and spatial distributions of waves with interharmonic frequencies.

3.3.2   Spectrum of the flow

In order to quantify the distribution of energy among different harmonics and interharmonics we estimated the average spectra of the flow in different regions for the different latitudes. The spectra reveal the most important spectral components of the flow and quantify their energetics.

Figure 3.10 shows the average spectra of the flow within 40 km of the ridge for the cases $\theta = 0°$, $10°$, $20°$, $30°$ and $40°$ N. Figure 3.11 shows the near-critical latitudes $\theta = 25°$, $26°$, $27°$, $28°$ and $28.82°$ N. Finally, figure 3.12 shows the spectra for the latitudes above the critical one, namely $\theta = 31°$, $32°$, $33°$, $34°$ and $35°$ N, characterized by strong peaks in the subinertial range. To get an idea of how spectra behave on higher frequencies, the spectra in figure 3.12 are shown on a larger range of frequencies, up to the Nyquist frequency of about $12.4\omega_0$. The spectra are calculated from the horizontal velocity time-series in the barotropic-Lagrangian reference frame.

The spectra have self-similar structure with prominent peaks at a discrete set of tidal harmonics and interharmonics. The spectra are self-similar in the following sense: the shape of each spectrum in the low frequency range $(0, \omega_0]$ nearly copies itself in the further frequency ranges $(n\omega_0, (n+1)\omega_0]$ for $n \in \mathbb{N}$. As there are only a few dominant frequencies in the interval $(0, \omega_0]$, the spectrum is comprised of peaks at the tidal harmonics $\{n\omega_0\}$ and the interharmonics $\{\omega_\alpha + n\omega_0\}$, where $n \in \mathbb{N}$ and ω_α can be any of the subharmonics. For the spectra shown in figure 3.10, both harmonics $\{n\omega_0\}$ and interharmonics $\{\omega_\alpha + n\omega_0\}$ decay with n at a similar exponential rate.

One of the consequences of the observed self-similarity and exponential rate of decay is that if a subharmonic ω_α has less energy than the tidal frequency ω_0, then the higher interharmonics $\{\omega_\alpha + n\omega_0\}$ are also weaker than the corresponding harmonics $\{(n + 1)\omega_0\}$, where $n \in \mathbb{N}$. If, on

69
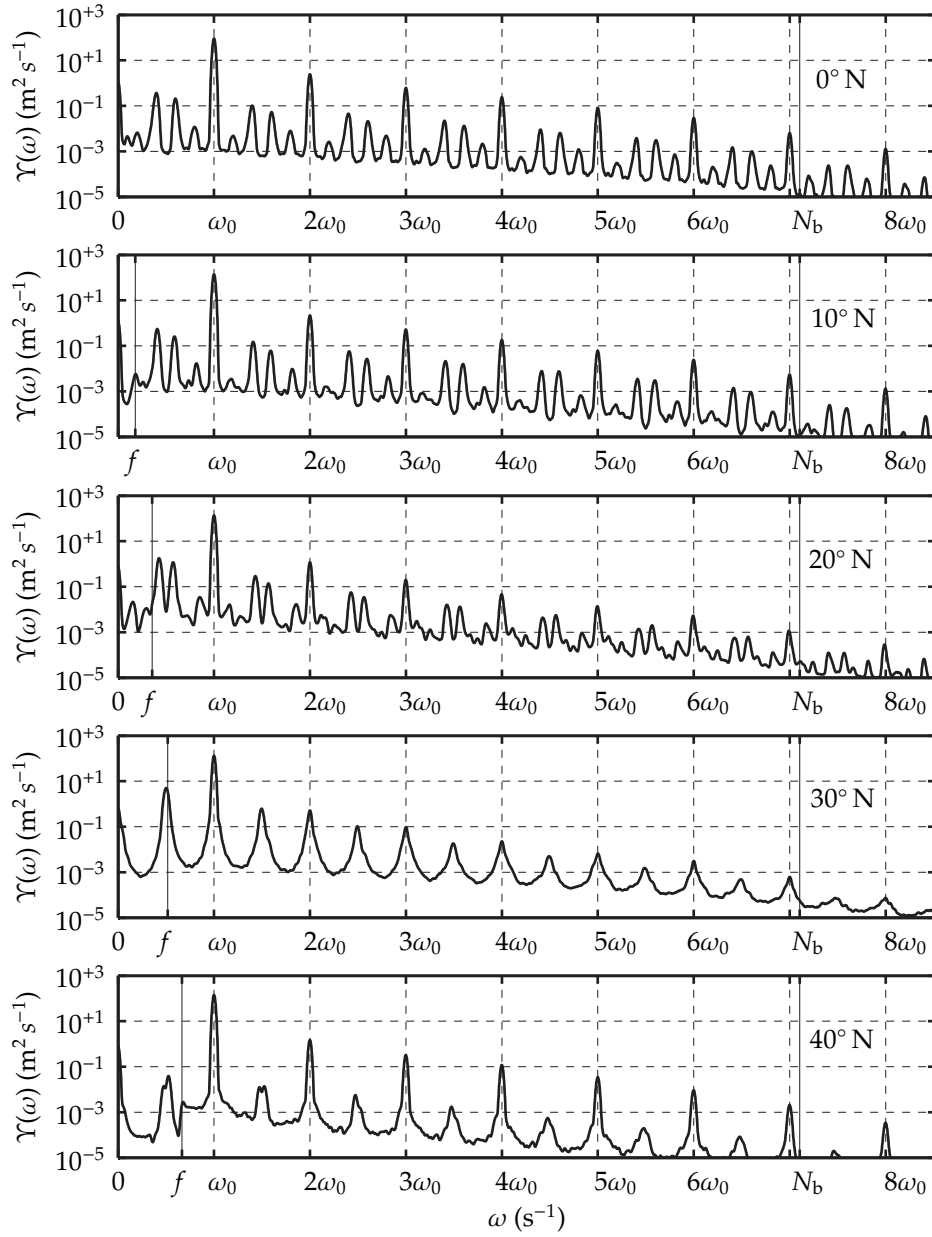
F   3.10: One-dimensional spectrum of the flow within 40 km of the ridge for the latitudes
$\theta = 0°, 10°, 20°, 30°$ and $40°$ N.
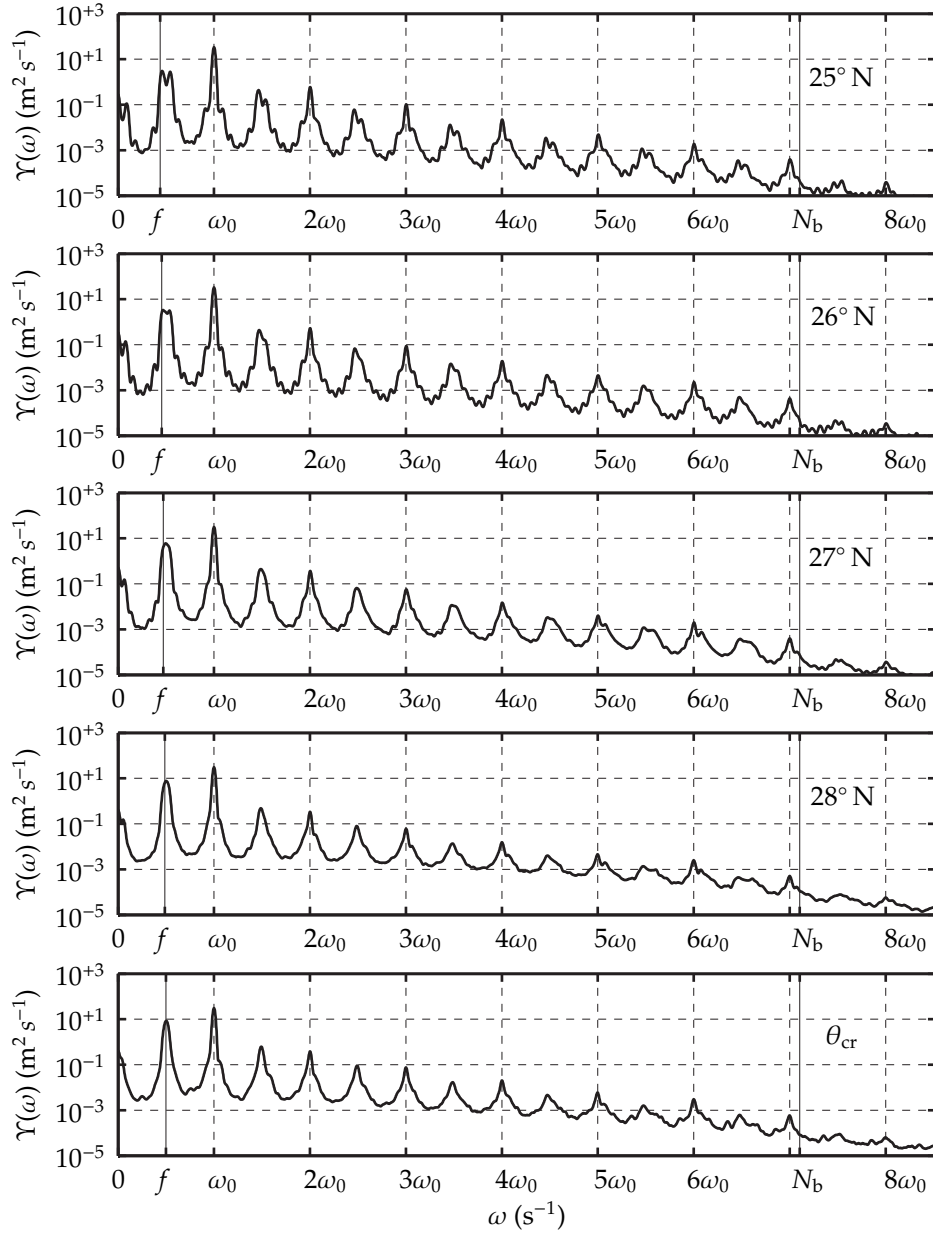
F   3.11: One-dimensional spectrum of the flow within 40 km of the ridge for the latitudes $\theta = 25°, 26°, 27°, 28°$ N and θ_{cr}.
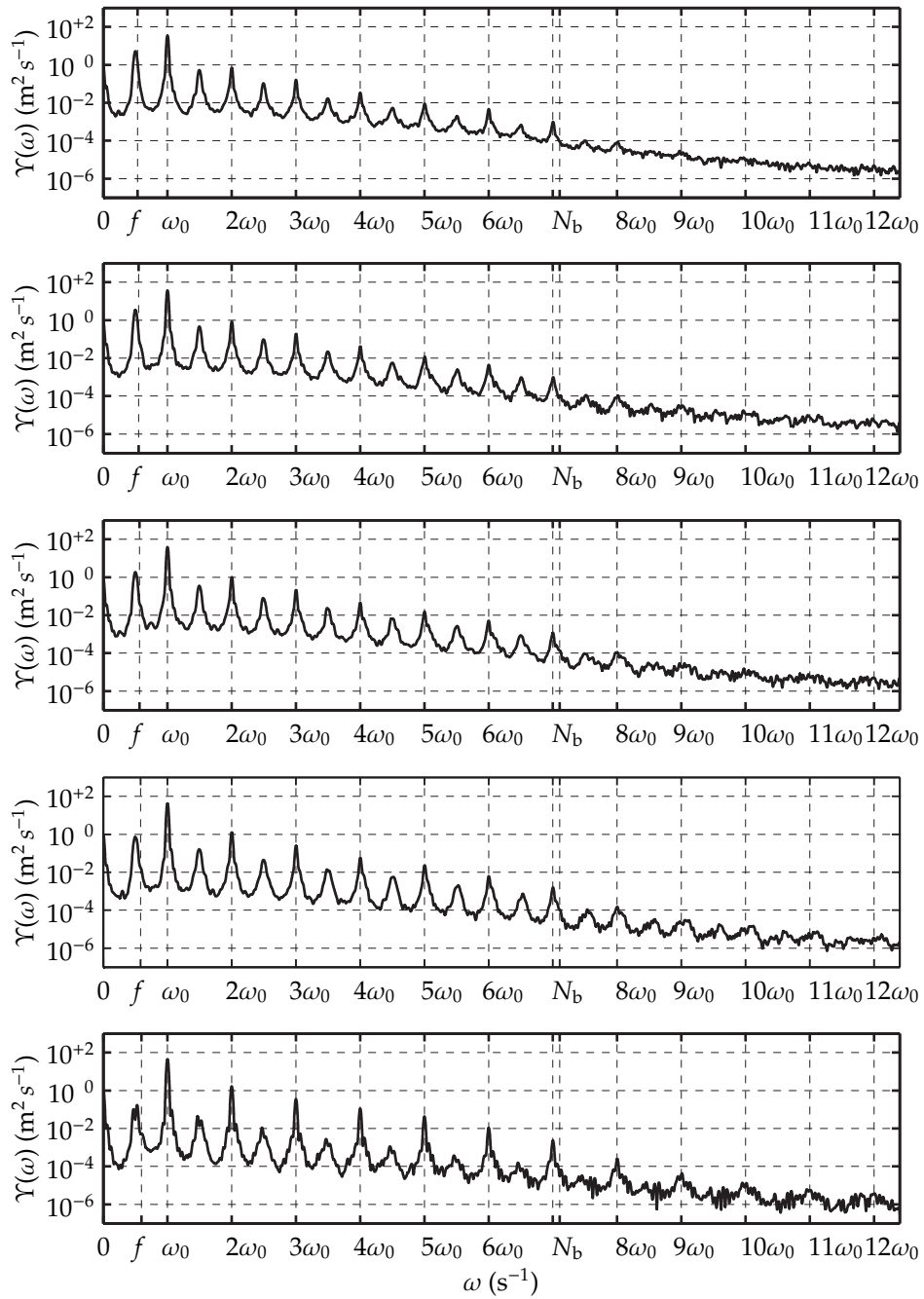
F   3.12: One-dimensional spectrum of the flow within 40 km of the ridge for the latitudes $\theta = 31°, 32°, 33°, 34°$ and $35°$ N.
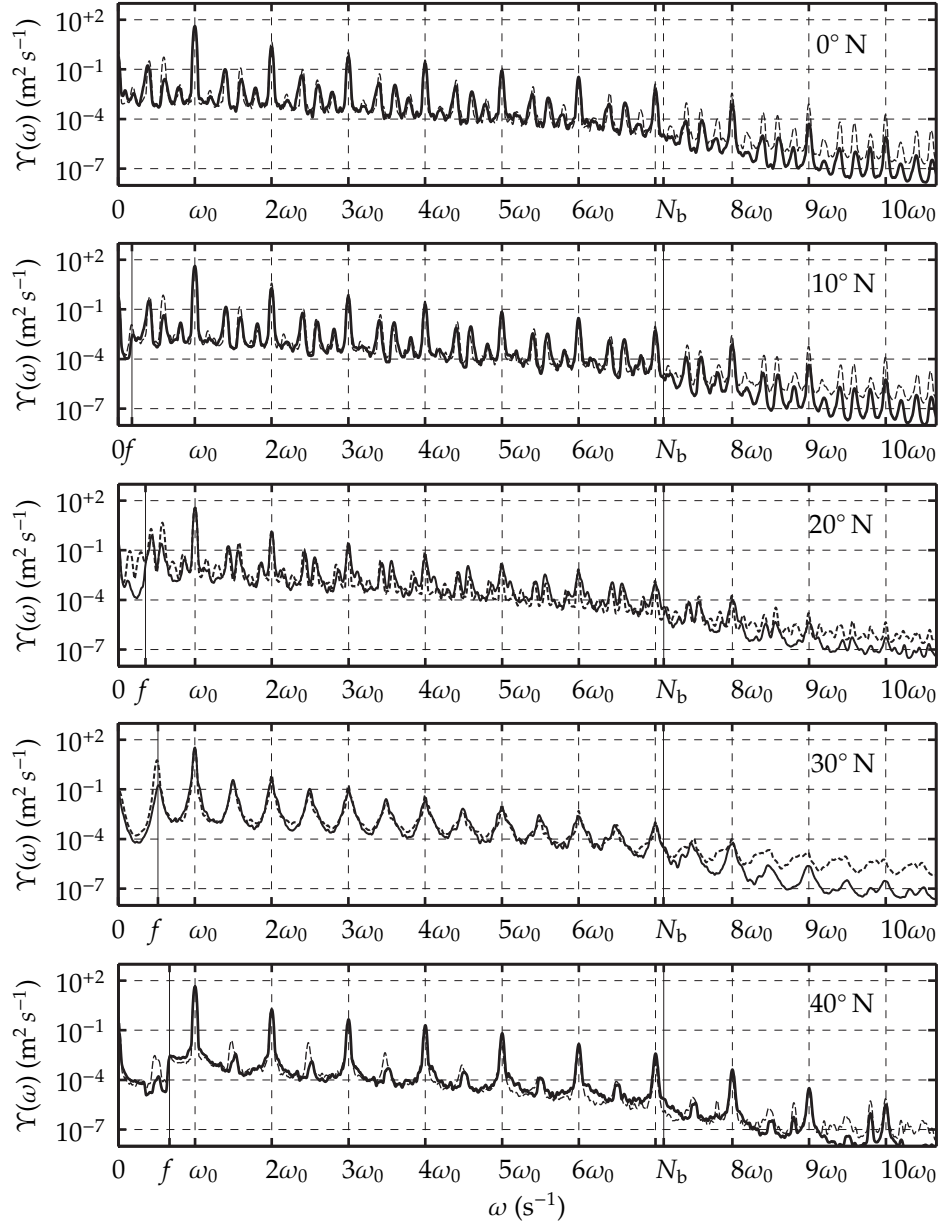
F   3.13: One-dimensional spectra of the flow for the cases $\theta = 0°$, $10°$, $20°$, $30°$, $40°$ N: $-5 \leq x \leq 5$ km (dashed line), $30 \leq x \leq 40$ km (solid line).
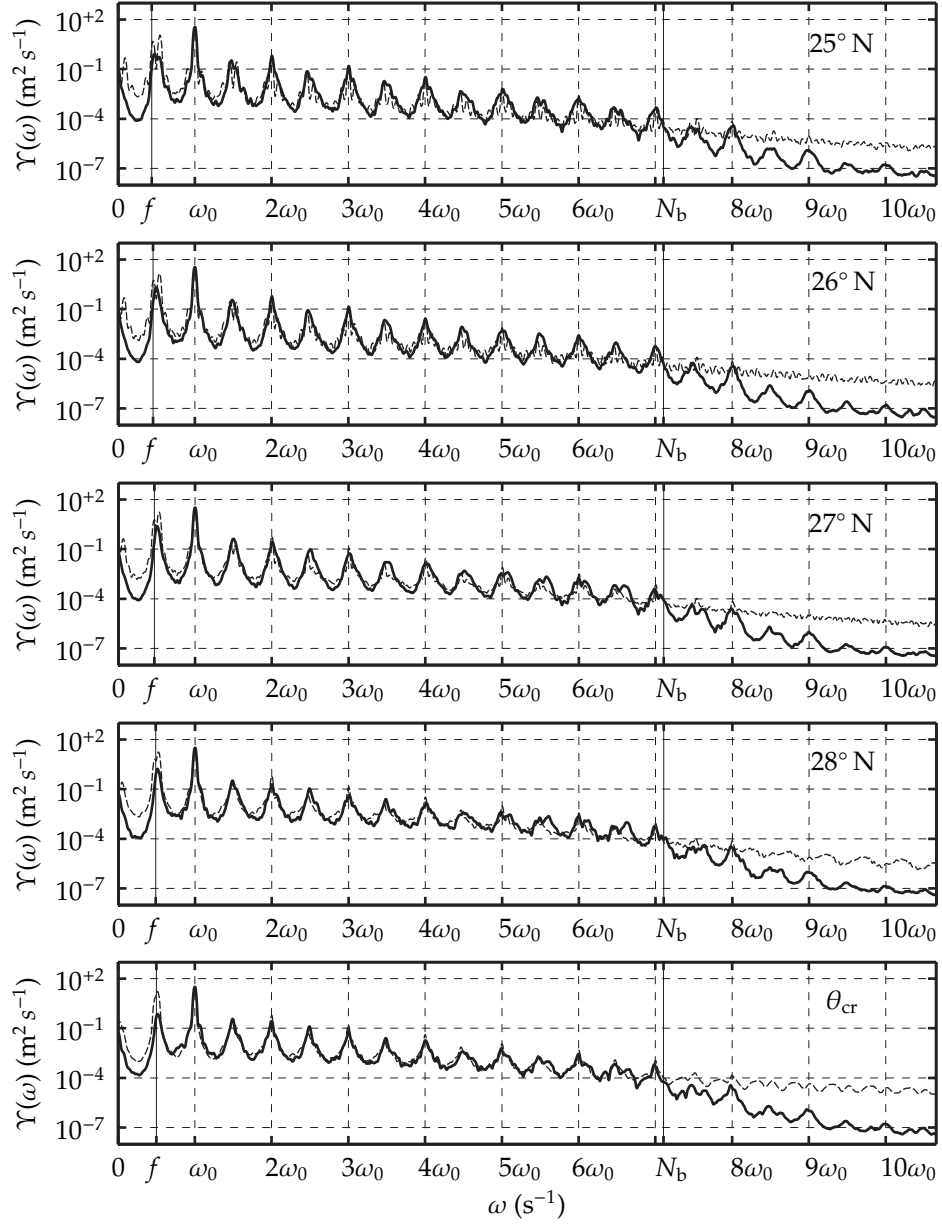
F   3.14: One-dimensional spectra of the flow for the cases $\theta = 25°, 26°, 27°, 28°$ and θ_{cr}: $-5 \leq x \leq 5$ km (dashed line), $30 \leq x \leq 40$ km (solid line).
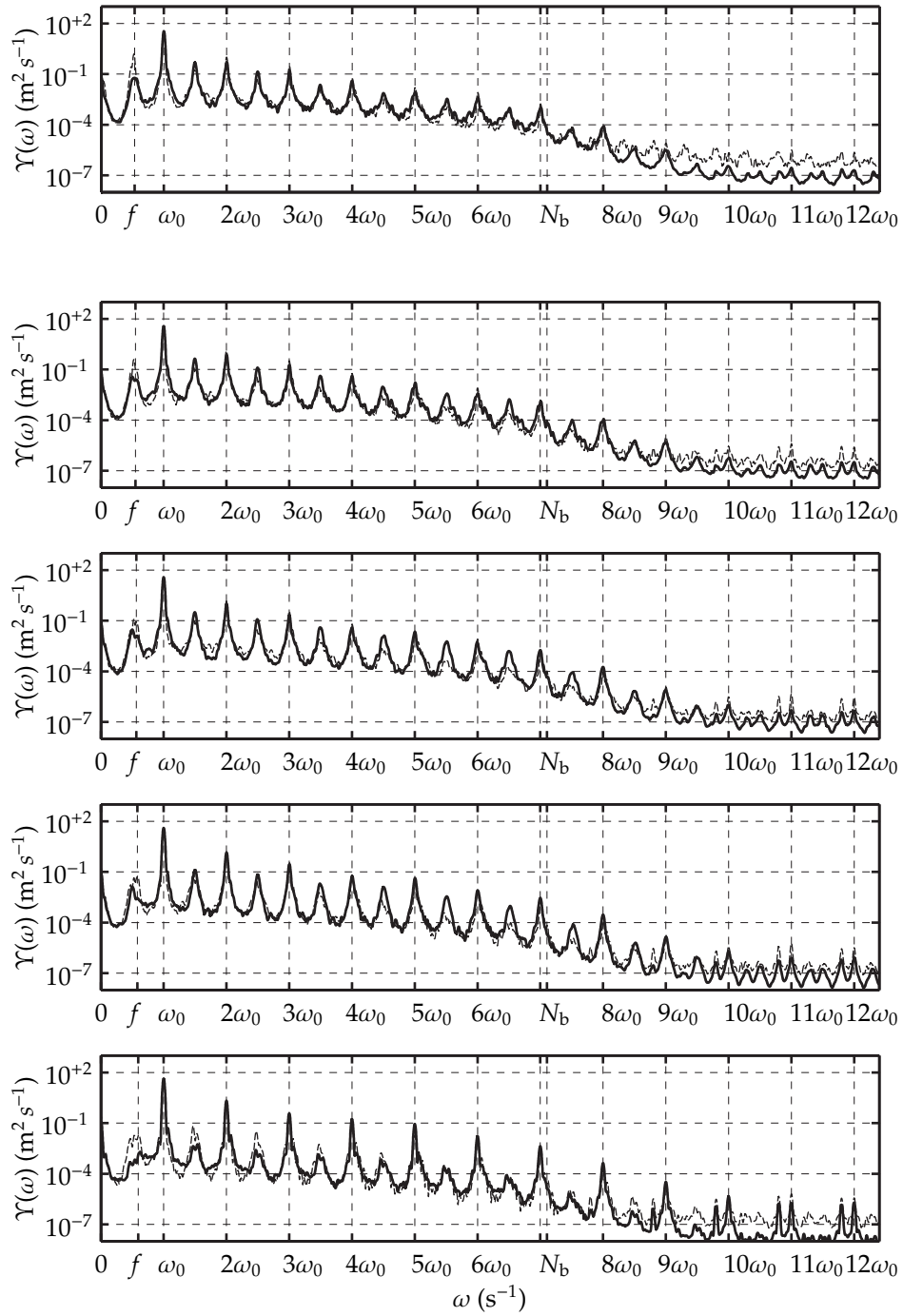
F   3.15: One-dimensional spectra of the flow for the cases $\theta = 31°, 32°, 33°$, $34°$ and $35°$ N: $-5 \leq x \leq 5$ km (dashed line), $30 \leq x \leq 40$ km (solid line).

the other hand, the subharmonics are stronger than the tidal frequency, as in the case of tidal-to-subtidal conversion of motion happening, for example, in certain locations near the ridge for the case $\theta = 30°$ N (not shown), then the higher interharmonics can also dominate higher harmonics.

The spectral peaks at frequencies within the range (f, N_b) correspond to progressive waves; the peaks outside the range (f, N_b), to trapped waves. As the trapped waves have amplitudes comparable to those of progressive waves, the shapes of the average spectra do not allow us to distinguish trapped waves from progressive. To see which waves are trapped near the ridge (the strongest generation site) and do not propagate away, we compare the average spectra in the region $-5 \leq x \leq 5$ km on top of the ridge and the average spectra in the region $30 \leq x \leq 40$ km away from the ridge. Figure 3.13 demonstrates the comparison for the latitudes 0°, 10°, 20°, 30° and 40°. For the case $\theta = 20°$ N, it is seen that the peaks at frequencies less than the Coriolis frequency are virtually absent in the spectrum for the region away from the ridge, indicating that waves of subinertial frequency are trapped and do not reach the far field region. For the higher frequencies $\omega > N_b$, the spectrum of the flow away from the ridge has a significantly higher drop-off rate than that of the spectrum near the ridge, which is seen for all latitudes.

Figure 3.14 provides the comparison of the spectra calculated for $-5 \leq x \leq 5$ km and $30 \leq x \leq 40$ km for the near-critical latitudes $\theta = 25°, 26°, 27°, 28°$ N and θ_{cr}. For these cases, the spectra of the flow on top of the ridge exhibit strong peaks at subharmonic frequencies less than the Coriolis frequency. In particular, one strong peak in the subinertial range corresponds to the difference of the two other subharmonics close to $\omega_0/2$ whose peaks are blending into one at $\omega_0/2$. In the spectra of the flow away from the topography the peaks in the subinertial range are either absent or much weaker. The decay of the spectra is more gradual for the flow on top of the ridge in comparison with the spectra corresponding to the flow away from the topography. The spectrum of the flow on top of the ridge also shows more prominent interharmonic peaks. For example, the spectrum at 26° N is much spikier on top of the ridge than it is far from the ridge. The explanation is that for the region near the ridge more energy flows into subharmonics and, consequently, into other interharmonics.

Similar spectra are shown for the latitudes $\theta = 31°, 32°, 33°, 34°$ and 35° N in figure 3.15. The spectra are shown for the frequency range $\omega \in [0, \omega_{Nyq}]$.

The cause of another effect for the near-critical latitudes is not clear. As the frequency increases the peaks corresponding to interharmonics attain magnitudes comparable with the magnitudes of the peaks corresponding to harmonics. For the frequencies $\omega > N_b$ the peaks corresponding to harmonics and interharmonics visibly merge into a smooth gradually-decaying spectrum. This effect is especially pronounced for the spectra of the flow within 5 km of the ridge (for example, cases 25°, 26° and 27° N). Similar smoothing happens for the spectra of the flow away from the topography, but to a smaller degree. Although it is not clear why the smoothing happens to a larger degree in the high-frequency range, the fact that interharmonics alone can lead to a smooth

spectrum, like the spectrum observed in the deep ocean, is quite remarkable.

Note that the effect of smoothing is not due to leakage. Figure 3.16 compares spectral estimations for the case 27° N using different windows. The decay rate of the spectral estimation using the window given by the discrete prolate spheroidal sequence (DPSS) of the first order, is slightly less than those of the spectral estimations with windows given by DPSS of the third and sixth order. The estimations using DPSS of the third and sixth order, on the other hand, exhibit similar structure of the spectrum and have similar rate of decay. This suggests that the spectral estimator using DPSS of the third order does not suffer appreciably from leakage. Moreover, if the ragged structure of the spectral estimations for the high-frequency range were due to leakage, i.e. if the peaks for $\omega > N_{\mathrm{b}}$ were side-lobes of the strongest peak in the spectrum, then the structure of the spectrum would be much finer: side-lobes corresponding to the window given by DPSS of the third window alternate every $0.016\omega_0$, approximately four times faster than the peaks in the corresponding spectral estimation. In the spectral estimations, in the high-frequency range, the peaks alternate every $0.065\omega_0$. Interestingly enough, the value $0.065\omega_0$ coincides with the frequency of the first visible peak (at $0.65\omega_0$) in the estimation of the flow within 5 km of the ridge (see figure 3.14, case 27° N). In the same spectral estimation, the value $0.65\omega_0$ is also approximately equal to the difference between frequencies $0.532\omega_0$ and $0.468\omega_0$ corresponding to the two strongest subharmonic peaks in the estimation. The above arguments suggest that the "smooth" spectrum in the high-frequency range is indeed composed of interharmonics which were generated through triad interactions.

The important result that can be extracted from the spectra is the existence of strong interharmonics for the near-critical latitudes. For the case $\theta = 40°$ N, the interharmonics are very weak, but are present. From our estimates, it follows that subharmonics, which have been observed before in spectra of internal waves (MacKinnon and Winters, 2007; Gerkema et al., 2006), happen to be just the strongest among other interharmonics. Consistent with the aforementioned studies, the interharmonics are particularly intense at near-critical latitudes, where the critical latitude is $\theta_{\mathrm{cr}} = 28.82°$ N where the Coriolis frequency is half the tidal frequency. For example, at the latitude 20° N we see that the frequencies $\omega \approx 0.4269\omega_0$ and $\omega \approx 0.5752\omega_0$ are the second and third strongest frequency in the spectrum after the tidal frequency ω_0.

Our results disagree with some statements made by MacKinnon and Winters (2007), who claim: "For the internal tide, energy can be drained through PSI only when the half-frequency recipient waves are within the internal wave band $\omega_0/2 \geq f$, a criterion only satisfied equatorward of 28.9°". In our simulations, subharmonics are generated for the cases when $\theta \leq \theta_{\mathrm{cr}}$ and both recipient subharmonic waves are within the internal wave band, for the cases when $\theta \leq \theta_{\mathrm{cr}}$ and only one recipient subharmonic wave is within the internal wave band, e.g. case $\theta = 28°$ and 28.82° N, and, finally, for the cases when $\theta > \theta_{\mathrm{cr}}$ and both recipient subharmonic waves are outside the internal wave band. As will be shown later, in the case $\theta = 34° > \theta_{\mathrm{cr}}$, both

77
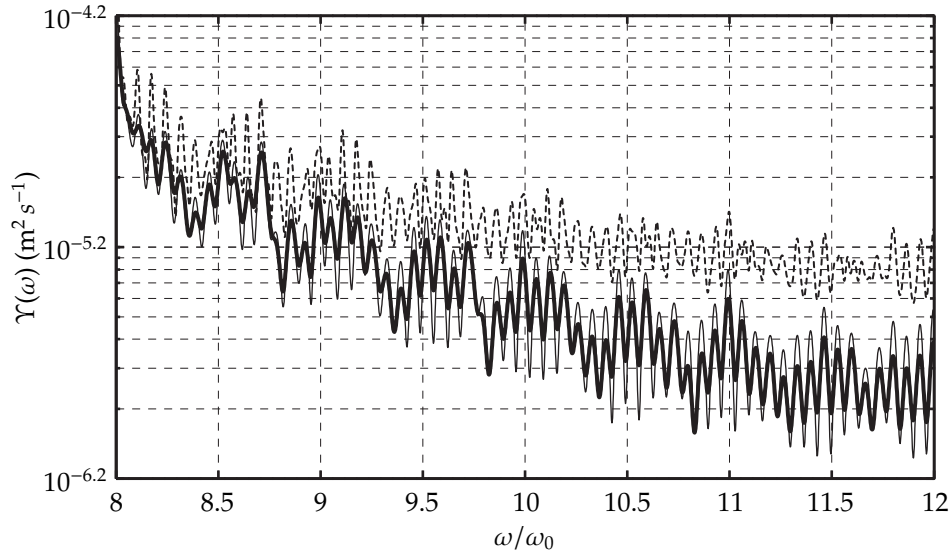
F   3.16: One-dimensional spectrum of the flow for the cases $\theta = 27°$ N within 5 km of the ridge: DPSS of the first order (dashed line), DPSS of the third order (thin solid line), DPSS of the sixth order (thick solid line).

subharmonics are subinertial, but the magnitude of their corresponding peaks is larger than that of subharmonics in the case $\theta = 0°$ N. Thus, the generated subharmonics can not always be a result of a resonant triad interaction. To explain the discrepancy we may refer to Phillips (1967) discussing the non-resonant triad interaction: "There is no prior reason why forced components, whose wavenumbers and frequencies do not obey the wave-dispersion relation, should not be generated with amplitudes comparable with those of the primary waves."

3.3.3   Spatial distribution of harmonics and interharmonics

Generated in various regions, propagating at numerous angles and exchanging energy, harmonics and interharmonics have a complex spatial distribution. The power spectra calculated for each spatial point indicate where a wave of a certain frequency is more or less energetic; thus, we can construct their spatial distribution. After examining spatial distributions of tidal harmonics and interharmonics at different latitudes, we found that:

I. The wave of a harmonic or an interharmonic frequency within the range (f, N_b) forms a beam whose slope is consistent with the linear dispersion relation (3.1).

78

II. The wave of a harmonic or an interharmonic frequency outside the range (f, N_b) forms a patch near the source.

III. The generation sites of a tidal harmonic include: the region near the edge of the ridge; a region where two harmonics collide; and a region where a harmonic reflects from the boundary.

IV. The generation sites of an interharmonic include: the regions where the beam of tidal frequency becomes unstable, i.e. above the ridge, on the side of the ridge, or where the tidal beam is reflected from the boundary; the regions where an interharmonic collides with another wave.

Figures 3.17, 3.18, 3.19, 3.20, 3.21 and 3.22 and 3.22 illustrate the points made above for a subset of tidal harmonics and interharmonics at latitudes $\theta = 0°, 10°, 20°, 25°, 28.82°$, and $30°$ N. For a particular frequency ω_α, we calculate the spectral matrix $\hat{S}_{ij}(\omega_\alpha)$ for the time-series $\{u_{ij}^n\}$. After sorting the matrix $\hat{S}_{ij}(\omega_\alpha)$, we choose approximately 32% of $\hat{S}_{ij}(\omega_\alpha)$ with the largest values and visualize those at the corresponding coordinates (x_{ij}, z_{ij}). The 5% of the matrix $\hat{S}_{ij}(\omega_\alpha)$ with the largest values are emphasized with a cross-hatched pattern. Below, we discuss latitudes $0°$, $20°$ and $30°$ N.

For the case $\theta = 0°$, figure 3.17 demonstrates the distribution of the following frequencies: $\omega = 0.4\omega_0, 0.6\omega_0, \omega_0, 1.4\omega_0, 1.6\omega_0, 2\omega_0$. The subharmonic $\omega = 0.4\omega_0$ corresponds to the strongest subharmonic peak in figure 3.10(a). The tidal harmonic has most of its energy in the tidal beams generated near the edges of the ridge. The second harmonic is manifested in several beams, some of which are generated near the edges of the ridge, some, where a tidal beam hits the boundary, and some, where tidal beams intersect. The subharmonic $0.4\omega_0$ is dominated by two beams, one of which originates from the unstable tidal beam above the ridge, and another, from the unstable tidal beam on the side of the ridge. The beams corresponding to the subharmonics are wider than those of harmonics. This is because the development of instability starts from the base of the beam and with time spreads further and further along the beam; accordingly, the sources of the subharmonics stretch out. For the same reason, the beams of the interharmonic $1.4\omega_0$ are also wide. All the beams corresponding to interharmonics are also seen to be generated in the regions of instability of the tidal beam.

For the case $\theta = 20°$ N, figure 3.19 demonstrates the two strong subharmonics $0.4269\omega_0$ and $0.5752\omega_0$ that appear in the velocity field (figure 3.6c) and in the spectra (figure 3.10c); also, the figure shows the spatial distribution of the corresponding interharmonics $1.4269\omega_0$ and $1.5752\omega_0$ and two harmonics ω_0 and $2\omega_0$. (All the approximate values of interharmonics are calculated according to the average spectra $\Upsilon(\omega)$ shown in figures 3.10–3.12.) The subharmonics are generated at three common generation sites, where the strong tidal beam becomes unstable: above the ridge, on the side of the ridge and where the tidal beam reflects from the bottom. The

beam of subharmonic frequency formed where the tidal beam reflects from the bottom is more clearly seen in the velocity field snapshot (figure 3.6c). All the shown interharmonics form beams. In particular, it is seen that the familiar "fan" of beams emanating from the edge of the ridge consists not only of harmonics, as in Bell's solution, but, also, of interharmonics in between. The weaker interharmonics, e.g. $0.1544\omega_0$ and $0.8504\omega_0$, are not shown here because they are more susceptible to error and have a noisy spatial distribution, which is hard to interpret. It is certain, however, that they exist at the regions of instability.

For the case $\theta = 30°$ N, figure 3.22 demonstrates the distribution of energy corresponding to the frequency $0.5\omega_0$, ω_0, $1.5\omega_0$ and $2\omega_0$. The peak at the frequency $0.5\omega_0$ seen in figure 3.10, as will be shown later, corresponds to two subharmonics close to the Coriolis frequency f. The spectral resolution renders the two subharmonics almost indistinguishable. One of the subharmonics is progressive and the other is trapped. This can be deduced, in part, from figure 3.13, $\theta = 30°$ N. The subharmonic peak corresponding to $-5 \leq x \leq 5$ km has its maximum at a frequency slightly less than the Coriolis frequency, while the weaker subharmonic peak corresponding to $30 \leq x \leq 40$ N has its maximum at a frequency slightly larger than the Coriolis frequency. Accordingly, figure 3.22(a) shows that the distribution of energy at frequency $0.5\omega_0$ has some non-zero slopes that can be attributed to the progressive wave; however, mostly, energy is concentrated near the ridge, which is the manifestation of the trapped wave. The energetic patches corresponding to the trapped subharmonic are gathered around the regions of instability of the tidal beam: above and on the side of the ridge; where the tidal beam is reflected from the boundary. The energetic interharmonic close to $1.5\omega_0$, generated at the same generation sites as the trapped subharmonic, forms a beam whose slope is given by the linear dispersion relation. The harmonics behave similarly to the case $\theta = 0°$ N.

The beam structure of the flow emerges here even more clearly than in the velocity snapshots. It is seen that the waves with subharmonic frequencies also form internal wave beams if the frequency is within the range (f, N_b), (see, for example, figure 3.17a). The slopes of the interharmonic beams agree with the linear dispersion relation (3.1). If the interharmonic is outside the range of freely propagating waves, the wave is trapped, as in the case of the trapped subharmonic at $\theta = 30°$ N.
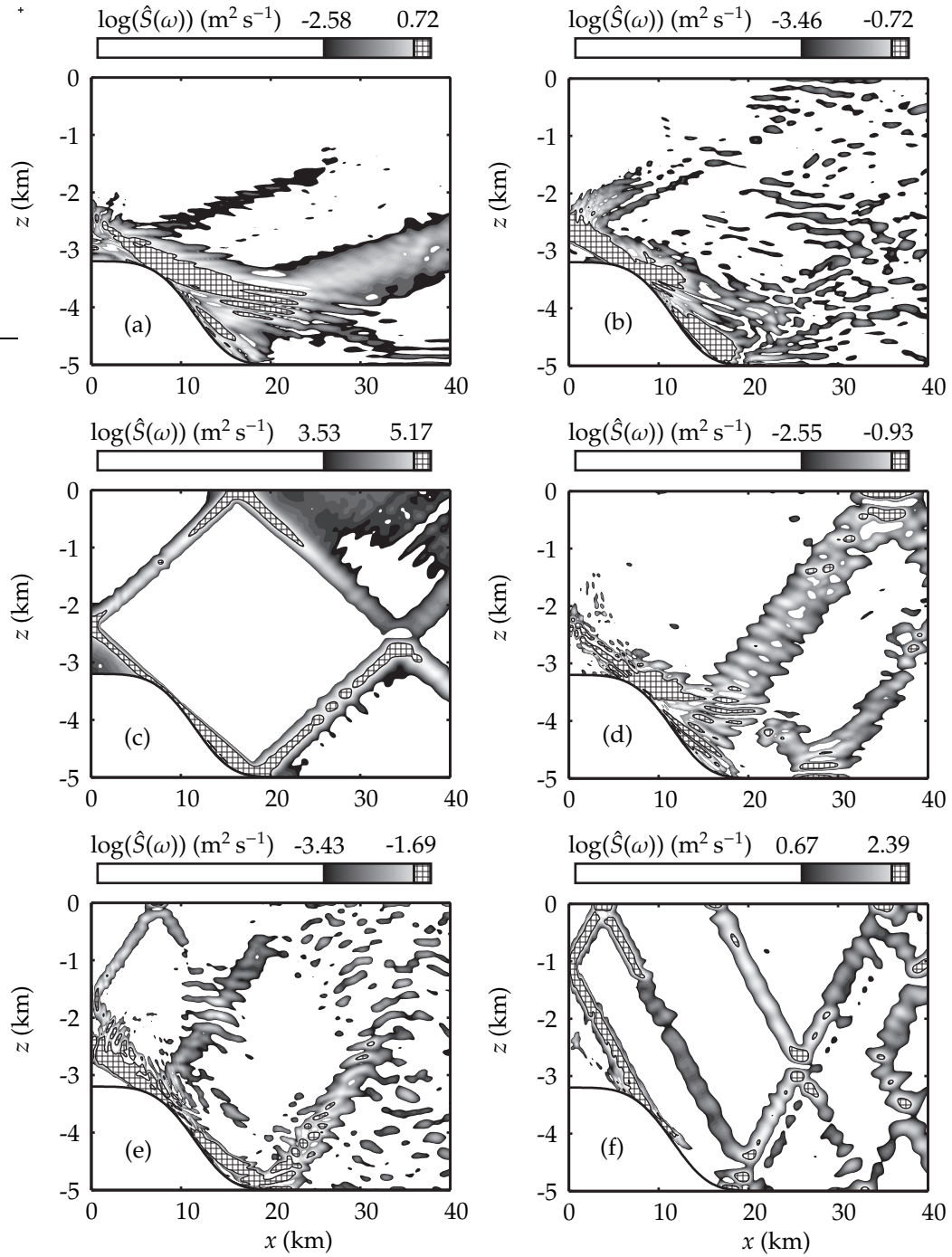
F 3.17: Spatial distribution of waves with different frequencies within 40 km of the ridge for the case $\theta = 0°$: (a) $\omega = 0.4\omega_0$, (b) $\omega = 0.6\omega_0$, (c) $\omega = \omega_0$, (d) $\omega = 1.4\omega_0$, (e) $\omega = 1.6\omega_0$, (f) $\omega = 2\omega_0$.
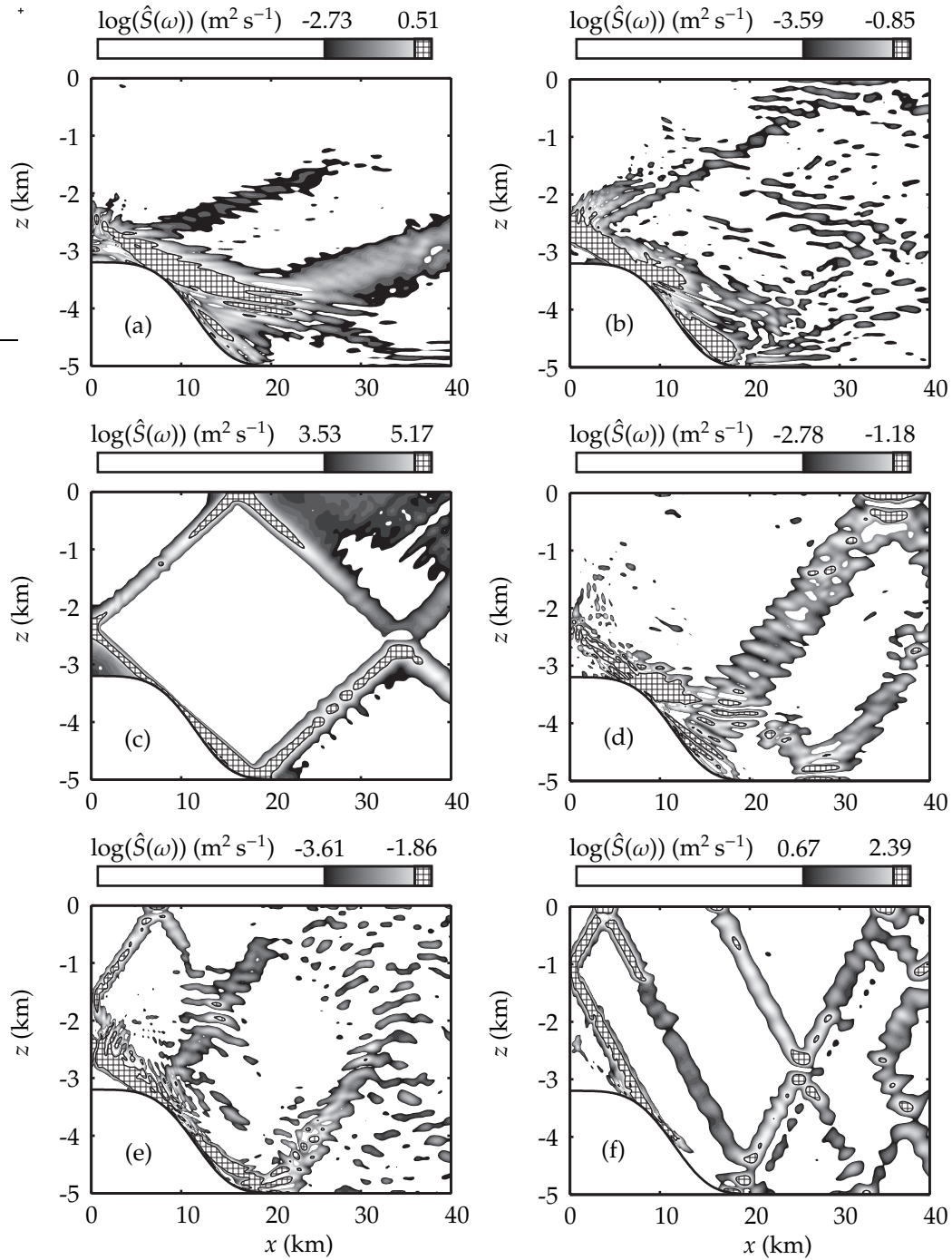
F   3.18: Spatial distribution of waves with different frequencies within 40 km of the ridge for the case $\theta = 10°$ N: (a) $\omega = 0.4087\omega_0$, (b) $\omega = 0.5913\omega_0$, (c) $\omega = \omega_0$, (d) $\omega = 1.4087\omega_0$, (e) $\omega = 1.5913\omega_0$, (f) $\omega = 2\omega_0$.

3.3.4 Spectrum evolution

Further insight into the nature of harmonics and interharmonics can be gained by quantifying the time evolution of their energetics. To do this, we calculate the spectrograms that provide the evolution of the short-term spectra. The spectrograms lack intricate details of the spectrum variation, but they show the overall trends. In this section, we consider spectrograms calculated for the time periods $[t_0, t_0 + 10 \text{ days}]$, where $t_0 \in [0, 20]$ days.

As a frequency is gaining or losing energy, the corresponding peak of the spectrum is either growing or decaying. Figure 3.23 illustrates the spectra for several cases calculated at an earlier time interval $[0, 10]$ days and at a later time interval $[10, 20]$ days. It is seen that with time the interharmonics gain energy, whereas the harmonics either stay unchanged or lose energy. In a similar fashion, we can analyze the energetics of each harmonic and interharmonic.

The time variation of a given harmonic or interharmonic changes smoothly with latitude. For example, figure 3.24 compares the evolution of the energy in the first tidal harmonic at the different latitudes. The same evolution for the latitudes approaching θ_{cr} is shown in figure 3.25. The critical latitude is the case where the most efficient harmonic-to-interharmonic energy transfers take place: according to the spectrogram for the critical latitude, the energy at the tidal frequency decreases by about 25% and then seems to stabilise.

The energy variation at several first harmonics and interharmonics is shown for latitudes 0°, 10°, 20°, 25°, 28.82° and 30° N in figures 3.26, 3.27, 3.28, 3.29, 3.30 and 3.31. Let us consider in more detail several first harmonics and interharmonics for the two representative latitudes, 0° N and 30° N (figures 3.26 and 3.31). At $\theta = 0°$, the energy in the first and second harmonics grow by a small amount for about five days (note that the spectrogram begins at $t = 5$ days so initial growth is lost), and then they behave in a manner similar to what could be the beginning of relaxation to a stable state. The supposition that the energy in harmonics approaches a stable state is supported by the more obvious stabilization observed in the case $\theta = 30°$ N and the fact that spectrograms vary smoothly from latitude to latitude. The interharmonics seem to have similar pattern of relaxation but on longer time-scales.

For the latitude $\theta = 30°$ N, the energy at the tidal harmonic decreases significantly (by $\approx 20\%$) to a stable state within approximately ten days. During the same ten days, the interharmonics efficiently gain energy. It is not seen that the interharmonics have stabilized by the end of the run to a particular level, but we can speculate that they are going to do so shortly, from the comparison with other latitudes.

Similar evolution of energy in the tidal and subtidal frequency was calculated by MacKinnon and Winters (2003). However, on average, they observed much stronger transfers of energy from tidal to subtidal motion. The reason is that they had a periodic domain, and the subharmonic
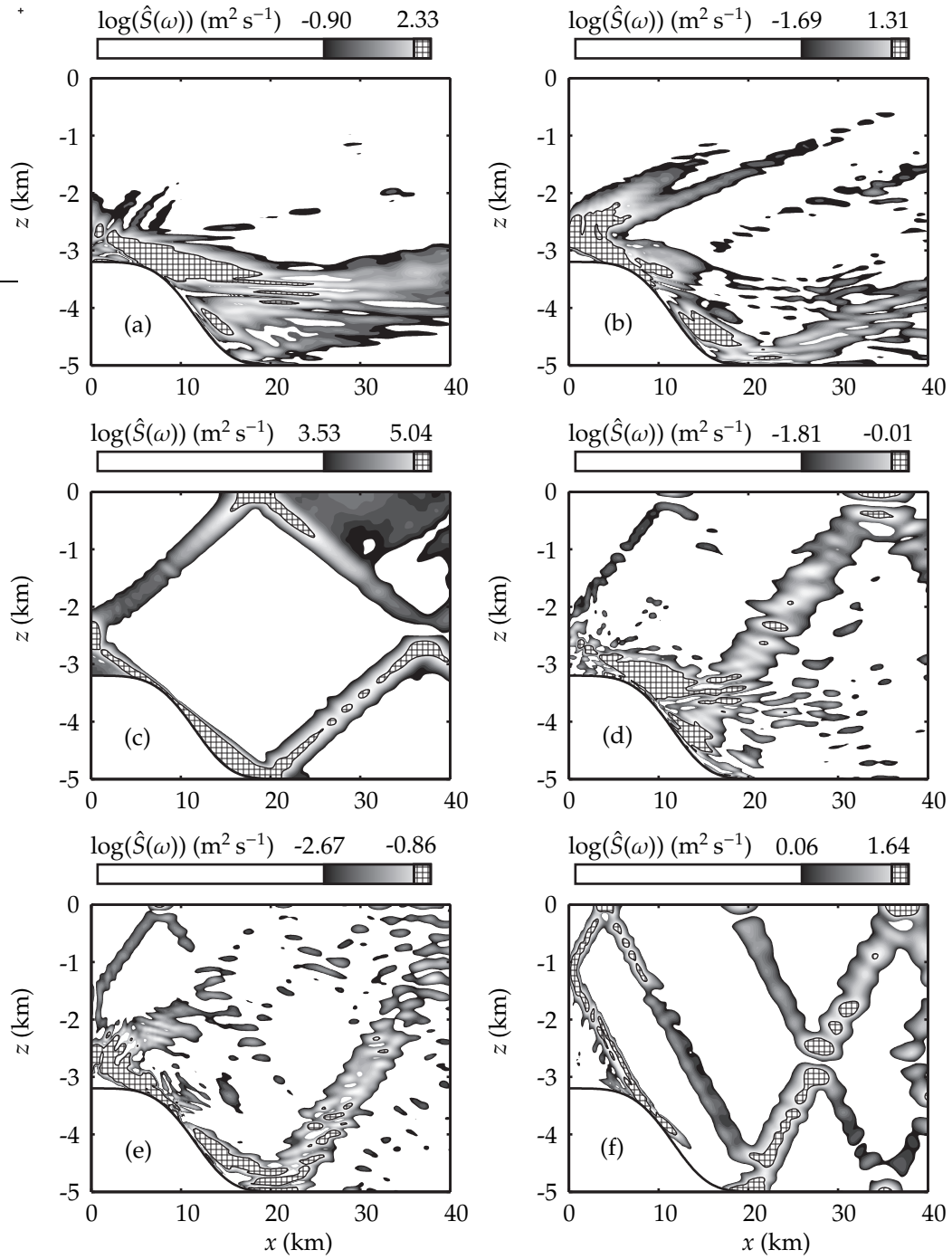
F   3.19: Spatial distribution of waves with different frequencies within 40 km of the ridge for the case $\theta = 20°$ N: (a) $\omega = 0.4269\omega_0$, (b) $\omega = 0.5752\omega_0$, (c) $\omega = \omega_0$, (d) $\omega = 1.4269\omega_0$, (e) $\omega = 1.5752\omega_0$, (f) $\omega = 2\omega_0$.
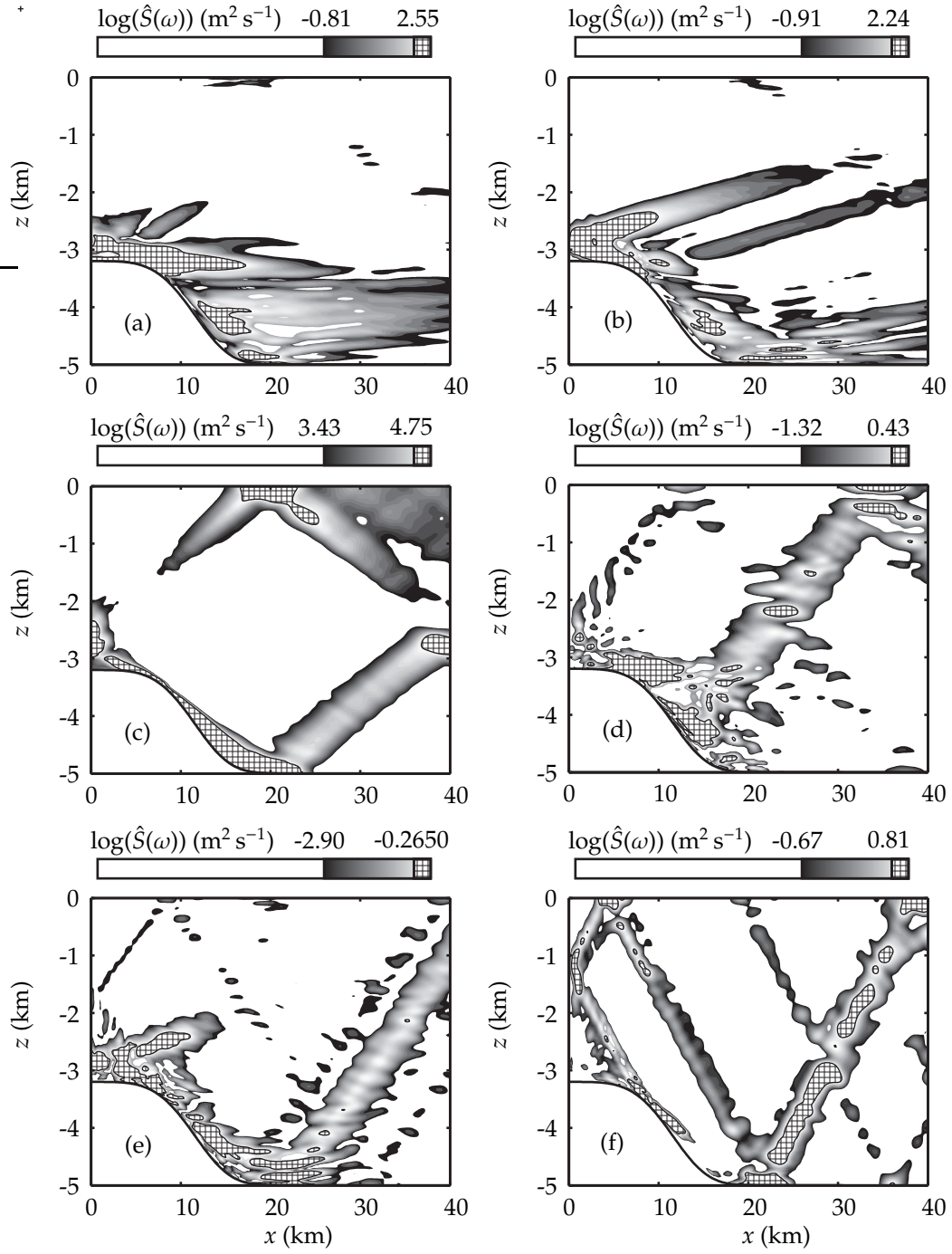
F   3.20: Spatial distribution of waves with different frequencies within 40 km of the ridge for the case $\theta = 25°$ N: (a) $\omega = 0.4590\omega_0$, (b) $\omega = 0.5430\omega_0$, (c) $\omega = \omega_0$, (d) $\omega = 1.4630\omega_0$, (e) $\omega = 1.5370\omega_0$, (f) $\omega = 2\omega_0$.
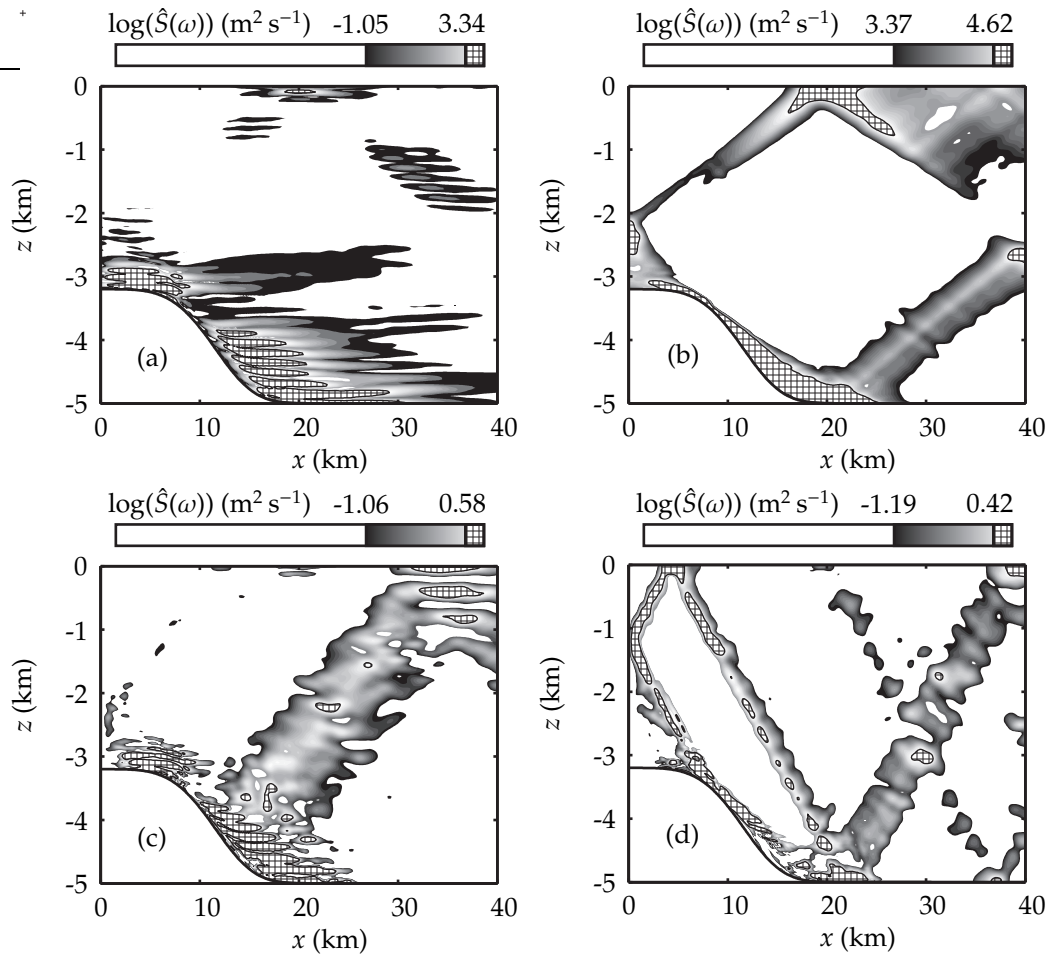
F   3.21: Spatial distribution of waves with different frequencies within 40 km of the ridge for the case $\theta = \theta_{cr}$: (a) $\omega = 0.5\omega_0$, (b) $\omega = 1.0\omega_0$, (c) $\omega = 1.5\omega_0$, (d) $\omega = 2.0\omega_0$.
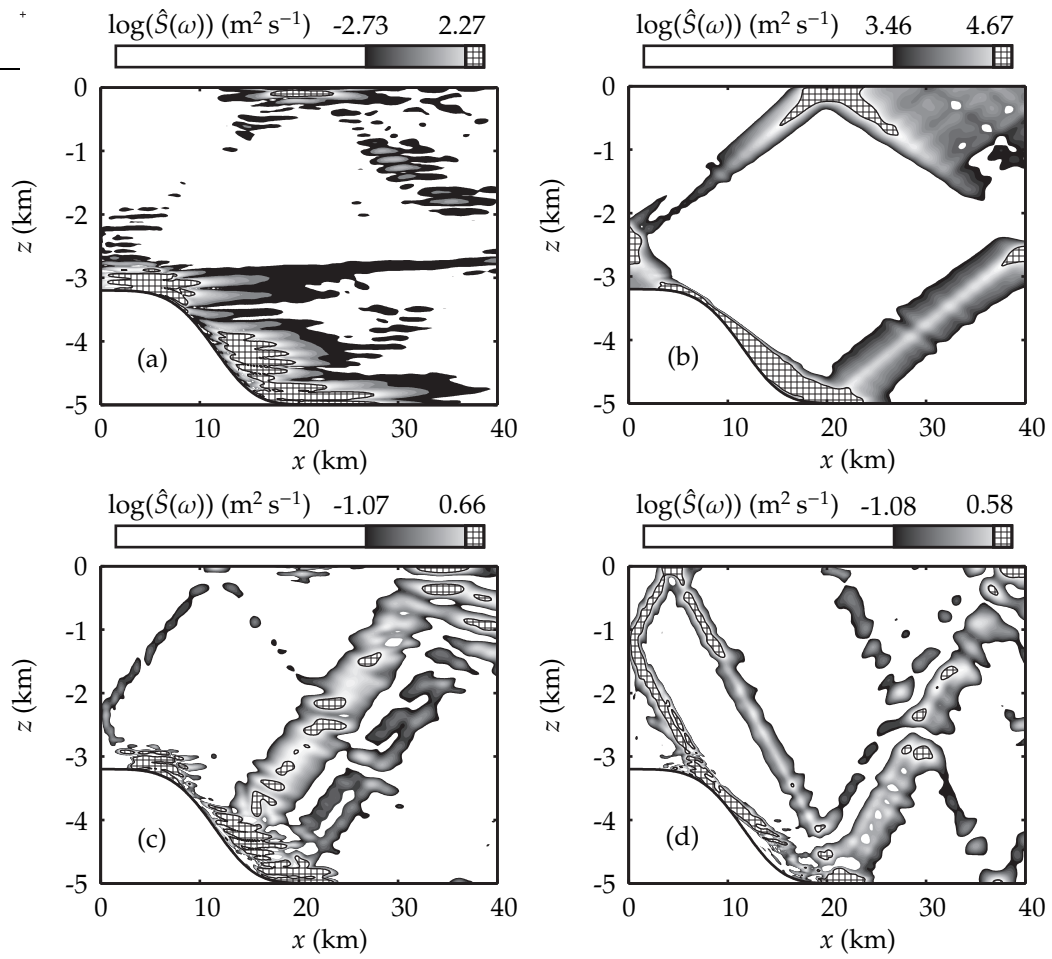
F   3.22: Spatial distribution of waves with different frequencies within 40 km of the ridge for the case $\theta = 30°$ N: (a) $\omega = 0.5\omega_0$, (b) $\omega = 1.0\omega_0$, (c) $\omega = 1.5\omega_0$, (d) $\omega = 2.0\omega_0$.
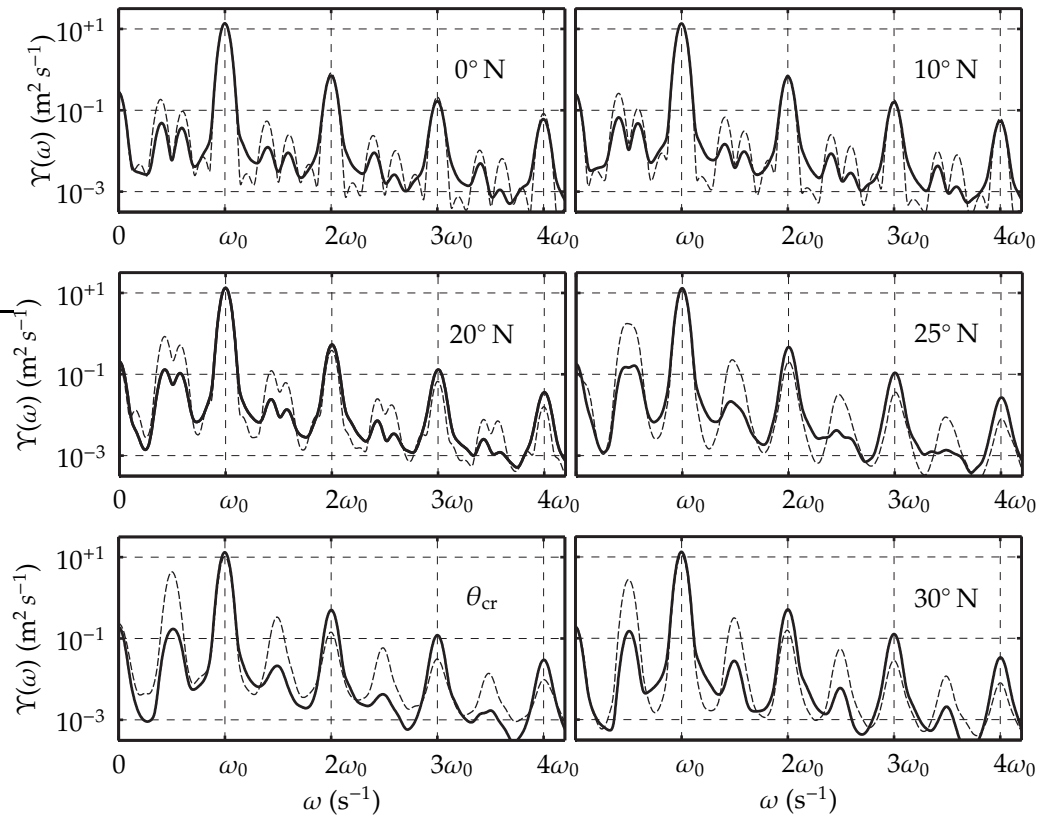
F   3.23: Fragments of spectra calculated for two time periods: $[0, 10]$ days (solid line); $[10, 20]$ days (dashed line).
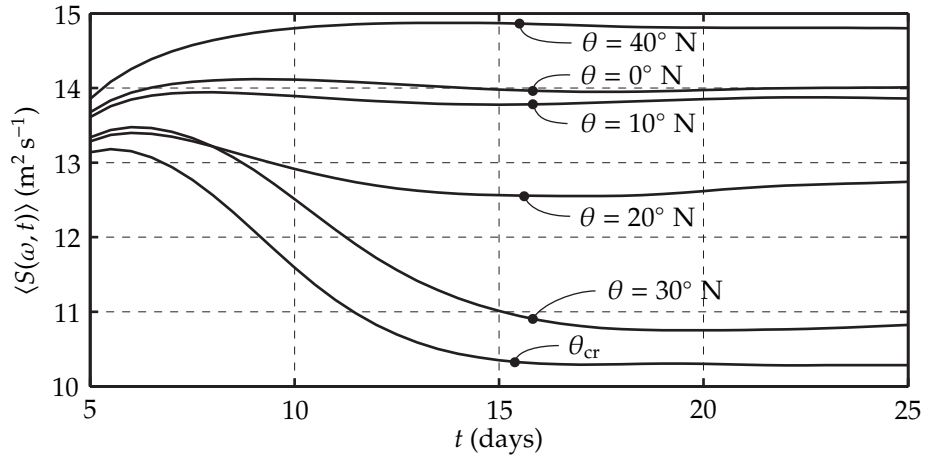
F   3.24: Energy of the tidal harmonic at latitudes 0°–40° N.
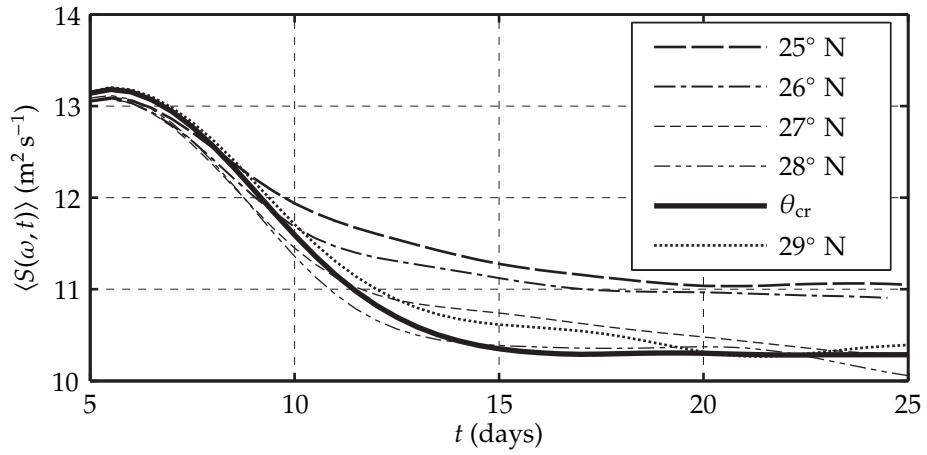
F   3.25: Energy of the tidal harmonic at the near-critical latitudes.
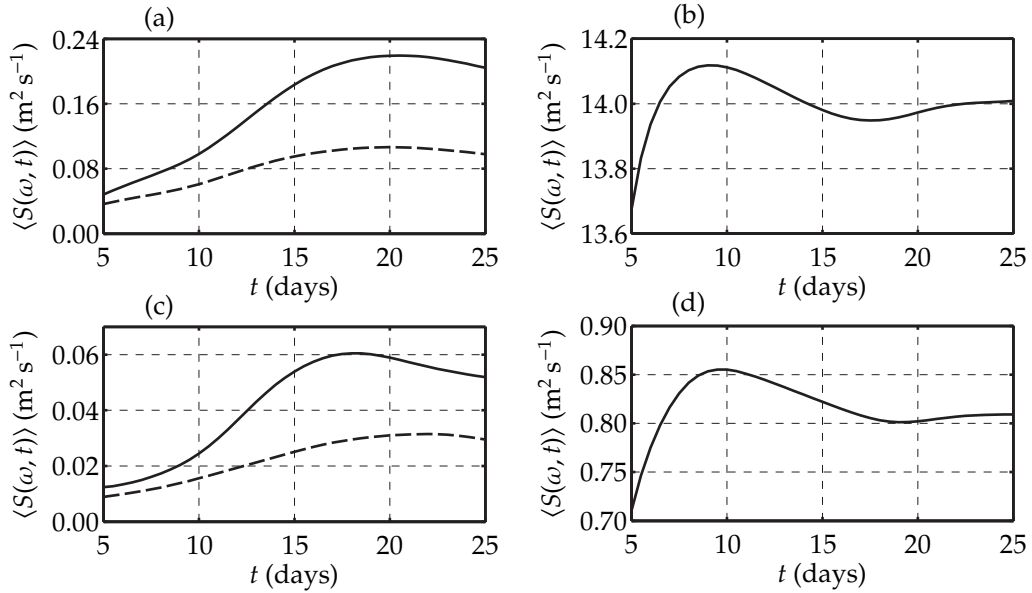
F   3.26: The averaged spectrogram for the flow within 40 km from the ridge at the latitude $\theta = 0°$ N: (a) $\omega = 0.4\omega_0$ (solid), $\omega = 0.6\omega_0$ (dashed), (b) $\omega = 1.0\omega_0$, (c) $\omega = 1.4\omega_0$ (solid), $\omega = 1.6\omega_0$ (dashed), (d) $\omega = 2.0\omega_0$.

instability occured throughout the domain. In our case, the instabilities are local; the actual tidal-to-subtidal conversion happens only in the vicinity of the strongly nonlinear regions.

3.3.5   Instability description

To illustrate how instability generates a wave with a subharmonic frequency, we consider an example of a local flow conversion from tidal frequency to a subharmonic one.

We choose the case of $\theta = 30°$ N as the instability processes are especially distinctive there and the energy transfers from the tidal frequency to the subharmonics are strong. From the spatial distribution of waves with different frequencies in figure 3.22 we see that the flow has particularly strong waves of the subharmonic frequency near the top of the ridge and on the side. Let us consider the particular location $(x, z) = (15.7, -4.321)$ km. There, according to the local velocity spectrum, the subharmonic frequency is particularly strong. Figure 3.32(*a*) demonstrates the velocity time-series in the barotropic-Lagrangian reference frame corresponding to this location. The tidal frequency dominates the time-series at the beginning, but after about 15 days the subtidal frequency dominates. From the spectrum in figure 3.32(*b*) obtained by averaging spectra at the location and the surrounding eight grid points, we infer that the subharmonic frequency that
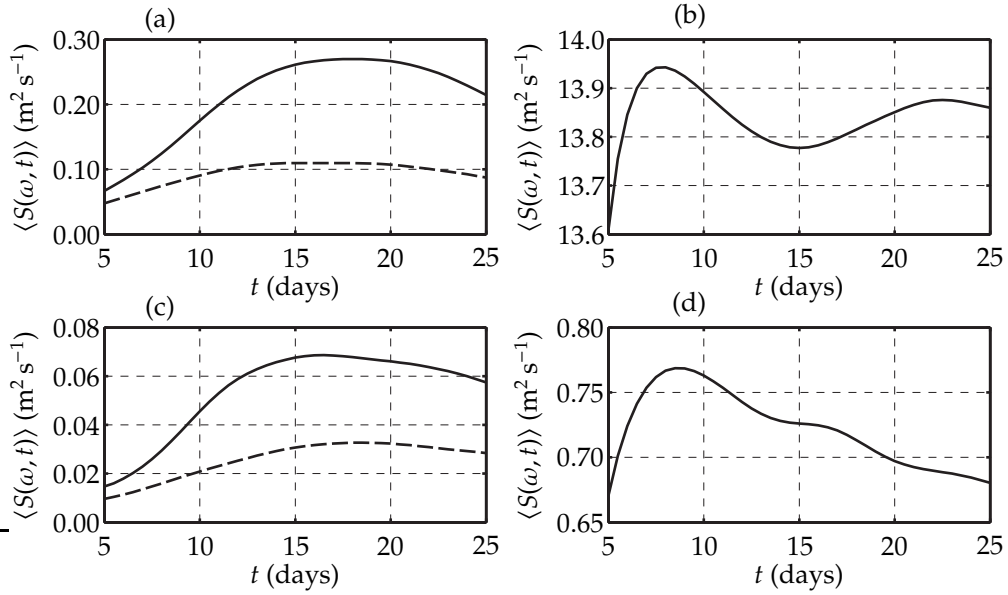
F   3.27: The averaged spectrogram for the flow within 40 km from the ridge at the latitude $\theta = 10°$ N: (a) $\omega = 0.4087\omega_0$ (solid), $\omega = 0.5913\omega_0$ (dashed), (b) $\omega = 1.0\omega_0$, (c) $\omega = 1.4087\omega_0$ (solid), $\omega = 1.5913\omega_0$ (dashed), (d) $\omega = 2.0\omega_0$.
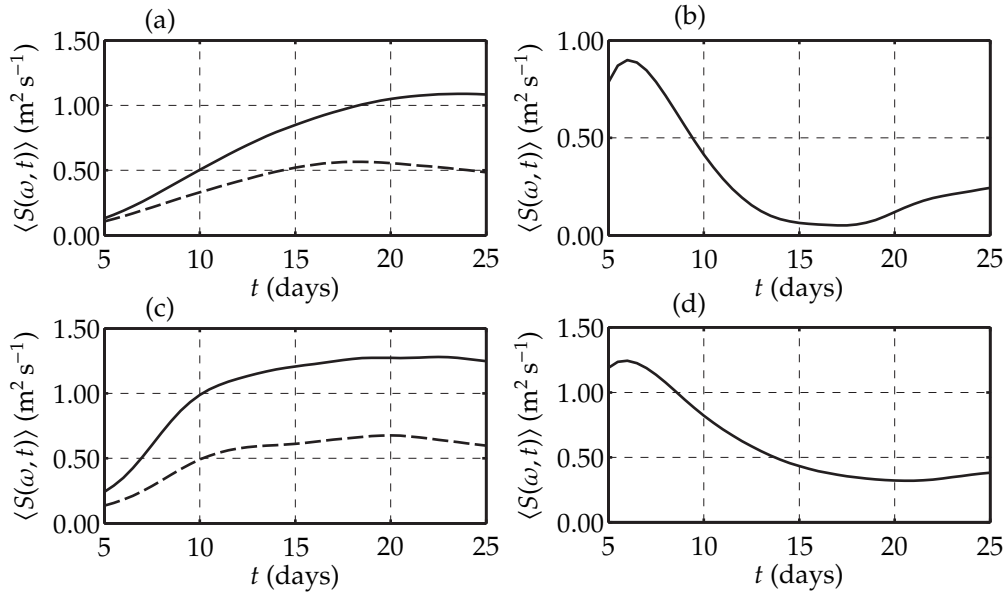
F   3.28: The averaged spectrogram for the flow within 40 km from the ridge at the latitude $\theta = 20°$ N: (a) $\omega = 0.4269\omega_0$ (solid), $\omega = 0.5752\omega_0$ (dashed), (b) $\omega = 1.0\omega_0$, (c) $\omega = 1.4269\omega_0$ (solid), $\omega = 1.5752\omega_0$ (dashed), (d) $\omega = 2.0\omega_0$.
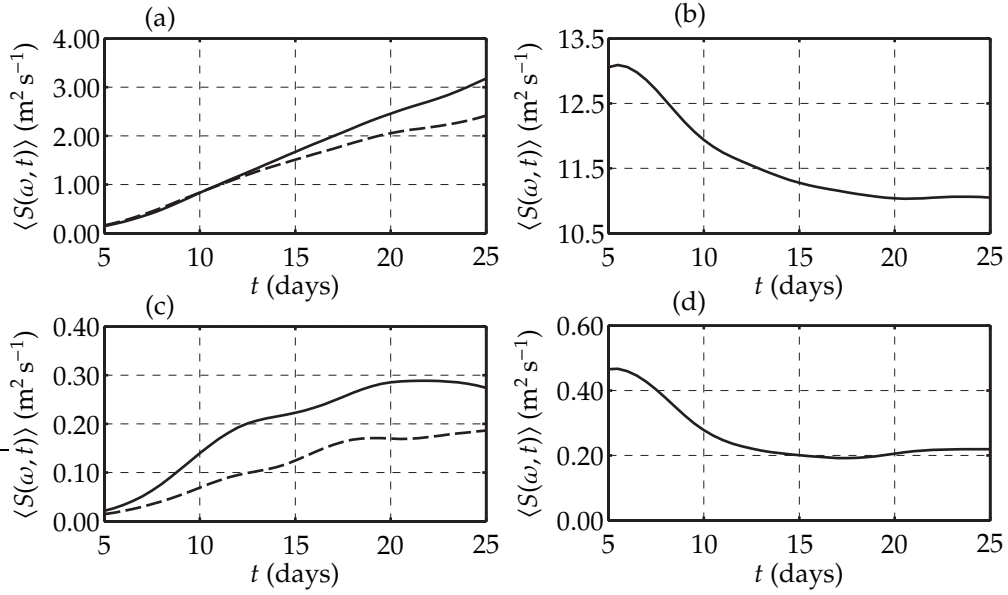
F   3.29: The averaged spectrogram for the flow within 40 km from the ridge at the latitude $\theta = 25° \text{N}$: (a) $\omega = 0.459\omega_0$ (solid), $\omega = 0.543\omega_0$ (dashed), (b) $\omega = 1.0\omega_0$, (c) $\omega = 1.463\omega_0$ (solid), $\omega = 1.537\omega_0$ (dashed), (d) $\omega = 2.0\omega_0$.
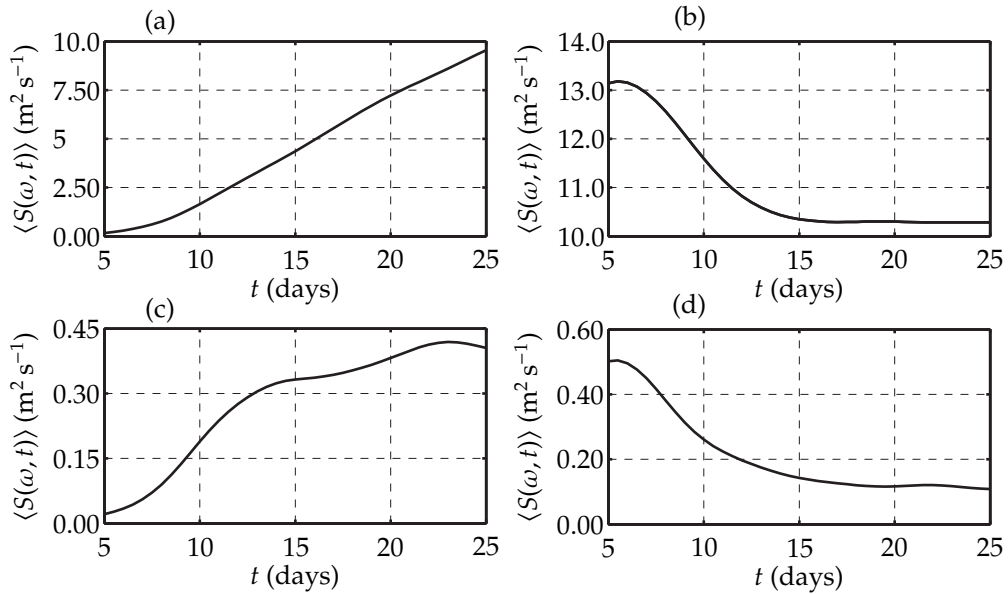
F   3.30: The averaged spectrogram for the flow within 40 km from the ridge at the latitude $\theta = \theta_{\text{cr}}$: (a) $\omega = 0.5\omega_0$, (b) $\omega = 1.0\omega_0$, (c) $\omega = 1.5\omega_0$, (d) $\omega = 2.0\omega_0$.
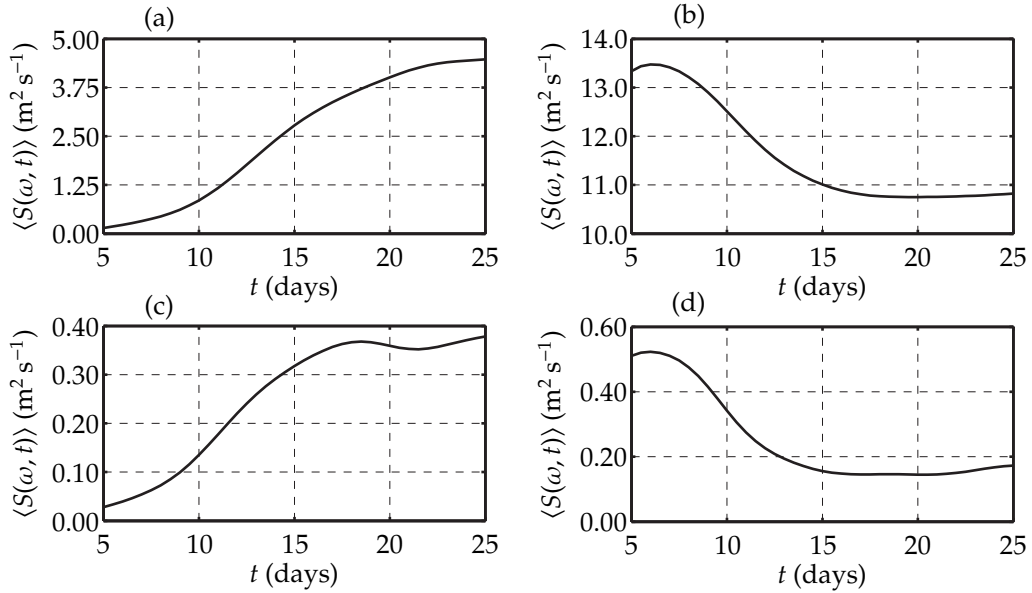
F   3.31: The averaged spectrogram for the flow within $40\,\mathrm{km}$ from the ridge at the latitude $\theta = 30°\,\mathrm{N}$: (a) $\omega = 0.5\omega_0$, (b) $\omega = 1.0\omega_0$, (c) $\omega = 1.5\omega_0$, (d) $\omega = 2.0\omega_0$.

gains energy is approximately $0.5\omega_0$. The subharmonic frequency in this case is, in fact, slightly stronger than the tidal frequency. Figure 3.32(c) quantifies the transfer of energy from the tidal frequency to the subtidal one, and shows how the spectrogram captures the conversion from tidal to subtidal motion and, then, back to tidal near the end of time-series.

The instabilities occuring at a certain region form patches that spread spatially in a manner similar to that described by Teoh et al. (1997). Figure 3.33 demonstrates the development of the instability as in figure 3.32, but shows the contour plot of the velocity $\tilde{u}_{ij}^{n}$ in the lower 800 m of the water column, i.e. index i corresponding to $x = 15.7$ km is fixed, $j = 1, 2, \ldots, 40$ and $n = 1, 2, \ldots, 1440$. It is seen that after about one day a strong core with large horizontal velocities starts forming in the center of the vertical cross-section. The core, alternating with frequency ω_0 becomes larger and after approximately ten days the core splits into two pieces, then, into three and so on. As the energy is injected into the region through the instability the patch dominated by waves of subharmonic frequency is constantly expanding. Similar expansion of the instability patch is observed in other regions: for example, at a vertical cross-section near the point $(x, z) = (15.7, -4.321)$ km. This expansion is another factor that makes forced instabilities important: although the waves are not propagating from the vicinity of the instability, the region of instability is constantly growing and, thus, an overturning, which may eventually occur in the region, may affect regions as far as several kilometers from the center of the instability.

93
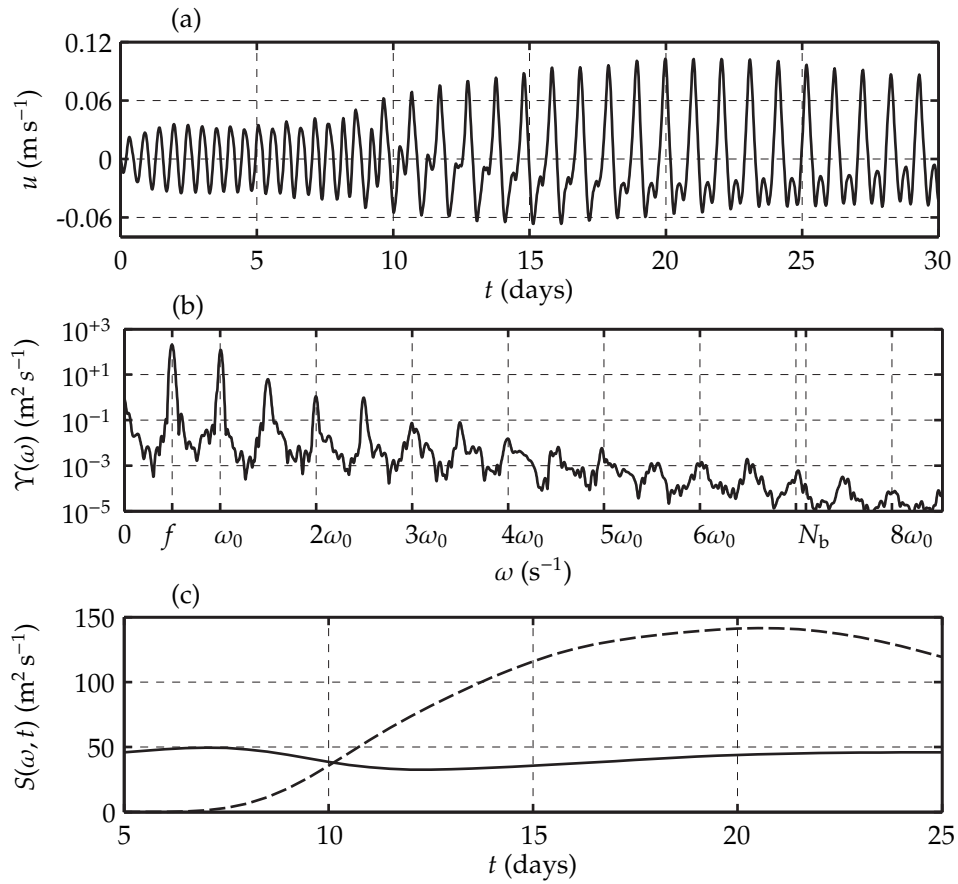
F   3.32: Development of instability at $\theta = 30°$ N near the location $x = 15.7$ km and $z = -4.321$ km: (a) the time-series of the horizontal velocity in the barotropic-Lagrangian reference frame, (b) averaged spectrum over 30 days, (c) spectrogram of the tidal frequency (solid) and frequency $0.5\omega_0$ (dashed).
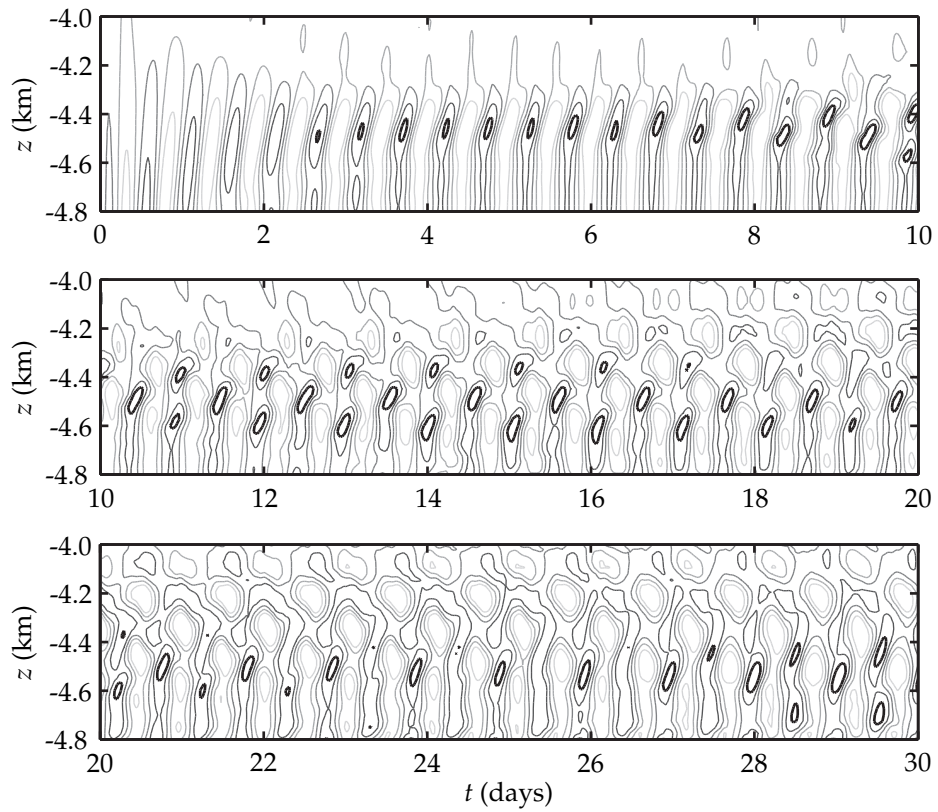
F   3.33: Contour plot of the horizontal velocity in the barotropic-Lagrangian reference frame for a vertical cross-section near the location $x = 15.7$ km and $z = -4.321$ km.

3.4 Discussion

In this chapter, we investigated the dynamics and spectra of internal wave field generated by tidal flow over topography. As a final remark, we would like to discuss two papers where similar questions were addressed.

Gerkema et al. (2006) investigated internal-tide generation at a continental shelf-break. They solved the nonhydrostatic equations for a time period of about 15 tidal periods, which is approximately one quarter of the time period that we use in our simulations. The spatial resolution in the work by Gerkema et al. is close to ours: in the deep part of the domain (waterdepth 4 km), they use cells 100 m in the horizontal by 25 m in the vertical, whereas we use cells 100 m by 26.042 m. They also used strong damping in the form of a sponge layer to absorb baroclinic waves away from the source. Their kinetic energy spectra estimations are similar to ours but have larger amount of leakage (mainly due to the short total model time); consequently, their estimations do not capture most of the interharmonics except for the strongest ones. For example, in the case of $\theta = 27.5°$ N, their spectra have the interharmonic of the frequency $\omega = 0.5\omega_0$ and $\omega \approx 1.5\omega_0$. They suspected that the interharmonic frequency was the result of the Doppler shift due to advection of the subharmonic waves by the tidal frequency waves. Our results suggest that the interharmonic frequencies observed in the spectrum are not Doppler shifted.

First, our results show that the Eulerian, barotropic-Lagrangian and Lagrangian spectra are similar implying that advection does not play a crucial role. Moreover, comparing their spectra for the case $\theta = 27.5°$ N with ours for the case $\theta = 30°$ N, we see that the waves of frequency $\omega \approx 0.5\omega_0$ and $1.5\omega_0$ have different natures: waves of frequency close to $0.5\omega_0$ are mostly trapped waves, whereas for the frequency $1.5\omega_0$ we see beams with the slope given by the dispersion relation (see figure 3.22*a,c*). If it was true that the waves of frequency $1.5\omega_0$ are the result of the Doppler shift, then they would only be seen in the regions where the waves of frequency $\omega \approx 0.5\omega_0$ are present.

In a certain sense, our results are also similar to the ones obtained by MacKinnon and Winters (2003). They used a three-dimensional spectral model to solve the non-hydrostatic equations of motion with hyperviscosity terms. Their model was initialized at rest and forced with a bottom-localized, narrow-band field of upward-propagating internal waves of tidal frequency. The forcing was realized by adding a forcing term to the vertical momentum equation designed to represent idealized topographically generated waves. According to their simulations, energy at tidal frequency is growing until it reaches its peak after about 5–10 days; then energy decays at approximately the same rate to a stable level. In contrast to our estimations, MacKinnon and Winters observe a much stronger exchange of energy between the tidal and subharmonic frequencies. In particular, for the case of $\theta = 21°$ N, they observe a transition of the flow from dominantly tidal to lower frequency motion: after about 10 days the strongest frequency of the

flow is the subharmonic frequency $\omega \approx 5.6 \times 10^{-5}$ s^{-1}. Our results, although suggesting that on average the tidal frequency stays dominant for all latitudes including latitude $\theta = 20°$ N, exhibit the tidal-to-subharmonic conversion locally near the ridge for the case $\theta = 30°$ N. The observed difference is to be expected: their periodic domain $50 \times 50 \times 5$ km^3 is quickly filled with energetic progressive internal waves, whereas in our simulation waves freely propagate away and, thus, are less susceptible to instabilities.

3.5   Summary

In this chapter, we considered numerical simulations of internal waves generated by tidal flow over an isolated supercritical ridge at several different latitudes. The emerging flow is dominated by waves of harmonic and interharmonic frequencies, some of which, according to the dispersion relation, are progressive and some, trapped. The strongest interharmonics are the subharmonics, which are produced as a result of the tidal beam destabilization near the strongly nonlinear regions. The interharmonic frequencies are the combination frequencies of the tidal harmonics and the subharmonics. Both harmonics $\{n\omega_0\}$ and interharmonics $\{\omega_\alpha + n\omega_0\}$, where $n \in \mathbb{N}$ and $\omega_\alpha \in (0, \omega_0]$, decay with n at a similar, nearly exponential rate. As a result, the spectrum has a self-similar structure, which decays in magnitude at an exponential rate. The instabilities are stronger for the near-critical latitudes; there, we observe strong waves of interharmonic frequencies. For the latitude $\theta = 30°$ N, which is supercritical, the strongest waves of subharmonic frequency are trapped. This suggests that the observed instabilities are of a forced non-resonant type.

Chapter 4

Temporal Spectral Analysis: Part II

4.1 Important factors

4.1.1 Latitude

An important question regarding waves of interharmonic frequencies is how their frequencies depend on latitude.

So far, we know that the strongest subharmonic frequencies appearing in the average spectrum deviate symmetrically from the frequency $\omega_0/2$. As will be shown in the next section, where we consider the wavenumbers of interharmonics, for latitudes $\theta \leq \theta_{cr}$, the subharmonics are generated through a resonant triad interaction occurring when the tidal beam becomes unstable. The two strongest subharmonic frequencies gradually approach $\omega_0/2$ as the latitude approaches the critical latitude θ_{cr}. How the values of the strongest subharmonics change with latitude is the subject of this section.

A series of figures 4.1–4.6 demonstrates fragments of the average spectra for the latitudes in question. Here, we are primarily interested in accurate values of the strong subharmonics, thus, we only consider the subharmonic range of frequencies $\omega \in [0, \omega_0]$. Two direct spectral estimations averaged over the region $\xi \in [0, 40]$ km are shown. One estimation uses the discrete prolate spheroidal sequence of the first order and provides high spectral resolution. It allows us to see fine features of the spectrum when two peaks get close. However, it suffers from bias due to leakage. The other estimation, which uses the discrete prolate spheroidal sequence of the third order, has lower spectral resolution, but suffers from less leakage. Thus, it allows us to see weaker statistically significant peaks in the spectrum.
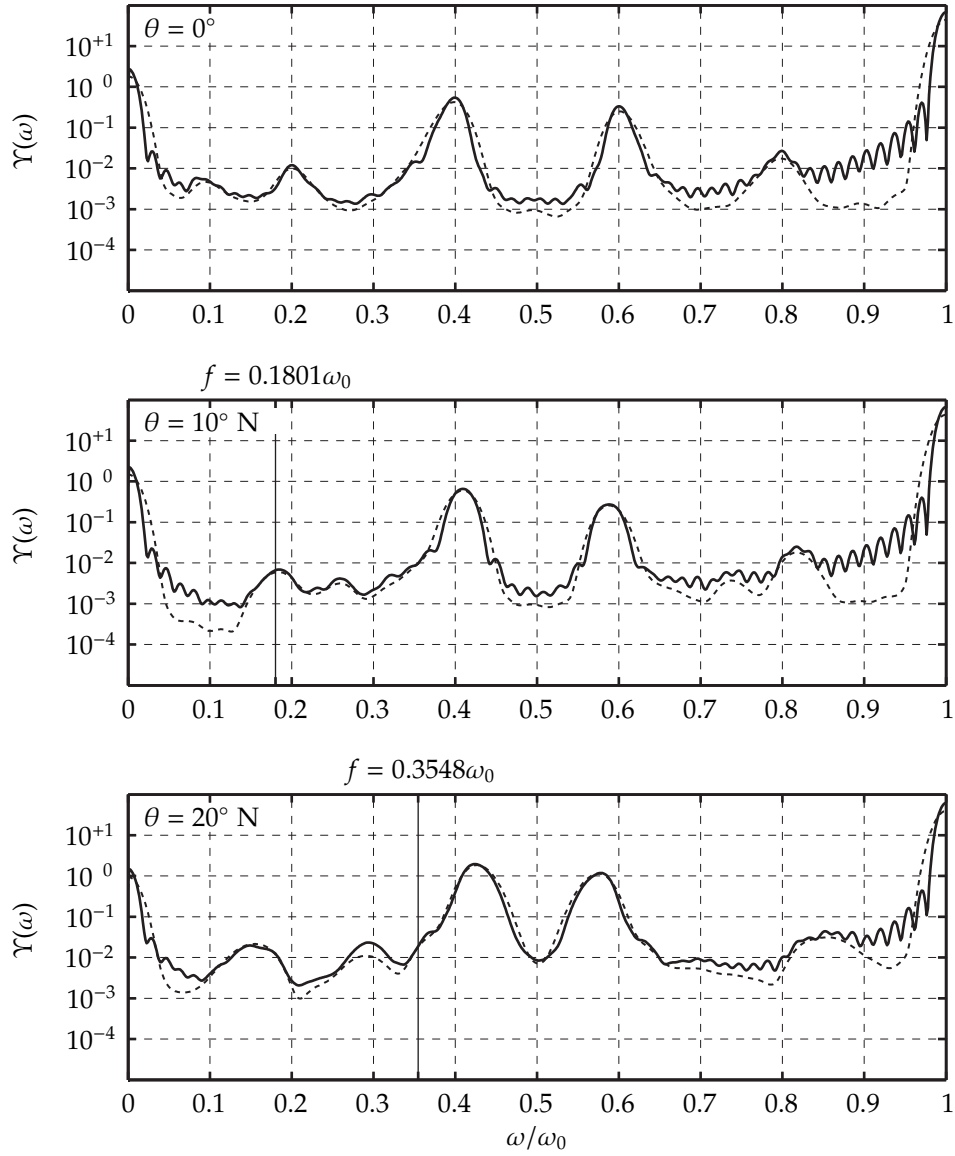
F   4.1: Fragments of the average spectra showing the subharmonic frequency range. Two direct spectral estimations are shown. They used discrete prolate spheroidal sequences of first (solid) third (dashed) order. Cases shown: 0°, 10°, and 20° N.
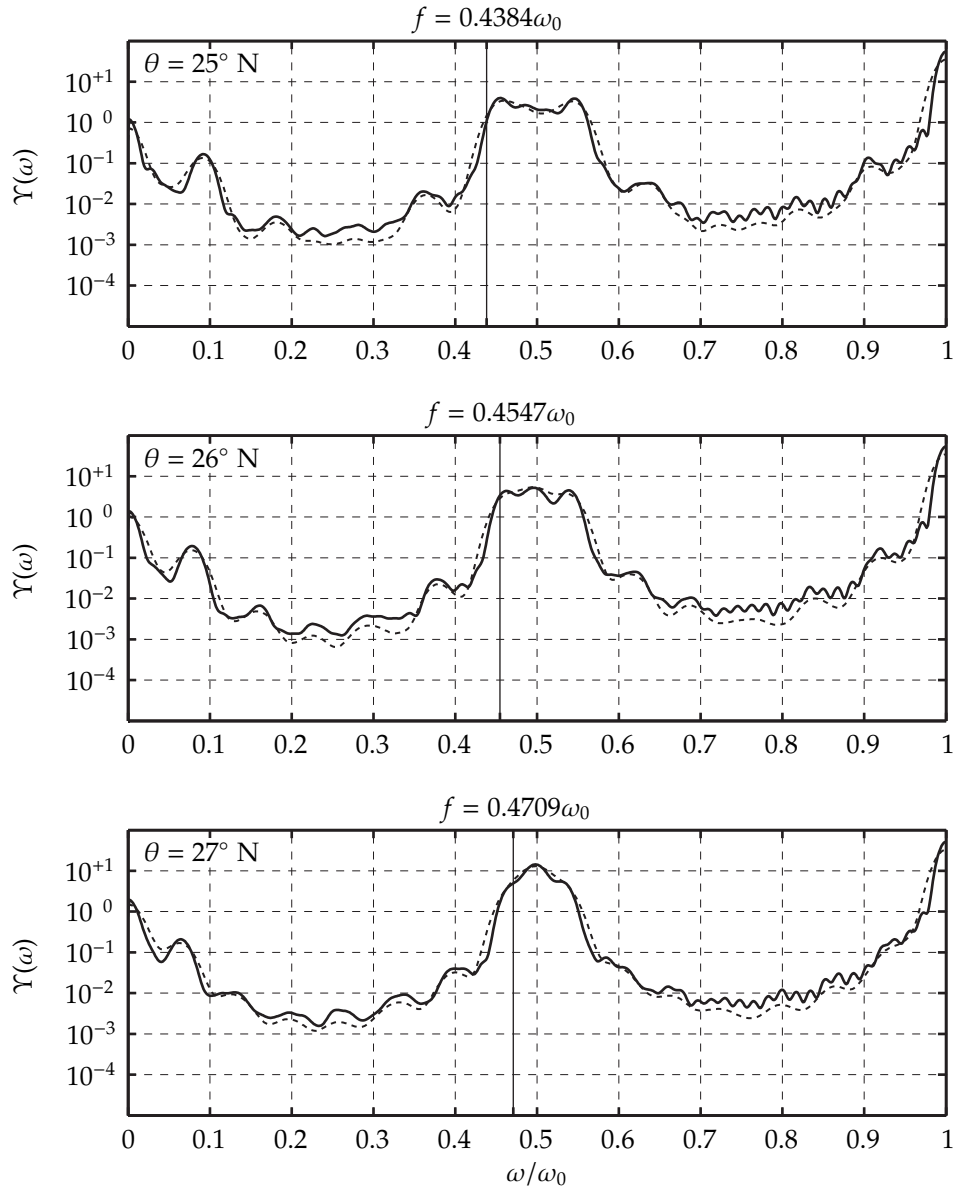
Figure 4.2: Same as in figure 4.1 for cases 25°, 26°, and 27° N.
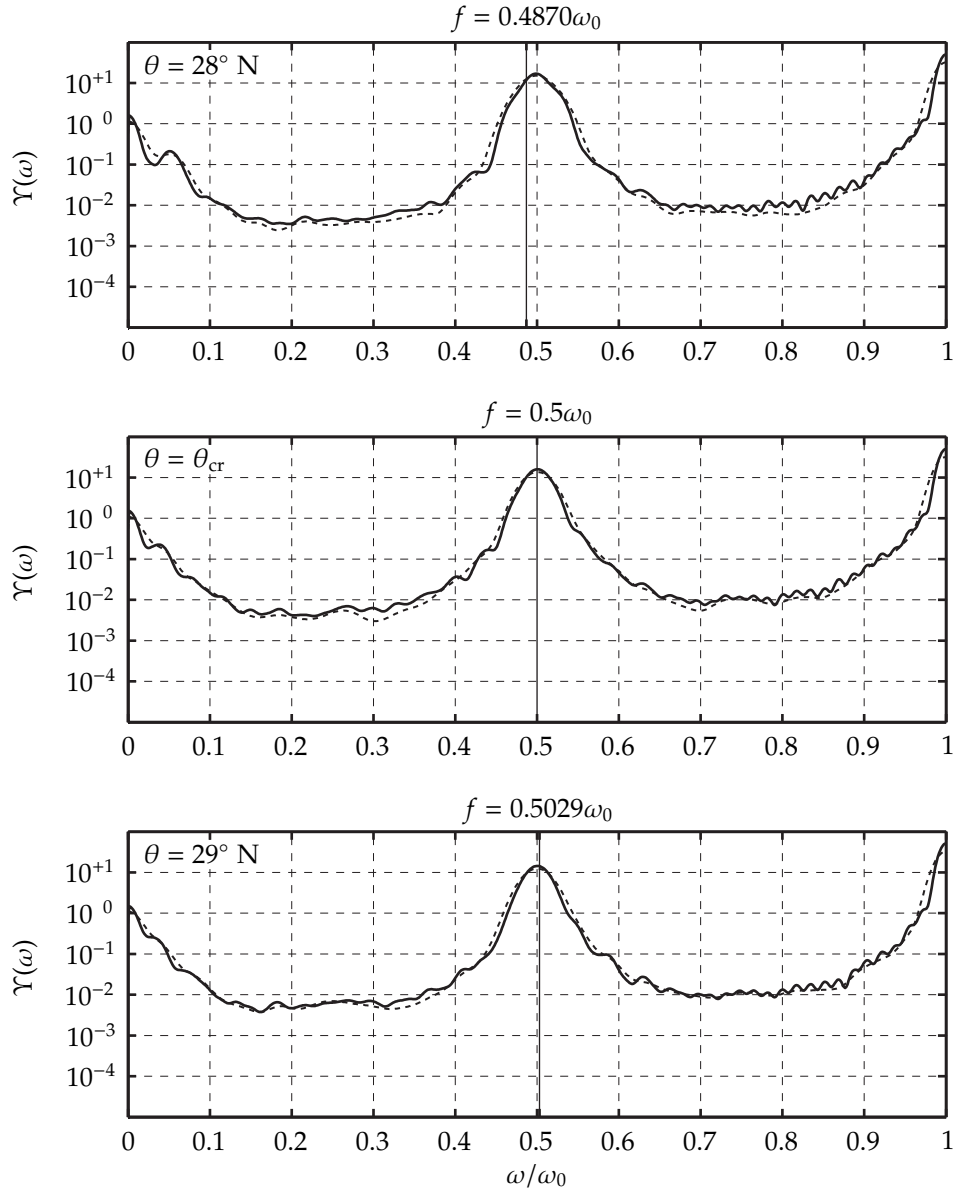
F   4.3: Same as in figure 4.1 for cases 28°, 28.82°, and 29° N.
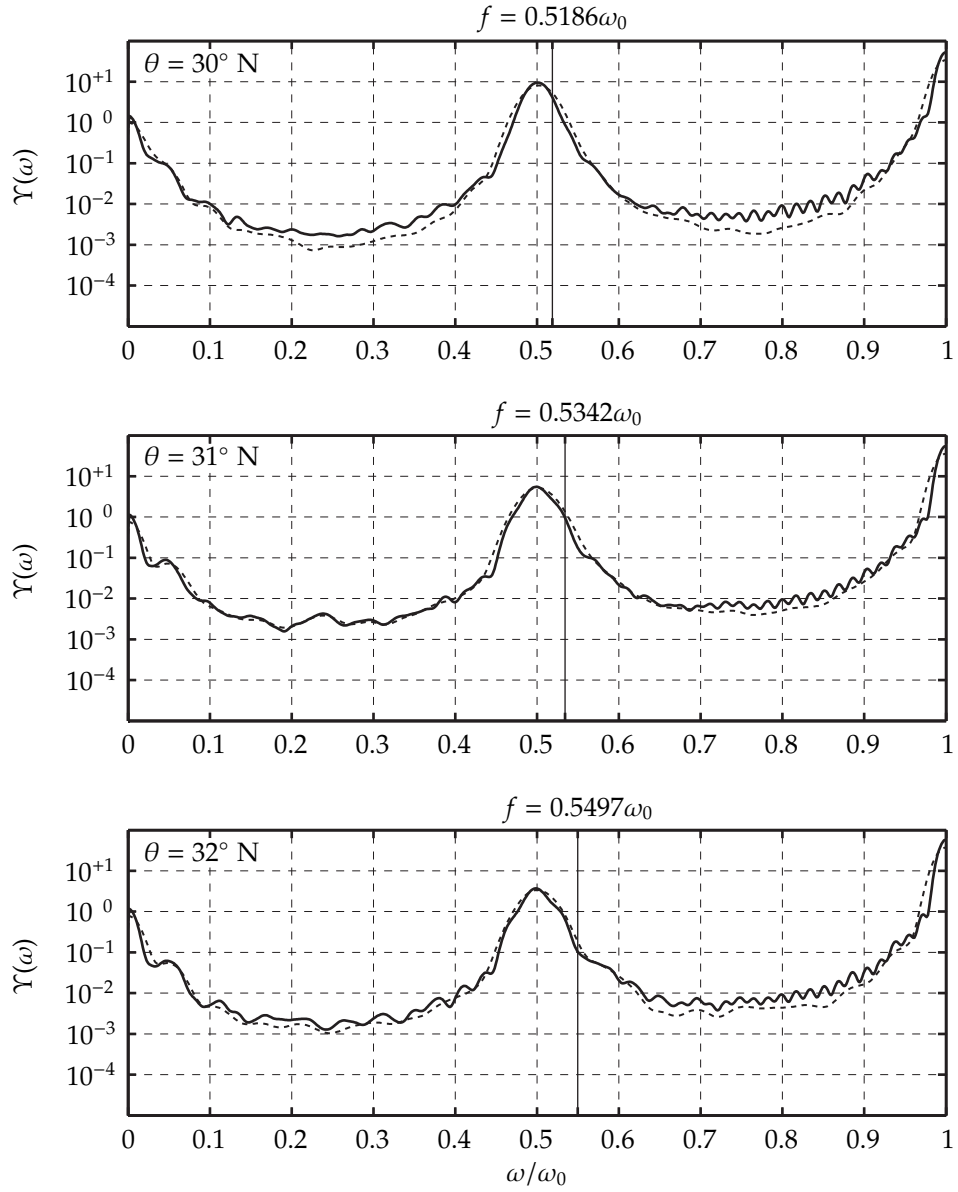
F   4.4: Same as in figure 4.1 for cases 30°, 31°, and 32° N.

$f = 0.5649\omega_0$

$\theta = 33°$ N

$f = 0.5800\omega_0$

$\theta = 34°$ N

$f = 0.5950\omega_0$

$\theta = 35°$ N

ω/ω_0
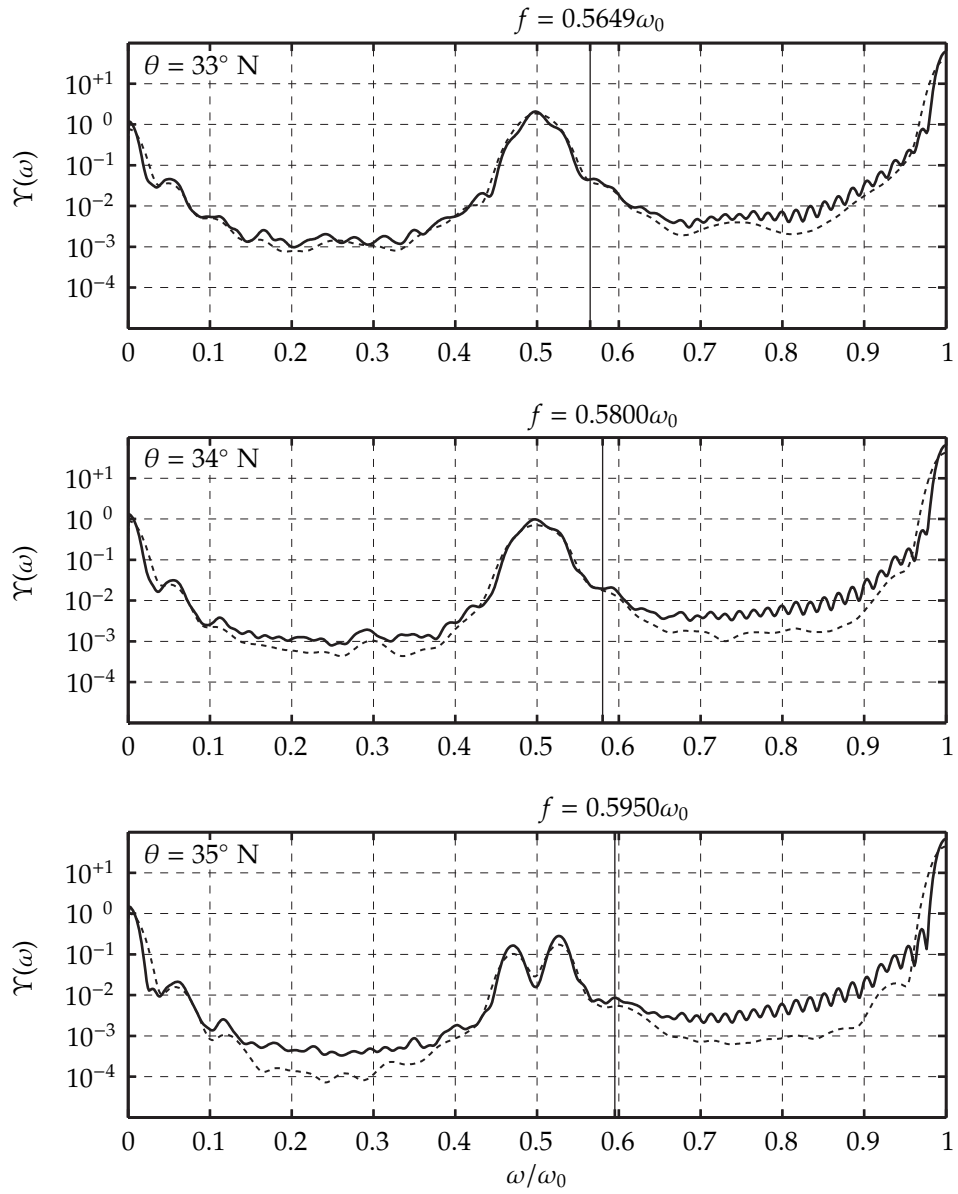
F   4.5: Same as in figure 4.1 for cases 33°, 34°, and 35° N.

$$f = 0.668\omega_0$$
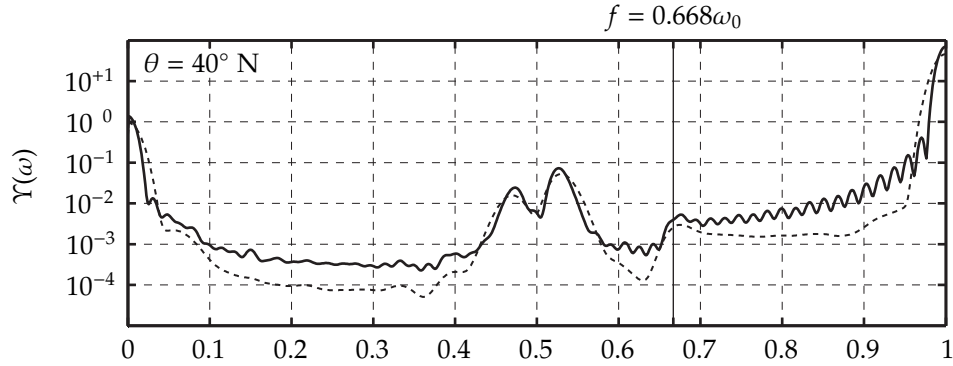
F   4.6: Same as in figure 4.1 for case 40° N.

The cases 0°–20°N were discussed earlier. The magnified fragments of the two spectral estimations shown in figure 4.1 confirm what was noticed before. The two subharmonic peaks at $0.4\omega_0$ and $0.6\omega_0$ observed in case 0° move closer together as the latitude increases. There are a number of smaller peaks, which are presumably generated through the secondary interaction between the two strongest subharmonics, e.g. in the case 0°, the difference interaction between subharmonics $0.4\omega_0$ and $0.6\omega_0$ gives rise to the subharmonic $0.2\omega_0$ seen in the spectrum. The secondary peaks move as the latitude changes, so that the triad relations among all subharmonics are preserved. For example, the subharmonic $0.2\omega_0$ in case 0° decreases as the latitude increases.

As the latitude reaches 25° N, the two peaks corresponding to the strongest subharmonics get so close that it may seem that there is only one subharmonic frequency, namely $\omega_0/2$ (see figure 4.2, case 25° N). Yet, both spectral estimations suggest that there are two strong subharmonics. In case 26° only the spectral estimation with higher resolution managed to capture the two peaks (see figure 4.2, case 26° N). For the cases 27°–34° close to the critical latitude, the two peaks in both spectral estimations are blended into one.

In spite of the blending of the peaks, we have some information about the two dominant subharmonic frequencies. This information is based on two features of the observed peak embedding the two frequencies: the width of the peak and its regularity. As the latitude approaches θ_{cr}, the width of the peak decreases (see cases 25°–28.82 N). Beyond the critical latitude, the opposite takes place: the peak widens until it splits into two peaks (see figure 4.5, case 35° N and figure 4.6, case 40° N). Another feature betraying the two subharmonics embedded in the single peak is the regularity of the peak. If there was really only one energetic frequency, the peak would be symmetric and regular as the main lobe of a spectral estimation should be. The observed irregularity signifies more complicated spectral content, not just a single frequency.

When the two peaks have blended into one, we can observe other secondary peaks, e.g. a peak

104

at $0.1\omega_0$ in case 25° N. These peaks are not an artifact solely due to leakage for two reasons. First, if those peaks were due to leakage their structure would be different for different estimations. Second, the structure of the leakage, present for example in case 25° N for $\omega \in [0.7\omega_0, 0.9\omega_0]$ is much finer than the typical distances between the secondary peaks.

The secondary peaks, in particular, the one close to the origin, can be used for an estimation of the two strongest subharmonic frequencies when their peaks are very close or blended. For example, let us consider the case 25° N when the two peaks of dominant subharmonics are on the verge of blending into one. The strongest secondary subharmonic has a value of $0.09233\omega_0$. Thus, the two dominant subharmonics can be estimated to have the following values: $0.5\omega \pm 0.0923\omega_0/2$, that is $0.4538\omega_0$ and $0.5462\omega_0$. The actually observed peaks of the dominant subharmonics have values $0.4586\omega_0$ and $0.5449\omega_0$. The dominant subharmonics predicted by the peaks in the two spectral estimations are slightly biased toward the frequency $0.5\omega_0$, which is what should happen when two peaks are superimposed. Thus, the technique provides an accurate alternative method to predict the dominant subharmonic frequencies even for the cases when the spectral resolution of the estimations is insufficient.

Taking into account the above considerations, we arrive at the following conclusion. The dominant subharmonic frequencies approach $\omega_0/2$ as the latitude approaches the critical latitude (or latitude very close to it). Above the critical latitude, subharmonics either "overshoot" and continue changing in the same direction or they start moving in reverse. Before the critical latitude, the magnitude of the dominant subharmonic frequency less than $\omega_0/2$ is larger than the magnitude of its counterpart. For the case $\theta = \theta_{cr}$, the subharmonics are different from $\omega_0/2$. Their values are approximately $0.4753\omega_0$ and $0.5207\omega_0$ and can be estimated by measuring the spectrum in different parts of the domain. Above the critical latitude, the situation is reversed: the dominant subharmonic larger than $0.5\omega_0$ has the largest magnitude. The dominant subharmonics are accompanied by a number of secondary subharmonics generated through secondary interactions of the dominant subharmonics and tidal harmonics. There is no reason to assume that other subharmonics, not visible in the spectrum, can not be generated through interaction of secondary subharmonics and so on. A cascade of such type in most cases would suggest energetic frequencies filling the frequency space densely.

Figure 4.7 demonstrates the variation of the subharmonics with latitude. Both the two dominant and secondary subharmonics are shown. The variation of one of the dominant subharmonics, except in the neighbourhood of the critical latitude where the separation of the two subharmonics was problematic, was approximated using spline interpolation. The resulting curve $\omega_1(\theta)/\omega_0$ was used (solid curve in figure 4.7) in order to predict the variation of the other subharmonics. The curve $1 - \omega_1(\theta)/\omega_0$ approximated the second dominant subharmonic. The variation of secondary subharmonics, which should be at combination frequencies, follow the curves $1 - 2\omega_1(\theta)/\omega_0$, $2\omega_1(\theta)/\omega_0$, $3\omega_1(\theta)/\omega_0 - 1$, etc.
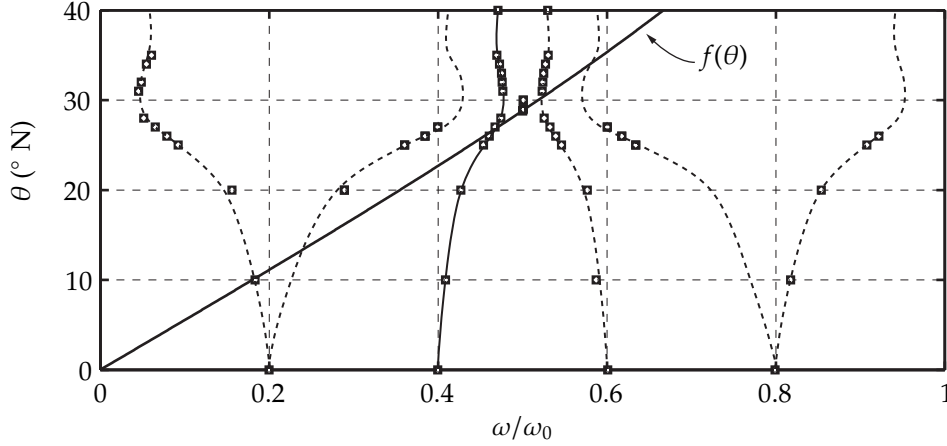
F   4.7: Variation of subharmonic frequencies with latitude: subharmonics observed in the spectra (rectangles), smoothed variation (dashed line) based on the spline interpolation of the variation of the dominant subharmonic frequency (thin solid line).

4.1.2 Amplitude of topography

Latitude is an important parameter affecting the flow. As we have seen in the previous sections, latitude defines interharmonics present in the spectrum and their strength. In this section, we consider another imporant factor affecting the flow, the topography.

First, let us consider how the amplitude of the topography affects the spectrum of the flow. For the case 20° N, we perform two additional runs. In one of the runs we use the amplitude of the topography $0.8A = 1440$ m instead of $A = 1800$ m, and in another run we use the amplitude $1.2A = 2160$ m. Figure 4.8 shows snapshots of the baroclinic velocity in the Eulerian reference frame, i.e. $u(x, z, t) - HU(t)/[H - h(x)]$, for the three comparison cases at $t = 55T_0$, where $T_0 = 12.4$ is the tidal period. As we can see the structure of the flow adjusts to the changing topography, but, does not undergo any major changes. All of the cases are supercritical and, essentially, the structure of the flow is given by the same beams, of comparable strength and width, emanating from the edges of the ridge. As the edges of the ridge, where internal waves are originally generated, move, the beam-pattern of internal waves changes, but the spectral content stays essentially the same.

Figure 4.9 compares the spectra $\Upsilon(\omega)$ for the three cases with amplitudes of topography $0.8A$, A and $1.2A$. As the amplitude of the ridge increases, the internal wave field becomes more
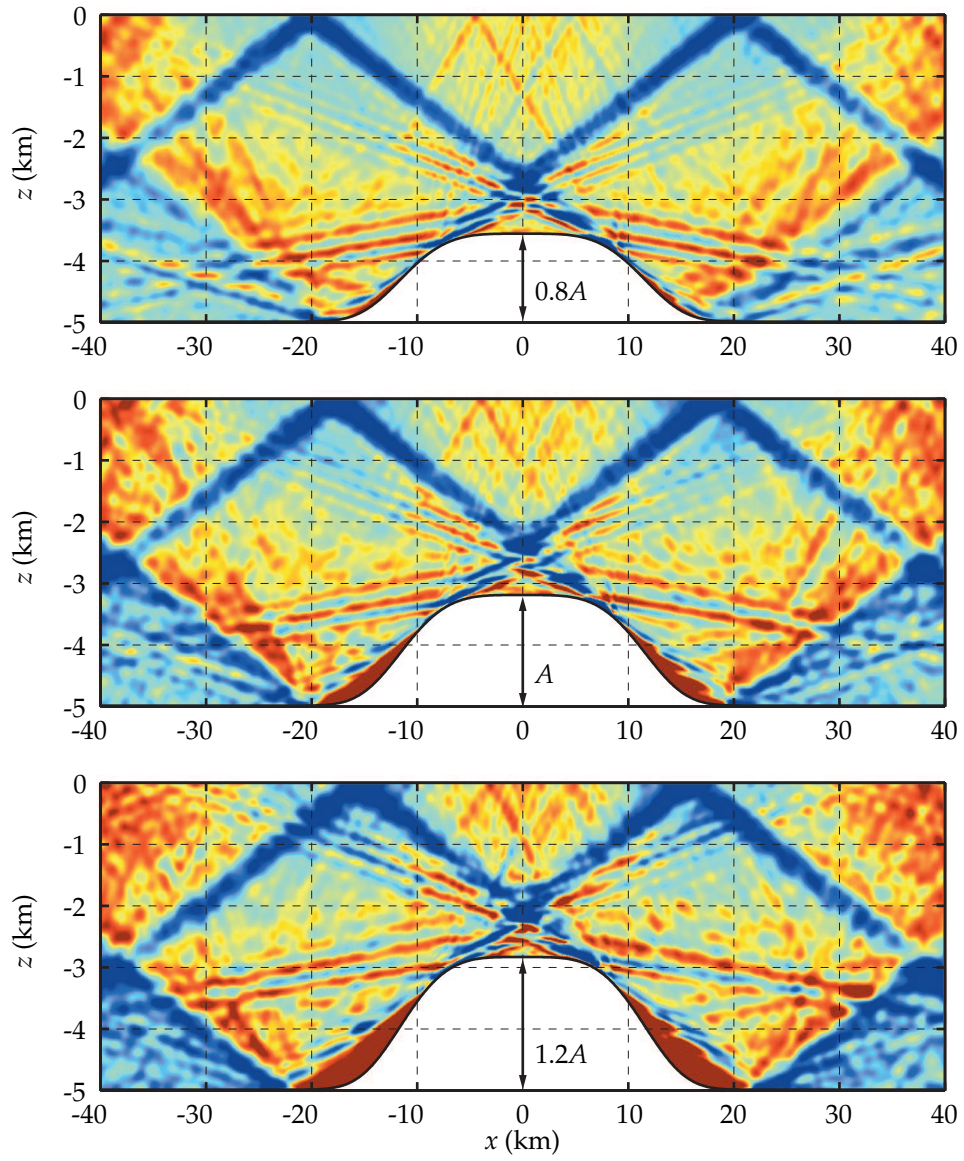
F   4.8: Baroclinic horizontal velocity at $t = 55T_0$ for different amplitudes of the ridge.
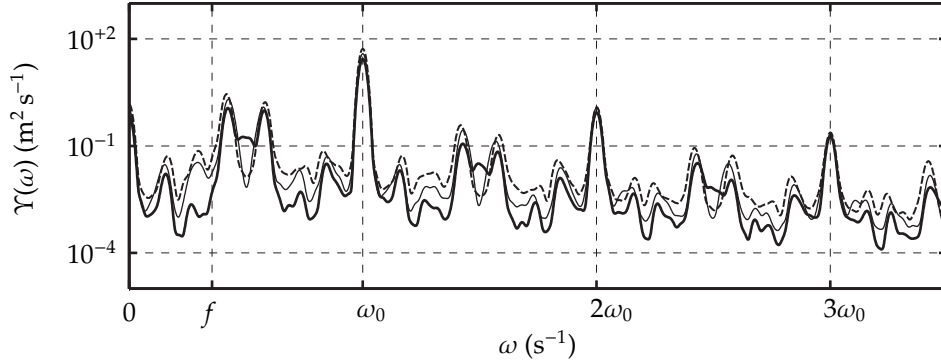
F   4.9: Comparison of the spectra $\Upsilon(\omega)$ for the case 20° N with different amplitudes of the topography: $0.8A$ (thick solid line), A (thin solid line), $1.2A$ (dashed line).

energetic. Let us compare the average power of the time series in each case. If P_0 is the average power for the case when amplitude is A, then we have:

- Case $0.8A$:

$$\int_{\omega}^{\omega_{\mathrm{Nyq}}} \Upsilon(\omega)\mathrm{d}\omega \approx 0.70 P_0,$$

- Case A:

$$\int_{\omega}^{\omega_{\mathrm{Nyq}}} \Upsilon(\omega)\mathrm{d}\omega = P_0,$$

- Case $1.2A$:

$$\int_{\omega}^{\omega_{\mathrm{Nyq}}} \Upsilon(\omega)\mathrm{d}\omega \approx 1.37 P_0.$$

This suggests that the average power in a time series on the domain $x \in [0, 40]$ km grows slightly more slowly than a quadratic function of amplitude. If the power was a quadratic function of amplitude a of the topography, then $P(a) = ca^2$ and c could be evaluated as $c = P(A)/A^2 = P_0/A^2$. This would imply $P(0.8A) = 0.64P_0$ and $P(1.2A) = 1.44P_0$ instead of $0.7P_0$ and $1.37P_0$ observed in the simulation. Note, however, that the energy flux into the region is not exactly proportional to the average power in time series due to the change of the domain.

Although the power of signals in the three cases is different, the spectral content is practically identical. As the amplitude of the topography increases, the values of interharmonics do not appreciably change. The slight shifts of the peak centres can be attributed to the change of the peak strengths. Any peak in the spectrum is affected by the leakage of a neighbouring peak. Because of leakage, the values of two close peaks are biased toward each other. As one peak grows, the centre of another one seems to be moving toward the growing peak (in the limiting

case the smaller peak becomes absorbed in the larger one). The strength of the interharmonic peaks increases as the amplitude of the topography increases. Some of the peaks grow faster than the other. For example, when the amplitude is $0.8A$, the peak at frequency just before the Coriolis frequency is weaker than the neighbouring peak on the left. When the amplitude is A, both peaks have comparable magnitude. And, finally, when the amplitude is $1.2A$, the previously stronger peak becomes the weaker.

4.1.3 Background flow

Here, we compare the spectra of the flow at $\theta = 20°$ N for the three cases with maximum tidal speed $0.8U_0 = 0.02$ m s^{-1}, $U_0 = 0.025$ m s^{-1} and $1.2U_0 = 0.03$ m s^{-1}. The three cases compare similarly as the cases with different amplitudes of topography. Figure 4.10 shows the corresponding spectra. As the background flow strengthens, the baroclinic velocities increase. The average power in the signal for each case is described by the following:

- Case $0.8U_0$:
$$\int_{\omega}^{\omega_{\text{Nyq}}} \Upsilon(\omega)\mathrm{d}\omega \approx 0.65P_0,$$

- Case U_0:
$$\int_{\omega}^{\omega_{\text{Nyq}}} \Upsilon(\omega)\mathrm{d}\omega = P_0,$$

- Case $1.2U_0$:
$$\int_{\omega}^{\omega_{\text{Nyq}}} \Upsilon(\omega)\mathrm{d}\omega \approx 1.76P_0.$$

This suggests that the average power grows with the tidal amplitude U_0 at a rate higher than that of a quadratic function.

4.1.4 Roughness of topography

Here, we consider the case $0°$ with a more realistic topography constructed using the spectrum based primarily on topographic data from the eastern central North Pacific.

The topography is constructed as follows. The "roughness" of two-dimensional topography at the bottom of the ocean is given by the power spectrum of sea-floor elevation (Bell, 1975):

$$F(k) = \frac{F_0}{k^2 + k_0^2}, \quad k \in [0, k_c], \tag{4.1}$$
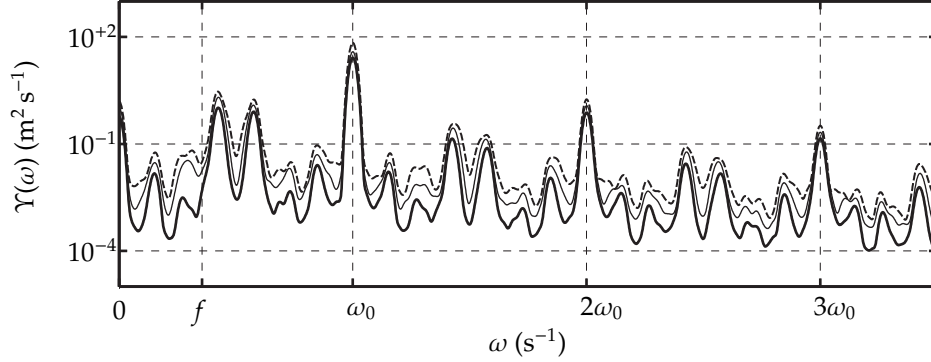
F   4.10: Comparison of the spectra $\Upsilon(\omega)$ for the case 20° N with different amplitudes of the background flow: $0.8U_0$ (thick solid line), U_0 (thin solid line), $1.2U_0$ (dashed line).

where $k_0 = 1.5708 \times 10^{-4}$ m^{-1}, $F_0 = 3.9789 \times 10^{-2}$ m and $k_c = 2\pi/400$ m^{-1} is the cut-off wavenumber corresponding to the wavelength 400 m. We truncate the domain of the spectrum $F(k)$ to wavenumbers up to $k_r = 2\pi/1000$ m^{-1} corresponding to the scales of 1 km that can be appropriately resolved using horizontal resolution of 100 m. The significant features of the spectrum are the approximate k^{-2} falloff at high wavenumbers and a flattening at low wavenumbers. Figure 4.11 demonstrates the shape of the spectrum.

For our purposes we use a discrete version of the spectrum $F(k)$:

$$F_i = F(k_i), \ k_i = i\Delta k, \ i = 1, 2, \ldots, 80, \tag{4.2}$$

where $\Delta k = 2\pi/80000$ m^{-1}. Then, the model topography corresponding to the spectrum $F(k)$ can be constructed as follows:

$$\epsilon(x) = \sum_{i=0}^{80} a_i \sin(k_i x + \phi_i), \tag{4.3}$$

where $a_i = \sqrt{2F_i \Delta k}$ is the amplitude corresponding to each wavenumber k_i, and ϕ_i is a random phase between 0 and 2π generated for each i using a uniform distribution.

In the model, we use the corrugation $\epsilon(x)$ superimposed on the topographic ridge similar to that used in most simulations. Let us define two auxiliary functions $h_1(x)$ and $h_2(x)$:

$$h_1(x) = \exp\left[-\left(\frac{x}{30000}\right)^4\right]; \tag{4.4}$$

$$h_2(x) = \exp\left[-\left(\frac{x}{12500}\right)^4\right]. \tag{4.5}$$
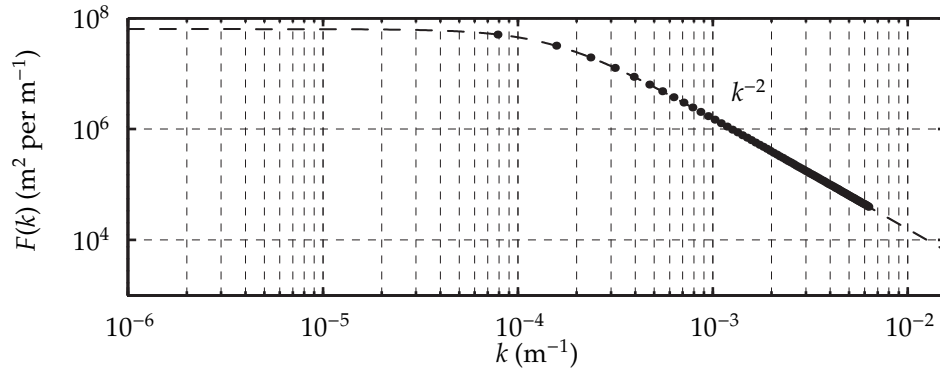
F   4.11: Power spectrum of the ocean bottom: continuous spectrum (dashed line), discretized version (dots).

Then the final corrugated topography is given by

$$h(x) = 1500h_2(x) + 300h_1(x) + \epsilon(x). \tag{4.6}$$

Figure 4.12 demonstrates the velocity field for the corrugated topography at $t = 50T_0$. The beams of tidal frequency are now scattered throughout the domain, as opposed to the case with smooth topography when there were only two pronounced beams of tidal frequency emanating from the edges of the ridge. Beams of subharmonic frequencies are not seen. Thus, adding the realistic corrugation to the topographic ridge changes both the beam pattern and the spectral content of the flow.

Figures 4.13 show the spectrum of the flow within 40 km of the ridge. The interharmonics are much weaker than in the case of smooth topography. This is because the tidal beams subject to instabilities are now much weaker: instead of two strong pronounced tidal beams at the two edges of the ridge, there are many tidal beams of lower amplitude emanating from every hump on the ridge. The dominant subharmonic peaks are no longer at frequencies $0.4\omega_0$ and $0.6\omega_0$ but at frequencies close to $0.3\omega_0$ and $0.7\omega_0$. Although it is not clear why the dominant subharmonic frequencies change so much when the topography is corrugated, the fact that they do change is important. The consequence is that in the ocean, at any given latitude, the subharmonic instabilities give rise to a continuum of subharmonics spanning $(0, \omega_0)$, solely due to the variability of topography.

111
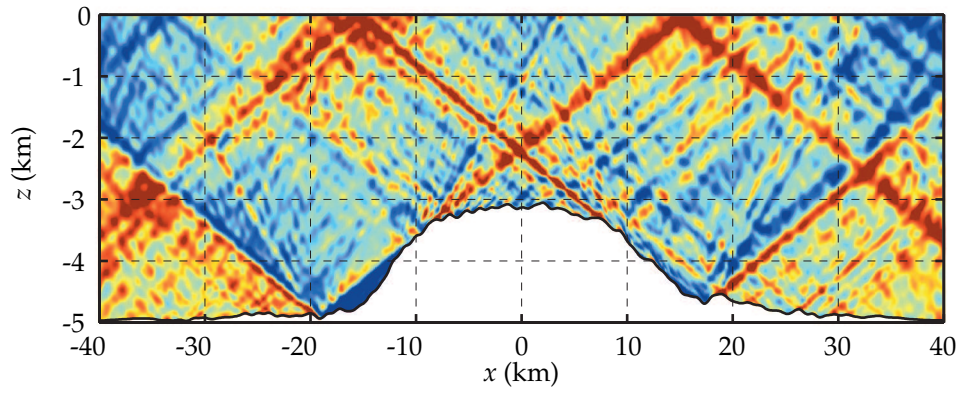
F   4.12: Baroclinic horizontal velocity at $t = 50T_0$ for the corrugated ridge.
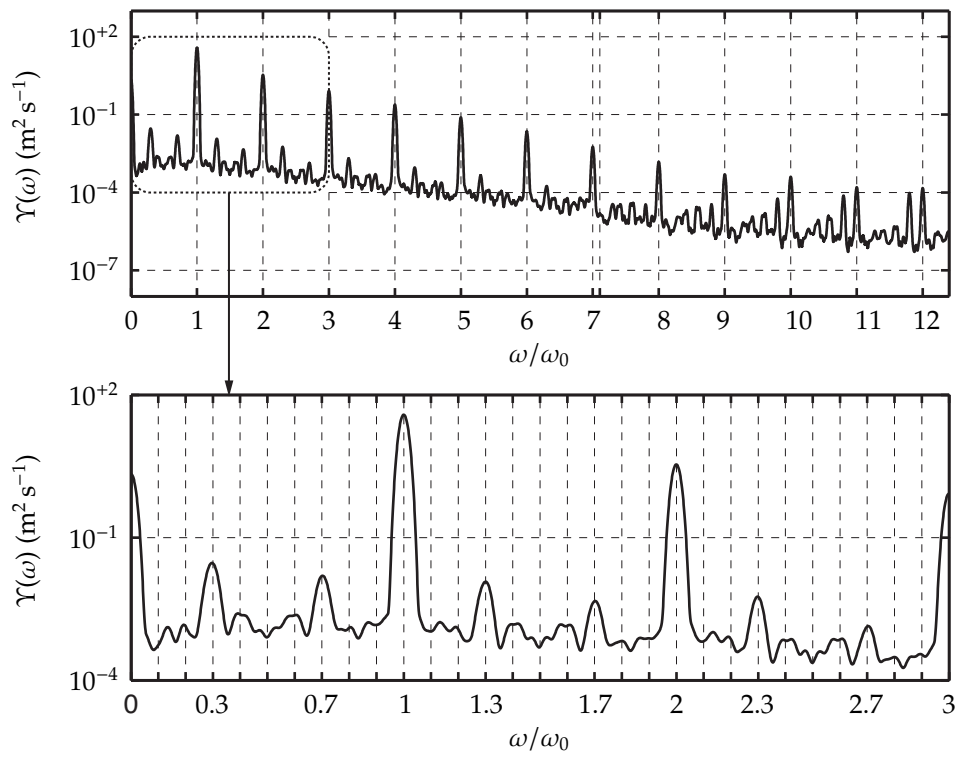
F   4.13: The spectrum $\Upsilon(\omega)$ for the case with the corrugated ridge.

112

4.2 Alternative techniques

In this section we discuss two alternative techniques for the analysis of internal wave velocities in our runs. Although the assortment of techniques for general signal analysis is large, some methods are more appropriate when dealing with internal waves. Among them, the most important are bispectral and wavelet analysis.

Bispectra can be employed to search for nonlinear triad interactions within realizations of a stochastic process. By using the bispectrum, one can also estimate energy transfers associated with each nonlinear interaction. In our runs where we have a coherent flow, the use of statistical bispectrum analysis is problematic.

Wavelets provide a flexible approach for the analysis of different scales involved in a process. Wavelet analysis for an oscillatory process is akin to the short-time Fourier transform (or spectrogram). There is a variety of different wavelet shapes, and each one leads to different analysis diagrams. It is important to choose an appropriate shape of the wavelet to obtain meaningful results. In our numerical experiments the wavelet analysis can be used as an alternative to the spectrogram. However, used this way, it does not provide any important new information. Besides, the quantitative evaluation of energetics based on wavelet analysis is problematic.

4.2.1 Bispectrum

Hasselman, Munk, and MacDonald (1963) suggested the bispectrum as a statistical tool to analyse nonlinear interaction of internal waves in the deep ocean. Since then, bispectra were found useful to detect and quantify nonlinear interactions in other applications: for example, Godfrey (1965) analysed economic time series; Lii et al. (1976) investigated energy transfers in fluid turbulence; Kim and Powers (1979) applied the bispectral analysis to plasma fluctuations.

Let $q(t)$ be a realization of a stochastic process, where time is defined on the domain $[0, T_0]$ days. The function $q(t)$ has the following Fourier representation:

$$q(t) = \sum_{n=-\infty}^{+\infty} Q_n \exp(-i\omega_n t), \tag{4.7}$$

where $\omega_n = 2\pi n / T_0$, and Q_n is the corresponding Fourier transform given by

$$Q_n = \frac{1}{T_0} \int_{t=0}^{T_0} q(t) \exp(-i\omega_n t) dt, \ n \in \mathbb{Z}. \tag{4.8}$$

Given a large number of statistically independent realizations $q(t)$, the discrete power spectrum of the stochastic process can be defined as $P(\omega_n) = \mathsf{E}\{|Q_n|^2\} = \mathsf{E}\{Q_n \overline{Q_n}\}$. The discrete

bispectrum is another spectral function, dependent on two frequncies, defined through the following:

$$B(\omega_n, \omega_m) = \mathsf{E}\{Q_n Q_m \overline{Q_{n+m}}\}, \text{ where } n, m \in \mathbb{Z}. \tag{4.9}$$

If the power spectrum selects energetic frequencies in the signal, the bispectrum selects pairs of energetic frequencies ω_n and ω_m whose sum is also an energetic frequency. If the frequencies ω_1 and ω_2 according to the power spectrum are energetic, but their combination frequency $\omega_1 + \omega_2$ is not energetic, then the bispectrum will not have a large value at (ω_1, ω_2). Evaluated for one realization of a process, the bispectrum selects all energetic triads in the signal; this, however, does not necessarily mean that they are nonlinearly interacting. The averaging over different realizations serves as a means to select nonlinearly interacting triads among random ones.

To see how the averaging selects nonlinearly interacting frequencies, let us consider the product $Q_n Q_m \overline{Q_{n+m}}$ for one realization in more detail. The product $Q_n Q_m \overline{Q_{n+m}}$ can be rewritten as

$$\begin{aligned} Q_n Q_m \overline{Q_{n+m}} &= |Q_n| e^{i\phi_n} |Q_m| e^{i\phi_m} |Q_{n+m}| e^{-i\phi_{n+m}} \\ &= |Q_n||Q_m||Q_{n+m}| e^{i(\phi_n + \phi_m - \phi_{n+m})}, \end{aligned} \tag{4.10}$$

where ϕ_n, ϕ_m and ϕ_{n+m} are the phases corresponding to frequencies ω_n, ω_m and ω_{n+m}. If the three waves are not interacting, then their phases in different realizations are independent, and the average of the product $Q_n Q_m \overline{Q_{n+m}}$ will be small. However, if the three waves do interact and are coupled nonlinearly, then their phases are dependent so that the phase sum $\phi_n + \phi_m - \phi_{n+m}$ is constant (Kim and Powers, 1979), and the average of the product $Q_n Q_m \overline{Q_{n+m}}$ has a non-zero magnitude $|Q_n||Q_m||Q_{n+m}|$.

The symmetry of the Fourier transform ($Q_n = \overline{Q_{-n}}$ for $n \in \mathbb{N}$) defines the following symmetry of the bispectrum $B(\omega_n, \omega_m)$:

$$B(\omega_n, \omega_m) = B(\omega_m, \omega_n) = \overline{B(\omega_{-n}, \omega_{-m})} = B(\omega_{-n-m}, \omega_m) = B(\omega_n, \omega_{-n-m}), \text{ for } n \in \mathbb{N}. \tag{4.11}$$

Note that for a finite number of realizations, the error in the estimation of the average $\mathsf{E}\{Q_n Q_m \overline{Q_{n+m}}\}$ is proportional to the magnitude $|Q_n||Q_m||Q_{n+m}|$, which may result in large values of the bispectrum even in those frequencies where the degree of phase-locking is low. A normalization is needed.

The bicoherence $b(\omega_n, \omega_m)$ between three waves with frequencies ω_n, ω_m and ω_{n+m} in a signal measures the degree of nonlinear coupling and is given by by the following normalization of the bispectrum:

$$b^2(\omega_n, \omega_m) = \frac{|B(n, m)|^2}{\mathsf{E}\{|Q_n Q_m|^2\}\mathsf{E}\{|Q_{n+m}|^2\}}, \quad b(\omega_n, \omega_m) \in [0, 1]. \tag{4.12}$$

The bicoherence $b(\omega_n, \omega_m)$ takes values close to unity when the wave of frequency ω_{n+m} is a result

of nonlinear interaction between waves of frequency ω_n and ω_m, and, oppositely, the bicoherence $b(\omega_n, \omega_m)$ takes values close to zero when the corresponding waves are not nonlinearly interacting. In addition, the squared bicoherence $b^2(\omega_n, \omega_m)$ quantifies the fraction of energy in frequency ω_{n+m} due to nonlinear interaction of the three waves; the fraction is given by $b^2(\omega_n, \omega_m)P(\omega_{n+m})$.

Application of the bispectral analysis for identification of nonlinearly interacting triads requires a large number of independent realizations of a stochastic process in order to identify for which frequencies the waves are phase-locked. Consequently, for our deterministic wave dynamics, the bispectral analysis, relying on statistical averaging, does not prove to be a useful technique. Suppose, we chose time-series of velocity at different spatial coordinates to be different realizations of the same process. The fluid motion is coherent everywhere, and the argument with the elimination of non-interacting triads through the use of random phases falls apart. There are no random phases. (As a matter of fact, some people viewed the coherence as the essence of a fluid motion generated by a periodic forcing, e.g. Görtler, 1943). It should be noted that in our application, there is no need to search what waves were generated through a nonlinear interaction, as we already know that all waves having frequencies different from ω_0 were generated through nonlinear interaction.

4.2.2 Wavelet analysis

Wavelet analysis has become one of the most popular tools in signal analysis. The applications are too numerous to list them all. The applications in the oceanic context include studies on the dispersion of ocean waves (Meyers et al., 1993), wave breaking (Liu, 1994) and turbulence (Farge, 1992).

The continuous wavelet transform can be constructed by analogy with the continuous Fourier transform. Using the continuous Fourier transform $F(\omega)$, the function $f(t)$ can be written as

$$f(t) = \int_{-\infty}^{+\infty} F(\omega)w(\omega, t)\, dt, \tag{4.13}$$

where $w(\omega, t) = \exp(i\omega t)$. Essentially the decomposition (4.13) means that the function $f(t)$ is constructed by dilates of the complex wave function $\exp(it)$. More generally, the function $f(t)$ can be synthesized using translated dilates of a given shape, a function $\psi(t, \tau, s)$ depending on the scale s, translation τ and time t. This idea is realized in the continuous wavelet transform defined by

$$\gamma(\tau, s) = \int_{-\infty}^{+\infty} f(t) \frac{1}{\sqrt{|s|}} \overline{\psi\left(\frac{t - \tau}{s}\right)}\, dt. \tag{4.14}$$

The synthesis equation for the continuous wavelet transform takes the following form:

$$f(t) = \frac{1}{C_\psi} \int_{-\infty}^{+\infty} \int_{-\infty}^{+\infty} \gamma(\tau,s) \frac{1}{\sqrt{|s|}} \psi\left(\frac{t-\tau}{s}\right) d\tau \frac{ds}{s^2}, \tag{4.15}$$

where

$$C_\psi = \int_{-\infty}^{+\infty} \frac{|\hat{\psi}(\zeta)|^2}{|\zeta|} d\zeta, \; C_\psi \in (0, +\infty) \tag{4.16}$$

is the admissibility constant and $\hat{\psi}$ is the Fourier transform of ψ. The continuous wavelet transform $\gamma(\tau, s)$ provides a way to separate scales in a signal and show where they are localized and what their energetics are.

When the function $f(t)$ is given by a discrete vector f_n, corresponding to the set of time moments $t_n = n\Delta t$ for $n = 0, 1, \ldots, N-1$, the continuous wavelet transform is evaluated using a piecewise constant interpolation of the function $f(t)$. For our purposes, we calculate the wavelet transform $\gamma(\tau, s)$ using a discrete set $\tau_n = n\Delta t$ and $s = 1, 2, \ldots, N$.

Let us consider a time-series of the horizontal velocity near the location of instability in the case $30°$ N. A wavelet diagram for the time-series is shown in figure 4.14. The diagram was evaluated with the Gauss wavelet of the 24th order (for the shape of the Gauss wavelet see figure 4.15). Two main scales are shown with the contour lines: the scale corresponding to the tidal frequency and the scale corresponding to a frequency close to $0.5\omega_0$. Figure 4.16 shows two cross-sections of the diagram at $s = 28$ and 56. The evolution of the two spectral components closely resembles the spectrogram shown in figure 3.32(c). Performing a power spectral estimation with respect to t for each scale s, we arrive at a frequency-scale diagram (figure 4.17) highlighting the energetic frequencies, which coincide with those provided by the power spectrum. By using different wavelets we can improve the resolution of the frequency-scale diagram. For example, figure 4.18 shows the same diagram as in figure 4.17 but for the Gauss wavelet of the 64th order (for the shape of the Gauss wavelet see figure 4.15).

Using wavelet diagrams as a primary tool for analysis of a signal is complicated by the fact that different wavelet shapes provide significantly different diagrams. In our runs, where the motion is primarily periodic the contribution from wavelet analysis is questionable.

By separating scales explicitly, wavelets provide an alternative way to extract spectral components in a signal. Let us use the frequency-scale diagram in order to check whether there are one or two strong subharmonic frequencies near $\omega_0/2$ in case $\theta = \theta_{\text{cr}}$. Using direct spectral estimation of the baroclinic velocity $u(x, z, t)$ at the vicinity of instability on top of the ridge, we obtained spectra suggesting two peaks at frequencies $0.472\omega_0$ and $0.5207\omega_0$ (figure 4.19, left panel). However, as the peaks are very close and the peak at $0.472\omega_0$ is much weaker, it is not clear whether the weaker peak is indeed there, or it is just a sidelobe corresponding to a single energetic frequency. In addition to this doubt, the spectra averaged over the total domain ($0 \leq x \leq 40$ km) show a
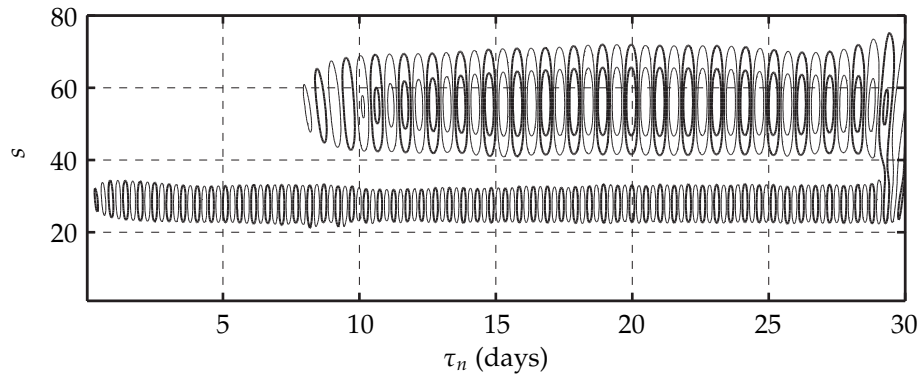
F   4.14: Wavelet diagram for the instability in case 30° N.
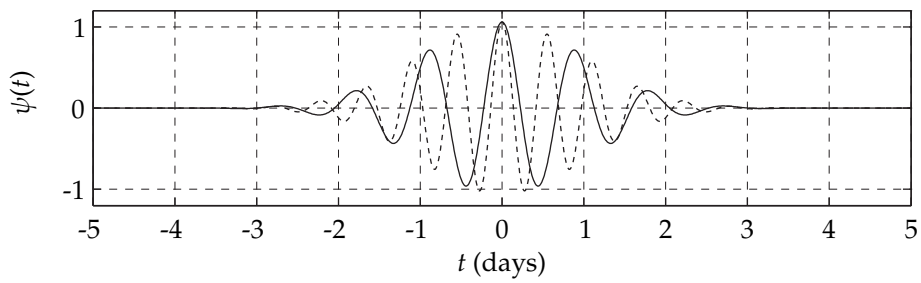
F   4.15: Shape of the Gauss wavelet function: 24th order (solid), 64th order (dashed).
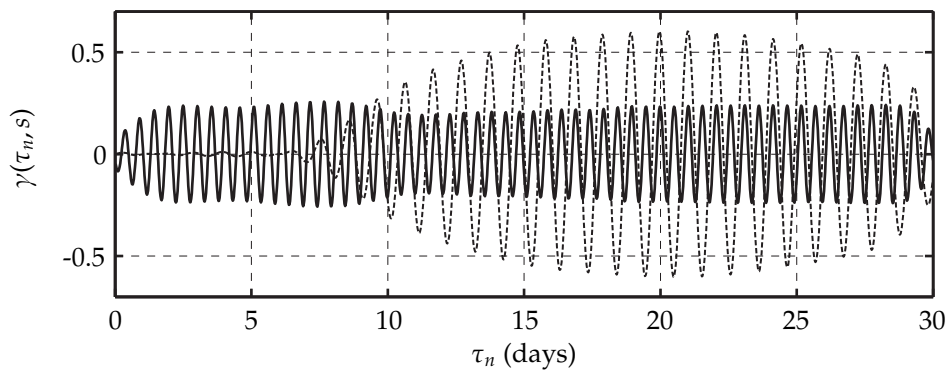
F   4.16: Wavelet coefficients $\gamma(\tau_n, 28)$ (solid line) and $\gamma(\tau_n, 56)$ (dashed line) for the instability in case 30° N.

117
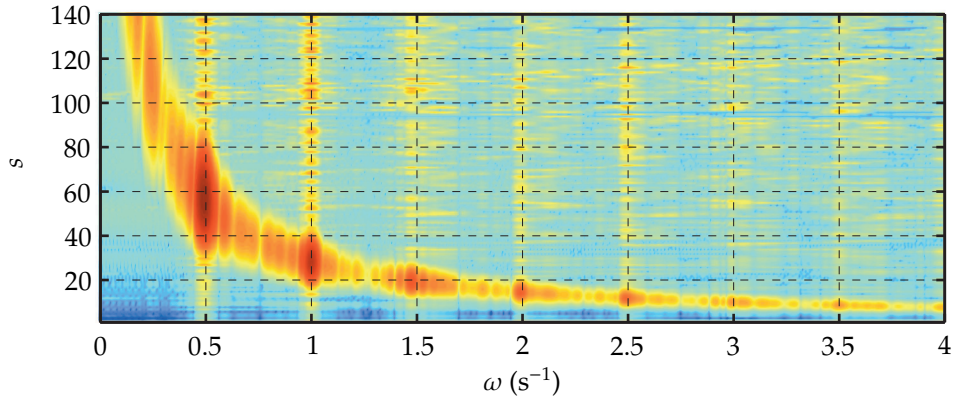
F   4.17: Frequency-scale diagram for the Gauss wavelet of 24th order.
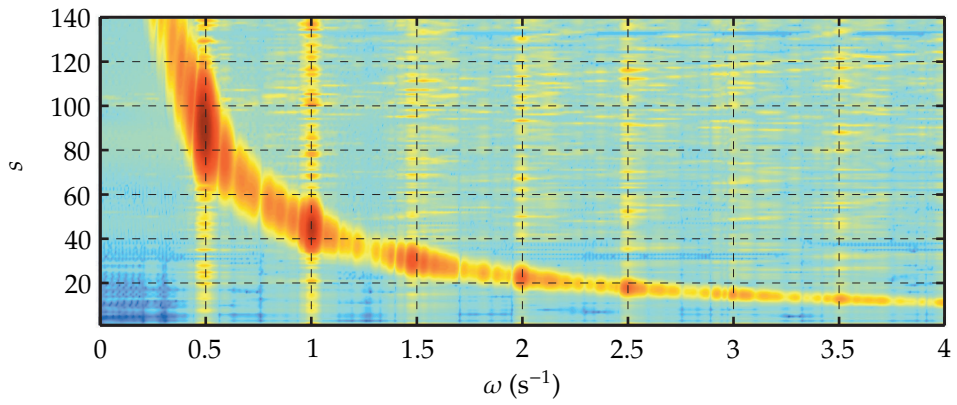
F   4.18: Frequency-scale diagram for the Gauss wavelet of 64th order.
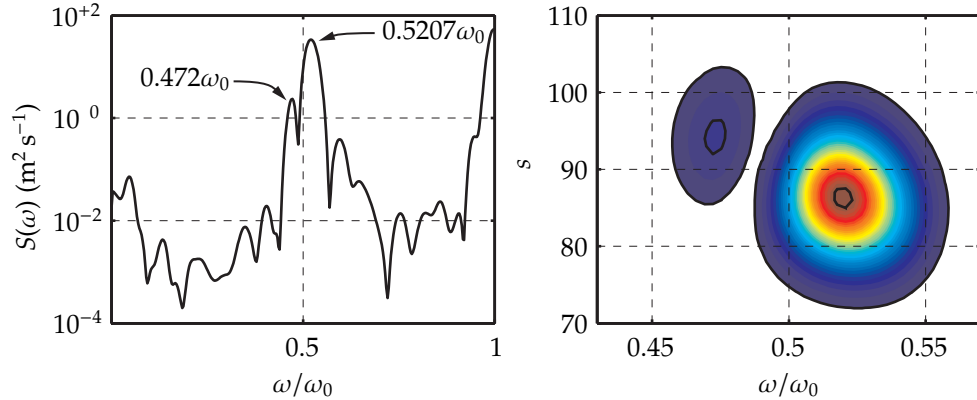
F   4.19: Close spectral peaks for the case $\theta = \theta_{cr}$: power spectral density (left panel), frequency-scale diagram (right panel).

single peak. Figure 4.19 shows a frequency-scale diagram evaluated with the Gauss wavelet of the 64th order, which clearly captures two peaks as well at nearly identical frequencies. If the smaller peak was a result of leakage only, the two peaks on the frequency-scale diagram would appear at the same scale s, which is clearly not the case.

4.3   Summary

In this chapter, we considered the dependence of the one-dimensional flow spectra on several important factors: latitude, the amplitude of topography and the strength of the background flow. The values of interharmonics change continuously with latitude. Changing the amplitude of topography or the strength of the flow by 20% (either increasing of decreasing) does not change the interharmonic frequencies significantly. As latitude becomes larger than the critical latitude, the strong subharmonics become subinertial and, thus, represent forced waves; they can no longer be generated by resonant triad interactions. We also considered the influence of roughness of topography on the subharmonics and interharmonics. Apart from reducing the magnitude of interharmonics, adding realistic roughness to the topography changes the values of the strongest interharmonic peaks. We speculated that, in the case of real topography in the deep ocean, the subharmonic instabilities of the same type as in our simulations can give rise to the waves of all subharmonic frequencies covering the frequency interval $(0, \omega_0)$.

In addition to considering various factors affecting the values of interharmonics, we considered two alternative techniques, which often appear in studies of internal waves: bispectral and wavelet analysis. We found that the use of bispectral analysis is questionable as in our runs the

flow is coherent: firstly, there is no need to filter "random" waves from the nonlinearly generated waves (as all waves are nonlinearly generated), and, secondly, the estimation of the energy transfers based on an inherently statistical approach would be poorly justified (as statistical averaging of non-random values would lead to a large bias). If the bispectral analysis was found to be an inappropriate tool for our purposes, the wavelet analysis was found to be a possible substitute for the spectrogram used in the previous chapter. However, wavelet analysis did not really provide any new information. At the same time, the use of wavelet analysis for quantitative evaluation of energetics is much more complicated than simple spectrograms. Based on these considerations, both of the alternative techniques were not used in the further research.

Chapter 5

Spatial Spectral Analysis

In the previous two chapters, we considered temporal spectral analysis of the internal wave field in our simulations. In this chapter we analyse the energy distribution with respect to spatial coordinates and spatial scales.

Given a series of snapshots of horizontal velocity, one can characterize how internal wave energy is distributed with respect to spatial/temporal coordinates, and, also, one can characterize the energetics of spatial/temporal scales involved. In this chapter we present the evolution of the following energy dependencies:

- Vertically integrated energy $E(x)$;

- Horizontally integrated energy $E(z)$;

- Depth-averaged spectrum $E(k)$;

- Horizontally averaged spectrum $E(m)$;

- Two-dimensional spectrum $E(k, m)$;

All of the dependencies above were previously used for analysis in the papers listed in table 5.1. Whenever possible we compare their results with ours. We also extended the list of the functions above by including the following dependencies:

- Spectrum $E(\omega)$ derived from the spectrum $E(k, m)$;

- Spectra $E(k, m)$, $E(k)$, $E(\omega)$ corresponding to Bell's linear solution.

Paper	Function
Hibiya et al. (1998)	$E(m)$, $E(k, m)$
Furue (2003)	$E(m)$
MacKinnon and Winters (2003)	$E(z)$, $E(k)$, $E(m)$, $E(\omega, m)$
Lamb (2006)	$E(x)$
Legg and Huijts (2006)	$E(m)$

Function	Type	Units
$E(x)$	energy	$m^3 s^{-2}$
$E(z)$	energy	$m^3 s^{-2}$
$E(k)$	power density	$m^2 s^{-2}$ per m^{-1}
$E(m)$	discrete power spectrum	$m^2 s^{-2}$ per mode
$E(k, m)$	power spectrum	$m^2 s^{-2}$ per m^{-1} per mode
$E(\omega, m)$	power spectrum	$m^2 s^{-2}$ per s^{-1} per mode
$E(\omega)$	power spectrum	$m^2 s^{-2}$ per s^{-1}
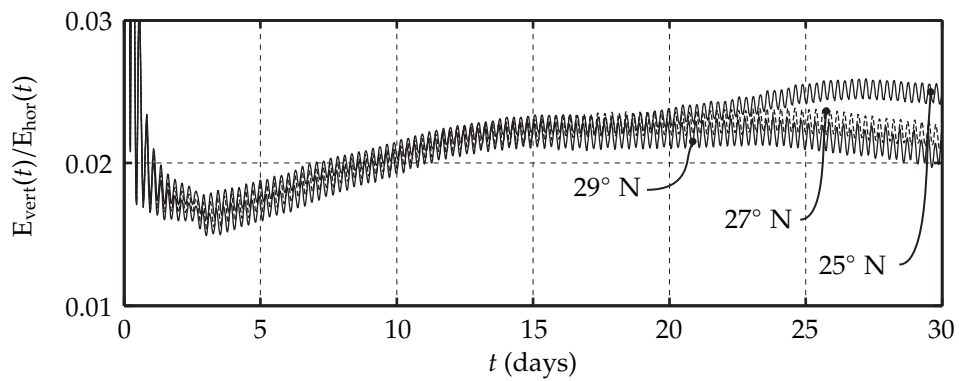
F   5.1: Ratio of the vertical and horizontal kinetic energy.

Table 5.2 classifies types of dependencies and shows their units.

In order to calculate the energy dependencies listed in table 5.2, we use only the horizontal velocity $\tilde{u}(\xi, \eta, t)$ in the barotropic-Lagrangian reference frame. The use of the horizontal component of velocity only is a common practice when energetics of an internal wave field are investigated (see, for example, papers listed in table 5.1). Energetics of the function $\tilde{u}(\xi, \eta, t)$ can be associated with the energetics of the internal wave field because the contribution to the kinetic energy from the vertical velocity is relatively small: in our runs, vertical kinetic energy constitutes less than 3% of the horizontal kinetic energy. For example, let us consider the following ratio:

$$
\begin{aligned}
E_{\text{vert}}(t)/E_{\text{hor}}(t) = \\
= \int_{z=-H}^{0} \int_{x=30\text{ km}}^{330\text{ km}} [\tilde{w}(x, z, t)]^2 \, \mathrm{d}x \, \mathrm{d}z \bigg/ \int_{z=-H}^{0} \int_{x=30\text{ km}}^{330\text{ km}} [\tilde{u}(x, z, t)]^2 \mathrm{d}x \, \mathrm{d}z,
\end{aligned}
\tag{5.1}
$$

where $\tilde{u}(x, z, t)$ and $\tilde{w}(x, z, t)$ are the horizontal and vertical velocity in the barotropic-Lagrangian reference frame with x and z defining the initial position (ξ, η). $E_{\text{vert}}(t)$ is the contribution to the kinetic energy of the baroclinic velocity field from the vertical velocity component, and $E_{\text{hor}}(t)$, from the horizontal component. As an example, figure 5.1 demonstrates the ratio $E_{\text{vert}}(t)/E_{\text{hor}}(t)$ for the case $\theta = 25°$ N. It is seen that, except for the early times when the horizontal kinetic energy E_{hor} is close to zero, the fraction of energy contributed to the baroclinic internal wave field by the vertical velocity is small. Similar values of the ratio (5.1), not exceeding 3%, were also observed for the latitudes 27° and 29° N.

5.1 Horizontal distribution of energy $E(x)$

The distribution of energy with respect to the horizontal coordinate at different periods of time signifies how energy spreads away from the main source. At earlier times the pattern of the energy spreading in the x-direction is as follows: energy is initially injected into the wave field near the ridge; as time passes, energy spreads horizontally, carried by progressive internal waves, mostly of tidal frequency; nonlinear interactions transfer energy from waves of tidal frequency to higher harmonics. There are two main factors affecting the shape of the function $E(x)$: linear dynamics of vertical modes and nonlinear dynamics of strong internal waves, occurring predominantly near sources. A vertical mode travels with the group velocity proportional to $1/l$, where l is the mode number. Thus, the low mode energy arrives first. Hence the gradually decaying shape of the function $E(x)$ during the earlier stages of the flow development. As the energy in higher modes arrives to remote locations further away from the ridge, the shape of the function $E(x)$ becomes less steep. In the cases 0°, 10°, 20° and 40°, where the nonlinear interactions are comparatively weak, the vertical mode dynamics predefines the shape of the function $E(x)$.
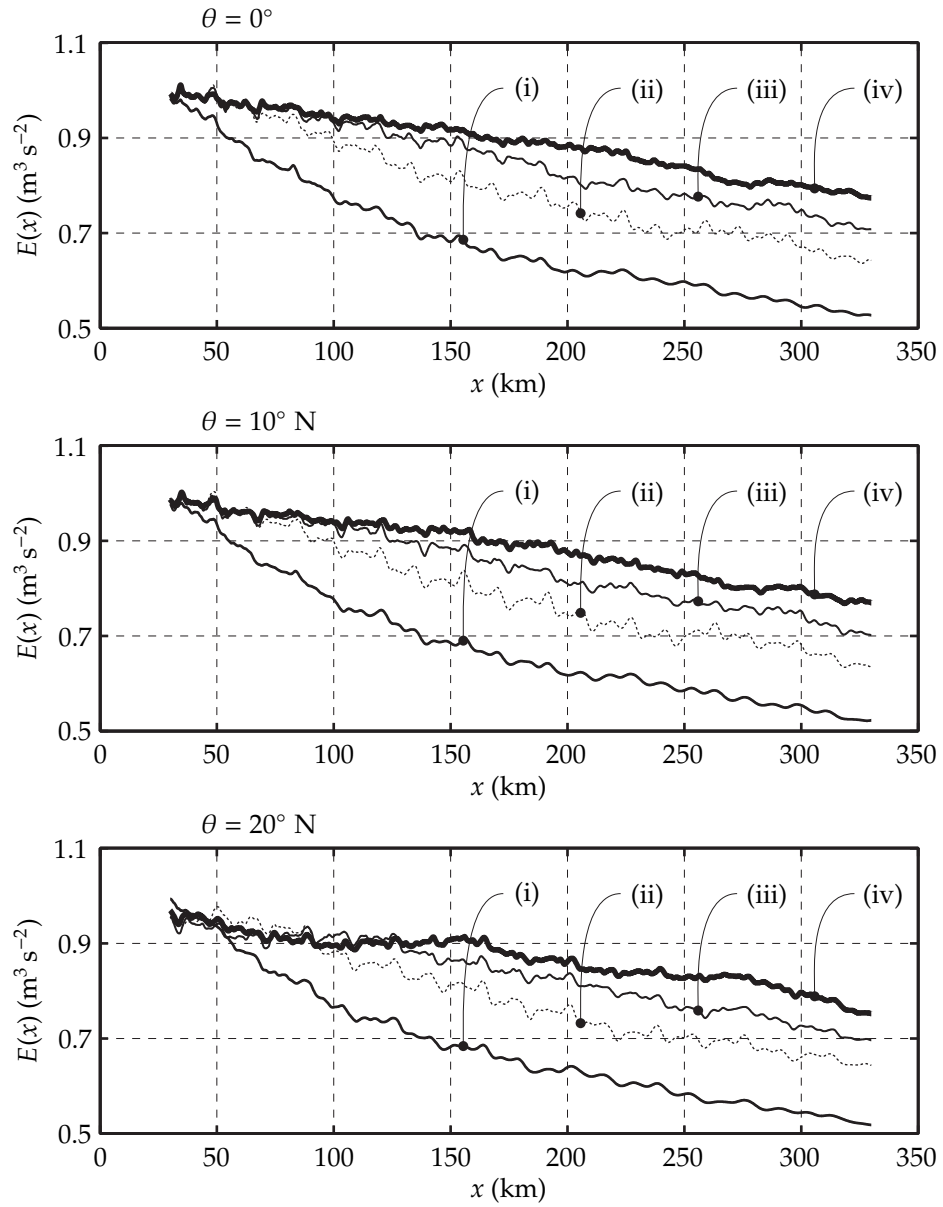
F   5.2: Vertically integrated kinetic energy as a function of x averaged over the following time intervals: (i) $[10T_0, 15T_0]$, (ii) $[20T_0, 25T_0]$, (iii) $[30T_0, 35T_0]$, (iv) $[40T_0, 45T_0]$.
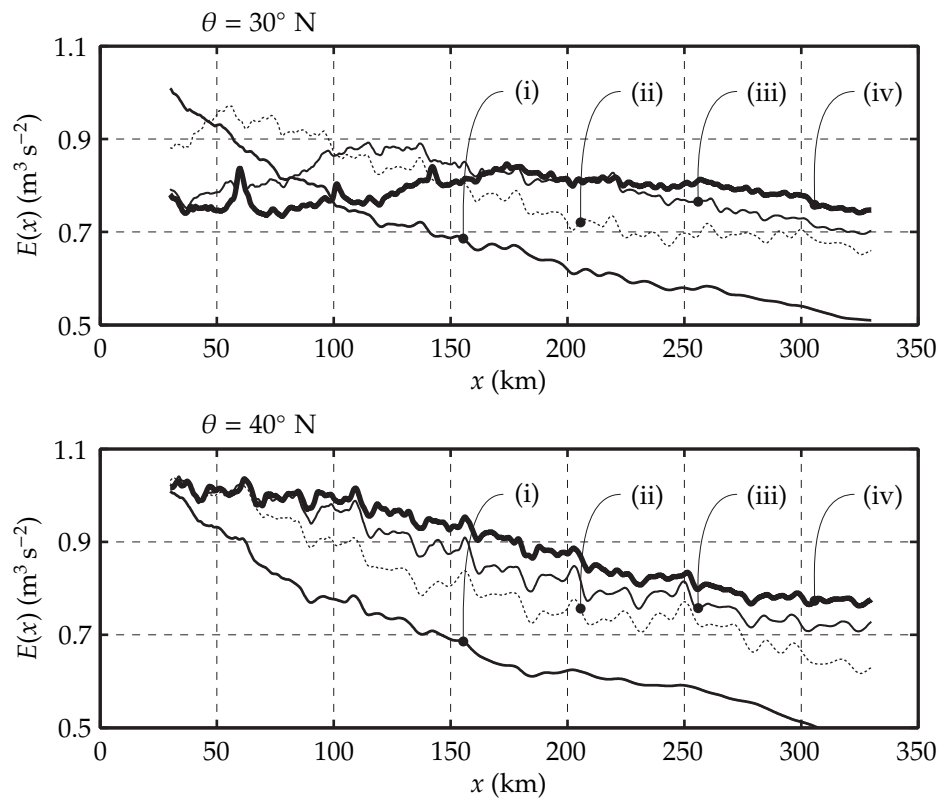
F   5.3: Vertically integrated kinetic energy as a function of x averaged over the following time intervals: (i) $[10T_0, 15T_0]$, (ii) $[20T_0, 25T_0]$, (iii) $[30T_0, 35T_0]$, (iv) $[40T_0, 45T_0]$.

For the near-critical latitudes at later times, when the highly nonlinear regions of the flow become dominated by trapped waves of subinertial frequencies, another pattern of horizontal distribution of energy emerges: progressive waves of tidal frequency already generated, propagate away, and energy accumulates in the vicinity of the strongly nonlinear regions. In other words, after the instabilities set in, the energy flux into the region $30 \lessgtr x \lessgtr 150$ km is less than the energy flux out of that region. Most of the energy is, thus, trapped in the vicinity of the ridge ($-20 \lessgtr x \lessgtr 20$ km), and the function $E(x)$ starts rapidly decaying in the region $30 \lessgtr x \lessgtr 150$ km. However, at the coordinates x corresponding to the highly nonlinear regions, e.g. where the tidal beam hits the surface or bottom, the energy is accumulated in the forced waves and the peaks in the profile $E(x)$ emerge. For example, in case $30°$ N, the tidal beams are reflected from the boundaries at $x \approx 60, 100, 140$ km; at these coordinates the function $E(x)$ has pronounced peaks (see figure 5.3, $\theta = 30°$ N).

To quantify the evolution of horizontal distribution of energy, we consider the vertically integrated kinetic energy (based on the horizontal baroclinic velocity $\tilde{u}(x, z, t)$) averaged over different time intervals:

$$
\begin{aligned}
E(x) = \langle E(x, t) \rangle_{t \in [T_1, T_1 + 5T_0]} &= \left\langle \int_{-H}^{0} |\tilde{u}(x, z, t)|^2 \, \mathrm{d}z \right\rangle_{t \in [T_1, T_1 + 5T_0]} \\
&= \frac{1}{5T_0} \int_{t=T_1}^{T_1 + 5T_0} \int_{z=-H}^{0} |\tilde{u}(x, z, t)|^2 \, \mathrm{d}z \, \mathrm{d}t,
\end{aligned}
\tag{5.2}
$$

where T_1 was chosen to be $10, 20, 30$ and 40 tidal periods, to illustrate the evolution. Averaging was used in order to eliminate high-amplitude variation in the function $E(x)$ dependent on the phase of the tidal flow. The function $\langle E(x, t) \rangle_{t \in [T_1, T_1 + 5T_0]}$ was calculated on the interval $x \in [30, 330]$ km using the following numerical approximation:

$$
E(x_i) = \langle E(x_i, t) \rangle_{t \in [T_1, T_1 + 5T_0]} \approx \frac{\Delta t}{5T_0} \sum_{n=T_1/\Delta t}^{(T_1 + 5T_0)/\Delta t - 1} \sum_{j=0}^{J-1} |\tilde{u}_{ij}^n|^2 \Delta z,
\tag{5.3}
$$

$$
x_i = -L_{\mathrm{cent}}/2 + (i + 1/2)\Delta x,
\tag{5.4}
$$

where $\Delta z = 26.042$ m, $\Delta x = 100$ m and the index i corresponds to horizontal coordinates $x_i \in [30, 330]$ km.

Figures 5.2–5.3 show the horizontal energy distribution $E(x)$ for the latitudes $\theta = 0°, 10°, 20°$, $30°$ and $40°$ N. For the latitudes other than $30°$ N, the following statements are true:

(i) Energy distribution $E(x)$ is gradually decaying with x;

(ii) Energy tends to a quasi-stable level, which is only reached for the regions close to the ridge;

(iii) The shape of the function $E(x)$ is close to linear.

126

As the waves generated near the ridge can freely propagate to the left and right, we should expect the energy distribution to be uniform with respect to x at large times. However, due to the numerical dissipation, the distribution $E(x)$ does not converge to a uniform distribution, but to a quasi-linear slowly decaying function.

The case 30° N differs from others as none of the statements (i)–(iii) above is true. In the case of the tidal-to-subtidal conversion, happening at the latitude $\theta = 30°$ N, most of the waves of subtidal frequency are trapped near their generation sites. Hypothetically, after a long time these sites could become mixing spots as the energy would grow there to a very large extent. A similar phenomenon was, in fact, observed experimentally by Teoh et al. (1997).

5.2   Vertical distribution of energy $E(z)$

The vertical distribution of energy $E(z)$ characterizes the vertical structure of the horizontal current in the internal wave field. In the linearly stratified fluid away from the topography, the vertical structure is dominated by normal modes, which correspond to the exact solutions of the linear hydrostatic equations of motion. Under the rigid lid approximation, the vertical modes are given by the following cosine distribution (Kundu and Cohen, 2002):

$$\psi_l = \cos \frac{\pi l z}{H}, \; l = 0, 1, \ldots \tag{5.5}$$

and the correspondings representation of horizontal velocity $u(x, z, t)$ is given by

$$u(x, z, t) = \sum_{l=0}^{+\infty} a_l \psi_l(z). \tag{5.6}$$

In our case, the predominance of vertical modes in the profile of $\tilde{u}(x, z, t)$ results in a symmetrical profile of energy $E(z)$.

To quantify the evolution of vertical distribution of energy, we consider the horizontally integrated kinetic energy (based on the horizontal baroclinic velocity $\tilde{u}(x, z, t)$) averaged over different time intervals:

$$
\begin{aligned}
E(z) = \langle E(z, t) \rangle_{t \in [T_1, T_1 + 5T_0]} &= \left\langle \int_{30 \text{ km}}^{330 \text{ km}} |\tilde{u}(x, z, t)|^2 \mathrm{d}x \right\rangle_{t \in [T_1, T_1 + 5T_0]} \\
&= \frac{1}{5T_0} \int_{t=T_1}^{T_1 + 5T_0} \int_{x=30 \text{ km}}^{330 \text{ km}} |\tilde{u}(x, z, t)|^2 \mathrm{d}x \, \mathrm{d}t,
\end{aligned}
\tag{5.7}
$$

where the initial time of each time interval T_1 was chosen to be ten and forty tidal periods, to illustrate the evolution. The curves evaluated for the intermediate time intervals lie between
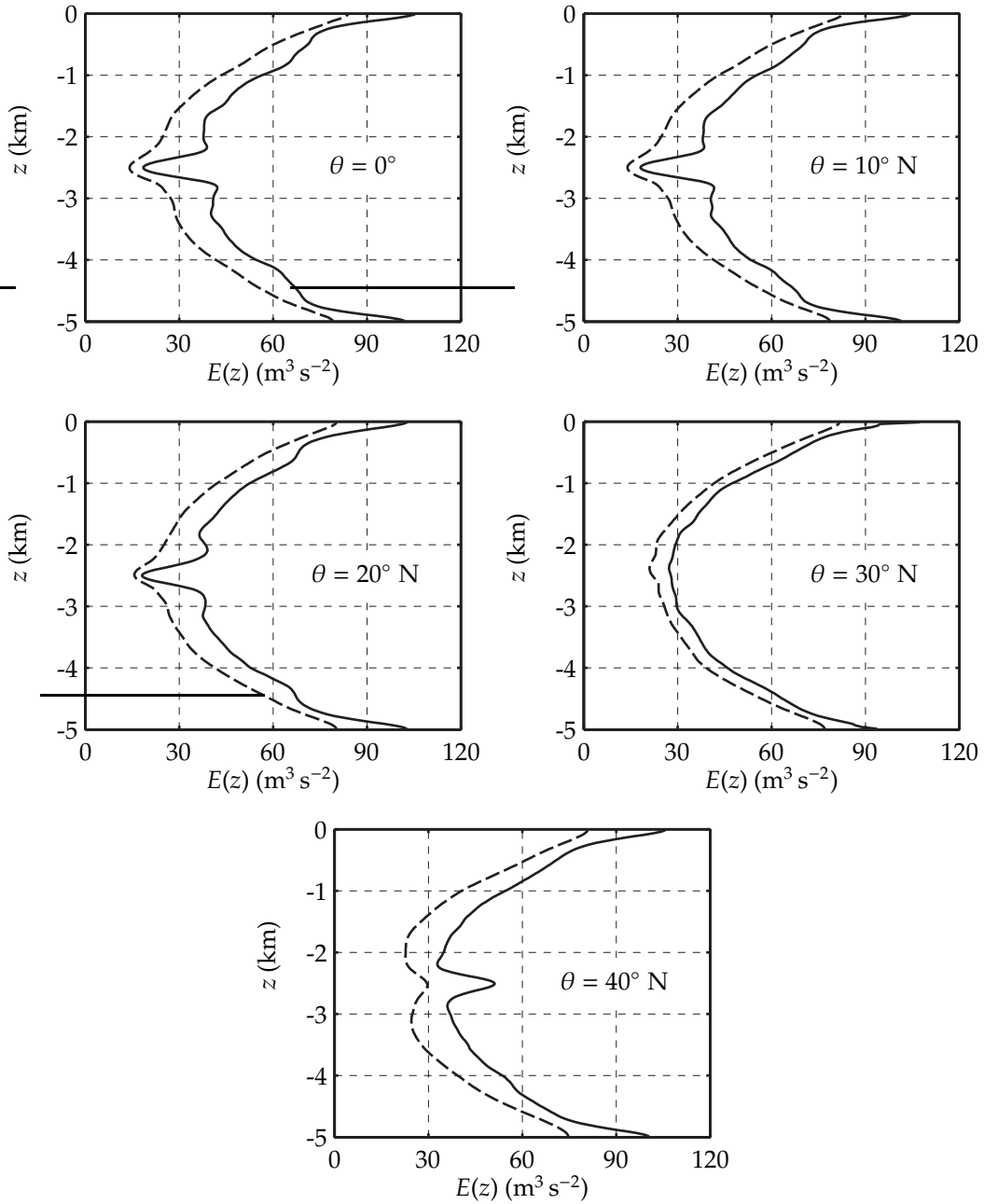
F   5.4: Kinetic energy integrated over $x \in [30, 330]$ km as a function of z averaged over the time intervals $[5T_0, 10T_0]$ (dashed line) and $[40T_0, 45T_0]$ (solid line).

the shown curves. The function $\langle E(z) \rangle_{t \in [T_1, T_1 + 5T_0]}$ was calculated using the following numerical approximation:

$$E(z_j) = \left\langle E(z_j, t) \right\rangle_{t \in [T_1, T_1 + 5T_0]} \approx \frac{\Delta t}{5T_0} \sum_{n = T_1/\Delta t}^{(T_1 + 5T_0)/\Delta t - 1} \sum_i |\tilde{u}_{ij}^n|^2 \Delta x, \tag{5.8}$$

$$z_j = -H + \left(j + \frac{1}{2} \right) \Delta z, \ j = 0, 1, \ldots, J - 1. \tag{5.9}$$

Here $\Delta z = 26.042$ m, $\Delta x = 100$ m, and the summation over the index i is performed for all i such that $x_i \in [30, 330]$ km.

Figure 5.4 demonstrates the horizontally integrated kinetic energy $E(z)$. The shape of the function $E(z)$ follows from the vertical mode structure. The modal decomposition will be discussed in more detail in one of the following sections dedicated to investigation of typical vertical scales. Here, we consider the consequences of the modal structure on the function $E(z)$. Mode $n = 1$ is the dominant mode for all cases, so energy is concentrated near the bottom and top of the domain, as the first mode of the horizontal velocity $u(x, z, t)$ is proportional to $\cos(\pi z/H)$. Note, that the first mode of the vertical velocity $w(x, z, t)$ and density $\rho(x, z, t)$ is proportional to $\sin(\pi z/H)$, and, thus, the shape of the vertical kinetic energy and potential energy would have maxima at mid-depth $z = -H/2$.

For $\theta < \theta_{cr}$, odd modes seem to dominate the flow, which results in a sharp, narrow minimum of $E(z)$ at $z = -H/2$. For $\theta \approx \theta_{cr}$, the profile $E(z)$ becomes smooth without a sharp minimum, which may suggest a smooth gradual decay of energy with respect to modes. Lastly, for $\theta > \theta_{cr}$, even modes come into play; $E(z)$ at $z = -H/2$ now has a peak.

5.3 Typical horizontal scales

To identify typical horizontal scales, we calculate the power spectrum $E(k, t)$ by applying the following operations to the baroclinic velocity $\tilde{u}(x, z, t)$ with $x \in [30, 330]$ km, $z = [-H, 0]$ and $t \in [0, 30]$ days:

I. Spectral estimation in the horizontal: $\tilde{u}(x, z, t) \rightarrow E(k, z, t)$;

II. Averaging in the vertical: $E(k, z, t) \rightarrow E(k, t)$.

The resulting spectrum $E(k, t)$ is a depth-averaged spectrum of horizontal kinetic energy. The function $E(k, t)$ is calculated using the following numerical approximation, which involves direct
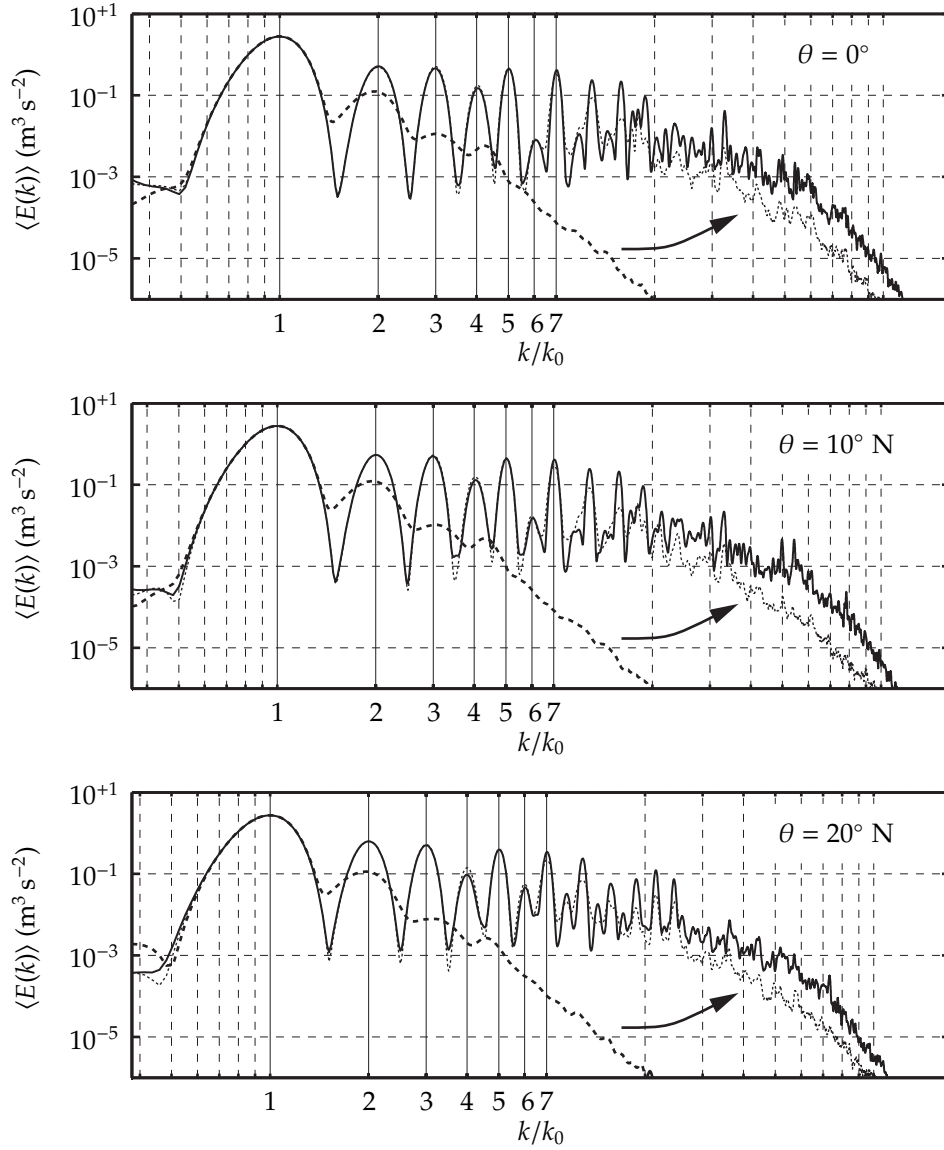
F   5.5: Development of the depth-averaged spectrum of horizontal kinetic energy as a function of horizontal wavenumber k (k_0 is the wavenumber corresponding to the tidal beam bouncing up and down once in the deep water). The spectra were for the times $5T_0$, $25T_0$ and $45T_0$, where $T_0 = 12.4$ hrs, and latitudes $0°$, $10°$ and $20°$ N. The arrow shows the direction of development.
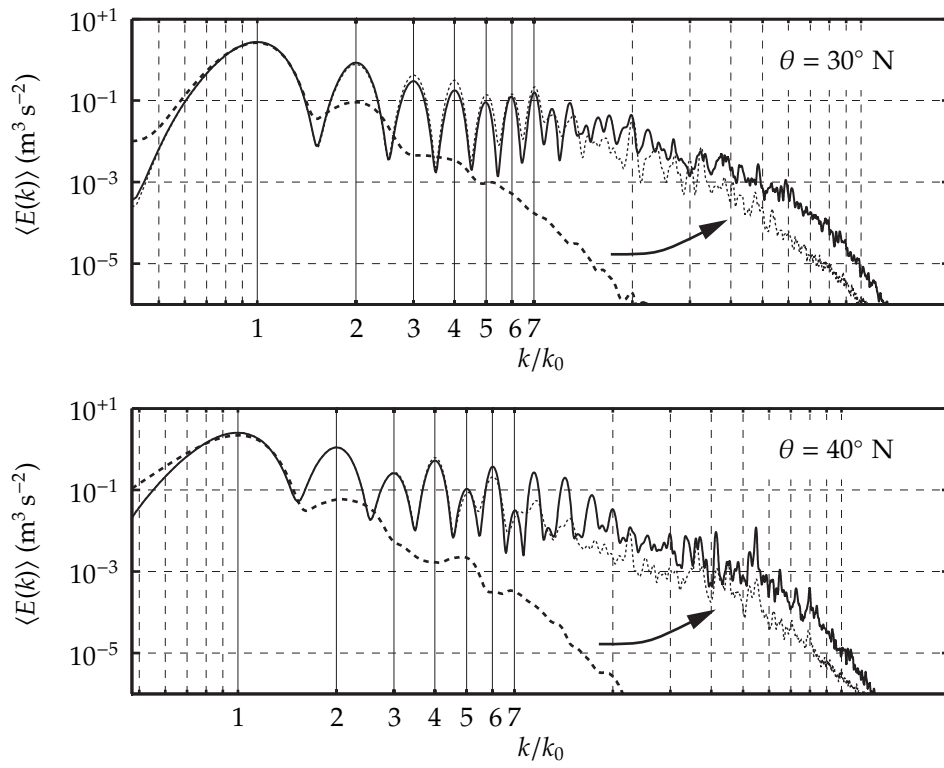
F   5.6: Same as figure 5.5 but for latitudes 30° and 40° N.

spectral estimation in the horizontal:

$$E(k, t_n) \approx \frac{\Delta z}{H} \sum_{j=1}^{J} \frac{\Delta x}{\pi} \left| \sum_i g_i \tilde{u}_{ij}^n \exp(-\mathrm{i}k x_i) \right|^2 , \tag{5.10}$$

where $n = 0, 1, \ldots, N - 1$ and the summation over the index i is performed for all i such that $x_i \in [30, 300]$ km. The window $\{g_i\}$ was chosen to be a discrete prolate spheroidal sequence of the second order, i.e. corresponding to the bandwidth of four Fourier sampling frequencies: $8\pi/(300, 000 \text{ m}) \approx 8.3776 \times 10^{-5} \text{ m}^{-1}$. The performance of the chosen window was found optimal in terms of visible leakage in comparison with discrete prolate spheroidal sequences of the first and third order.

Figures 5.5 and 5.6 demonstrate the spectrum $E(k, t)$ for different times.

MacKinnon and Winters (2003), whose numerical simulations we described earlier, compare early and late depth-averaged spectra of horizontal kinetic energy as a function of horizontal wavenumber. At the beginning this spectrum shows the dominant horizontal wavenumber with which they force their simulations and, also, peaks at what could be the multiples of that wavenumber. At a later stage (after 82 tidal periods), their spectrum becomes mostly smooth without pronounced peaks at characteristic wavenumbers. In contrast to their observations, our estimations of the same spectrum (covering a significantly larger range of wavenumbers) demonstrate clearly that energy tends to occupy multiples of the horizontal wavenumber k_0 corresponding to mode-one tidal frequency waves (or the internal tidal beam bouncing up and down in the deep water). The wavenumber k_0 in our simulation ranges from 6.6×10^{-5} m^{-1} at $\theta = 40°$ N to 8.9×10^{-5} m^{-1} at $\theta = 0°$, which means that it is from 7 to 9 times smaller than the forcing wavenumber k_{x_0} of MacKinnon and Winters. Starting with the wavenumber k_0, energy tends to fill higher and higher multiples of k_0. It approaches a certain "steady" spectrum, which does not change in time much. The discrete nature of our spectrum *vs.* the continuous nature of the estimation by MacKinnon and Winters can be explained by the fact that they have explicit dissipation terms in their governing equations. According to MacKinnon and Winters, most of the transition between the narrow and broad spectral shapes occurs when the dissipation becomes significant.

5.4   Typical vertical scales

To identify typical vertical scales, we calculate the power spectrum $E(m, t)$ by applying the following operations to the baroclinic velocity $\tilde{u}(x, z, t)$ with $x \in [30, 330]$ km, $z = [-H, 0]$ and $t \in [0, 30]$ days:
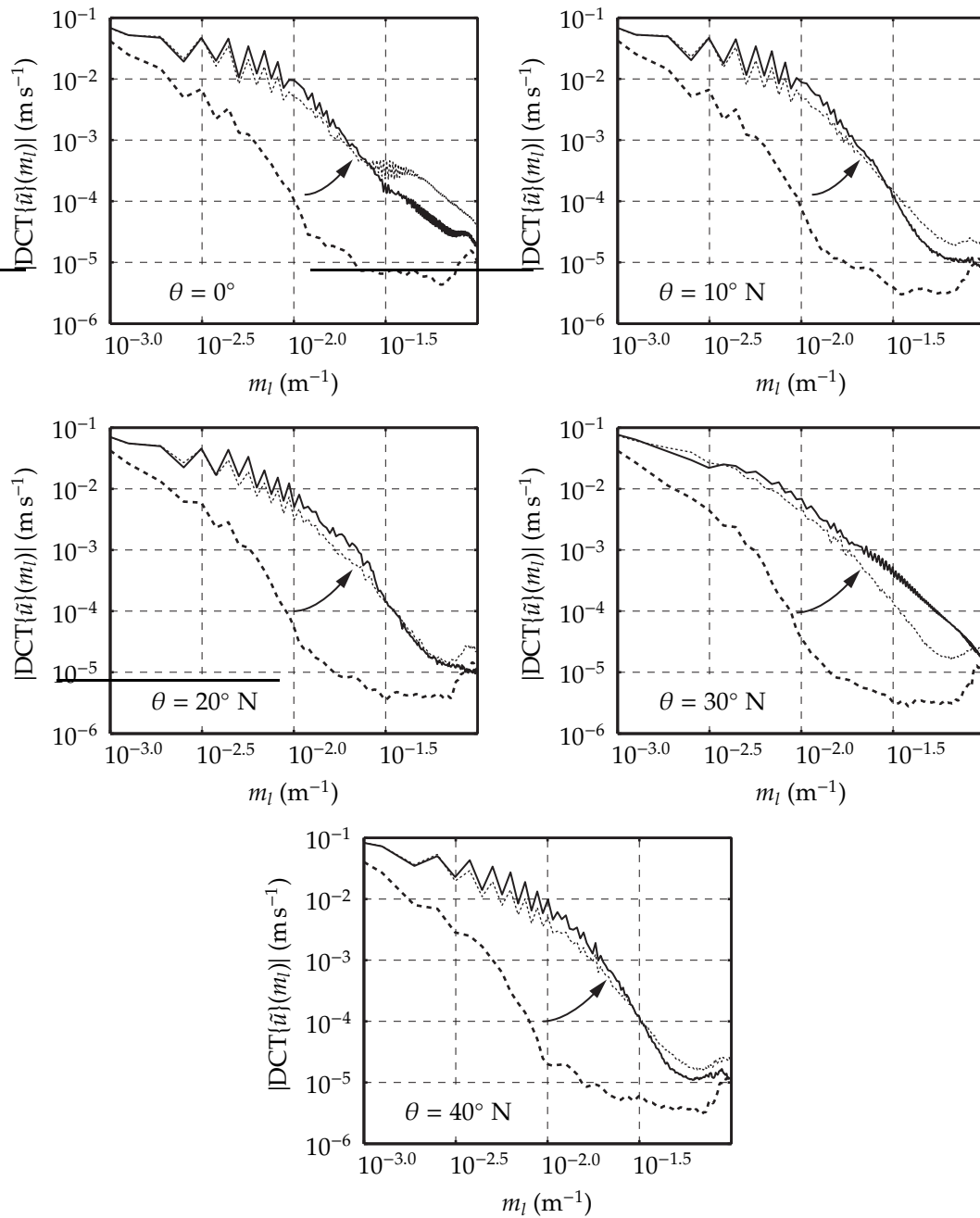
F   5.7: Evolution of the horizontally averaged discrete cosine transform of the horizontal velocity. The spectra were calculated for the following times: $5T_0$, $25T_0$ and $45T_0$. The arrow shows the direction of evolution.

I. Spectral estimation in the vertical: $\tilde{u}(x, z, t) \to E(x, m_l, t)$;

II. Averaging in the horizontal: $E(x, m_l, t) \to E(m_l, t)$.

The resulting spectrum $E(m_l, t)$ is a horizontally averaged power spectrum of horizontal kinetic energy with respect to the discrete wavenumbers $m_l = \pi l / H$, where $l = 0, 1, \ldots, J - 1$. The function $E(m_l, t)$ is calculated using the following numerical approximation, which involves a discrete cosine transform in the vertical:

$$E(m_l, t_n) = \left\langle \frac{1}{N} \left| \mathsf{DCT}\{\tilde{u}_{ij}^n\}(x_i, m_l, t_n) \right|^2 \right\rangle_{x_i \in [30, 330] \text{ km}}, \tag{5.11}$$

where the discrete cosine transform is defined by the following:

$$\mathsf{DCT}\{\tilde{u}_{ij}^n\}(x_i, m_l, t_n) = \beta(l) \sum_{j=0}^{J-1} \tilde{u}_{ij}^n \cos\left[(z_j + H)m_l\right], \quad l = 0, 1, \ldots, J - 1, \tag{5.12}$$

and

$$\beta(l) = \begin{cases} \sqrt{1/J}, & l = 0; \\ \sqrt{2/J}, & l = 1, 2, \ldots, J - 1. \end{cases} \tag{5.13}$$

The discrete cosine transform in the vertical has a simple interpretation: it is proportional to the amplitudes of the normal modes a_l. Figure 5.7 shows absolute values of the horizontally averaged discrete cosine transform of the matrix $\tilde{u}_{ij}^n$, at the following time moments: $5T_0$, $25T_0$, $45T_0$. As the velocity is defined on a vertically bounded domain, the DCT transform is an accurate way to define the spectrum, as no assumptions about the function outside the boundaries have to be made. The DCT provides the typical leakage decay rate of n^{-2} (compared to the DFT decay rate of n^{-1}). In some situations this decay rate is sufficient to observe the most important spectrum features (see, for example, Bertrand and Laprise, 2002). In most cases, however, when the amount of energy in small-scale features is small, the power law decay n^{-2} would render those features invisible in the spectrum.

The DCTs shown in figure 5.7 have a typical zigzag shape confirming that for cases $\theta < \theta_{\mathrm{cr}}$ odd modes dominate the vertical structure of the velocity field, and for cases $\theta > \theta_{\mathrm{cr}}$, even modes do. For example, let us consider the fifth mode that has the vertical wavenumber of $5\pi/H \approx 10^{-2.5}$ m^{-1} that coincides with one of the grid lines in the axes of figure 5.7. For cases $\theta < \theta_{\mathrm{cr}}$ the fifth mode is larger than the surrounding modes four and six and for cases $\theta < \theta_{\mathrm{cr}}$ it is smaller.

The vertical structure of the velocity field, just like the horizontal structure, tends to a quasi-stable state: the averaged DCT transforms taken at time moments separated by equal time intervals reveal the convergence.

Typical vertical scales at different stages of an internal wave fluid motion were previously analyzed in papers by Hibiya et al. (1998); Furue (2003); MacKinnon and Winters (2003, 2005). Different authors used different approaches in order to characterize vertical scales of internal wave fields. Hibiya et al., for example, considers the time variations of the horizontally averaged Froude spectrum. In the paper, the Froude spectrum has the following somewhat obscure definition: "the vertical wavenumber spectrum of the vertical shear of horizontal current velocity normalized by the square of background buoyancy frequency". As it is not clear what exactly is meant by "the wavenumber spectrum" (energy spectrum, power spectrum, amplitude spectrum, etc.), we can only assume, judging by the discrete appearance, that the spectrum was given by the squared amplitudes of a Fourier series. In our simulations, the vertical shear of horizontal velocity at any fixed x and t can be written using the normal mode decomposition:

$$\frac{\partial u(z)}{\partial z} = -\sum_{l=0}^{+\infty} a_l m_l \sin(m_l z). \tag{5.14}$$

Thus, the Froude spectrum is given by $|a_l m_l|^2/N_b^2$; the Froude spectrum is proportional to the spectrum $E(m_l, t_n)$ and the squared discrete cosine transform (both multiplied by m_l^2). Essentially, all the important information comes from the discrete cosine transform. Hibiya et al. (1998) considers the Froude spectrum in a quasi-equilibrium state and in most of their numerical experiments the spectrum is nearly uniform in time. Our spectrum seems to be approaching a shape that is qualitatively similar to the one observed by Hibiya et al.: energy at wavenumbers within the range $[10^{-2.5}, 10^{-1.5}]$ m^{-1} grows to a quasi-steady level.

In the papers by MacKinnon and Winters (2003, 2005) the vertical wavenumber spectrum has a similar evolution as that of the horizontal wavenumber spectrum: initially, energy is concentrated around the forcing wavenumber, and after eighty tidal periods it has spread out to a wide range of scales.

5.5 Two-dimensional spectra $E(\omega, m_l)$

The time variation of the distribution of energy with respect to the frequency and vertical wavenumber helps to understand energy transfers within the spectrum. In particular, it helps to clarify at what vertical scales the interharmonics are generated, and what frequencies (harmonics or interharmonics) are more susceptible to mixing, due to their small vertical scales.

Figures 5.8, 5.9 show two-dimensional spectra of horizontal velocity as a function of frequency and vertical wavenumber. The spectrum $E(\omega, m_l)$ is obtained by

- applying the DCT in the vertical;
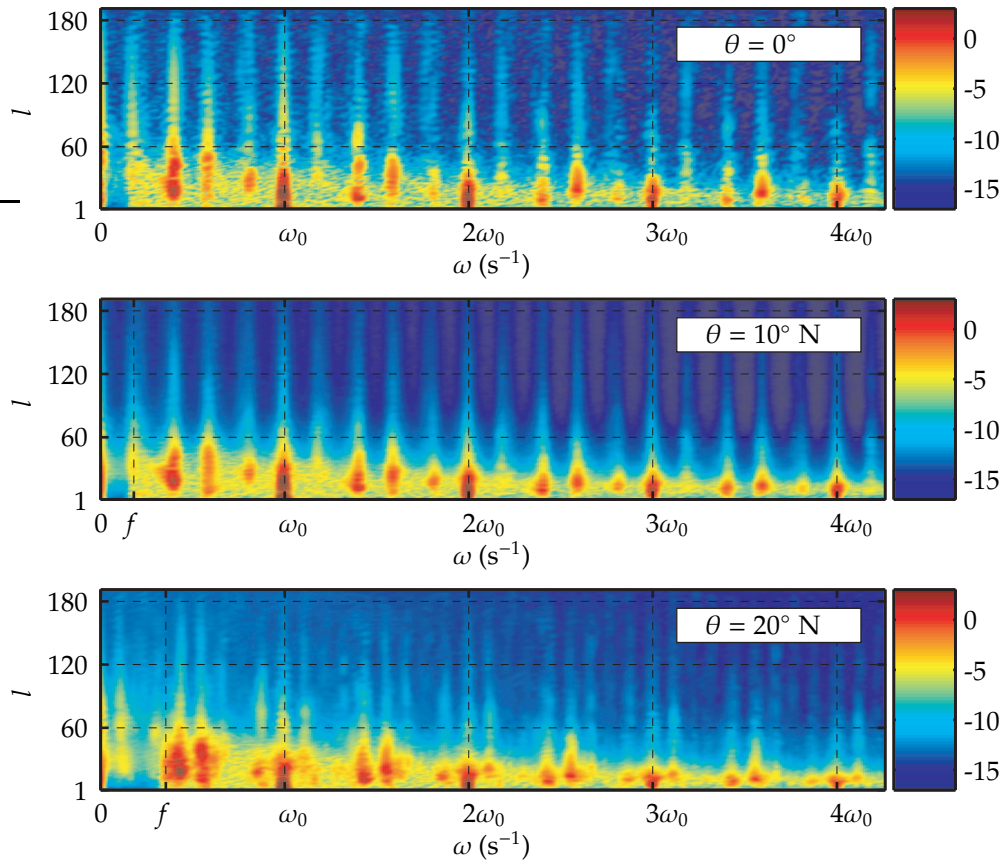
F   5.8: Two-dimensional spectra $E(\omega, m_l)$ ($m^2 s^{-2}$ per s^{-1} per mode) on the logarithmic scale calculated for $x \in [20, 40]$ km. Latitudes shown: 0°–20° N.
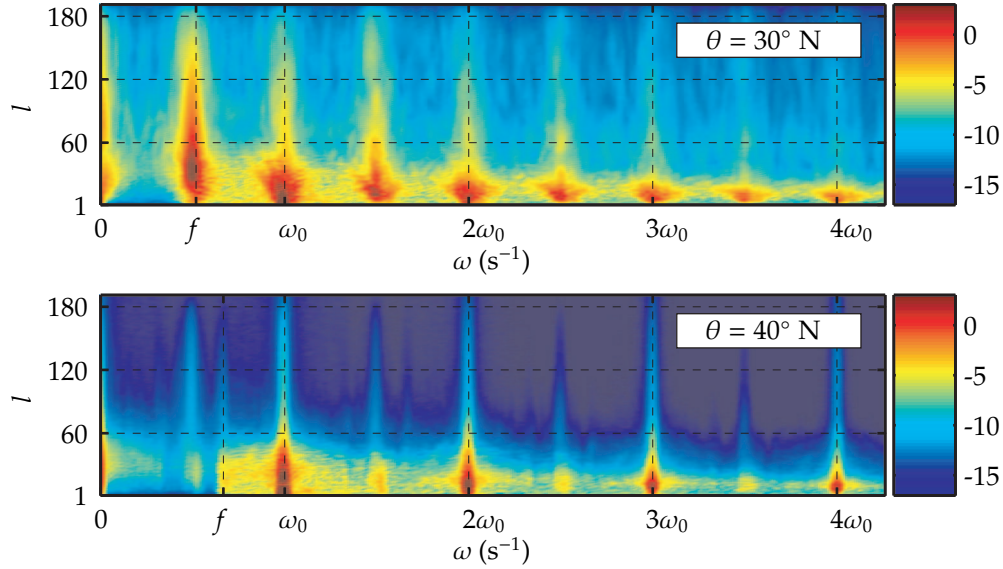
F   5.9: Same as in figure 5.8 but for latitudes 30°–40° N.

- estimating the power spectral density for each time series corresponding to a particular vertical wave number and a horizontal coordinate;

- averaging in the horizontal.

The expression for $E(\omega, m_l)$:

$$E(\omega, m_l) = \left\langle \frac{\Delta t}{\pi} \left| \sum_{n=0}^{N-1} g_n \left[\mathsf{DCT}\{u_{ij}^n\}(x_i, m_l, n) \right] \exp(-i\omega t_n) \right|^2 \right\rangle_{x_i \in [20,40] \text{ km}}, \tag{5.15}$$

where g_n is a prolate spheroidal sequence of the third order. Essentially, $E(\omega, m_l)$ is an extended version of the power spectral density $E(\omega)$. The power spectral density $E(\omega)$ and $E(\omega, m_l)$ obtained on the same region are related as follows:

$$E(\omega) = \frac{1}{J} \sum_{l=0}^{J-1} E(\omega, m_l). \tag{5.16}$$

Total energy of the baroclinic horizontal velocity is related to the spectrum $E(\omega, m_l)$ as follows:

$$\left\langle \frac{1}{T_{\text{tot}}} \int_0^{T_{\text{tot}}} |\tilde{u}(\xi, \eta, t)|^2 \, dt \right\rangle_{(\xi,\eta)} = \frac{1}{J} \sum_{l=0}^{J-1} \int_0^{\omega_{\text{Nyq}}} E(\omega, m_l) \, d\omega, \tag{5.17}$$

137

where the averaging on the left side is performed over (ξ, η) such that $\xi(0) \in [20, 40]$ km.

From figures 5.8, 5.9 it is seen that the vertical scales of the interharmonics are consistently smaller than the vertical scales of the surrounding harmonics. This feature is especially pronounced for the case $\theta = 30°$ N, where the energetic peaks of the spectrum change from higher vertical wavenumbers to lower ones. This feature was observed for subharmonics in similar spectra by MacKinnon and Winters (2003, 2005).

For the cases $10°$, $20°$ and $40°$, the subinertial regions $\omega < f$ in the spectra $E(\omega, m_l)$ are much less energetic in comparison with other regions. However, for the case $\theta = 30°$ there is clearly a subinertial peak at $\omega_0/2$.

5.6 Two-dimensional spectra $E(k, m_l)$

A comprehensive view of the spatial scales involved is given by the two-dimensional spectrum $E(k, m_l)$ that changes in time. In order to reduce the noise level in the estimations, we average the two dimensional spectra in time over five tidal periods. Thus, the spectrum $E(k, m_l)$ is estimated on time intervals $[T_1, T_1 + 5T_0]$ for different T_1. The expression for $E(k, m_l)$ evaluated for the time interval $[T_1, T_1 + 5T_0]$ is given by

$$E(k, m_l) = \left\langle \frac{\Delta x}{\pi} \left| \sum_i g_i \left[\mathrm{DCT}\{u_{ij}^n\}(x_i, m_l, n) \right] \exp(-ikx_i) \right|^2 \right\rangle_{t\in[T_1, T_1+5T_0]}, \tag{5.18}$$

Total energy of the spectrum $E(k, m_l)$ evaluated for the time interval $[T_1, T_1 + 5T_0]$ is related to the total baroclinic energy as follows:

$$\left\langle \frac{1}{XH} \int_{z=-H}^{0} \int_{x=30\,\mathrm{km}}^{330\,\mathrm{km}} |\tilde{u}(x, z, t)|^2 \, dx \, dz \right\rangle_{t\in[T_1, T_1+5T_0]} = \sum_{l=0}^{J-1} \int_{0}^{k_{\mathrm{Nyq}}} E(k, m_l) \, dk. \tag{5.19}$$

Figures 5.10–5.14 show two-dimensional spectra of horizontal velocity as a function of the horizontal and vertical wavenumber. The spectrum $E(k, m_l)$ is obtained by first applying the DCT in the vertical and then estimating the power spectral density with respect to the wavenumber k. The baroclinic velocity used to calculate this spectrum corresponded to coordinates $\{x_{ij}, z_{ij}\}$ with $x_{ij} \in [30, 330]$ km.

The development of the spectrum shows that energy spreads along the rays corresponding to different frequencies away from the origin $(k, m) = (0, 0)$. The frequencies include harmonics and interharmonics. First, the rays corresponding to harmonics appear, and then the rays
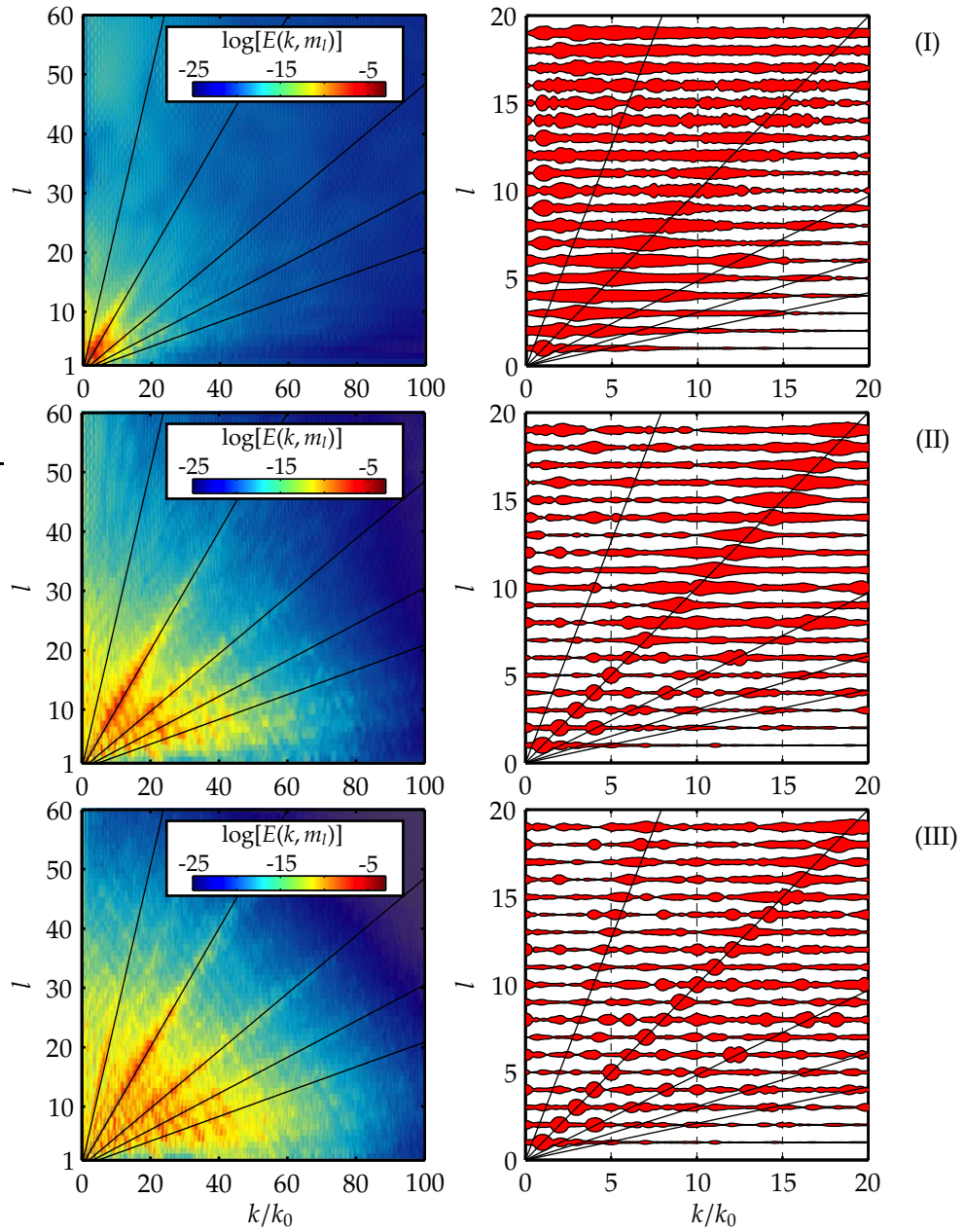
F   5.10: Two-dimensional spectrum $E(k, m_l)$ at $\theta = 0°$. Panels on the right show a magnified version of the spectrum near the origin; the width of the band at each vertical mode number l is proportional to $\log[E(k, m_l)]$ normalized by the maximum of $\log[E(k, m_l)]$ for mode number l. The development is shown for three time intervals: (I) $[5T_0, 10T_0]$, (II) $[25T_0, 30T_0]$, and (III) $[45T_0, 50T_0]$. Thin lines indicate the strongest subharmonic and first four harmonics.
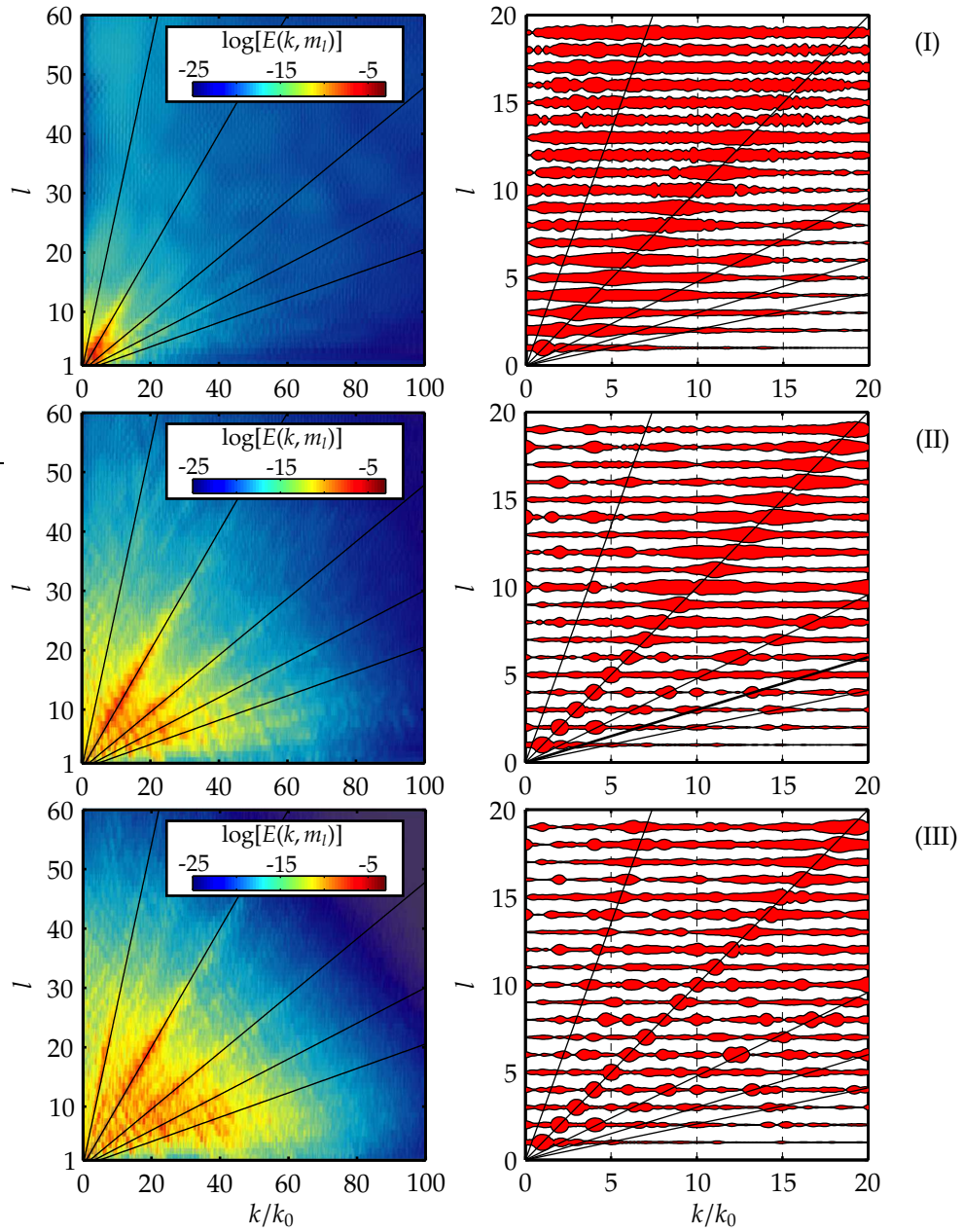
F   5.11: Same as in figure 5.10 but for latitude $\theta = 10°$ N.
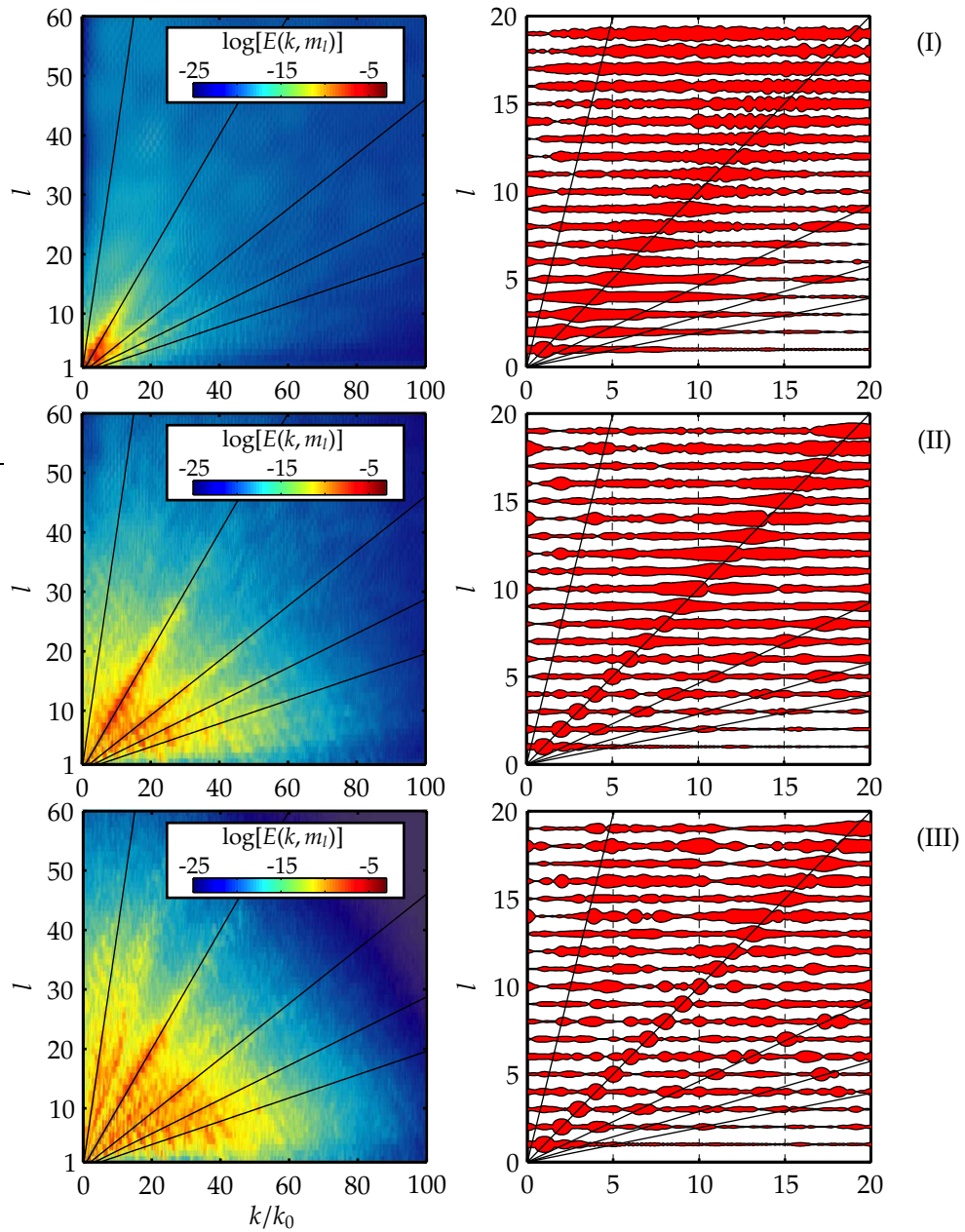
F   5.12: Same as in figure 5.10 but for latitude $\theta = 20°$ N.
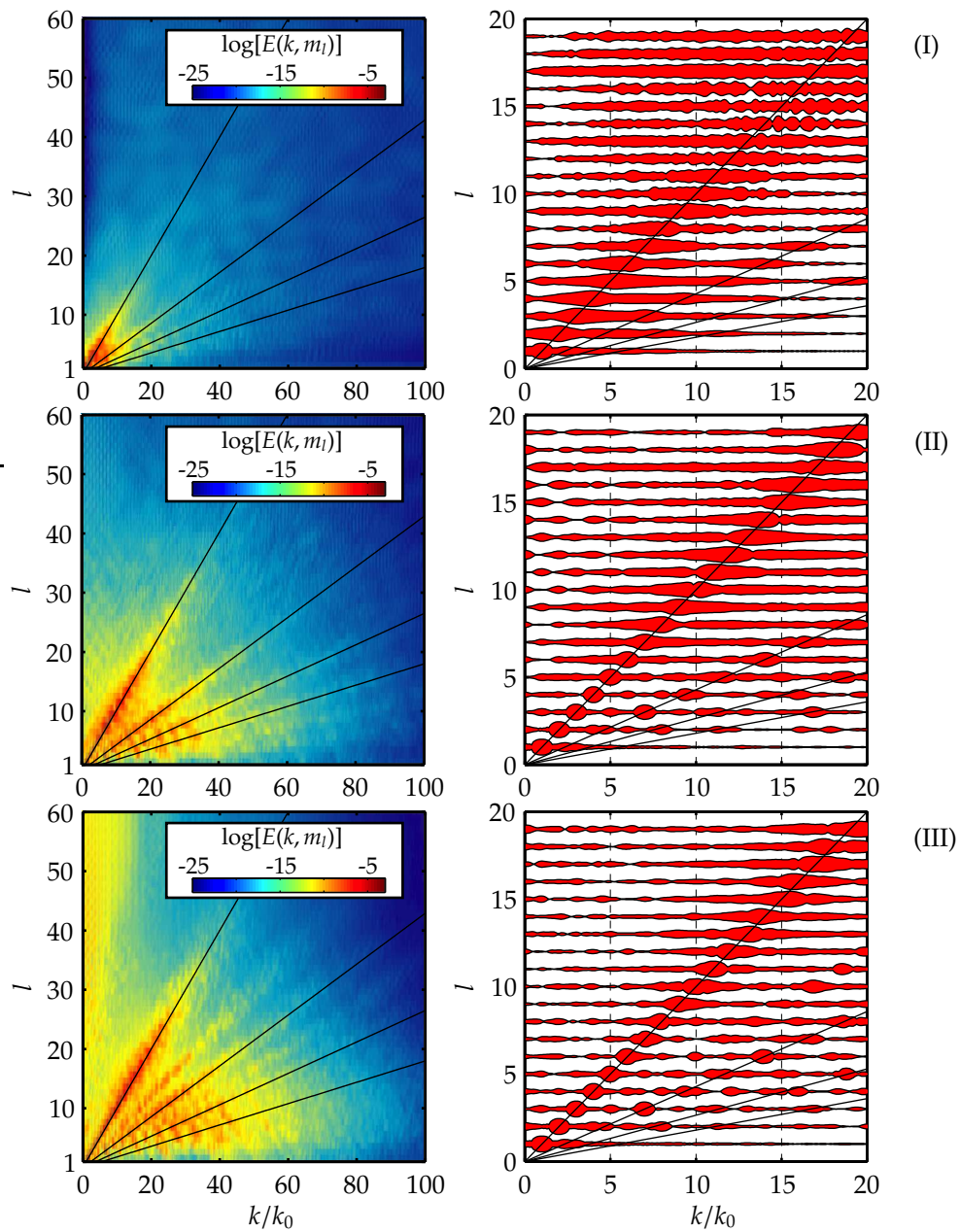
F   5.13: Same as in figure 5.10 but for latitude $\theta = 30°$ N. Thin lines indicate first four harmonics.
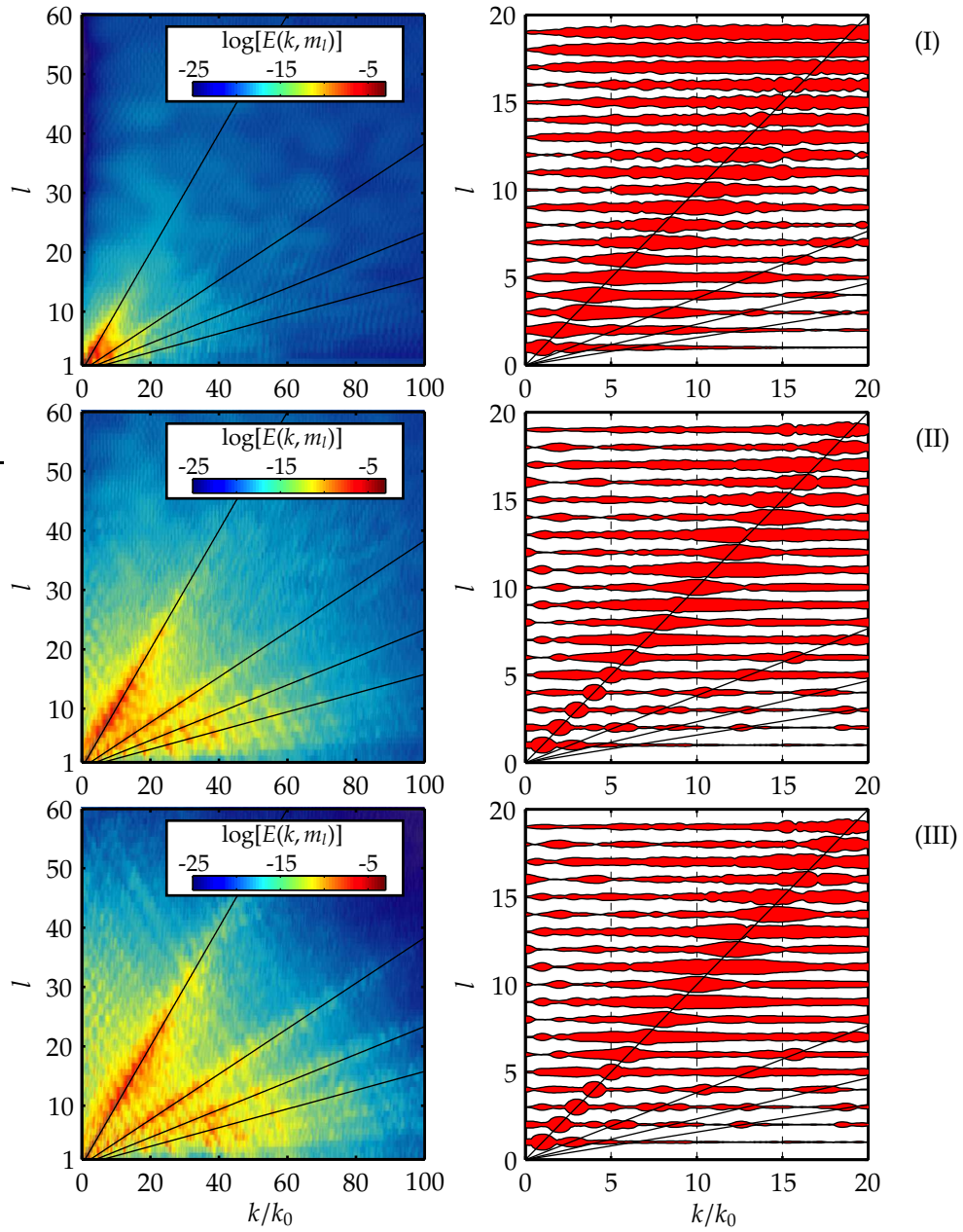
F   5.14: Same as in figure 5.10 but for latitude $\theta = 40°$ N. Thin lines indicate first four harmonics.

corresponding to interharmonics. The leakage due to the DCT transform is manifested in the checkered pattern appearing near energetic rays.

5.7   Spectrum $E(\omega)$ derived from $E(k, m)$

Changing variables from k to ω according to the dispersion relation, we can define the spectrum $E(\omega, m_l)$. The function $E(\omega, m_l)$ was evaluated numerically at the discrete set of frequencies $\omega_i = f + (i + 1/2)\Delta\omega$, where $i = 0, 1, \ldots, 299$ and $\Delta\omega = (N_b - f)/300$, using the following approximation:

$$E(\omega_i, m_l) = \frac{1}{\Delta\omega} \int_{k_{\text{left}}(\omega_i, m_l)}^{k_{\text{right}}(\omega_i, m_l)} E(k, m_l)\, \mathrm{d}k, \tag{5.20}$$

where

$$
\begin{aligned}
k_{\text{left}}(\omega_i, m_l) &= m_l \sqrt{\frac{(\omega_i - \Delta\omega/2)^2 - f^2}{N_b^2 - (\omega_i - \Delta\omega/2)^2}}, \\
k_{\text{right}}(\omega_i, m_l) &= m_l \sqrt{\frac{(\omega_i + \Delta\omega/2)^2 - f^2}{N_b^2 - (\omega_i + \Delta\omega/2)^2}}.
\end{aligned}
\tag{5.21}
$$

The integration in (5.20) was performed using the adaptive Simpson quadrature (Gander and Gautschi, 2000). Then, the time frequency spectrum can be estimated as follows:

$$E(\omega_i) = \sum_{l=0}^{60} E(\omega_i, m_l), \tag{5.22}$$

where summation was truncated to 60 vertical wavenumbers. Units of the function $E(\omega)$ are $\mathrm{m^2\,s^{-2}}$ per $\mathrm{s^{-1}}$. The total energy of the two-dimensional spectrum $E(k, m)$ is related to the total energy of the spectrum $E(\omega)$ as follows:

$$\int_{\omega=f}^{N_b} E(\omega)\, \mathrm{d}\omega = \sum_{l=0}^{J-1} \int_0^{k_{\text{Nyq}}} E(k, m_l)\, \mathrm{d}k. \tag{5.23}$$

As the spectrum $E(k, m_l)$ is calculated for different time intervals, we can evaluate the evolution of the derived spectrum $E(\omega)$.

Figures 5.15–5.17 demonstrate the development of the spectrum $E(\omega)$ for latitudes $0°$, $10°$, $20°$, $30°$ and $40°$ N. The spectra $E(\omega)$ are shown for the three time intervals: $[5T_0, 10T_0]$, $[25T_0, 30T_0]$ and $[45T_0, 50T_0]$. The structure of the spectrum $E(\omega)$ derived from the two-dimensional spectrum $E(k, m)$, based on the internal wave field for $x \in [30, 330]$ km, is qualitatively similar to the spectrum $\Upsilon(\omega)$ calculated for the time series within 40 km of the ridge. Both harmonics and interharmonics are apparent in the spectrum structure. The values of interharmonics observed

in the spectra $E(\omega)$ are similar to those observed in the spectra $\Upsilon(\omega)$. For example, in case $\theta = 0°$, two distinguished peaks at subharmonic frequencies $0.4\omega_0$ and $0.6\omega_0$ are seen.

5.8   Interharmonics are resonant triads

There is evidence that the strong subharmonics observed in the spectra within the frequency range $[f, N_b]$, are generated through resonant triad interactions. There is a discrete number of resonant triad interactions occuring in the highly nonlinear regions that generate the two strongest subharmonics. For example, in the case $\theta = 20°$ N, there is one resonant triad corresponding to the destabilization of the tidal beam on top of the ridge and there is another corresponding to the instability on the side of the ridge. The instability of the internal tidal beam occurring on top of the ridge generates two subharmonic waves with frequencies ω_1 and ω_2 such that $\omega_1 + \omega_2 = \omega_0$. The two subharmonics are characterized by two distinct wavevectors: $\mathbf{K}_1 = (k_1, m_1)$ and $\mathbf{K}_2 = (k_2, m_2)$. The tidal beam, on the other hand, does not have any dominant wavenumbers: the energy is distributed over a continuum of wavenumbers. The linear dispersion relation indicates that the sum combination of the wavevectors corresponding to the subharmonics on top of the ridge, i.e. $\mathbf{K}_1 + \mathbf{K}_2$, corresponds to the wave of the tidal frequency. Similarly, the two subharmonics generated on the side of the ridge are in resonance with the tidal beam.

Let us consider the example case $\theta = 20°$ in more detail and estimate the dominant wavenumbers corresponding to the energetic subharmonic frequencies $\omega_1 = 0.4269\omega_0$ and $\omega_2 = 0.5752\omega_0$. The values of the subharmonic frequencies are obtained from the one-dimensional spectrum $\Upsilon(\omega)$. Apart from the wavenumbers corresponding to the subharmonics, we will also need to estimate the energetic wavenumbers characterizing the tidal beam.

The spatial distribution of the waves with a given frequency ω_α can be analyzed using the following Fourier transform of the baroclinic velocities $\tilde{u}_{ij}^n$:

$$\chi_{ij}(\omega_\alpha) = \sum_{n=0}^{N-1} g_n \tilde{u}_{ij}^n \exp(-i\omega_\alpha t_n), \tag{5.24}$$

where g_n is the same as for the spectral estimator $S_{ij}(\omega_\alpha)$. We consider the distribution $\chi_{ij}(\omega_\alpha)$ over the domain $\xi_{ij} \in [0, 40]$ km and restrict our attention to the three frequencies ω_1, ω_2 and ω_0. Note, that the transform $\chi_{ij}(\omega_\alpha)$ is the essential part of the direct spectral estimator $S_{ij}(\omega_\alpha)$; the two are related as follows: $S_{ij}(\omega_\alpha) = (\Delta t/\pi)|\chi_{ij}(\omega_\alpha)|^2$. As opposed to the spatial distribution $S_{ij}(\omega_\alpha)$, the transform $\chi_{ij}(\omega_\alpha)$ allows us to obtain the information about the relative phase of a wave at each coordinate (ξ_{ij}, η_{ij}). Using that information we can estimate the wavenumbers of a wave.

145
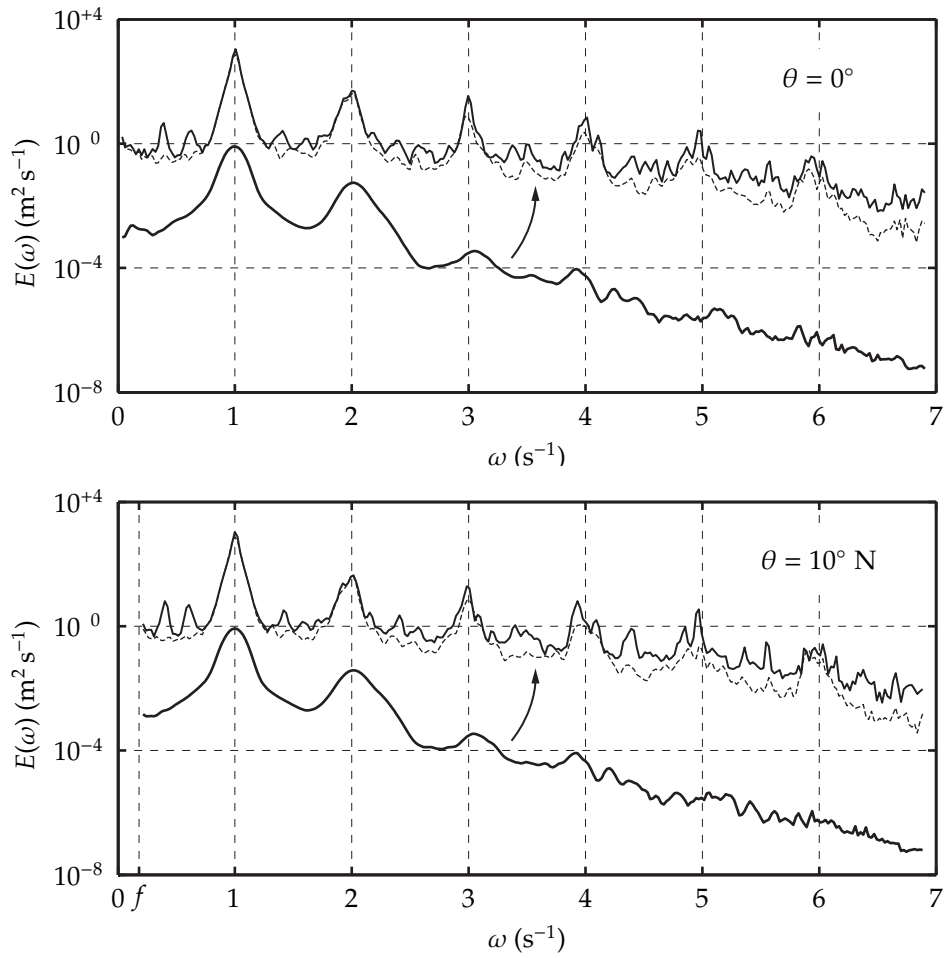
F   5.15: Development of the spectrum $E(\omega)$ for $\theta = 0°$ and $10°$ N. Curves are evaluated for the time intervals $[5T_0, 10T_0]$, $[25T_0, 30T_0]$ and $[45T_0, 50T_0]$. The arrow shows the direction of evolution.

146
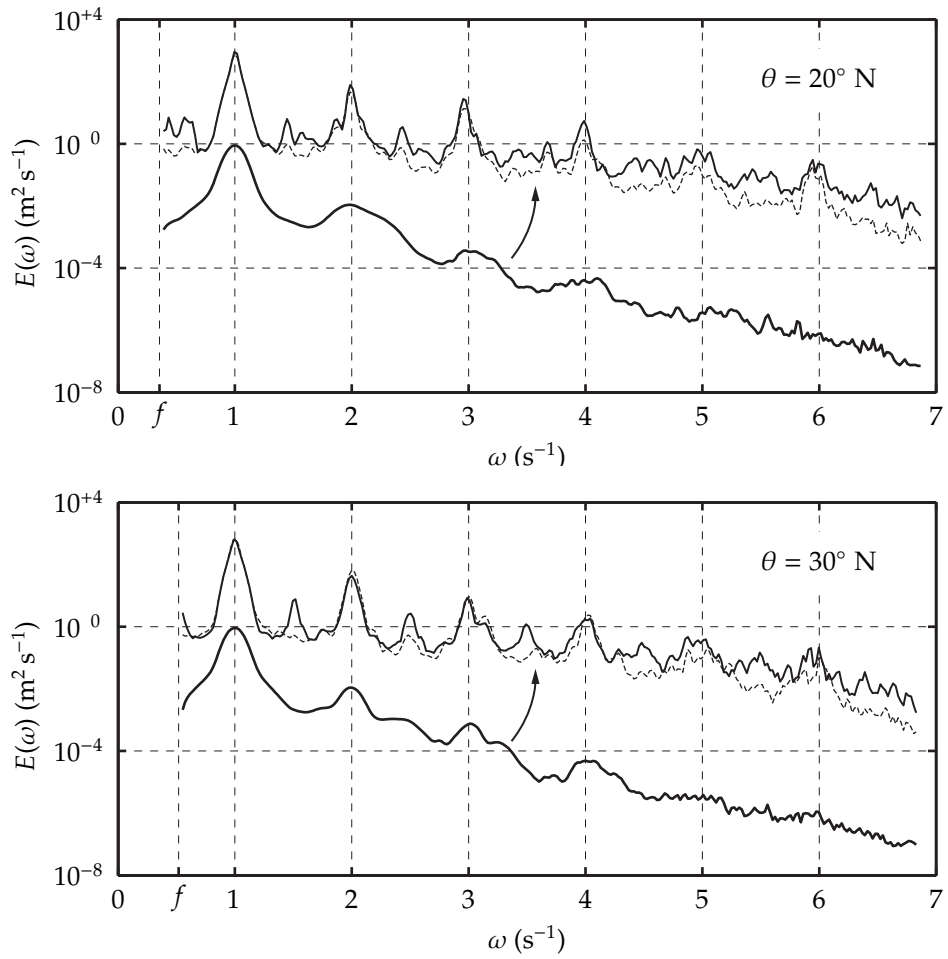
F   5.16: Same as in figure 5.15 but for latitudes $\theta = 20°$ and $30°$ N.
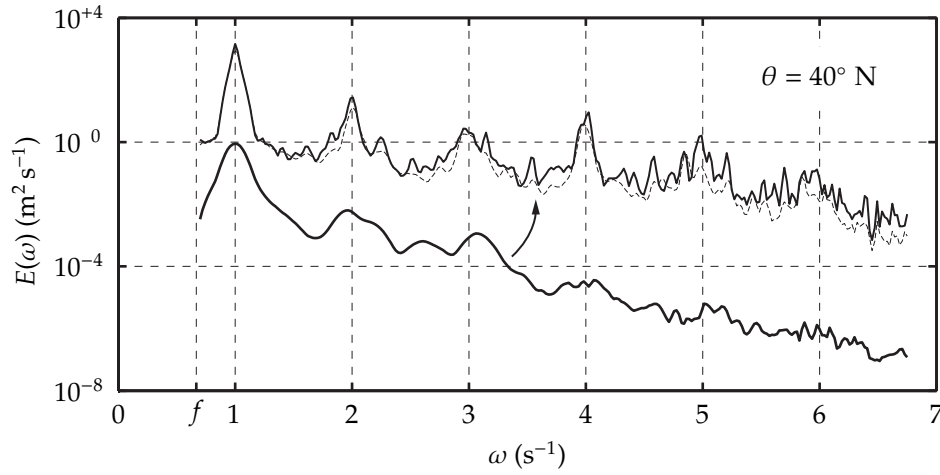
F   5.17: Same as in figure 5.15 but for latitude $\theta = 40°$ N.

The phase field corresponding to frequency ω_α can be defined as follows:

$$\phi_{ij}(\omega_\alpha) = \Im\{\log(\chi_{ij}(\omega_\alpha)\}, \ \phi_{ij}(\omega_\alpha) \in [-\pi, \pi], \tag{5.25}$$

where $\Im$ stands for the imaginary part. As the phase field φ_{ij} is discontinous and the phase itself is ambiguously defined, a better way to visualize the local phase of a wave is to consider either the real or imaginary part of the matrix $\chi_{ij}(\omega_\alpha)$ normalized by the absolute value of $\chi_{ij}(\omega_\alpha)$ at each point, e.g.

$$\varphi_{ij}(\omega_\alpha) = \Re\{\chi_{ij}(\omega_\alpha)\}/|\chi_{ij}(\omega_\alpha)|, \ \varphi \in [-1, 1], \tag{5.26}$$

where $\Re$ stands for the real part. Figures 5.18, 5.19 and 5.20 demonstrate the phase fields $\varphi_{ij}(\omega_\alpha)$ for $\omega_\alpha = \omega_1$, ω_2 and ω_0. Lines of constant phase have the typical slope corresponding to the frequency of the wave. The actual distribution of each wave is much less regular than the phase field. To emphasize where the wave is most energetic, a contour of the field $|\chi_{ij}(\omega_\alpha)|$ is shown as a shaded patch on top of each of the phase fields.

The structure of the phase fields $\varphi_{ij}(\omega_1)$ and $\varphi_{ij}(\omega_2)$ shows that there are dominant wavenumbers for each subharmonic. However, as is seen in the field $\varphi_{ij}(\omega_1)$ the wavenumbers corresponding to the beams of subharmonic frequency emanating from the top of the ridge and from the side, are quite different. Accordingly, the distribution $\chi_{ij}(\omega_\alpha)$ has different wavenumbers: see, for example, the profile $\Re\{\chi_{ij}(\omega_1)\}$ at $\xi_{ij} = 11$ km and 30 km, shown in figure 5.21. On the other hand, the structure of the phase field corresponding to the wave of tidal frequency, i.e. $\varphi_{ij}(\omega_0)$, does not suggest any dominant wavenumbers.

148
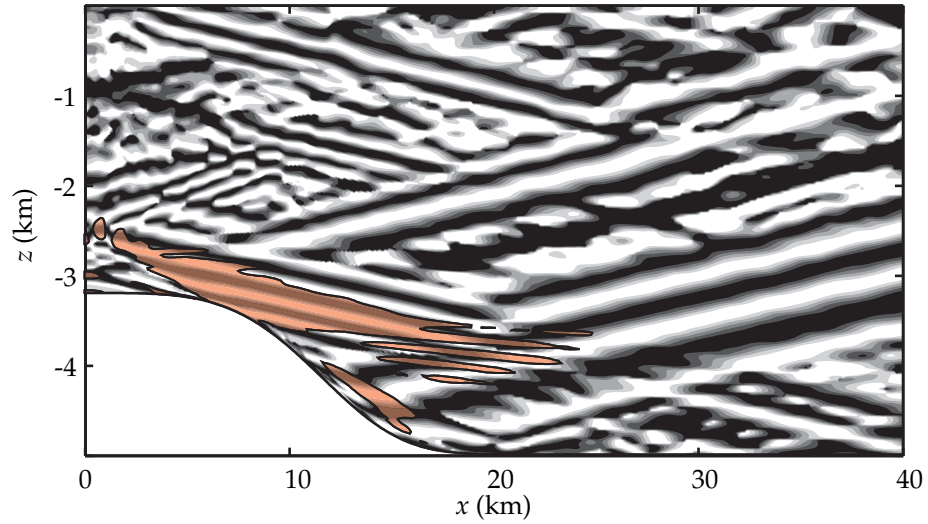
F   5.18: The phase field $\varphi_{ij}(\omega_1)$ at latitude $\theta = 20°$ N. The patch on top indicates the energetic region.
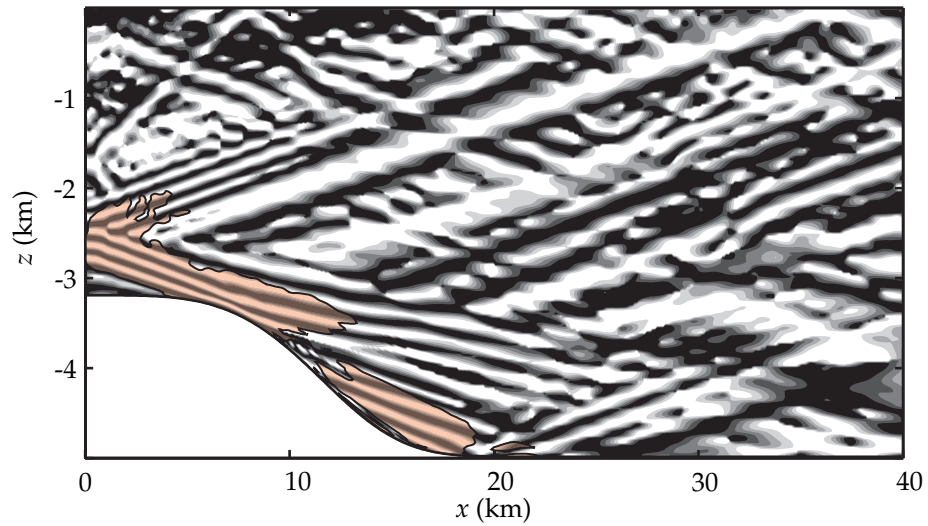
F   5.19: The phase field $\varphi_{ij}(\omega_2)$ at latitude $\theta = 20°$ N. The patch on top indicates the energetic region.
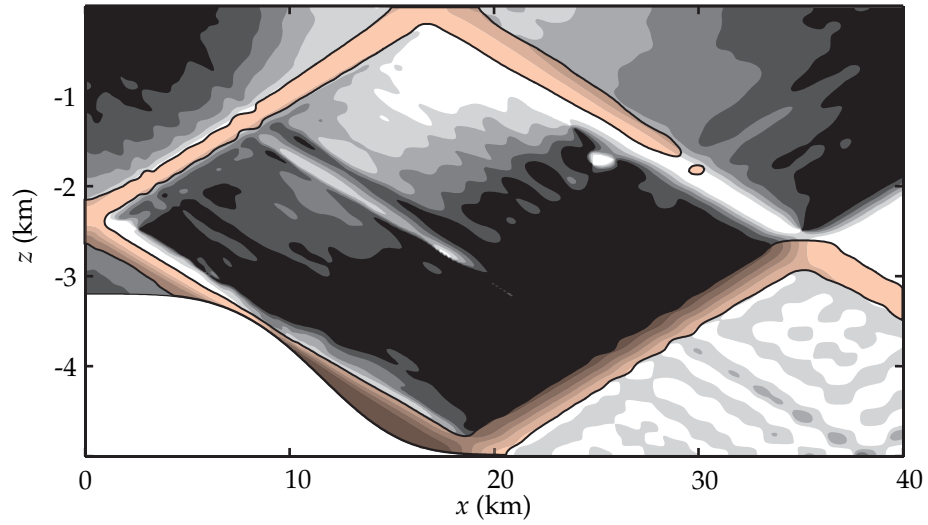
F   5.20: The phase field $\varphi_{ij}(\omega_0)$ at latitude $\theta = 20°$ N. The patch on top indicates the energetic region.
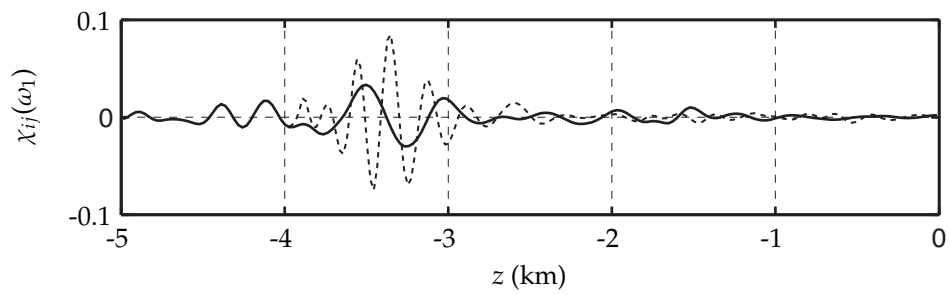
F   5.21: The profile $\chi_{ij}(\omega_1)$ for $\xi_{ij} = 11$ km (dashed line) and 30 km (solid line).

To define the dominant vertical wavenumbers of the distribution $\chi_{ij}(\omega_\alpha)$ we apply a zero-padded discrete Fourier transform in the vertical for each index i. Thus, for each frequency we obtain a distribution $\hat{\chi}(x, m)$ that shows the dominant wavenumbers. Figures 5.22 and 5.23 show the two fragments of the distribution $\hat{\chi}(x, m)$ with the two dominant vertical wavenumbers. One vertical wavenumber (m_1^{top}) corresponds to the instability on the top and another, to the instability on the side (m_1^{side}). Figures 5.24 and 5.25 show the energetic wavenumbers for the frequency ω_2.

Figures 5.26–5.27 show the distribution of the energetic wavenumbers of the waves of tidal frequency. The important difference in comparison with the case of subharmonics is that there are no localized peaks signifying dominant wavenumbers. Rather, the distribution of the energetic wavenumbers for the tidal frequency is decaying with the the vertical wavenumber. The pattern of the distribution reflects the fact that the upward propagating beam has more energy in high vertical wavenumbers in the region $0 \lessgtr x \lessgtr 10$ km, i.e. on top of the ridge. The downward propagating beam has more energy in higher vertical wavenumbers in the region $10 \lessgtr x \lessgtr 20$ km, i.e. on the side of the ridge. The alternating black 'ribbons' in the distribution are the manifestation of what the vertical mode structure turns into over topography.

Once the dominant vertical wavenumber is found, the corresponding horizontal wavenumber can be constructed using the dispersion relation:

$$k = m \sqrt{\frac{\omega^2 - f^2}{N_b^2 - \omega^2}}. \tag{5.27}$$

Table 5.3 lists the resulting wavenumbers for the two subharmonics. Note that the sign of the actual wavenumbers in the internal wave field can be different from what is shown in the table due to our method of the wavenumber detection. The waves characterized by $(\omega_1, k_1^{\text{top}}, m_1^{\text{top}})$ and $(\omega_2, k_2^{\text{top}}, m_2^{\text{top}})$ form a resonant triad with the wave $(\omega_0^{\text{top}}, k_0^{\text{top}}, m_0^{\text{top}}) = (\omega_1 + \omega_2, k_1^{\text{top}} + k_2^{\text{top}}, m_1^{\text{top}} + m_2^{\text{top}})$, where $\omega_0^{\text{top}} \approx \omega_0$ and the wavenumbers of the sum wave satisfy the dispersion relation:

$$\left(\frac{m_0^{\text{top}}}{k_0^{\text{top}}} \right)^2 \approx \frac{N_b^2 - \omega_0^2}{\omega_0^2 - f^2}. \tag{5.28}$$

Thus, the waves of frequencies ω_1 and ω_2 on top of the ridge form a resonant triad with the wave of tidal frequency. Similarly, it can be shown that the subharmonic waves on the side of the ridge also form a triad with the wave of tidal frequency.

T   5.3: Dominant wavenumbers of the resonant triads for the case 20° N

ω	Top	Side
ω_1	$(k_1^{\text{top}}, m_1^{\text{top}}) = (-9.2765 \times 10^{-4}, -0.0277) \text{ m}^{-1}$	$(k_1^{\text{side}}, m_1^{\text{side}}) = (4.4205 \times 10^{-4}, 0.0132) \text{ m}^{-1}$
ω_2	$(k_2^{\text{top}}, m_2^{\text{top}}) = (2.4937 \times 10^{-3}, 0.039) \text{ m}^{-1}$	$(k_2^{\text{side}}, m_2^{\text{side}}) = (-2.174 \times 10^{-3}, -0.034) \text{ m}^{-1}$
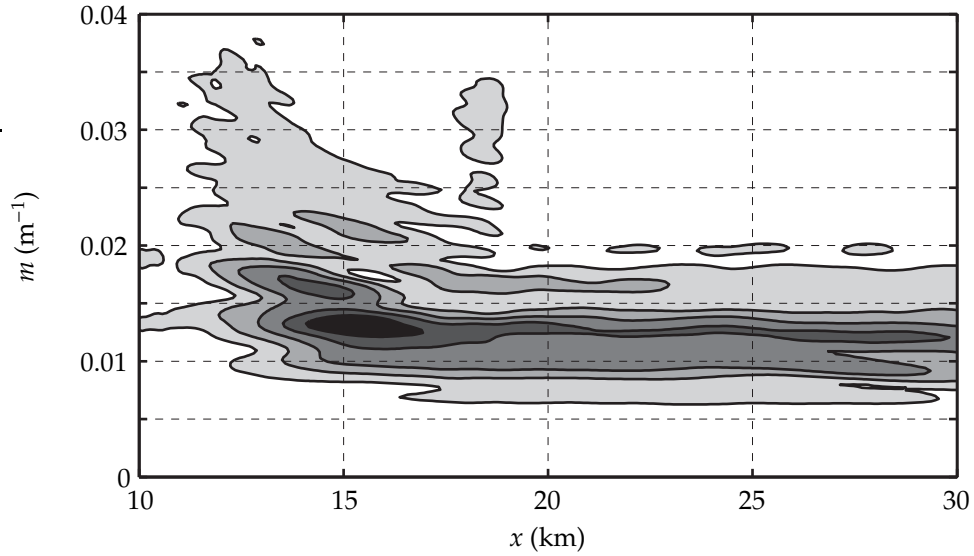
F   5.22: The distribution $\hat{\chi}_{ij}(x, m)$ for the frequency ω_1 shown for the positive wavenumbers. The maximum (black patch) corresponds to a resonant triad interaction on the side of the ridge.
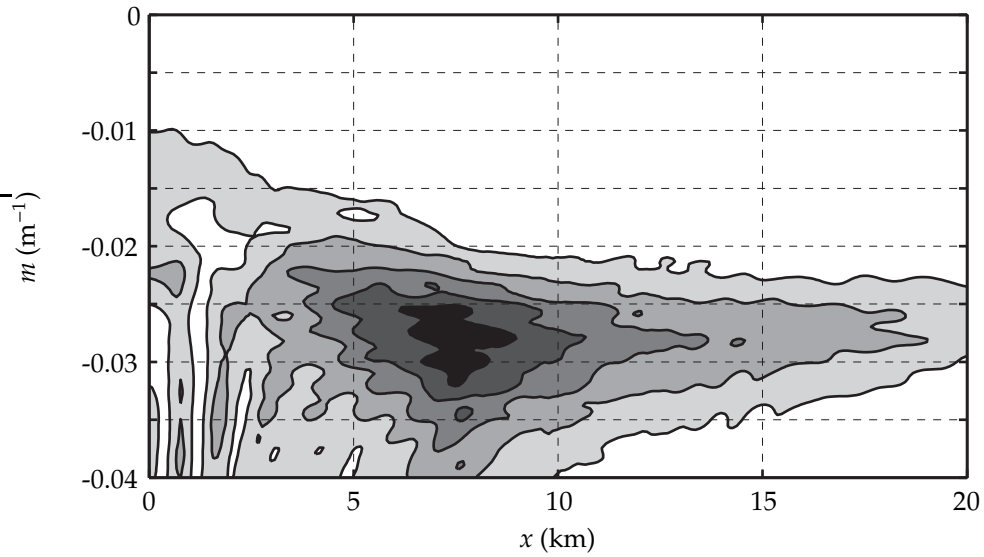
F   5.23: The distribution $\hat{\chi}_{ij}(x, m)$ for the frequency ω_1 shown for the negative wavenumbers. The maximum (black patch) corresponds to a resonant triad interaction on top of the ridge.
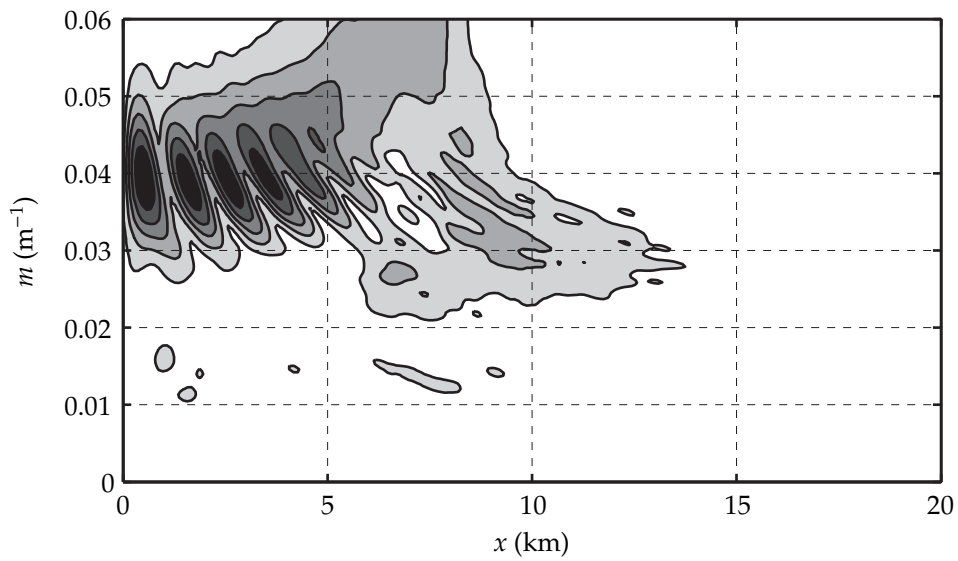
F   5.24: The distribution $\hat{\chi}_{ij}(x, m)$ for the frequency ω_2 shown for the positive wavenumbers. The maximum (black patch) corresponds to a resonant triad interaction on top of the ridge.
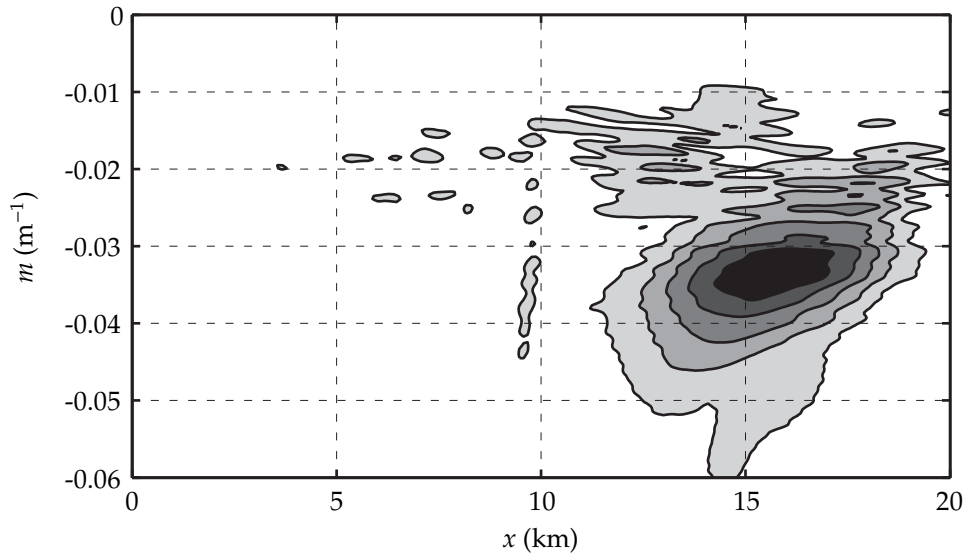
F   5.25: The distribution $\hat{\chi}_{ij}(x, m)$ for the frequency ω_2 shown for the negative wavenumbers. The maximum (black patch) corresponds to a resonant triad interaction on the side of the ridge.
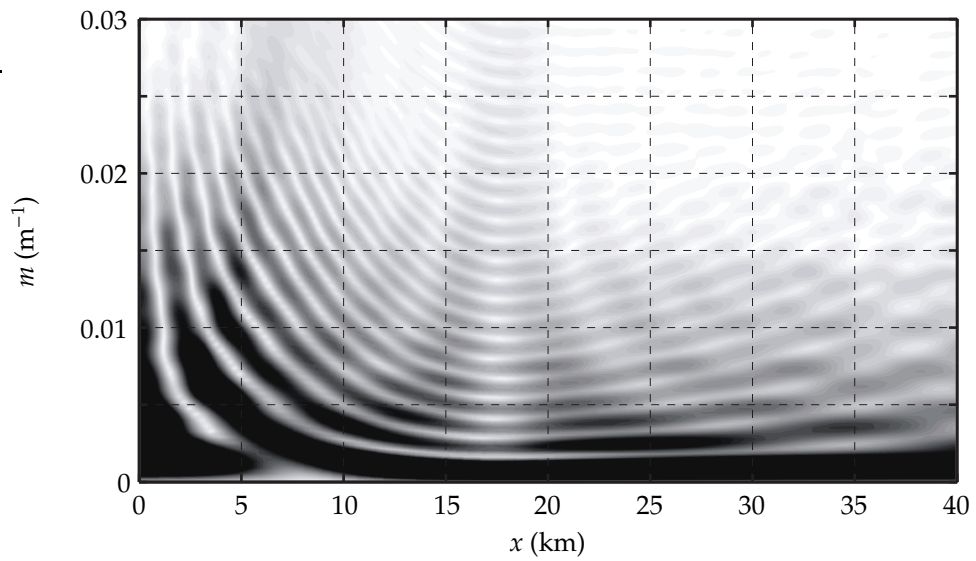
F   5.26: Vertical transform of the field $\chi_{ij}(\omega_0)$. Positive wavenumbers corresponding to the upward propagating beam.
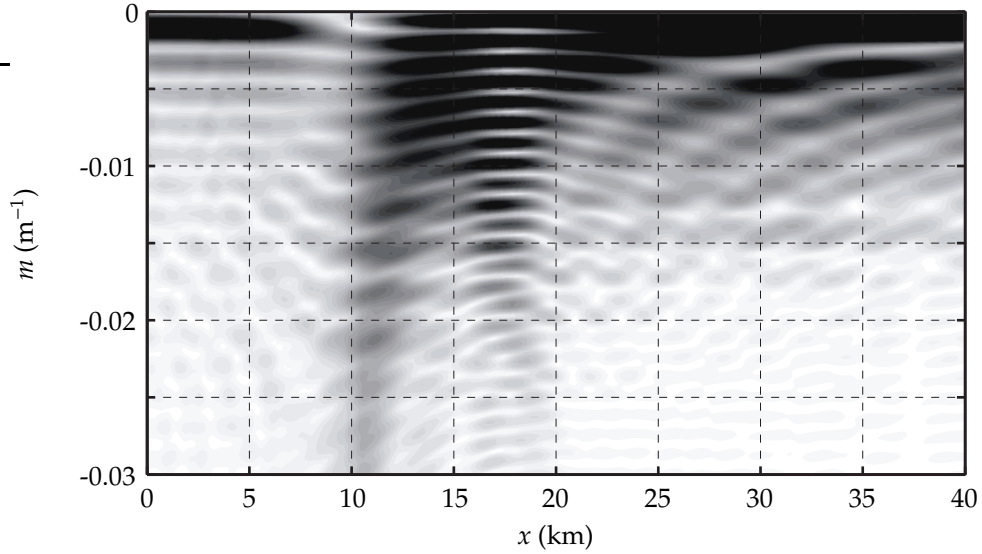
F   5.27: Vertical transform of the field $\chi_{ij}(\omega_0)$. Negative wavenumbers corresponding to the downward propagating beam.

5.9   Linear spectra based on Bell's solution

The wavelike part of the linear solution of the flow over an idealized topography $h(x)$, which contains the majority of the energy in the linear case, can be written for the vertical displacement as in Bell (1975):

$$\eta(x,z,t) = \frac{1}{\pi} \sum_{n=1}^{n_0} \Re \left\{ \int_{-\infty}^{+\infty} \hat{h}(k) J_n\left(\frac{kU_0}{\omega_0}\right) \exp[i(k\xi + \mu_n z + n\omega_0 t)] \mathrm{d}k \right\}, \tag{5.29}$$

where the following notation in agreement with Bell was used:

- symbol $\Re$ stands for the "real part of";

- ξ is the horizontal coordinate moving with the barotropic flow:

$$\xi = x - \int_0^t U(t)\mathrm{d}t;$$

- $\hat{h}(k)$ is the non-unitary Fourier transform of the topography $h(x)$:

$$\hat{h}(k) = \int_{-\infty}^{+\infty} h(x) \exp(ikx)\mathrm{d}x;$$

155

- $n_0 = \lfloor N_b/\omega_0 \rfloor$ is the number of freely propagating harmonics;

- μ_n is the vertical wavenumber associated with the frequency and horizontal wavenumber as follows:

$$\mu_n = \frac{|k|}{n\omega_0}(n^2\omega_0^2 - N_b^2)^{1/2}, \ n = 1, 2, \ldots, n_0.$$

For each value of the harmonic number n, the spectrum with respect to the horizontal wavenumber k is represented by

$$E_n^{\text{Bell}}(k) = \left| \hat{h}(k)J_n\left(\frac{kU_0}{\omega_0}\right) \right|^2.$$

For our particular choice of topography, i.e. $h(x) = A\exp(-x^4/d^4)$, the Fourier transform $\hat{h}(k)$ can be evaluated explicitly using symbolic computation in M   :

$$
\begin{aligned}
\hat{h}(k) = &\frac{\pi A d}{\sqrt{2}\Gamma(3/4)} {}_0F_2\left([\ ]; \left[\frac{1}{2}, \frac{3}{4}\right]; \frac{1}{256}k^4 d^4\right) \\
&- \frac{1}{4}\Gamma\left(\frac{3}{4}\right) A d^3 k^2 {}_0F_2\left([\ ]; \left[\frac{5}{4}, \frac{3}{2}\right]; \frac{1}{256}k^4 d^4\right).
\end{aligned}
\tag{5.30}
$$

The transform is expressed in terms of Bessel functions of the first kind $J_n(\cdot)$, gamma functions $\Gamma(\cdot)$ and hypergeometric functions ${}_0F_2(\cdot)$. The latter are power series defined as follows:

$$
{}_0F_2([]; [d_1, d_2]; z) = \sum_{k=0}^{+\infty} z^k \Big/ \left(k!\, d_1^{\bar{k}}\, d_2^{\bar{k}}\right),
\tag{5.31}
$$

where $a^{\bar{k}}$ denotes the rising factorial (notation adapted from Knuth, 1992):

$$a^{\bar{k}} = a(a+1)\ldots(a+k-1).$$

The shape of the function $\hat{h}(k)$ is shown in figure 5.28.

Figure 5.29 shows spectra $E_n^{\text{Bell}}(k)$ for different harmonics. The structure of the spectrum $E_n^{\text{Bell}}(k)$ for each harmonic is composed of peaks at a discrete set of horizontal wavenumbers k. In this sense, the spectrum $E_n^{\text{Bell}}(k)$ is similar to the nonlinear spectrum $E(k)$ for the case $\theta = 0°$. However, the peaks in the two spectra are quite different. In the nonlinear spectrum, the peaks correspond to the periodicity in the pattern of beams on the domain $[30, 330]$ km, whereas the peaks in the spectrum $E_n^{\text{Bell}}(k)$ characterizes the scales of the beams themselves (the pattern of beams corresponding to Bell's solution is not periodic at all, as he assumes the ocean depth to be infinite). Thus, the peaks in the two spectra are at different wavenumbers. For example, the strongest peak in the spectrum $E(k)$ shown in figure 5.5 is at $k = k_0 \approx 8.9 \times 10^{-5}$, whereas the
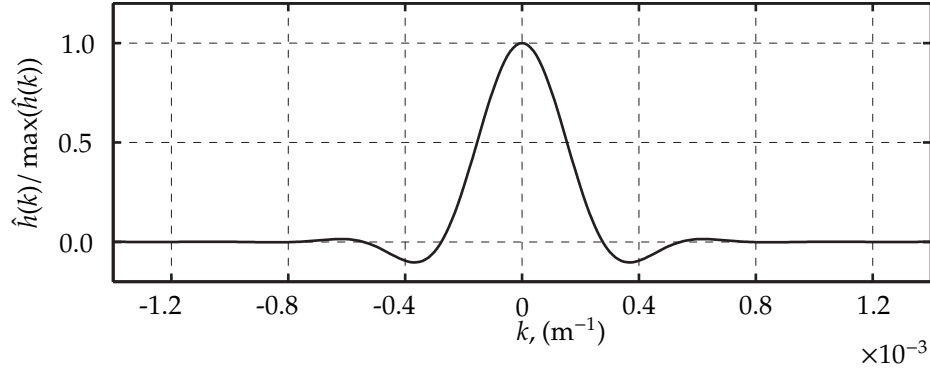
F   5.28: The Fourier transform of the topography, $\hat{h}(k)$.

strongest peak of $E_n^{\text{Bell}}(k)$ shown in figure 5.29 is at $k = 1.3 \times 10^{-4}$. Moreover, the wavenumbers of peaks in the spectrum $E_n^{\text{Bell}}(k)$ vary with the number of harmonic n.

In order to draw an analogy between the two-dimensional spectrum $E(k, m_l)$, evaluated for the nonlinear solution, and the spectrum corresponding to Bell's solution, we construct the following function based on Bell's solution in the wavenumber space. Using the dispersion relation (3.1) we can transform the spectrum $E_n^{\text{Bell}}(k)$ for each harmonics into a function $E_n^{\text{Bell}}(k, m)$ defined for the wavenumbers (m, k) such that

$$\frac{m}{k} = \sqrt{\frac{N_{\text{b}}^2 - (n\omega_0)^2}{(n\omega_0)^2 - f^2}}, \quad n = 0, 1, \ldots, 7.$$

In order to visualize the structure of the solution in the wavenumber space we perform the following: (1) smooth the functions $E_n^{\text{Bell}}(k, m)$ for each n by convolving them with the Gaussian two-dimensional function whose standard deviation is 5×10^{-5} m^{-1}; (2) normalize the resulting functions so that each harmonic would have equal maximum; (3) superimpose the smoothed and normalized functions. The resulting pseudo-spectrum is shown in figure 5.30. The pseudo-spectrum, in contrast to the spectrum of the nonlinear flow $E(k, m_l)$, is continuous with respect to the vertical wavenumber. The peaks occur at unique vertical and horizontal wavenumbers, and, thus, do not suggest a discrete nature of the spectrum with respect to the horizontal or vertical wavenumber. The main difference, however, between the linear and nonlinear case is the absence of energy in the wavenumbers corresponding to interharmonics.
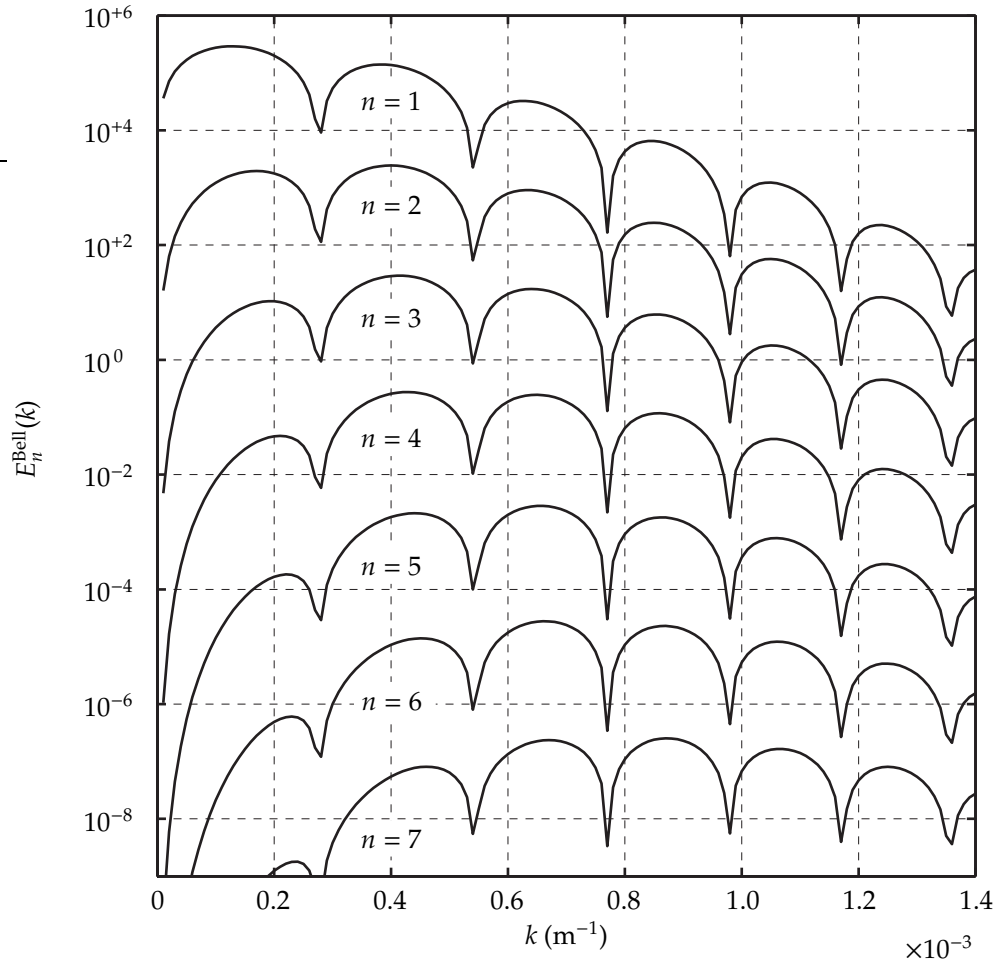
F   5.29: The linear spectrum $E_n^{\text{Bell}}(k)$ for different harmonics.
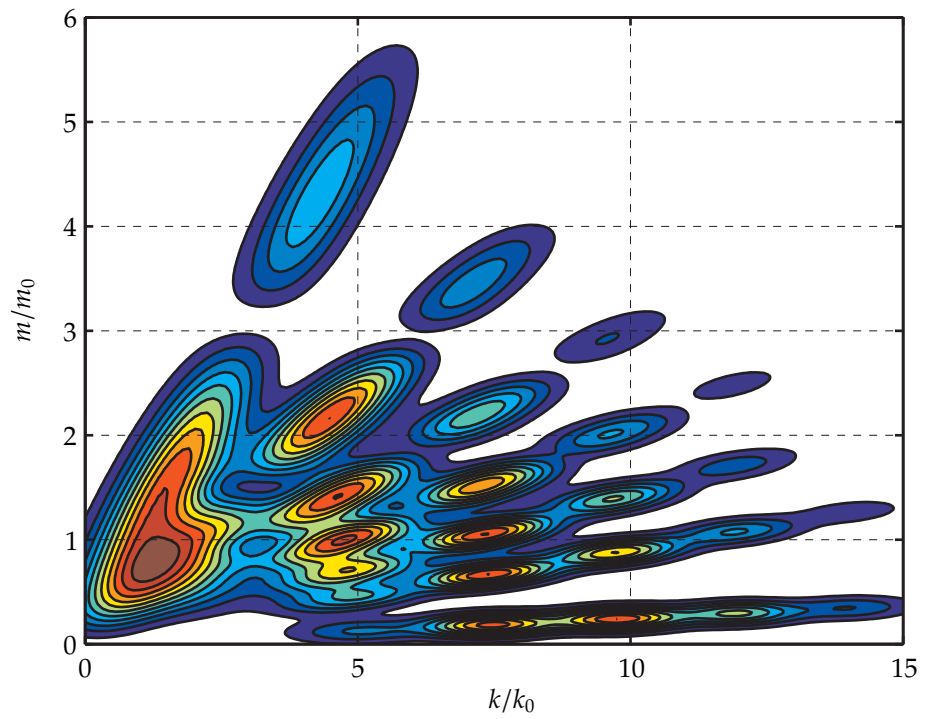
F   5.30: The pseudo-spectrum based on the linear spectrum $E_n^{\text{Bell}}(k)$, constructed in the wavenumber space by using convolution with a two-dimensional Gaussian function.

5.10 Summary

In this chapter, we considered the dependence of energy on spatial coordinates and wavenumbers. One of the important results is that the vertical scales of the inteharmonics are typically smaller than those of harmonics, with the vertical scales of subharmonics being the smallest. The conjecture is that, in the real world, the subharmonics generated in a similar fashion as in our runs are the most susceptible to the vertical mixing. Using the two-dimensional spectra $E(k, m_l)$, we showed that, with time, internal wave energy spreads from small wavenumbers toward larger wavenumbers (both horizontal and vertical) until the spectrum reaches semi-steady state.

Another important result of this chapter is the following: when the two strong subharmonics are within the free internal wave range, they are generated from the tidal beam through the parametric subharmonic instability. This was shown by investigating the wavenumbers of each of the three waves. A similar instability mechanism may generate subharmonics out of the free internal wave range (for supercritical latitudes); in this case the waves are forced.

Chapter 6

Conclusions

6.1 Summary of the results

In this research we investigated two-dimensional stratified tidal flow over topography. We looked at how the resulting internal wave field depends on latitude, topography and background flow. Using temporal spectral analysis, we showed that the inviscid flow in our numerical experiments consists of harmonics and interharmonics. Previously, the attention was centered around harmonics and strong subharmonics only. Interharmonics, ignited by instabilities in the highly nonlinear regions, and multiplied through triad interactions, represent the next logical step in understanding the process of energy cascade in internal waves. Using spatial spectral analysis, we studied the typical horizontal and vertical scales of the internal wave field. In particular, we showed that, according to vertical and horizontal wavenumbers, waves of interharmonic frequencies within the free internal wave range are generated through resonant triad interaction.

6.2 Misleading stereotypes

There seem to be several stereotypes in the current literature on internal wave energy transfers that must be discredited or, at least, reconsidered. All of these stereotypes, described below, are interconnected and, arguably, stem from the older linear and weakly-nonlinear theories: trying to use the old terms when the old assumptions do not hold leads to misunderstanding and confusion.

Using the old term Parametric Subharmonic Instability for the description of the main cause of the subharmonics leads to confusion. First of all, PSI was originally thought of as an instability

acting on a single wave not perturbed by topography or coherent surrounding waves. Clearly, the old term fails to describe the fact that the development of an instability in a violently perturbed wave is much faster than in the classical PSI. Secondly, the term PSI works only if the generated subharmonics are within the free internal wave frequency range (then PSI falls into the category of resonant-triad interactions). Identifying the main cause of subharmonics with PSI (what seems to be the case in the work by MacKinnon and Winters, 2003, 2007), then, leads to a false conclusion that, once we go beyond the critical latitude where both subharmonics are forced, then there is no instability altogether. In our work, however, we observe a smooth transition of the instability while passing the critical latitude; moreover, the forced subharmonics for the case $35°$ N are stronger than in cases $0°$ and $10°$ N. This signifies that the term PSI should be either replaced or generalized.

Forced internal waves seem to be underestimated or overlooked in comparison with progressive ones. The dispersion relation (3.1) from linear theory suggests that progressive internal waves are characterized by frequencies in the range (f, N_b), thus overlooking other internal waves. However, as we have shown, internal waves of comparable energies are observed in the ranges $[0, f)$ and $(N_b, +\infty)$. The impact of forced waves on mixing, however, as was suggested in the work by Teoh et al. (1997), can be even greater than that of progressive waves. Trapped waves accumulate energy more quickly and hence are more susceptible to overturning.

The critical latitude is not the limit beyond which subharmonics are not generated. This misconception was discussed above in relation with PSI. In addition, we should add that, as the frequencies of subharmonics generated by PSI are not exactly $\omega_0/2$, the forced waves of subharmonic frequencies outside the range (f, N_b) are generated before the critical latitude θ_{cr} and, thus, formally, PSI ceases to exist even earlier than latitude reaches θ_{cr}. The subharmonic instability is rather insensitive to whether the participating waves are forced or progressive: it exists when both generated subharmonics are progressive, when only one of them is progressive and, lastly, when none of them is progressive.

Interharmonics are not Doppler shifted frequencies. This follows from the comparison of spectra in the Eulerian, Lagrangian and barotropic-Lagrangian reference frames. Moreover, and here we return once again to the forced *vs.* progressive waves concept, the waves of subharmonic frequencies in the subinertial range are trapped waves localized in patches near the generation sites, whereas their counterparts, interharmonics separated from them by multiples of tidal frequency, are progressive internal waves manifested in internal wave beams.

The last idea concerns resonant versus non-resonant triad interaction. Both types are present in the simulations. We showed that the subharmonics generated by an instability of the internal wave beam of tidal frequency are generated through a discrete set of resonant triad interactions. In the example shown in this thesis, one dominant resonant triad interaction occurred in the vicinity of the tidal beam on top of the ridge and another resonant triad interaction occurred on

the side of the ridge. The fact that the two subharmonics and the tidal frequency waves form a resonant triad was not obvious. Even less obvious is the fact that in several cases a similar mechanism, which, however, cannot be classified as a resonant triad interaction, generates forced subharmonics of comparable energies. This mechanism can not be explained in terms of resonant triad interaction, as the term no longer applies.

Moreover, if two waves of different frequencies already exist (for example, two strong subharmonics are already generated) they will generate other waves at the combination frequencies, regardless of whether those waves fall into the free internal wave range or not. The wave of a combination frequency at a given location is generated by the forcing coming from the nonlinear term $\mathbf{u} \cdot \nabla \mathbf{u}$. One could think of this forcing as of a small oscillating cylinder put at the location. An oscillating cylinder produces St Andrew's Cross pattern corresponding to internal waves satisfying the dispersion relation. The particular direction of motion is irrelevant to the pattern of emerging waves: the cylinder can oscillate in the vertical, in the horizontal or in a diagonal direction. Similarly, in the vicinity of the oscillation, the wave at a combination frequency can have arbitrary wavenumbers, but the progressive internal waves emanating from the region will have wavenumbers consistent with the dispersion relation. Thus, once two waves of different frequencies intersect, the waves at all the combination frequencies must be generated. If their frequencies fall within the free internal wave range, they will be progressive internal waves with appropriate wavenumbers. If their frequencies fall out of the range, they will be forced waves.

6.3   Energy cascade scenario

As the final point of the thesis, let us project some of the obtained results and generalizations onto the internal wave interaction in the deep ocean. This can be done in the form of a hypothetical energy cascade scenario. Think of the ocean as a hypothetical tank with stratified fluid; the ocean has limited energy capacity.

I. Tidal flows over topography and wind feed energy into internal waves at two main frequencies ω_0 and f.

II. Energy distributes in the continuum of frequencies through nonlinear interactions:

- Energy flows into combination frequencies of ω_0 and f (in particular, into tidal harmonics $n\omega_0$, $n \in \mathbb{N}$). As the Coriolis frequency f changes with latitude, the combination frequencies cover the continuum of frequencies.

- Internal waves are intrinsically unstable and the instabilities, like the ones considered in this thesis, lead to further flow of energy from the strong frequencies to a continuum

163

of frequencies consisting of harmonics and interharmonics. Values of interharmonics depend on both topography and latitude, so the set of interharmonic and harmonic frequencies fills the frequency space densely.

III. The spectrum relaxes to the smooth quasi-stable spectrum without pronounced peaks (reminiscent of Kolmogoroff's spectrum) due to the following mechanisms:

- Dissipation plays a role in broadening the strong peaks in the spectrum.
- Stronger waves are more nonlinear, weaker waves are less so. Thus, the stronger peaks in the spectrum will continually lose energy toward the weaker ones through nonlinear interactions, whereas the weaker peaks (such as interharmonics) will continually grow, until they merge with the rest.

IV. Energy from tides and winds is fed into internal wave field at an almost constant rate. As the energy of internal wave field in the ocean rises, so does the dissipation and mixing rate. Eventually, a balance is achieved when the dissipation rate equals the rate at which energy is injected.

V. Forced waves are the first candidates to break. At any given location, the strong progressive waves, like the tidal harmonics for $n \leq \lfloor N_{\mathrm{b}}/\omega_0 \rfloor$, can release their energy to the background spectrum through nonlinear interactions and instabilities, thus generating other progressive waves that carry energy away from the energetic spot. The forced waves, on the other hand, do not have this luxury: they accumulate energy locally until they break.

Behind the complexity of internal wave dynamics in the deep ocean stands a relatively simple mathematical function representing the stable Garrett-Munk spectrum. In this thesis, we discerned some rules that may play a role in governing the existence of this function.

Bibliography

Bartlett, M. (1950). Periodogram analysis and continuous spectra. *Biometrika 37*, 1–16.

Bell, B., D. B. Percival, and A. T. Walden (1993). Calculating Thomson's spectral multitapers by inverse iteration. *Journal of Computational and Graphical Statistics 2*, 119–130.

Bell, J., P. Collela, and H. Glaz (1989). A second-order projection method for the incompressible Navier-Stokes equations. *Journal of Computational Physics 85*, 257–283.

Bell, J. and D. Marcus (1992). A second-order projection method for variable-density flows. *Journal of Computational Physics 101*, 334–348.

Bell, J., J. Solomon, and W. Szymczak (1989). A second-order projection method for the incompressible Navier-Stokes equations on quadrilateral grids. In *AIAA 9th Computational Fluids Dynamics Conference*, Buffalo, New York. American Institute of Aeronautics and Astronautics.

Bell, T. (1975). Lee waves in stratified flows with simple harmonic time dependence. *Journal of Fluid Mechanics 67*, 705–722.

Bernoulli, D. (1753). Mèmoire sur l'orbite apparente du soleil autour de la terre, en ayant égard aux perturbations produites par les actions de la lune et des planètes principales. *Mémoires de l'Académie Royale des Sciences et Belles Lettres, Berlin*.

Bertrand, D. and R. Laprise (2002). Spectral decomposition of two-dimensional atmospheric fields on limited-area domains using the discrete cosine transform (dct). *Monthly Weather Review 130*, 1812–1829.

Beveridge, W. (1921). Weather and harvest cycles. *The Economic Journal 31*(124), 429–452.

Bigelow, H. (1931). *Oceanography: Its scope, problems, and economic importance.* The Riverside Press Cambridge.

Broersen, P. M. T. (2000). Facts and fiction in spectral analysis. *IEEE Transactions on Instrumentation and Measurement 49*(4).

Cameron, W. L. (1995, December). Precise expression relating the fourier transform of a continuous signal to the fast fourier transform of signal samples. *IEEE Transactions on Signal Processing 43*(12), 2811–2821.

Carter, G. and M. Gregg (2006). Persistent near-diurnal internal waves observed above a site of m2 barotropic-to-baroclinic conversion. *Journal of Physical Oceanography*. in press.

Chashechkin, Y. D. and V. Nekludov (1990). Nonlinear interaction of bundles of short two-dimensional monochromatic internal waves in an exponentially stratified liquid. *Dokl. Earth Sci. Sect. 311*, 235–238.

Clairaut, A.-C. (1754). Mèmoire sur l'orbite apparente du soleil autour de la terre, en ayant égard aux perturbations produites par les actions de la lune et des planètes principales. *Mémoires de Mathématique et de Physique de l'Académie Royale des Sciences* (9), 521–564.

Cooley, J. and J. Tukey (1965, April). An algorithm for the machine computation of complex fourier series. *Mathematics of Computation 19*(2), 297–301.

Copenhaver, B. P. (1991). A tale of two fishes: magical objects in natural history from antiquity through the scientific revolution. *Journal of the History of Ideas 52*, 373–398.

Cramér, H. (1942). On harmonic analysis in certain functional spaces. *Arkiv för Matematik, Astronomi och Fysik 28B*, 1–7.

Daniell, P. (1946). Discussion on the symposium on autocorrelation in time series. *Journal of the Royal Statistical Society 8*, 88–90.

de Silva, I., J. Imberger, and G. Ivey (1997). Localized mixing due to a breaking internal wave ray at a sloping bed. *Journal of Fluid Mechanics 350*, 1–27.

DeFerrari, H. A. and H. B. Nguyen (1986). Acoustic reciprocal transmission experiments, florida straits. *Journal of the Acoustical Society of America 79*(2), 299–315.

Dewar, W. K., R. J. Bingham, R. L. Iverson, D. P. Nowacek, L. C. S. Laurent, and P. H. Wiebe (2006). Does the marine biosphere mix the ocean? *Journal of Marine Research 64*, 541–561.

Eberhard, A. (1973, February). An optimal discrete window for the calculation of power spectra. *IEEE Transactions on Audio and Electroacoustics AU-21*(1), 37–43.

Einstein, A. (1914). Méthode pour la détermination de valeurs statistiques d'observations concernant des grandeurs soumises á des fluctuations irréguliéres. *Archives des sciences physiques et naturelles 4 37*, 254–256.

Ekman, V. W. (1904). On dead water. *Scientific results of the North Polar Expedition, 1893–1896 5*, 1–152.

Ekman, V. W. (1931, March 27th). On internal waves. In *The mixing question, viewed theoretically and practically, together with a consideration of internal waves. Reports of the proceedings of a special meeting*, Copenhagen, pp. 5–34.

Errico, R. M. (1985). Spectra computed from a limited area grid. *Monthly Weather Review 113*, 1554–1562.

Ersoy, O. K. (1994). A comparative review of real and complex Fourier-related transforms. *Proceedings of IEEE 82*(3), 429–447.

Euler, L. (1748). *Introductio in Analysin Infinitorum*. Lausanne: Marc-Michel Bousquet.

Farge, M. (1992). Wavelet transforms and their applications to turbulence. *Annual Reviews of Fluid Mechanics 24*, 395–457.

Fjeldstad, J. E. (1933). *Interne Wellen*, Volume 10. Geofys. Publikasjoner.

Flatté, S. M., R. Dashen, W. Munk, K. M. Watson, and F. Zachariasen (1979). *Sound transmission through a fluctuating ocean*. Cambridge University Press.

Fourier, J. (1822). *Théorie Analytique de la Chaleur*. Paris: F. Didot.

Furuchi, N., T. Hibiya, and Y. Niwa (2005). Bispectral analysis of energy transfer within the two-dimensional oceanic internal wave field. *Journal of Physical Oceanography 35*, 2104–2109.

Furue, R. (2003). Energy transfer within the small-scale oceanic internal wave spectrum. *Journal of Physical Oceanography 33*, 267–282.

Gade, S. and H. Herlufsen (1987). Use of weighted functions in dft/fft analysis (part 1). *Brüel & Kjær Technical Review* (3), 338–352.

Gander, W. and W. Gautschi (2000). Adaptive quadrature—revisited. *BIT 40*(1), 84–101.

Garrett, C. (2003). Mixing with latitude. *Nature 422*, 477–478.

Garrett, C. and E. Kunze (2007). Internal tide generation in the deep ocean. *Annual Review of Fluid Mechanics 39*, 57–87.

Garrett, C. and W. Munk (1975). Space-time scales of internal waves: a progress report. *Journal of Geophysical Research 80*, 291–297.

Gassendi, P. (1654). *Opera Omnia*, Volume I.

Gauss, C. F. (1866). Nachlass: Theoria interpolationis methodo nova tractata. In *Carl Friedrich Gauss, Werke, Band 3*, pp. 265–303. Göttingen: Königlichen Gesellschaft der Wissenschaften.

Gerkema, T., C. Staquet, and P. Bouruet-Aubertot (2006). Decay of semi-diurnal internal-tide beams due to subharmonic resonance. *Geophysical Research Letters 33*(L08604).

Godfrey, M. D. (1965). An exploratory study of the bispectrum of economic time series. *Applied Statistics (London 14*, 48–69.

Goldsteine, H. (1977). *A History of Numerical Analysis from the 16th Through 19h Century*, pp. 249–253. New York: Heidelberg.

Görtler, H. (1943). Uber eine schwingungserscheinung in flussigkeiten mit stabiler dichteschichtung. *Zeitschrift für angewandte Mathematik und Mechanik 23*, 65.

Gudger, E. W. (1930). Some old figures of the shipholder, echeneis or remora, holding the ship. *Isis 13*(2), 340–352.

Harris, F. J. (1978, January). On the use of windows for harmonic analysis with the discrete fourier transform. *Proceedings of the IEEE 66*(1), 51–83.

Hasselman, K., W. Munk, and G. MacDonald (1963). *Bispectra of ocean waves*, pp. 125–139. New York: Wiley.

Hasselmann, K. (1967). A criterion for nonlinear wave stability. *Journal of Fluid Mechanics 30*, 737–739.

Heideman, M. T., D. H. Johnson, and C. S. Burrus (1985). Gauss and the history of the fast Fourier transform. *Archive for History of Exact Science 34*, 265–277.

Helland-Hansen, B. and F. Nansen (1909). *The Norwegian Sea: Report on Norwegian fishery and marine investigations*, Volume II. Kristiania.

Hendershott, M. C. (1980). *Evolution of physical oceanography: Scientific surveys in honor of Henry Stommel*, pp. 292–341. The MIT Press.

Hibiya, T., Y. Niwa, and K. Fujiwara (1998). Numerical experiments of nonlinear energy transfer within the oceanic internal wave spectrum. *Journal of Geophysical Research 103*(C9), 18715–18722.

Holloway, G. (1980). Oceanic internal waves are not weak waves. *Journal of Physical Oceanography 10*, 906–914.

Holloway, P. and M. Merrifield (1999). Internal tide generation by seamounts, ridges and islands. *Journal of Geophysical Research 104*(25), 937–951.

Javam, A., J. Imberger, and S. Armfield (1999). Numerical study of internal wave reflection from sloping boundaries. *Journal of Fluid Mechanics 396*, 183–201.

Javam, A., J. Imberger, and S. Armfield (2000). Numerical study of internal wave-wave interactions in a stratified fluid. *Journal of Fluid Mechanics 415*, 65–87.

Kammler, D. W. (2000). *A first course in Fourier analysis*. Prentice Hall.

Kamykowski, D. (1974). Possible interactions between phytoplankton and semidiurnal internal tides. *Journal of Marine Research 32*, 67–89.

Khatiwala, S. (2003). Generation of internal tides in an ocean of finite depth: analytical and numerical calculations. *Deep-Sea Research 50*, 3–21.

Kim, Y. C. and E. J. Powers (1979). Digital bispectral analysis and its applications to nonlinear wave interactions. *IEEE Transactions on Plasma Science PS-7*(2), 120–131.

Kistovich, A. and Y. Chashechkin (1991). Nonlinear interaction of two-dimensional packets of monochromatic internal waves. *Izv. Atmos. Ocean Phys. 27*, 946–951.

Knuth, D. E. (1992). Two notes on notation. *American Mathematical Monthly 99*(5), 403–422.

Koudella, C. and C. Staquet (2006). Instability mechanisms of a two-dimensional progressive internal gravity wave. *Journal of Fluid Mechanics 548*, 165–196.

Kundu, P. K. and I. M. Cohen (2002). *Fluid mechanics* (Second ed.). Elsevier Science.

LaFond, E. C. (1962). *The sea*, Volume I, pp. 731–763. Interscience Publishers.

Lagrange, J. L. (1762). Solution de différents problèmes de calcul intégral. *Miscellanea Taurinensia ou Mélanges de Turin III*.

Lamb, H. (1932). *Hydrodynamics* (sixth ed.). New York: Dover.

Lamb, K. (1994). Numerical experiments of internal wave generation by strong tidal flow across a finite amplitude bank edge. *Journal of Geophysical Research 99*, 843–864.

Lamb, K. (2004). Nonlinear interaction among internal wave beams generated by tidal flow over supercritical topography. *Geophysical Research Letters 31*(L09313).

Lamb, K. G. (2006). Energy and pseudoenergy flux in the internal wave field generated by tidal flow over topography. *Continental Shelf Research*. submitted.

LeBlond, P. (2002). Ocean waves: half-a-century of discovery. *Journal of Oceanography 58*, 3–9.

Legg, S. and K. M. H. Huijts (2006). Preliminary simulations of internal waves and mixing generated by finite amplitude tidal flow over isolated topography. *Deep-Sea Research II 53*, 140–156.

Lii, K. S., M. Rosenblatt, and C. VanAtta (1976). Bispectral measurements in turbulence. *Journal of Fluid Mechanics 77*, 45–62.

Liu, P. (1994). *Wavelets in geophysics*, pp. 151–166. Academic Press.

MacKinnon, J. and K. Winters (2003). Spectral evolution of bottom-forced internal waves. In *Proceedings of the 13th 'Aha Huliko'a Hawaiian Winter Workshop*, pp. 73–83.

MacKinnon, J. and K. Winters (2005). Tidal mixing hotspots governed by rapid parametric subharmonic instability. *Journal of Physical Oceanography*. submitted.

MacKinnon, J. A. and K. B. Winters (2007). Tidal mixing hotspots governed by rapid parametric subharmonic instability. *Journal of Physical Oceanography*. submitted.

McEwan, A. (1971). Degeneration of resonantly excited standing internal gravity waves. *Journal of Fluid Mechanics 50*, 431–448.

McEwan, A. (1973). Interactions between internal gravity waves and their traumatic effect on a continuous stratification. *Boundary-Layer Meteorology 5*, 159–175.

McGowan, J. A. and T. L. Hayward (1978). Mixing and oceanic productivity. *Deep-Sea Research 25*, 771–793.

Meyers, S. D., B. G. Kelly, and J. J. O'Brien (1993). An introduction to wavelet analysis in oceanography and meteorology: With application to the dispersion of Yanai waves. *Monthly Weather Review 121*, 2858–2866.

Moore, S. E. and R.-C. Lien (2007). Pilot whales follow internal solitary waves in the South China Sea. *Marine Mammal Science 23*(1), 193–196.

Mowbray, D. and B. Rarity (1967). A theoretical and experimental investigation of the phase configuration of internal waves of small amplitude in a density stratified fluid. *Journal of Fluid Mechanics 28*, 1–16.

Müller, P., G. Holloway, F. Henyey, and N. Pomphrey (1986). Nonlinear interactions among internal gravity waves. *Reviews of Geophysics 24*(3), 493–536.

Munk, W. (1980). *Evolution of physical oceanography: Scientific surveys in honor of Henry Stommel*, pp. 264–291. The MIT Press.

Munk, W. and C. Wunsch (1998). Abyssal recipes II: energetics of tidal and wind mixing. *Deep Sea Research 45*, 1977–2010.

Nansen, F. (1902). Oceanography of the North Polar Basin. The Norwegian north polar expedition 1893-96. *Scietific Results III*(9).

New, A. L. (1988). Internal tidal mixing in the bay of biscay. *Deep-Sea Research 35*, 691–697.

Olbers, D. (1983). Models of the oceanic internal wave field. *Reviews of Geophysics and Space Physics 21*, 1567–1606.

Olbers, D. and N. Pomphrey (1981). Disqualifying two candidates for the energy balance of oceanic internal waves. *Journal of Physical Oceanography 11*, 1423–1425.

Orlanski, I. (1981). Energy transfer among internal gravity modes: weak and strong interactions. *Journal of Geophysical Research 86*, 4103–4124.

Osborne, A. R. and T. L. Burch (1980). Internal solitons in the Andaman sea. *Science 208*(4443), 451–460.

Parker, B. (1999). Waves beneath the sea. *Mariners Weather Log 43*(2), 11–17.

Peacock, T. and A. Tabaei (2005). Visualization of nonlinear effects in reflecting internal wave beams. *Physics of Fluids 17*(061702).

Percival, D. and A. Walden (1993). *Spectral analysis for physical applications: multitaper and conventional univariate techniques*. Cambridge University Press.

Percival, D. B. (1993). Three curious properties of the sample variance and autocovariance for stationary processes with unknown mean. *The American Statistician 47*(4), 274–276.

Pettersson, O. (1908). Strömstudier vid ö stersjöns portar. *Svenska Hydrografisk-Biologiska Kommissionens Skrifter III*.

Phillips, O. (1967). Theoretical and experimental studies of gravity wave interactions. *Proceedings of the Royal Society of London 299*(1456), 104–119.

Pingree, R. and A. New (1991). Abyssal penetration and bottom reflection of internal tidal energy in the bay of biscay. *Journal of Physical Oceanography 21*, 28–39.

Press, W. H., S. A. Teukolsky, W. T. Vetterling, and B. P. Flannery (1992). *Numerical Recipes in C*. Cambridge University Press.

Rayleigh, L. (1883). Investigation of the character of the equilibrium of an incompressible heavy fluid of variable density. *Proceedings of the London Mathematical Society 14*, 170–178.

Schuster, A. (1906). On the periodicities of sunspots. *Philosophical Transactions of the Royal Society of London 206*, 69–100.

Shea, R. E. and W. W. Broenkow (1982). The role of internal tides in the nutrient enrichment of Monterey Bay, california. *Estuarine, Coastal and Shelf Science 15*, 57–66.

Shore, J. A. (1996). *Tidal residual circulation over an axisymmetric seamount: seamount geometry effects*. Ph. D. thesis, University of British Columbia.

Silber, G. K. and M. A. Smultea (1990). Harbor porpoises utilize tidally-induced internal waves. *Bulletin of the Southern California Academy of Sciences 86*(3), 139–142.

Slepian, D. (1978). Prolate spheroidal wave functions, fourier analysis, and uncertainty — v: The discrete case. *The Bell System Technical Journal 57*, 1371–1430.

Staquet, C. and J. Sommeria (2002). Internal gravity waves: from instabilities to turbulence. *Annual Review of Fluid Mechanics 34*, 559–593.

Stashchuk, N. and V. Vlasenko (2005). Topographic generation of internal waves by nonlinear superposition of tidal harmonics. *Deep-Sea Research I 52*, 605–620.

Stewart, B. and W. Dodgson (1879). Preliminary report to the committee on solar physics on a method of detecting the unknown inequalities of a series of observations. *Proceedings of the Royal Society of London 29*, 106–122.

Stokes, G. (1847). On the theory of oscillating waves. *Transactions of the Cambridge Philosophical Society 8*, 441–455.

Stokes, G. (1879). Note on the paper by stewart and dodgson. *Proceedings of the Royal Society of London 29*, 122–123.

Sverdrup, H. U. (1955). The place of physical oceanography in oceanographic research. *Journal of Marine Research 14*, 287–294.

Tabaei, A., T. Akylas, and K. Lamb (2005). Nonlinear effects in reflecting and colliding internal wave beams. *Journal of Fluid Mechanics 526*, 217–243.

Tang, X. and F. D. Tappert (1997). Effects of internal waves on sound pulse propagation in the Straits of Florida. *IEEE Journal of Oceanic Engineering 22*(2), 245–255.

Teoh, S., G. Ivey, and J. Imberger (1997). Experimental study of two intersecting internal waves. *Journal of Fluid Mechanics 336*, 91–122.

Thomson, W. (1878). Harmonic analyzer. *Proceedings of the Royal Society of London 27*, 371–373.

Thorpe, S. (1968). On the shape of progressive internal waves. *Philosophical Transactions of the Royal Society of London. Series A, Mathematical and Physical Sciences 263*(1145), 563–614.

van Haren, H., L. Maas, and H. van Aken (2002). On the nature of internal wave spectra near a continental slope. *Geophysical Research Letters 29*(12).

Walker, J. M. (1991). Farthest North, dead water and the Ekman spiral. Part 2: Invisible waves and a new direction in current theory. *Weather 46*(1), 158–164.

Welch, P. (1967). The use of Fast Fourier Transform for the estimation of power spectra:A method based on time averaging over short, modified periodograms. *IEEE Transactions on Audio and Electroacoustics 15*, 70–73.

Whittaker, E. and G. Robinson (1944). *The Calculus of Observations* (4 ed.). London: Blackie and Son.

Winters, K. B. and E. A. D'Asaro (1997). Direct simulation of internal wave energy transfer. *Journal of Physical Oceanography 27*, 1937–1945.

Zeilon, N. (1912). On tidal boundary-waves and related hydrodynamical problems. *Kungl. Svenska Vet. Akad. Handl. B47*(4).

Zeilon, N. (1913). On the seiches of the gullmar fjord. *Svenska Hydrogr.-Biolog. Kommissionens skrifter V*.

Zeilon, N. (1934). Experiments on boundary tides. *Goteborg Vetenskamh. Handl Folj.5 B3*(10).